FLUX-FREE ULTRASONIC SOLDERING OF ALUMINUM AND STAINLESS STEEL

Hamid Reza Faridi

M.S. University of Pierre and Marie Curie, 1988

A thesis presented to the faculty of the
Oregon Graduate institute of Science and Technology
In partial fulfillment of the
requirements for the degree
Doctor of Philosophy
in
Materials Science and Engineering

February 2000

The dissertation "Flux-Free Ultrasonic Soldering of Aluminum and Stainless Steel" by Hamid Reza Faridi has been examined and approved by the following Examination Committee:

Jack H. Devletian, Thesis Advisor
Professor
Department of Materials Science and Engineering
Oregon Graduate Institute of Science and Technology

William E. Wood
Professor
Department of Materials Science and Engineering
Oregon Graduate Institute of Science and Technology

Lemmy L. Meekisho
Associate Professor
Department of Materials Science and Engineering
Oregon Graduate Institute of Science and Technology

Jack McCarthy
Assistant Professor
Department of Materials Science and Engineering
Oregon Graduate Institute of Science and Technology

ACKNOWLEDGMENTS

First of all, I would like to thank my thesis advisor, Dr. Jack Devletian for providing financial support and his guidance during the course of this research. I would also like to thank Dr. Bill Wood for providing additional financial support.

I am very grateful to my committee members, Dr. Bill Wood, Dr. Lemmy Meekisho, and Dr. Jack McCarthy from the Materials Science and Engineering Department at OGI, for their time and effort in reviewing this manuscript.

I must thank Dr. David G. Atteridge, Dr. Margaret Ziomek-Moroz and Dr. Milton R. Scholl for their generous support and advice, as well as the staff of the Materials Science Department: Mr. Robert Turpin, Ms. Roxanne Metzker, Mr. Douglas Davis and Mr. Andrew Huffstutter. Also to my fellow students in the Materials Science and Engineering Department, especially my dear friends Dr. Xiao Chen, Dr. Jinhong Yang and Dr. Wei Su. Without them, my study at O.G.I. would not be such a pleasant experience.

Furthermore I must extend my deep appreciation to Mr. Frederick J. Neimann and Mr. Kenneth E. Schultz for their support and advice.

Additional thanks go to Tektronix, Inc. for providing partial financial support during the course of this research.

Special thanks to my wife Hengameh, who makes this world a much better place.

TABLE OF CONTENTS

Abstract

Flux-free ultrasonic soldering of 2024 Alclad and 304 stainless steel was conducted to determine the conditions to produce the highest joint shear strength in lap joints. Prior to this time, ultrasonic energy was always applied directly to the molten liquid pool to promote excellent coupling and fluxing by a mechanism of cavitation of the substrate. In this study, the ultrasonic energy was applied to a solid aluminum manifold (heated to the soldering temperature) and further transmitted through the aluminum or stainless steel test sheets to form a lap joint containing solder. Fundamental studies on aluminum and stainless steel samples revealed that the oxide removal and subsequent solder wetting resulted from the erosion of the substrate surface by the cavitation action caused by the ultrasonic vibrations. Although aluminum was successfully joined by the ultrasonic soldering, stainless steel could not be ultrasonically soldered regardless of the surface preparation. Therefore, it may be impractical to chemically clean stainless steel and expect any wetting without a strong fluxing agent. In fact, the results showed that practical soldering of stainless steel could only be achieved by plating the stainless steel substrate surfaces prior to soldering. The Al_2O_3 oxidation reaction is far more stable than the Cr_2O_3 reaction, however, the results imply that the rate of oxide formation and growth after chemical cleaning of stainless steel was several times faster than that for aluminum and the applied ultrasonic vibrations were not able to remove the thicker Cr_2O_3 from the stainless steel substrate surfaces. with the results of this research, it is now possible to transmit ultrasonic energy through a solid to joint aluminum or stainless steel in a lap joint, it is also more feasible to optimize the most effective soldering variables for increasing the reliability and integrity of an ultrasonic soldering operation.

LIST OF FIGURES

LIST OF TABLES

Abstract

Flux-free ultrasonic soldering of 2024 Alclad and 304 stainless steel was conducted to determine the conditions that produce the highest shear strength in lap joints. Prior to this time, ultrasonic energy was always applied directly to the molten liquid pool to promote excellent coupling and fluxing by a mechanism of cavitation of the substrate. In this study, the ultrasonic energy was applied to a solid aluminum manifold (heated to the soldering temperature) and further transmitted through the aluminum or stainless steel test sheets to form a lap joint containing solder. The effect of shielding gas and surface preparation on the effectiveness of ultrasonic soldering was determined. Surface preparations included: (a) degreasing, (b) chemical cleaning, (c) tin-plating without solder filler metal addition and tin-plating with solder filler metal addition. Other variables such as ultrasonic soldering time and soldering temperature were investigated. In all cases, the solder alloy used in this study was the near eutectic (Sn-rich) 70Sn-30Pb composition, which has a freezing range of approximately 192 ° – 183 °C. Fundamental studies on aluminum and stainless steel samples revealed that the oxide removal and subsequent solder wetting resulted from the erosion of the substrate surface by the cavitation action caused by the ultrasonic vibrations. Although aluminum was successfully joined by ultrasonic soldering, stainless steel could not be ultrasonically soldered regardless of the surface preparation. The Al_2O_3 oxidation reaction is far more stable than the Cr_2O_3 reaction, however the results imply that the rate of oxide formation and growth after chemical cleaning of stainless steel was several times faster than that for aluminum and the applied ultrasonic vibrations were not able to remove the thicker Cr_2O_3 from the stainless steel substrate surfaces for further wetting. Therefore, it may be impractical to chemically clean stainless steel and expect any wetting without a chemical fluxing agent. In fact, the results showed that practical soldering of stainless steel could only be achieved by plating the stainless steel substrate with Sn or other solder-compatible coatings. The Sn plating procedure effectively removes the Cr_2O_3 layer of the substrate and provides a pristine surface for soldering. Sn plating is always preceded by a Ni strike which replaces the Cr_2O_3 layer with a thin film of Ni which not only bonds the stainless steel to the subsequent Sn plating but also provides a diffusion barrier during the subsequent soldering reactions as proven in this study. The results also showed that increasing the soldering temperature and time improves the quality of the solder joint and increase the joint strength. The joints prepared in an argon environment demonstrated higher strength. Argon prevented the oxidation of substrate surfaces and the molten solder. The effect of solder joint spacing on its strength was investigated through the experimental results and with the aid of finite element method (FEM). The results confirmed that there is an optimum joint spacing in which the strength is at maximum. with the results of this research, it is now possible to transmit ultrasonic energy through a solid to join aluminum and stainless steel in a lap joint, it is also more feasible to optimize the most effective soldering variables for increasing the reliability and integrity of an ultrasonic soldering operation.

Chapter 1

Introduction and Problem Definition

Soldering is an old, well-known technology that produces a joint by heating the filler metal to a suitable temperature[1]. Today, soldering technology is applied to a vast range of fields from the fabrication of industrial heat exchangers, air conditioners, and refrigerators to the packaging of integrated circuit chips and printed circuit boards[2-4].

Soldering is a metallurgical joining process that is generally divided in three major stages:

Physical Stage: Consists of the heating of the work piece, melting and flowing the solder to wet the substrate and filling the joint gap by the capillary effect.

Metallurgical Stage: May consist of a substantial, uneven mass transfer across the interface and could be characterized by solid-liquid interaction.

Solidification Stage: Depends on the cooling rate and is characterized by the solder joint microstructure[5-7].

Soldering relies on the wetting and the capillary attraction effect and it may not require diffusion or intermetallic phase formation at the joint interfaces. However, intermetallic compound formation at the solder-base metal interface is often an indication of good wetting. Usually, formation of an intermetallic layer at solder-substrate interface affects the wettability and may provide a stronger joint. If the compound completely isolates the substrate surface from the molten solder, the contact angle would increase and de-wetting might happen because the surface tension of the compound is generally lower than that of the base metal[8-10]. Formation and growth of the intermetallics at the interfaces may also affect the mechanical and physical properties of the joint. Hard and brittle intermetallic layers at the joint interfaces are more desirable sites for initiating the crack and failure when the solder joint is subjected to deformation conditions. In service or even during the storage, most intermetallics continue to grow. This growth is the result of aging. If the growth is then too fast, it would be detrimental not only because the intermetallic layer becomes thicker, but in addition, the joint will also be depleted from its element constituents[11 - 18].

Conventional soldering generally requires a fluxing agent to promote wetting and improve solderability. Flux removes the oxide film and protects the clean surface. It also improves spreading by modifying the interfacial tensions and assists to remove the reaction products, but the flux residues are corrosive and must be removed. The cleaning process is costly and the cleaning agents are not environmentally friendly. They can damage the drinking water reservoirs and cause ozone layer depletion. The need for using chemical solvents such as CFC's, to remove non-conductive and corrosive residues as a result of conventional flux based soldering makes flux-free soldering an attractive alternate.

Fluxless ultrasonic soldering was first used in Germany in 1936. Since then many high-intensity ultrasonic instruments have been manufactured and used to achieve a fluxless operation. One of the primary applications of high-intensity ultrasonics is in soldering difficult-to-solder materials such as aluminum and stainless steel. Early ultrasonic soldering machines were similar to conventional solder guns and operated in the same manner. In the earliest models, the working end of the transducers were used to apply sonic energy to the work piece or molten solder as a soldering tip. In modern models, the soldering tips are separated from the transducers and different sizes of soldering pots with a heating system attached to them are available. There are numerous parameters that affect a fluxless ultrasonic soldering. Among these parameters, degreasing the substrate surface, preparing a suitable preheating, and the type of solder alloy have major impacts on the solder joint. Other factors such as, surface tension, fluidity of the molten solder, and intensity of the applied ultrasonic energy have also fundamental effects on soldering[4, 19, 20].

Currently the state-of-art in ultrasonic soldering is extremely active due to the need for new flux-free soldering methods for the electronics industry. Although ultrasonic soldering has been well known as a "fluxless" means of soldering since the 1940's, it was not until 1976, that Antonevich[4] and Hunicke[21] provided fundamental evidence of the mechanism of ultrasonic soldering. They showed that structural shapes of aluminum alloys could be readily "tinned" in a bath activated by ultrasonic energy without the aid of fluxes. This technique was utilized in large-scale manufacturing processes in the late 1970's to join aluminum bell tube air conditioner assemblies. Furthermore, Hunike[21] showed that it was possible to wet stainless steel without flux by dipping into a zinc-based solder activated by ultrasonic energy. Although these early uses of ultrasonic energy for flux free soldering of aluminum (primarily) continued, it is only within this decade that the potential cost benefits of flux-free soldering have been actively pursued by the electronics assembly industry. In 1988, AT&T Bell Laboratories[22] patented the use of ultrasonic soldering as a coating method for electronic components. This technique produces solder bumps on silicon chips, chip carriers and circuit boards. The component is covered with a photoresist mask, leaving exposed the pads on the component. Then, solder is applied by immersing the component surface while ultrasonic energy is activated for 5 seconds in the bath, so that the solder wets the exposed pads. The mask acts as a mold for the solder to control the solder bump height[22]. In 1998, the first outstanding application of ultrasonic energy for high-production soldering of through-hole joints on printed circuit boards was achieved without the need to apply flux (and subsequent flux removal after soldering) by Garrecht et al[23] of Ersa Lottechnik Company in Germany. Garrecht et al[23] patented the application of ultrasonic vibrations to wave soldering of printed circuit boards. This represents the first major breakthrough for the use on ultrasonic energy in a high-production electronic process. In this patent, the solder wave is vibrated by means of at least one ultrasonic sonotrode. The surface of the sonotrode is directly in contact with the passing solder wave; and, the printed circuit boards are guided just above the surface of the sonotrode. The ultrasonic vibrations causes cavitation and rapid disintegration of the oxide layer on the copper tracks of the printed circuit board to produce excellent wetting (without flux). In addition to cost savings arising from flux-free and residue-free soldering, Kurtz[24] showed that ultrasonic soldering required far less nitrogen shielding gas to protect the copper during soldering. International Business Machines[25] patented a method to utilize ultrasonic energy to remove destructive solder balls from electronics assemblies. Biancini[26], Chu et al[27] and Ogashiwa et al[28] have used ultrasonically assisted methods to produce solder bumps individually on flip chips without masks. Ultrasonic soldering can provide small quantities of devices without the need for expensive solder masks. Saxty[29] in England also report that ultrasonically tinned leads have higher solderability and resistance to aging compared with flux tinned leads. Due to the cavitation produced by ultrasonic soldering, gold plating can be removed thoroughly and quickly. It can be used to replace conventional soldering provided the joining procedure is changed[29]. Hoskings[30] and Jellison et al[31] present ultrasonic soldering as an advanced process that is materials and geometry dependent.

Flux-free ultrasonic soldering of large surfaces in lap joints of thin aluminum and stainless sheets are the major concerns in this study. Regarding this problem, Vianco et al[32] conducted an extensive study of the wetting and capillary between two parallel sheets of copper when dipped into an ultrasonically activated solder bath. Owing to the requirement that solder must contact the faying surfaces in order to support the oxide removal (cavitation) process, capillary rise above the reservoir surface was not achieved. Although the ultrasonic energy was dispersed within the substrate body so that the cavitation process could potentially operate on surfaces of the substrate that were not in line-of-sight of the ultrasonic horn, Vianco et al[32] showed that immersion of the substrate into the solder bath would be a requirement for ultrasonic soldering to produce a joint. Immersion in pure tin was shown to wet better than immersion in tin-lead alloys. Furthermore, they[32] proved that cavitatioin was not the only mechanism of oxide removal and wetting. In experiments using a point source ultrasonic horn, Vianco et al[32] demonstrated that oxide removal by means solder cavitation resulted from a combination of mechanical erosion and coupling of the ultrasonic energy to the substrate geometry.

Research Objectives

Understanding the mechanism of flux-free ultrasonic soldering is important. One key benefit that can be gained from this knowledge is exploring means to optimize the soldering operation so as to achieve maximum joint strengths. To this end, this study has several objectives, namely:

1. Feasibility of fluxless ultrasonic soldering of aluminum and stainless steel by transmitting sonic energy through a solid medium.

2. Determination of the lap joint shear strengths as a function of soldering temperature, soldering time and shielding environment under various surface conditions for the ultrasonically soldered specimens.

3. Determination of the effects of sonic energy on, the joint microstructure, dissolution of the substrate surface and the solder wetting pattern.

4. Determination of the joint thickness as a function of soldering temperature.

5. Determination of the effect of soldering temperature on the wetted area fraction.

6. Simulation of the solder joint strengths as a function of thickness using finite element analysis and comparing the results with the experiments.

Thesis Outline

Chapter 1 is dedicated to a brief introduction concerning a flux-free ultrasonic soldering, and the research objectives for presenting the experimental and numerical approaches used in this study.

Chapter 2 presents a comprehensive literature review regarding the mechanism of flux-free ultrasonic soldering, interfacial tensions and the contact angle, the wetting phenomena under chemical equilibrium and non-equilibrium conditions, and the kinetics of spreading.

Chapter 3 is dedicated to the experimental procedures regarding specimen preparation and flux-free ultrasonic soldering operation, shear testing, ultrasonic non-destructive testing, optical and scanning electron microscopy.

Chapter 4 presents and analyzes the results (including the tables, graphs, and pictures).

Chapter 5 reviews the literature regarding the influence of joint thickness on the joint strength, numerical approaches, and finite element simulation results, and then compares them with the experimental results.

Chapter 6 is dedicated to discussions regarding the experimental and numerical results, and conclusions.

Chapter 2

Literature Survey

2.1 Soldering and the Solder Bonding

In a traditional soldering process, the temperature of the assembly will be raised to the point where the solder and flux become molten (below 450° C). Then, distribution of molten filler metal at the joint gap by the capillary forces can produce a solder joint after solidification. Therefore, melting, flowing, and solidification are the most important factors in a soldering process[33].

According to the American Welding Society's definition of soldering[34]:

1. Only the filler metal would be melted during the soldering process.
2. The molten solder must flow, wet the substrate and be held through the joint by the capillary forces.

Wetting the base metal and flowing molten solder through the joint gap by the capillary attraction forces are both complicated phenomena. They are influenced by the surface conditions, the joint geometry, and intermetallic phases formation at the interface or within the bulk solder joint by the chemical reactions. Therefore, increasing the wettability and maintaining strong capillary attractions are essential if the soldering process is to obtain good joints[35].

Without any chemical reactions at or mass transfer across the solid-liquid interface, a solder bond relies only on the surface tensions of the substrate. Energetically unbalanced atoms on the surface or close to the surface of a base metal attract the atoms from filler metal to create a metallic bond. These unbalanced atoms with unsaturated bonds generate the surface energies that play a very important role in characterizing the wetting or non-wetting for a specific system. Although atoms inside a solid substrate are energetically balanced, there are regions that have almost the same atomic arrangement as those of a solid surface, because of the voids and dislocations. The effects of these structural defects on the solid surface, however, are negligible on the soldering process[8]. It should also be noted that formation of the intermetallic compounds at the solid-liquid interfaces is the most effective driving force and it affects the wetting in a system[20].

2.2 Surface Stress and Surface Free Energy

By definition, a solid is a rigid portion of matter that resists stress. It is true that the surface free energy of a solid characterizes its surface, but in general, we deal with the interface between two phases in which its stability depends on the free energy of formation. It is good to mention here that a positive amount of the free energy of formation is necessary for interface existence. If the free energy of formation of the interface becomes negative or zero, then there would be a dispersion of one material into the other.

Now consider a surface that is cut by a plane normal to it. The surface stress is then defined to be equal to an applied external force per unit length to the atoms on either side of the cut in order to maintain the equilibrium. The surface tension in this situation is half the sum of the two surface stresses along mutually perpendicular cuts. These two surface stresses are equal in the case of a liquid or an isotropic solid, but different for a crystalline or non-isotropic solid[36-39].

The surface free energy of the solid materials can be estimated theoretically. Calculation of the surface energy of diamond would be rather the simplest one in which the sites of a covalently bonded crystal are occupied by atoms with no long-range interactions. There is a simple equation to evaluate the surface energy of diamond:

$$E^S = \frac{E_{cohesion}}{2} \qquad (2.1)$$

This surface energy is one-half of the energy needed to rupture the bonds passing through one square centimeter. By using the above formula, the surface energy for (111) planes and (100) planes were calculated to be 5650 $ergs/cm^2$ and 9820 $ergs/cm^2$ at zero Kelvin, respectively. As known, surface tension is temperature dependent and generally weakened as the temperature increases. However, it was found that the entropy correction at 25°C for diamond is negligible and the above values would be also accepted for room temperature.

There are preferably two different approaches to determine the surface energy of metals. The first model, which, in its simplest form, correlates the surface energy to the energy of vaporization, would then be rationalized between the nearest neighbors of a surface atom and an interior atom. The second model is a quantum mechanical approach and it is basically independent of the type of lattice involved. In its simplest version, the following equation was proposed:

$$E^S = 56400\left(\frac{D}{A}\right)^{4/3} \frac{ergs}{cm^2} \qquad (2.2)$$

Where E^S is the surface energy, D is the density of the metal and A is its atomic number.

The first model is reasonably correct and matches with the empirical results, but the second model usually gives the values up to three times larger than the empirical results for different metals[36, 40].

It is quite helpful to mention here that the interfacial tension γ is related to the specific surface free energy "*f*" by the following equation:

$$f = \gamma + \sum_{i=1}^{K} \Gamma_i \mu_i \qquad (2)$$

Where: Γ_i is the surface excess of component *i* per unit area, μ_i is the chemical potential of compounds *i* and K is the number of components in the system. In one component system, with no absorption of a solvent, these two quantities are considered to be equal. The following equations define the interfacial tension and specific surface free energy.

$$V = \left(\frac{dF}{dA}\right)_{T,V,N_i} \qquad (2.4) \qquad\qquad f = \frac{(F - F\alpha - F\beta)}{A} \qquad (2.5)$$

Where F is Helmholtz free energy of the system, A is the surface area of interface, T is the temperature, N_i is the number of moles of component i, $F\alpha$ is the Helmholtz free energy of a unit of volume in the homogeneous part of α multiplied by the volume of $F\alpha$, and $F\beta$ is the Helmholtz free energy for homogeneous part of β.

If the absorption exists at the interface of a system, then the interfacial tension is absolutely different from the specific surface free energy and Young's Equation would only be valid in terms of the interfacial tension. In the absence of any absorption at the interfaces of a solid-liquid-vapor system, the equilibrium wetting behavior is described mathematically by the Young-Dupre equation in which the interfacial tensions for the solid-liquid, solid-vapor and liquid-vapor interfaces and mechanically related by the wetting angle[36, 41, 42].

2.3 Tin-Lead Binary System and Lead-Free Solder Alloys

Tin-lead solder alloys are the most well known materials for interconnection in the refrigeration, automobile, aircraft industries, telecommunications and electronics fields. Unlike materials for structural use, solder alloys always form a ligament to join other materials. Therefore, a chemical reaction at the joint interface with the substrate, the reaction product and possible aging play very important roles in insuring joint integrity.

Near equilibrium microstructures of the tin-lead binary system can be classified into hypoeutectic, eutectic, and hypereutectic based on the bulk composition. A single eutectic reaction occurs at 183°C for an alloy with 61.9 (wt%) tin content. Tin-lead solder with the eutectic composition shows a stable homogeneous liquid solution above eutectic temperature. At equilibrium solidification, below 183°C and slow cooling rate, there are two stable solid phases in the microstructure; α - $Pb(FCC)$ and $\beta - Sn(BCT)$. This eutectic microstructure consists of alternating lamellae of α and β phase. The cooling rate affects the lamella characteristic. At a sufficiently fast cooling rate, the eutectic structure will change by losing its lamellae morphological characteristic. The cooling rate also affects the interlamellar spacing and the colony size (colony is a region of microstructure with the unidirectional oriented lamellae). At slower cooling rates, larger colonies with wider interlamellar spacing will be formed. The interlamellar spacing is inversely proportional to the velocity of the reaction front.

$$S \propto R^{\frac{1}{2}} \qquad (2.6)$$

Where: S is the interlamellar spacing and R is the velocity of the reaction front. Both colony size and interlamellar spacing are important factors, because the isothermal fatigue life, tensile strength and ductility of a eutectic solder alloy can be affected by its colony size and interlamellar spacing.

For off eutectic tin-lead solder alloys, an additional pro-eutectic phase appears in the solidified microstructure. It could be a primary α phase for the hypoeutectic alloys and β phase for the hypereutectics.

Precipitation and coarsening in a tin-lead solder joint microstructure would also affect its properties. Coarsening which can occur even at room temperature during an extended period of time will be accelerated at elevated temperatures. The coarsening phenomenon shows a direct relationship between total interfacial energy and total interfacial area within the microstructure that leads the grains or the feature size to grow.

Precipitation occurs in $\alpha - Pb$ phase because at high temperatures, a large amount of tin is soluble in lead at 183 °C. However, at room temperature, this solubility rate drops sharply and the $\beta - Sn$ phase will precipitate in α phase. A solution treatment or simple aging also can cause the precipitation[1, 8, 14, 43 - 45].

The major problem encountered with the tin-lead solder alloys is the fact that lead metal and its compounds are among the most toxic of substances. They are hazardous to the environment and new legislation and regulations threaten to limit or ban the use of the lead-containing solders. These concerns originated a substantial effort for the developing of substitute solder alloys. These new lead-free solder materials offer some desirable characteristics, such as: melting point, wettability, thermal expansion coefficient, thermal and electrical conductivities, strength and ductility, thermal fatigue resistance, creep resistance, manufacturability, corrosion resistance, and low cost which make them comparable to tin-lead solders. There are different candidates proposed to substitute the tin-lead solders, but many of them cannot satisfy the factors such as, process requirement, mass production applications and reliability objectives. The following table shows the bulk properties of some binary lead-free solder alloys compared to $Sn - 38Pb$ solder.

Table 2.1 Melting temperatures and the properties of some lead-free solder alloys.

Solder	**Melting Point degree C**	**Ultimate Tensile Str. (MPa)**	**Elongation (%)**	**Shear Strength (MPa)**	**Stress Rupture Life**		**Low Cycle Fatigue Life (cycles)**
					at: 24 °C 0.69 MPa	**at: 60 °C 0.62 MPa**	
Sn-51 In	120	11.9	83	11.2	-	-	-
Sn-57 Bi	139	45-80	40-200	48.3	16.7	1.1	8500
Sn-3.5 Ag	221	55	35	32.1	-	-	-
Sn-5 Sb	238	36.6	38	31.8	-	-	-
Sn-38 Pb	183	31-46	35-176	28.4	8.3	0.4	1900

Several lead-free ternary solder alloys are also proposed. Among them *Sn – 3.5% Ag – 1% In (wt%)* with a higher melting temperature compared to *Sn – 3.5% Ag (wt%)* provides good mechanical creep and thermal fatigue resistance because the zinc content is only soluble in solid *Ag*, not *Sn*. *Sn – Zn – In* based alloys with melting temperature (~185° C), close to near eutectic lead-tin solder alloys, is useful in electronic packaging.

Sn – 4.7 Ag – 1.7 Cu solder alloy with a ternary eutectic reaction at (216.8 ± 1° C) can be a good substitute for traditional lead-tin solders because of its compatible melting temperature, its good wetting behavior, its availability, and its low cost.

There are other ternary solder alloys available, such as, *Sn – Bi – Ag* alloys, *Sn – In – Ag* alloys, *Sn – Sb – In* alloys, and *Sn – Sb – Ag* alloys. These alloys are suitable for the soldering in electronic packaging. *Sn – 9% Zn (wt%)* with the melting temperature of 198° C offers excellent mechanical properties, but its susceptibility to oxidation and corrosion decrease drastically its reliability. However, by using inert atmospheres in new soldering technologies, the *Sn – Zn* solder alloys are acceptable and reliable[18, 46 - 51].

Choosing a lead-free solder requires considering different metallurgical issues such as, the melting point, microstructure, solder-substrate interactions, physical and mechanical properties. In a soldering operation, the melting point of the solder material is critical. It limits the minimum operating temperature in which the soldered components can survive. Thermal and electrical conductivities of a solder joint increasingly play important roles in most modern electrical applications and they must be considered when lead-free solder is designed. Among the physical properties, the surface tension in a solid-liquid-vapor (flux) system is crucial because a relatively high surface tension is desirable for a solder material. Composition of the filler metal and the cooling rate usually define the solder joint microstructure. Small grain size with fine precipitates that, dispersed uniformly, would be beneficial. Over long periods of time, a stable microstructure is desirable because as mentioned before, any microstructural changes such as, grain growth (coarsening) and further precipitation or intermetallic growth along the interfaces or into the solder would be detrimental to mechanical properties of the joint[32, 52 - 58].

2.4 Fluxing Agents

Base material, filler metal and fluxing agents are three principal components in the soldering process, either for the manufacturing of electronic products or structural assemblies. In general, environmental attack on the base materials and the filler metals produces a thin film of corrosive products, such as oxides, sulfides, and carbonates, on the surface. These products decrease the wettability and act as a barrier to metallic bond formation at the joint interfaces and must be removed. Choosing the right flux, which is usually a corrosive agent, solves this problem. Upon heating and during soldering, the flux prevents the formation of new oxide films on the cleaned surfaces. Also as a surfactant, it will reduce the surface tension to improve the wettability and flow[8, 14, 59].

2.5 Ultrasonic Soldering

The existence of a strong and tenacious oxide film on the metallic substrate surfaces, such as copper and aluminum during soldering prevents the molten solder from directly contact the metallic surface for bonding. Implementing a traditional soldering requires a suitable fluxing agent dependent mostly on the base metal and soldering temperature. Using a flux agent is costly and harmful to the environment. The flux residues are also corrosive and difficult to completely remove from the joint area[59, 60].

Although ultrasonic soldering has been available since the 1930's and high frequency mechanical vibration due to ultrasonic energy has been used in ultrasonic cleaning, nondestructive testing, metal cutting and metal forming since then, but ultrasonic soldering has been used more frequently since 1970's in refrigeration and later in electronics industry. More recently, powerful ultrasonic equipment for the soldering industry has been employed.

Ultrasonic soldering can be preformed in two ways:

1. Submerging the joint into the solder bath and activating the molten filler metal by mechanical vibrations.

2. Contacting the ultrasonic horn directly to the joint area to create cavitation to promote the process[61].

In ultrasonic soldering, high frequency electrical impulses (20 to 50 kHz) will be generated by an electronic power oscillator. A transducer then converts these electrical impulses to mechanical excitations. For commercial equipment, the oscillator is connected to the coil of a transducer with a nickel core. The nickel core will be constricted to a very small fraction of its length by being subjected to the electromagnetic impulses as the result of electrical currents flowing through the core. If the end of this vibrating core contacts the molten filler metal or the joint area, the mechanical vibration will produce cavitation erosion in the molten solder. This cavitation phenomenon is caused by numerous holes within the liquid. The collapse of these holes on the surface of the substrate will create erosive forces to break the oxide films and promote wetting[62]. However, according to recent observations, not only the cavitation erosion, but also the preheating, surface conditions the properties of the base material and filler metal will affect wettability[59].

The mechanical motions during the ultrasonic soldering process promotes deoxidation of the substrate, but it does not remove the surface tensions or protect cleaned surfaces from reoxidation.

Four basic bonding mechanisms may be involved in the soldering process[50]:

1. Formation of the intermetallic compounds at the joint interfaces.

2. Fusion bonding at the interfaces.

3. Metallic bonding at the interfaces.

4. Interlocking at the interfaces mechanically.

Ultrasonic equipment can also be used for the solder coating of metallic or non-metallic surfaces without using a fluxing agent. The process is the same as ultrasonic soldering, hanging the work piece in a solder bath, applying the ultrasonic mechanical vibrations by immersing the horn tip into the molten solder. Then, the solder will wet the surfaces and form a metallurgical bond with the substrate, provided the erosion force removes the oxide film[59].

The Alcoa 571 Process was developed in the early 1970's for soldering of hard-to-wet metals such as aluminum and stainless steel. Alcoa 571 is a fluxless ultrasonic soldering pot operation that is successfully used for joining aluminum heat exchanger coils. Alcoa 571 is basically a three-step process:

1. Vapor degreasing.
2. Preheating by hot air or gas flame.
3. Dipping into the solder for a short period of time and applying sonic energy.

In the Alcoa 571 Process, a very small amount of beryllium is added to improve the molten solder penetration into the joint gap and to decrease the surface tension[63, 64].

Hitachi[65] also developed a fluxless ultrasonic process for joining aluminum to copper tubes and pipes, a method quite useful in the refrigeration industry. In this process, one end of the aluminum pipe would be coated with solder, while the end of the copper pipe is flared. Once the solder is molten, ultrasonic vibrations are applied to the heated and coupled ends of the pipe. The mechanical vibrations as a result of sonic energy disrupt and disperse the oxide film. A metallic surface then contacts the molten solder for bonding. According to Hitachi, applying the sonic energy for a long period of time will increase the amount of aluminum dissolved into the solder[65].

Ultrasonic solder coating or metallizing is an effective way to improve the wettability of the work piece. The alloying of the active elements with titanium or using an aluminum base alloy as the filler metal, is quite useful for joining non-metallic materials by increasing the wettability. Formation of bubbles or voids in the solder and their further erosive actions on the substrate surface create annular or doughnut-shaped solder wetting patterns. These circular patterns, separating the wetted and non-wetted regions are caused by preferentially eroded areas at the bubble walls[59, 66, 67].

Soldering time, soldering temperature, and the bulk solder properties are three important factors influencing the strength of a solder joint. However, there are also other factors that strongly affect joint strength, such as surface conditions, the properties of the base materials, the formation of compounds at the joint interfaces, and preheating[66].

Factors affecting the fluxless ultrasonic soldering are:

- Increasing the time of the ultrasound will increase the solder ability and the joint strength. However, and excessive solder time may degrade the part and could cause fracturing or melting to occur at the areas away from the joint, especially at the holes and corners.

- An increase in soldering temperature increases the joint strength.

- Solder composition also influences the joint strength.

- Cavitation erosion and the sound wave propagation through the substrate are both important. The coupling of the ultrasonic energy with the substrate combined with the collapsing force of the bubbles breaks and removes the oxide films.

- Thickness, geometry, and mechanical properties of the substrate materials and their relationship to the acoustic energy transmission are important. Generally, better wetting is expected for thicker substrate.

- The horn configuration and its operating parameters, such as: frequency and power level, as well as the melting point and the solder alloy composition affect wettability as well[4, 20, 59, 66].

Metals can also be welded together by using ultrasonic energy without reaching the melting temperature and fusion bonding. Power, frequency, force, and time are the four major factors in this process. Scrubbing two parts against one another at high frequencies and holding them tightly for a short period of time will allow the diffusion of atoms across the interface to create a metallurgical bond. This is a very useful process for welding two different metals like copper and aluminum together. The fusion welding of copper to aluminum can result in an unreliable bond, due to the fact that these two metals are both highly conductive and exhibit different thermal conductivity that is detrimental to the bond. Also, a brittle intermetallic would form at the copper-aluminum bond that degrades its mechanical properties[57]. Cold-welding of the ends of small, aluminum tubes is another useful application of sonic energy for making hermetic closure. In this process, a high-frequency sonic vibration would be introduced into the clamped area without using heat, filler metal, or electrical current. This solid-state diffusion bonding creates a satisfactory metallurgical bond without any voids or pores. Power, frequency, force, and the welding time are the factors affecting the reliability and integrity of the weld joint. Increasing the power would decrease the joint thickness and increase the leak rate possibility. The frequency does not have a great effect on the joint thickness or leak rate. Increasing the force would decrease the joint thickness and lower the leak rate. Highly applied force could, however, create a thin joint which is usually more fragile. Increasing the weld time also has the same effects on the thickness and the leak rate[69, 70].

Soldering in the electronics industry has continuously progressed since 1920. Previously, interconnects used to be soldered with traditional soldering iron in a point-to-point wiring method. New mass soldering methods such as dip soldering, wave soldering, and reflow soldering have revolutionized the solder joint technology for through-hole and surface mount assemblies.

In the electronics industry, the operational temperature of the solder is restricted and the joints themselves must act as mechanical, electrical, and thermal conductors with the highest possible reliability. The mechanical integrity of a solder joint in an electronic package also plays a crucial role because the joint must consume the strains from its surrounding area with different thermal expansion coefficients.

There are two types of soldering operations for electronic applications:

1. The Component / Solder Process (CS).

2. Solder / Component Process (SC).

In the CS Process, the component is positioned onto the board before soldering. In SC, which is primarily used for surface mount assembly lines, the solder is applied before positioning the components onto printed circuit boards[71 - 74].

Chemical flux is a major component for a conventional soldering operation. It promotes solder wetting and flow. Flux residues must, however, be removed from the parts or the circuit boards.

Hologenated solvents and specially chlorofluorocarbons (CFC's) are generally used to remove these residues. Cost, as well as the environmental impact of the pro-cleaning processes creates opportunities to address and solve, or at least reduce the severity of these problems. There are strong efforts in microelectronics to develop new solvents, find alternative cleaning methods, and create alternative manufacturing techniques that are economically and environmentally compatible. Some substitute manufacturing techniques are laser soldering, solid state (diffusion) soldering, and ultrasonic soldering. These soldering operations can be conducted in the air or in a controlled atmosphere.

General applications of ultrasonic soldering in microelectronic packaging are:

- Hot solder coating of package input/output (I/OS).
- Solder coating the copper features on the printed circuit boards.
- Solder coating of the gold-plated package.
- Tinning of the connector leads.
- Tinning of the strand wires.
- Tinning the circuit paths on thick film substrates.
- Scrubbing the contact surfaces between the component lead and circuit board.
- Forming a bump selectively on an aluminum pad.
- Aluminum wire bonding to gold, thick film conductors[75 - 80].

2.6 Why Fluxless Ultrasonic Soldering?

Rapid soldering, eliminating the flux, reducing the need for special pre-cleaning or post-soldering cleaning with no corrosive consequences, using a wide range of filler metals, soldering dissimilar materials, and reducing cost, are the most important factors for choosing a fluxless ultrasonic soldering[21]. Oxide formed on the surface of a substrate prevents the molten solder to contact the base metal, wet it, and create a metallic bonding after the solidification. The surface energy of an oxide is generally lower than its metal. Therefore, its existence on a metallic surface will reduce the surface tension and the driving forces for wetting and spreading.

Using a suitable flux may overcome the oxide barrier, but fluxes and their residues are corrosive and must be removed from the joint areas. Expensive post-assembly cleaning processes that are not also friendly to the environment have brought immediate attention to finding fluxless methods of soldering.

Two governing thermodynamic equations explain the difficulties during a fluxless soldering operation:

1) At equilibrium, the contact angle Θ describes the driving force between a sessile liquid droplet spreading on a flat, horizontal solid substrate by satisfying the Young-Dupre Equation.

$$Cos\Theta = \frac{\gamma_{sv} - \gamma_{sl}}{\gamma_{lv}} \qquad (2.7)$$

Where γ_{sv}, γ_{sl}, and γ_{lv} are the surface energies at the solid-vapor, slid-liquid, and liquid-vapor interfaces and θ is the wetting angle.

Equation (2.7) demonstrates that the surface tension of the base material γ_{sv} is related proportionally to the contact angle.

2) At the same time, the Gibbs Relation states that any spontaneous changes such as oxide formation on the surface or at the interface will decrease the interfacial energy[21].

$$\Delta\gamma \leq 0 \qquad (2.8)$$

Therefore, the existence or formation of an oxide film on the substrate surface will decrease the surface tension and reduce the driving force for wetting.

As mentioned previously, using chlorofluorocarbons (CFC's) and hologenated solvents to remove the flux residues in the post-soldering process has a significant impact on the environment and especially on ozone layer depletion which, in turn, have detrimental effects on human health. Therefore, there are strong environmental motivations to develop new cleaning methods, new alternative solvents, and alternative soldering methods that would also be economically compatible, especially for microelectronics soldering, since the post-solder cleaning is always an important part of the manufacturing process[20, 21].

Understanding the difficulties in a fluxless soldering effort such as reducing or removing the surface oxides or prevention of the oxide formation prior or during a soldering operation, is helpful in developing and maintaining important key factors in the process. Some of these factors are controlling the atmosphere, applying thermomechanical, and applying a protective coat. Control of the atmosphere could be maintained by using reactive plasma, diluting the acid vapor-inert gas mixture, vacuum, inert or reducing gases. Also, reactive atmospheres such as ionic or atomic gases (i.e. hydrogen), are offering great potential for effectively reducing the surface oxides. Protective coating methods are usually complimentary to the other technologies for maintaining a non-oxidizing or reliable surface. The most suitable protective coatings are gold, nickel, tin and tin-lead alloys. The thickness of a coating layer would affect the wettability. Thick-coated layers may introduce excessive elements to the solder-base metal interface that could deteriorate the mechanical properties of a joint. Very thin layers, less than 0.5 microns could be porous and not able to protect the interface. Thermomechanical methods such as laser, solid-state diffusion, and ultrasonic processing use direct thermomechanical or mechanical vibration to break or reduce the oxide films for creating a metallic surface against the molten solder[20, 21,56, 71 - 73, 80, 81].

2.7 The Role of Wetting in Soldering and the Contact Angle Phenomenon

A soldering process basically depends upon the physical wetting of the substrate by molten solder to generate the joining interface that maintains the metallic continuity. An oxide film that is tarnishing the work piece or the solder acts as a barrier in a soldering operation. It decreases the wettability and opposes to a suitable joint formation[8].

There are two wetting characteristics governing the wettability of a solid surface by the molten solder:

1) Extent of the Wetting: Depends on the interfacial energies of the system that are controlled by the laws of thermodynamics.

2) Rate of the Wetting: Controlled by the system thermal demand, the mass transfer and/or the chemical reactions across the interfaces, the heat source to supply the necessary thermal energy for the operation, the viscosity of the molten solder, and the quantity of the flux (if used)[6, 8, 82].

There are two aspects to evaluate the quality of a solder bond, a suitable thermodynamic driving force for wetting and the kinetics of wetting or the rate of forming a bond. A soldering process is governed by two important thermodynamics equations. The Young-Dupre Equation states that the relation between the wetting angle and the interfacial tensions, and the Gibbs Relation states that any spontaneous changes at the interfaces would modify the interfacial tensions[6, 21, 81, 83].

Consider a droplet of molten solder resting on a flat horizontal surface. If there is no mass transfer or chemical reaction at the interfaces or in the molten solder, then the solid-liquid-vapor system would be brought to a total thermodynamic equilibrium by three balanced interfacial forces which would meet each other at a certain point of intersection to form the contact angle between the liquid and solid phases. According to the Young-Dupre Equation:

- The solid-liquid interfacial tension (γ_{SL} ; force between the molten solder and base metal) would be lowered, if a spontaneous chemical interaction produces a layer of intermetallic compound at the interface.
- The surface tension or wetting force (γ_{SV} ; force which spreads the molten solder on the solid surface) would increase, (by cleaning and coating the substrate surface with a thin layer of gold, nickel, tin or tin-lead alloys to protect the substrate from oxidation and contamination).
- The interfacial tension between the liquid and vapor phase (γ_{LV} ; the cohesion force, which is a tangent to the liquid curvature) is the force to minimize the liquid surface. This force can be controlled by using a proper flux[8, 82, 84].

There are other consideration affecting the wetting angle:

- The Molecular Hysteresis: the contact angle would be different if there is an oxide film or intermetallic formed or even some liquid molecules absorbed on the metallic surface.
- The Capillary Hysteresis: the contact angle also depends on the surface topography. The grooves on a rough surface may act as the capillaries and cause higher attraction forces and improve the spreading.
- Heterogeneous Solid Surface: could be considered as composite material:

$$Cos\Theta = A_1 Cos\Theta_1 + A_2 Cos\Theta_2 \quad (2.9)$$

Where A_1 and A_2 are the partial areas, $Cos\ \Theta_1$ and $Cos\ \Theta_2$ are the intrinsic contact angles.

- The Critical Temperature: for a given system, this is the temperature at which a sudden increase of spreading occurs.

Practical Wetting occurs when the contact angle between the solid and the liquid is less than 90°. Therefore, wetting increases by decreasing the contact angle. When the angle approaches zero, wettability is maximized and the liquid covers the entire solid surface[35, 61]. De-wetting is a situation where the contact angle becomes greater than 90°, then the liquid tends to ball up and run off the surface[36].

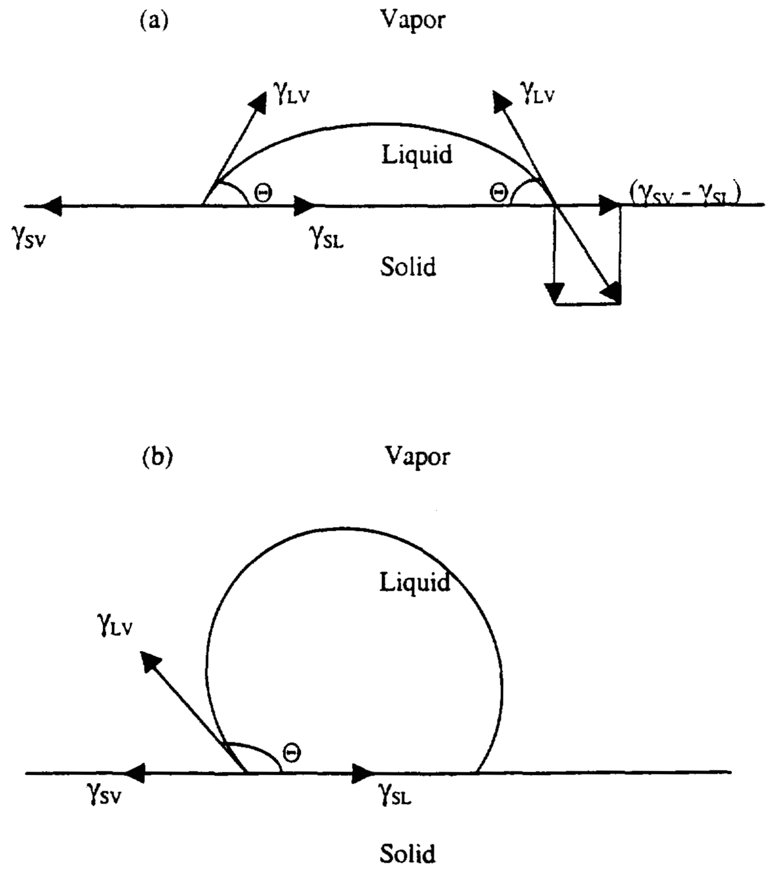

Figure 2.1.(a-b) Wetting and non-wetting conditions

2.8 Wetting Under Conditions of Chemical Equilibrium

No chemical reaction at or mass transfer across the interfaces is expected by assuming that, the solid-liquid-vapor system is in equilibrium condition. Spreading a liquid droplet on a flat, horizontal surface determines the degree of wetting and Young's Relationship, who uses a mechanical equilibrium, treats the problem by relating the wetting angle to the interfacial tensions[35].

Although the accuracy of Young's Equation in a gravitational field and for zero contact angle, was question at the Second International Congress of Surface Activity, Gibb's thermodynamical derivations of Young's Equation for a Non-Gravitational and a Gravitational Field proved that the equation is valid. There is also some confusion concerning the use of surface free energies instead of interfacial tensions for the quantities in Young's Equation. But in fact, the free energy term can be used only in the absence of the absorption in a solid-liquid-vapor system.

The terms Surface Tension, Surface Free Energy, Specific Surface Free Energy and Surface Energy are frequently used for identifying the forces in a system. In equation (2.10), Gibbs defined ζ_{SL} as "the superficial tension of a liquid in contact with a solid."

$$\zeta_{SL} = \gamma_{SL} - \gamma_{SO} \qquad (2.10)$$

Where γ_{SO} is the surface tension of a solid in vacuum and γ_{SL} was not given a name in relation with a solid surface[42]. Now, without considering the gravitational field, the total free energy for a solid-liquid-vapor system is[36, 41, 42]:

$$dG = \sum_i \mu_i^S dn_i^S + \sum_i \mu_i^L dn_i^L + \sum_i \mu_i^V dn_i + \sum_{\alpha\beta} \left\{ \sum_i \left(\frac{\partial G^{\alpha\beta}}{\partial n_i^\alpha} \right) dn_i^\alpha + \sum_i \left(\frac{\partial G^{\alpha\beta}}{\partial n_i^\beta} \right) dn_i^\beta \right.$$

$$+\sum_i\left(\frac{\partial G^{\alpha\beta}}{\partial n_i^{\alpha\beta}}\right)dn^{\alpha\beta}\Bigg\}+\gamma_{SL}dA_{SL}+\gamma_{SV}dA_{SV}+\gamma_{LV}dA_{LV} \qquad (2.11)$$

Where, μ_i is the chemical potential for component i , n_i is the total number of moles for component i , G is the total free energy, $G^{\alpha\beta}$ is the specific interfacial free energy times the corresponding interfacial area. Equation (2.11) is valid by assuming that the temperature and pressure are constant, the effect of pressure across the curvature is negligible, and the surface orientation does not affect the interfacial tensions. Now, dG would be zero if the system is in a state of total thermodynamic equilibrium, and the two parts of equation (2.11) summarize the conditions for chemical and mechanical equilibrium respectively[41].

$$\sum{}_i\mu_i^S dn_i^S+\sum{}_i\mu_i^L dn_i^L+\sum\mu_i^V dn_i^V+\sum{}_{\alpha\beta}\Bigg\{\sum{}_i\left(\frac{\partial G^{\alpha\beta}}{\partial n_i^{\alpha}}\right)dn_i^{\alpha}+\sum{}_i\left(\frac{\partial G^{\alpha\beta}}{\partial n_i^{\beta}}\right)dn_i^{\beta}$$

$$+\sum{}_i\left(\frac{\partial G^{\alpha\beta}}{\partial n_i^{\alpha\beta}}\right)dn_i^{\alpha\beta}\Bigg\}=0 \qquad (2.12)$$

$$\gamma_{SL}dA_{SL}+\gamma_{SV}dA_{SV}+\gamma_{LV}dA_{LV}=0 \qquad (2.13)$$

At a chemical equilibrium condition, equation (2.12) is totally satisfied and therefore, the surface free energy changes depend only on the interfacial area changes.

For a droplet placed on a flat solid surface and in the absence of the gravitational and attractive forces, a solid-liquid interface will form if the free energy of the system is less than zero. Thus, the negative amount of the free energy of the system (mathematically) will create the driving force to deform the liquid droplet, which, in the end, increases the interface. This deformation will continue until a mechanical equilibrium (stated by equation 2.13) is reached[36, 41, 42, 85].

2.9 Wetting Under Conditions of Chemical Non-Equilibrium

Mass transfer across or chemical reactions at the solid-liquid interface will continuously change the interfacial tension and the contact angle. Therefore, this brings into existence a non-equilibrium dynamic condition with a net decrease in the total free energy of the system. This condition will become a stable and static state when the system chemically reaches the equilibrium.

In a non-equilibrium condition, the free energy changes of the system depend on both changes in the wetted interfacial areas and diffusion or mass changes, as the result of an effective chemical reaction by a magnitude of ($-\Delta G/A$) at the interface. This process causes a reduction in interfacial tension in favor of the lower contact angle and higher wettability and spreading[41, 42].

The free energy of an interfacial reaction during a soldering process can be calculated from the following equation by assuming that Raoult's Law is applicable.

$$\Delta G = RT \; Ln \frac{C_C}{C_M} - \Delta G^0 \qquad (2.14)$$

Where ΔG^0 is the standard free energy of the reaction, R is the gas constant, T is the soldering temperature (in degrees Kelvin) in which the reaction took place, C_C is the concentration of compound formed at the interface, and C_M is the concentration of metal in the liquid phase.

In general, the wetting under soldering operations will not begin or might not be ended under chemical equilibrium conditions because there may be some interfacial diffusion (solution reactions and/or compound formation) at the solid-liquid interface. Therefore, Young's Equation cannot be applied directly in a chemical non-equilibrium condition[35, 41, 42, 86, 87].

Aksay et al.[88] addressed the wetting mechanism under chemical non-equilibrium. According to their analysis, in a solid-liquid-vapor system, the surface tension and the wetting angle are continuously changing before reaching the chemical equilibrium. However, in a soldering process, we assume that the chemical equilibrium is maintained at the solid-vapor interfaces.

According to Aksay et al.[88], wetting in a soldering process is mainly due to:

1) The formation of compounds at the solid-liquid interface.

2) Unsaturated solid and liquid phases with respect to the other.

Therefore, a decrease in the free energy of the system at the early stages of wetting can only be attributed to the reactions at the solid-liquid interface. The formation of the compounds at the solid-liquid interface will initially decrease the contact angle. As we approach chemical equilibrium, the surface tensions will decrease (formation of compound layers), and the result will be a larger wetting angle.

If the contact angle exceeds 90°, de-wetting is the consequence. As in the soldering or coating of *Cu/Cu* alloys with *Sn-Pb* solder, formation of Cu_6Sn_5 at the interface causes de-wetting[35].

2.10 The Kinetics of Spreading as an Interfacial Phenomenon

Under a chemical equilibrium condition, the driving force for wetting a solid surface by liquid droplet would be determined by the interfacial tensions in a triple system (solid, liquid and vapor) , according to Young's mechanical relationship. There is also an opposite force to prevent the droplet from spreading, this force is related to the viscosity flow of the liquid and encountered as the material property of the fluid.

Although Young's Equation defines the thermodynamics of wetting in relation to the contact angle and the surface tensions of the interfaces, spreading a liquid droplet on a solid surface must also be defined and considered in terms of a kinetic phenomena[35, 41, 42, 85].

T. P. Yin[85] theoretically treated the kinetics of spreading by assuming that the liquid droplet remains in its spherical shape and retains its circular interfacial contact area with a smooth, rigid, solid surface.

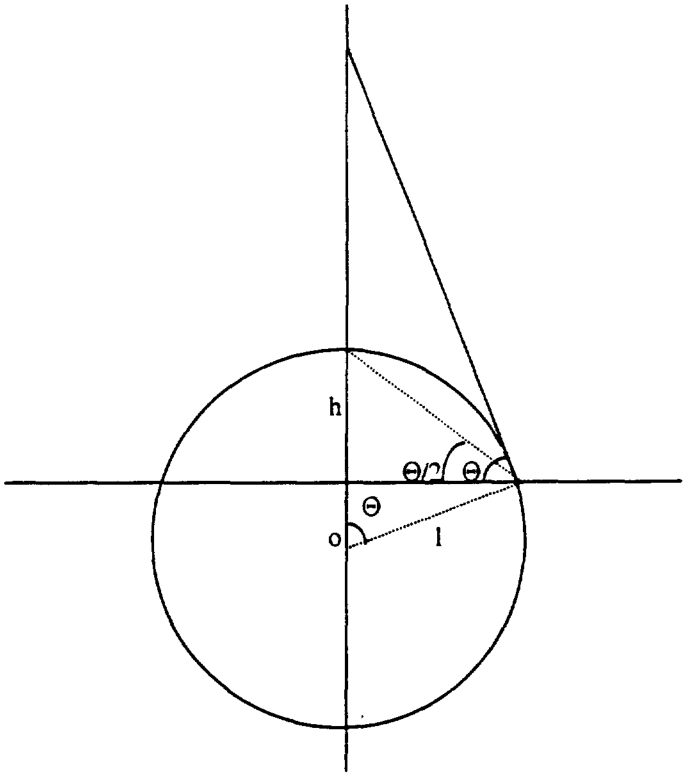

Figure 2.2 Spherical cap shape of a liquid droplet.

The spreading and resistance to the spreading forces in opposite directions respectively, are:

$$\vec{F} = 2\pi\ell S \qquad (2.15)$$

$$\vec{F} = -\left(\pi\ell^2\eta\right)\frac{dv}{dh} \qquad (2.16)$$

Where *S* is the instantaneous spreading coefficient, η is the viscosity of spreading (in Poise), *dv/dh* is the velocity gradient of the viscous flow with respect to *h* direction (in 1/sec), and l is the radius of the instantaneous contact area (in *cm*).

$$S = \gamma_{SV} - \gamma_{SL} - \gamma_{LV} Cos\Theta \qquad (2.17)$$

Where, γ_{SV} , γ_{SL} , and γ_{LV} are the interfacial tension in the solid-liquid-vapor system, Θ is the instantaneous contact angle at the triple point of the system.

In a steady-state spreading condition, Equations (2.15) and (2.16) would be equal if we ignore the gravitational field and the velocity gradient in the direction of spreading[85].

$$2\pi\ell S = -\left(\pi\ell^2\eta\right)\frac{dv}{dh} \qquad (2.18)$$

$$dv = -\frac{2S}{\ell\eta}dh \qquad (2.19)$$

Then, the instantaneous rate of spreading would be:

$$\left\langle \frac{dA}{dt} \right\rangle = \int_{0,\Theta}^{h,0} 2\pi\ell dV = -\frac{4\pi}{\eta} \int_{0,\Theta}^{h,0} S dh \qquad (2.20)$$

From Figure (2.2), we have:

$$h = \ell \tan\frac{\Theta}{2} \qquad (2.21)$$

$$\ell = R\sin\Theta \qquad (2.22)$$

By substituting Equation (2.22) in (2.21), we have:

$$\ell = R\sin\Theta = 2R\sin\frac{\Theta}{2}\cos\frac{\Theta}{2}$$

$$h = 2R\ \sin\frac{\Theta}{2}\cdot\cos\frac{\Theta}{2}\cdot\tan\frac{\Theta}{2} = 2R\ \frac{\sin\Theta}{2}\cdot\cos\frac{\Theta}{2}\cdot\frac{\sin\frac{\Theta}{2}}{\cos\frac{\Theta}{2}}$$

$$h = 2R\sin^2\frac{\Theta}{2} \qquad (2.23)$$

The volume of the droplet is constant and equal to V$_0$.

$$V_0 = \pi h^2\left(R - \frac{h}{3}\right) \qquad (2.24)$$

Where R is the radius of the hypothetical sphere.

From Equation (2.23), we have:

$$R = \frac{h}{2\sin^2\frac{\Theta}{2}}$$

Substituting Equation (2.24) in (2.23):

$$V_0 = \pi h^2\left(\frac{h}{2\sin^2\frac{\Theta}{2}} - \frac{h}{3}\right) = \pi h^2\left(\frac{3h - 2h\sin^2\frac{\Theta}{2}}{6\sin^2\frac{\Theta}{2}}\right) = \pi h^3\left(\frac{3 - 2\sin^2\frac{\Theta}{2}}{6\sin^2\frac{\Theta}{2}}\right)$$

Then:

$$h^3 = \left(\frac{V_0}{\pi}\right)\left(\frac{6\sin^2\frac{\Theta}{2}}{3 - 2\sin^2\frac{\Theta}{2}}\right) \qquad (2.25)$$

$$h=\left(\frac{V_0}{\pi}\right)^{1/3}\left(\frac{6\sin^2\frac{\Theta}{2}}{3-2\sin^2\frac{\Theta}{2}}\right)^{1/3}$$

Let Θ/2 =x, then:

$$\frac{dh}{dx}=\left(\frac{V_0}{\pi}\right)^{1/3}\left(\frac{6\sin^2 x}{3-2\sin^2 x}\right)^{-2/3}\left(\frac{36\sin x\cdot\cos x-24\sin^3 x\cdot\cos x+24\sin^3 x\cdot\cos x}{(3-2\sin^2 x)^2}\right)$$

$$\frac{dh}{dn}=\left(\frac{V_0}{\pi}\right)^{1/3}\frac{(6\sin^2 x)^{-2/3}(36\sin x\cdot\cos x)}{3(3-2\sin^2 x)^{-2/3}(3-2\sin^2 x)^2}$$

$$\frac{dh}{dx}=\frac{12\sin x\cdot\cos x}{(6\sin^2 x)^{2/3}(3-2\sin^2 x)^{4/3}} \qquad (2.26)$$

Let $2\sin^2 x=y$, then $dy=H$ Sin x Cos x.

$$\Rightarrow dh=\left(\frac{V_0}{\pi}\right)^{1/3}\left(\frac{3dy}{y^{2/3}(3-y)^{4/3}}\right)=\left(\frac{3V_0}{\pi}\right)^{1/3}F(y)dy \qquad (2.27)$$

Substitute (2.27) in (2.20):

$$\left\langle \frac{dA}{dt} \right\rangle = \int 2\pi \ell dV = -\frac{4\pi}{\eta}\left(\frac{3V_0}{\pi}\right)^{1/3} \int S F(y) dy$$

Let: $$K = \frac{4\pi}{\eta}\left(\frac{3V_0}{\pi}\right)^{1/3}$$

And: $S_0 = \gamma_{SV} - \gamma_{SL} - \gamma_{LV}$ (Spreading coefficient at $\Theta = 0$)

$$\left\langle \frac{dA}{dt} \right\rangle = -K \int \left(\gamma_{SV} - \gamma_{SL} - \gamma_{LV} \cos 2x\right) F(y) dy$$

$$= -K \int \left(\gamma_{SV} - \gamma_{SL} - \gamma_{LV}\right) F(y) dy + \left(2 \sin^2 x \gamma_{LV}\right) F(y) dy$$

Then: $$\left\langle \frac{dA}{dt} \right\rangle = -KS_0 \int F(y) dy - K\gamma_{LV} \int yF(y) dy$$

$$\left\langle \frac{dA}{dt} \right\rangle = KS_0 \int_0^{\Theta} F(y) dy + K\gamma_{LV} \int_0^{\Theta} yF(y) dy \qquad (2.28)$$

$$F(y)=\frac{1}{\left(2\sin^2\frac{\Theta}{2}\right)^{2/3}\left(3-2\sin^2\frac{\Theta}{2}\right)^{4/3}}$$

$$\left\langle\frac{dA}{dt}\right\rangle=KS_0\int_0^{\pi}\frac{1}{\left(2\sin^2\frac{\Theta}{2}\right)^{2/3}\left(3-2\sin^2\frac{\Theta}{2}\right)^{4/3}}+K\gamma_{LV}\int_0^{\pi}\frac{\left(2\sin^2\frac{\Theta}{2}\right)^{1/3}}{\left(3-2\sin^2\frac{\Theta}{2}\right)^{4/3}}$$

At $\Theta = 0°$; $\left\langle\frac{dA}{dt}\right\rangle=\infty$ (An infinite spontaneous spreading rate)

At $\Theta = 180° = \pi$; $\left\langle\frac{dA}{dt}\right\rangle=\frac{KS_0}{2^{2/3}(3-2)^{4/3}}+\frac{\sqrt[3]{2}K}{(3-2)^{4/3}}\cdot K_{LV}$

(Minimum spontaneous spreading rate)

$$\left\langle\frac{dA}{dt}\right\rangle=\left(\frac{4\pi}{\eta}\right)\left(\frac{3V_0}{\pi}\right)^{1/3}\left[\frac{(\gamma_{SV}-\gamma_{SL}-\gamma_{LV})}{\sqrt[3]{4}}+\sqrt[3]{2}\gamma_{LV}\right] \qquad (2.29)$$

Equation (2.29) shows that the spreading rate depends on the interfacial tension of the solid-liquid-vapor system[85].

2.11 Wetting as a Capillary Action Phenomenon and Flow in Soldering:

In the soldering process, the manner in which molten solder fills a joint gap or the surface imperfections, depends on the capillary attraction forces[89]. In the case of dust, laying on the surface, the molten solder must penetrate between dust particles, to spread and wet the surface. This driving force, called capillary attraction, is the difference in pressures across the curved surface of the meniscus as presented in Figure 2.3.

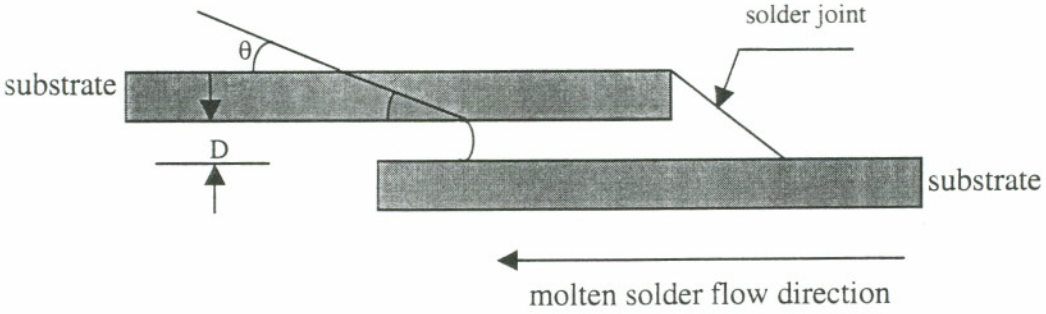

Figure 2.3 Molten solder flow into a solder joint gap of D

This pressure difference across the liquid-vapor interface can be expressed as:

$$\Delta P = \frac{-2\gamma_{LV}\cos\Theta}{D} \qquad (2.30)$$

Where, D is the joint gap and the gravity is ignored. By assuming that the fluid flow is laminar under the condition shown in Figure 2.3, then:

$$V = \left(\frac{1}{2\eta}\right)\left(\frac{dP}{dx}\right)\left(y^2 - yD\right) \qquad (2.31)$$

Where the fluid velocity (V) is a function of the distance y and η is the viscosity.

Now, by assuming that the plates are uniformly spaced:

$$\frac{dP}{dx} = \Delta\left(\frac{P}{x}\right)$$

Then, the average fluid velocity is:

$$\bar{V} = \frac{1}{6}\left(\frac{\gamma_{LV}\cos\Theta}{\eta}\right)\left(\frac{D}{X}\right) \qquad (2.32)$$

A simple integration gives the time require to flow a distance X:

$$V = \frac{dx}{dt} = D\gamma_{LV}\cos\Theta / 6\eta X$$

$$dt = \left(6\eta / D\gamma_{LV} \cos\Theta\right) X dX$$

$$t = \left(6\eta / D\gamma_{LV} \cos\Theta\right)\left(X^2 / 2\right)$$

$$t = \frac{3\eta X^2}{D\gamma_{LV} \cos\Theta}$$

Assuming that the gravity is not a factor:

$$X = \sqrt{\frac{Dt\cos\Theta}{3\eta}} \qquad (2.33)$$

In Equation (2.33), the distance, X in a given amount of time is directly proportional to D. This means that X can be increased by increasing the joint gap. However, the joint gap is limited by different factors such as the geometry of the joint and can not be increased substantially. At the same time, X is related to the viscosity of the molten solder. In reality, changing the temperature of the molten solder has the most influential effect on X, and by increasing the temperature, the viscosity will increase exponentially[35, 39].

In the case of a vertical joint, the pressure difference, or the capillary force across the meniscus curvature, is contrary to the weight of the liquid (molten solder)[35, 39, 47].

By ignoring the weight of the vapor phase, then:

$$\Delta P = \frac{-2\gamma_{LV}\cos\Theta}{D} + \rho g y \qquad (2.34)$$

Where ρ is the density of the solder, *g* is the gravitational constant, *y* is the liquid height, and *D* is the gap between the two plates. At a maximum capillary rise, $\Delta P = 0$, then:

$$\frac{-2\gamma_{LV}\cos\Theta}{D} + \rho g y = 0 \qquad (2.35)$$

And the maximum capillary rise would be:

$$h = \frac{2\gamma_{LV}\cos\Theta}{D\rho g} \qquad (2.36)$$

2.12 Formation of Intermetallic Compounds at the Joint Interfaces

An intermetallic compound is an ordered, homogenous alloy phase, which forms due to the reaction between two or more metals. In fact, intermetallic compounds are long-range ordered alloys with two or more sublattices in a superlattice structure. Each of these sublattices are occupied by various atomic species. During solidification, the atoms can be arranged randomly to form a substitutional solid solution lattice, or, they can be arranged in sublattice sites to form a superlattice as a long-range ordered structure. Here, the substitutional atoms occupy a very specific sublattice location in the matrix to form the superlattice structure[90,91].

The structure and properties of the intermetallic compounds put them in an intermediate position between the randomly ordered alloys and the ceramics. Intermetallic compounds are generally strong materials with high strength and modulus, even at elevated temperatures. Dislocation mobility is usually lower for the intermetallic compounds even at high temperatures. Dislocations in superlattices travel in pairs or groups. They show better creep resistance and lower diffusion process because they have stronger bonding and closer atomic packing[90, 91, 92].

At room temperature, the ordered intermetallics are usually hard and brittle and their brittleness is mostly caused by the bulk material properties, not by the grain boundaries. The brittleness of the grain boundaries are mainly caused by their high symmetry crystal structures with high ordering energy, (electronegativity, valence electron, and atomic size) large differences between the constituents. The results, poor cleavage strength, lack of sufficient deformation modes, low mobility of the superdislocations, planar slip, and grain boundary weakness, are the major causes for the brittleness of the intermetallic compound[91].

Formation and growth of the intermetallic compounds as the coherent layer at the joint interface are the basis for most problems in the soldering industry, due to their low conductivity, low coefficient of thermal expansion, and low ductility. These cause catastrophic failures at the interfaces[1, 8, 93].

Table 2.2 Intermetallic compounds formed between tin-lead and some alloying elements.

	Fe	Cr	Ni	Al	CU
Pb	None	None	None	None	None
Sn	$FeSn$	None	Ni_3Sn	None	Cu_3Sn
Sn	$FeSn_2$		Ni_3Sn_2		Cu_6Sn_5
Sn			Ni_3Sn_4		

Intermetallic compounds can be formed during the soldering process by the solid-liquid interaction or in service by solid-state diffusion. Their formation and growth depends on the elements that constitute the filler metal and the substrate. formation of compounds at the joint interfaces will increase the wettability and the solderability. However, their formation at the interfaces and into the body of solder can reduce the ductility and toughness. Dissolution of the substrate constituents into the molten solder or diffusion of the molten solder into the substrate, time and temperature are three important factors in soldering[1, 94 - 96].

Intermetallic compounds can also form during storage and operational services, especially at elevated temperatures through solid-state diffusion. For a particular solder-base metal system, the growth rate depends on the kinetics of the growth, time, and temperature. Equation (2.37) shows that the total thickness is related to time t and temperature T (Kelvin).

$$X(t,T) = X_0 + At^n e^{(-Q/RT)} \qquad (2.37)$$

Where X is the total thickness at time $t=0$, R is the universal gas constant, Q is the activation energy, A and n are constants. For highly reactive systems, the growth rate is linear, $n=1$. When the growth is controlled by bulk diffusion and declines with time, the growth rate is parabolic and $n=0.5$. In the case of sub-parabolic growth, $n=0.37$ [96 - 98].

2.13 The Soldering of Aluminum and its Alloys

The first problem with aluminum soldering is the removal of a tenacious aluminum oxide layer from its surface. The removal of this refractory oxide film is extremely difficult and it forms easily upon exposure to the air. Thus, for the soldering of aluminum and its alloys, special, strong fluxes are needed to break through the oxide layers. In a fluxless procedure, mechanical abrasion or ultrasonic vibration is necessary to push aside the oxide film from the surface[2, 7, 8]. Experience shows that the oxide films on the non-heat treatable aluminum alloys can be removed easier than the more adherent oxide films of the heat-treatable aluminum alloys. Alloying elements also affect the wetting behavior of an aluminum alloy. Soldering aluminum alloys is very difficult when the percentage of magnesium exceeds 1.5 wt%, and silicon 4.0 wt%. The presence of magnesium reduces the wettability and increases the intergranular penetration. More than 1.0 wt% magnesium also reduces the flux effectiveness. More than 4.0 wt% silicon in aluminum alloys also makes all flux types ineffective. A fluxless technique such as ultrasonic soldering is very helpful and should be ultilized when high amounts of magnesium and silicon are present[7].

The second problem is related to the occurrence of galvanic corrosion due to humidity at the joint with tin-lead solder, because of the position of aluminum in the electromotive series. Localized heating of the aluminum alloy during soldering is another problem, because of its extremely fast heat transfer compared with its low heat capacity. Also a large coefficient of thermal expansion combined with localized heating may result in distortion[8].

2.14 The Soldering of Stainless Steel

Stainless steels are generally protected from the corrosive environment by forming a chromium oxide layer on their surface. Breaking this strong protective layer in a flux soldering or especially in a fluxless process is very difficult. Therefore, a pre-coated surface with nickel, zinc, tin, or a tin-lead alloy is recommended. The main purpose of this coating is to improve the solderability of the stainless steel[2, 7].

2.15 Solder Joint Reliability

Microstructural stability of a solder joint is essential in relation to its mechanical properties and lifetime. A solder alloy can be subjected to microstructural changes during high temperature deformation and thermal or thermomechanical cycling. Understanding the relations among the process-structure-property in a solder joint strongly influences on further predictions and optimizations. It is obvious that heterogeneous coarsening of solder's microstructure due to thermal cycling and dynamic recrystallization as a result of creep, fatigue or coarsening during annealing or thermomechanical cycling affects the integrity and reliability of the joints. Thermal expansion differences between the joined materials or the solder and the substrate impose a strain that results in microstructural coarsening. The shear strain due to creep and fatigue also results in localized recrystallization. This recrystallized microstructural is equiaxed in contrast to the lamellar microstructure of eutectic tin-lead bulk solder.

The driving force for microstructural coarsening in a solid-state evolution stems from interfacial surface energy. Total interfacial energy for a given microstructure is reduced if its interfacial areas decreased. Such evolution shows the grain growth in a single-phase alloy and the feature sizes increase for as-solidified multiphase alloy [99-101]. The following equation was proposed for the static annealing condition:

$$d^4 - d_o^4 = \left(\frac{B_2 \gamma_i V C_o \zeta D_b}{KT} \right) \cdot t \qquad (2.38)$$

Where d is the mean phase size, d_o is the initial size, γ_I is the interfacial energy that drives the coarsening process, V is the molar volume of the second phase, C_o is the equilibrium solute concentration at the grain boundary, ζ is the grain boundary thickness, D_b is the grain boundary diffusity, t is the annealing time, B_2 is a geometric constant, T is the annealing temperature, and K is the Boltzman Constant.

By knowing:

$$\zeta D_b = \left(\zeta D_0 \exp \frac{-\Delta H_b}{KT} \right) \qquad (2.39)$$

Where ΔH_b is the activation energy for grain diffusion.

The coarsening of a solder joint microstructure, coefficient of thermal expansion mismatch and the internal strain of the joint are three factors influencing the tendency to crack. For a near eutectic or eutectic tin-lead solder joint, the heterogeneous coarsening causes intergranular cracking initiating in the tin-rich phase and propagating through the tin-tin grain boundaries[102].

In electronic equipment, coefficients of thermal expansion mismatches occur primarily because the devices and printed circuit boards are not made from the same material. Therefore, changes in ambient temperature or the heat gradient during operation induces a thermal displacement between the component and printing wiring board at the joint. This thermally induced strain can initiate a crack in which further crack propagation causes failure[13, 103 - 105].

In surface mount technology where solder pastes are used, the porosity is due to the paste material itself, because 35 to 65% of the volume of a paste is comprised of volatile material. The existence of these porosities in a joint reduces the thermal and electrical conductivities, induce crack initiation, weaken the joint strength, and shorten the fatigue life[103, 104].

The solder joints in electronic equipment can experience significant inelastic deformation, mainly because the service temperatures are usually above half of their absolute melting points. For the eutectic and near eutectic tin-lead solders, even room temperature will satisfy the above requirement and induce permanent deformation. The possibility of failure due to creep rupture or fatigue especially for surface mounted joints is high and known to be a major problem, because these joints must provide electrical continuity as well as mechanical strength. In this regard, the thermal fatigue, usually caused by thermal strain, raised by thermal expansion differences and influenced by the creep behavior of solder and the strain rate sensitivity is a major problem. Dislocation climb and grain boundary sliding are considered to be two mechanisms responsible for creep in tin-lead solder alloys. The latter is also encountered to be the mechanism for superplasticity in tin-lead eutectic alloys. Because of the large gaps between the thermal expansion of devices and the printed circuit boards, the joint that connect them together undergo very complex states of stress and strain in both through-hole and surface mount technologies.

Due to the expansion mismatches, a joint will experience inelastic deformation. There are six strain components corresponding to the normal and shear stresses. As a result, there are forces and moments exerted by a solder, posted on a chip or device in x, y, and z directions. These forces and moments could be obtained by integrating the stress component over the temperature gradient through the thickness of a printed circuit board. The board or even a chip carrier or device forced to be bent makes the problem much more complex.

Thermal fatigue resistance or creep resistance in a solder joint will decrease, since regions of inhomogeneous microstructure, due to coarsening, are the preferred sites for fatigue and creep cracks to initiate and propagate. Therefore, refined microstructure would be beneficial, due to the fast cooling rate. But such homogeneous and fine microstructure may not be stable for a long period of time because the microstructural coarsening would happen eventually even at room temperature[106 - 113].

2.16 Critical Review

Any components suitable to be joined by soldering have a degree of solderability, which is a complex processing parameter and mostly influenced by the wetting. Obtaining defect-free solder joints with acceptable properties for their intended applications depends directly on the wetting and flow of the molten solder. During a soldering process, the degree of wetting is related to the surface condition and the interfacial energies at the solid-liquid interface. Other factors such as thermal characteristics of the components, heat source ability, the flux (if used), chemical composition and viscosity of the molten solder, and chemical interfacial reaction, determine the rate of wetting.

In real materials systems, a variety of second-order effects, such as, the solder impurities, contamination of the molten solder by the substrate constituents, other possible contaminations (such as H_2S, SO_2, HCl and Carboxylic acids emitted from anisotropic coatings and packaging materials) in storage can affect and change the wettability.

The wetting behavior of the intermetallic compounds is intrinsically different from the base metal. Some have negligible effects on wetting; others may improve or inhibit wettability. A good metallurgical joint is usually accompanied by the presence of limited intermetallics.

The degreasing and pre-cleaning of the joint surfaces play a very important role in soldering. Grease and dirt (if kept on the surface), will decrease the wettable surface as well as reduce the capillary forces.

Inclusion and occlusions (such as metal oxides, sulfides, and so on) in either the filler metal or the base material, will affect the wettability and decrease the solderability. Non-metallic foreign particles or absorbed vapor on the surface will decrease the wettable surface at the joint area.

In flux-free ultrasonic soldering and coating, recent studies have shown that oxide removal and subsequent solder wetting results not only from the mechanical erosion, but also depends strictly on the coupling of sonic waves between the horn and the substrate. Thus, distribution of this coupled sonic energy on the substrate, combined with mechanical erosion removes the oxide film. This coupled sonic energy and its distribution on the surface can be influenced by different factors, such as the thickness of the substrate, direction of the energy transmission from the source to the surface, and the bulk properties of the substrate.

Chapter 3

Experimental Procedure

3.1 Fluxless Ultrasonic Soldering

The materials used in this study were 2024-T3 Alclad and 304 stainless steel sheets with a thickness of 0.8mm and 0.5mm, respectively. The fluxless ultrasonic soldering tests were performed on rectangular and square coupons, with dimensions of 50.8 x 25.4mm and 25.4 x 25.4mm. Soldered samples were prepared at different soldering temperatures, soldering times, and surface conditions and used to evaluate the shear strength of joints and the percentage of wetted area by non-destructive ultrasonic testing. For the samples prepared at different temperatures, the rectangular coupons were used to prepare the single lap shear joints as shown in Figure 3.1.a.

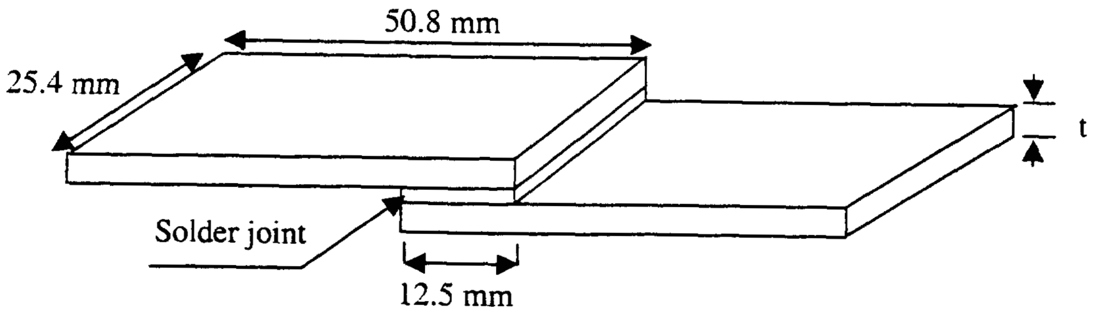

Figure 3.1a Rectangular coupons, single lap shear joint, t is 0.8 mm for aluminum and 0.64 mm for stainless steel.

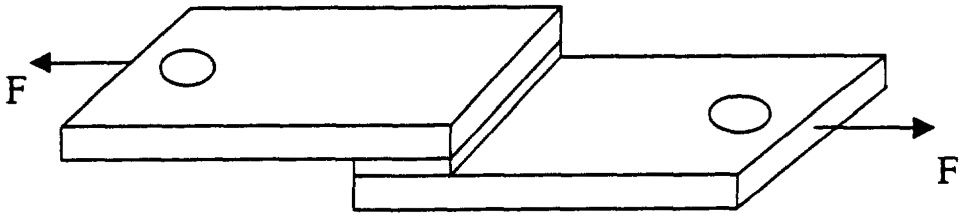

Figure 3.1b Shear Strength Test Sample Geometry

The non-destructive ultrasonic tests were performed on a single lap joint square coupon as shown in Figure 3.2. These specimens then prepared for optical and scanning electron microscopy.

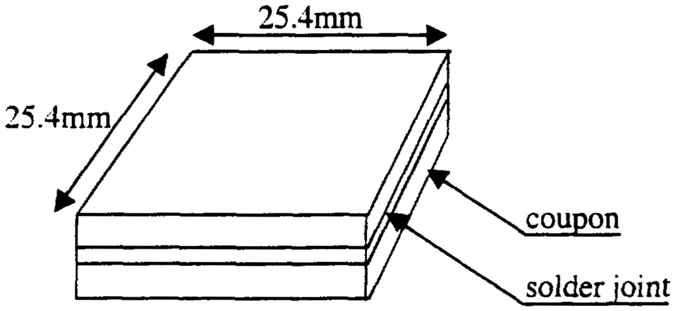

Figure 3.2 Non-Destructive Test Sample Geometry

The ultrasonic soldering tests were performed by contacting the horn directly to the joint area, which was preheated in the range of 200 to 300 °C. The schematic diagram of the flux-free ultrasonic soldering test set up is shown in Figure 3.3.

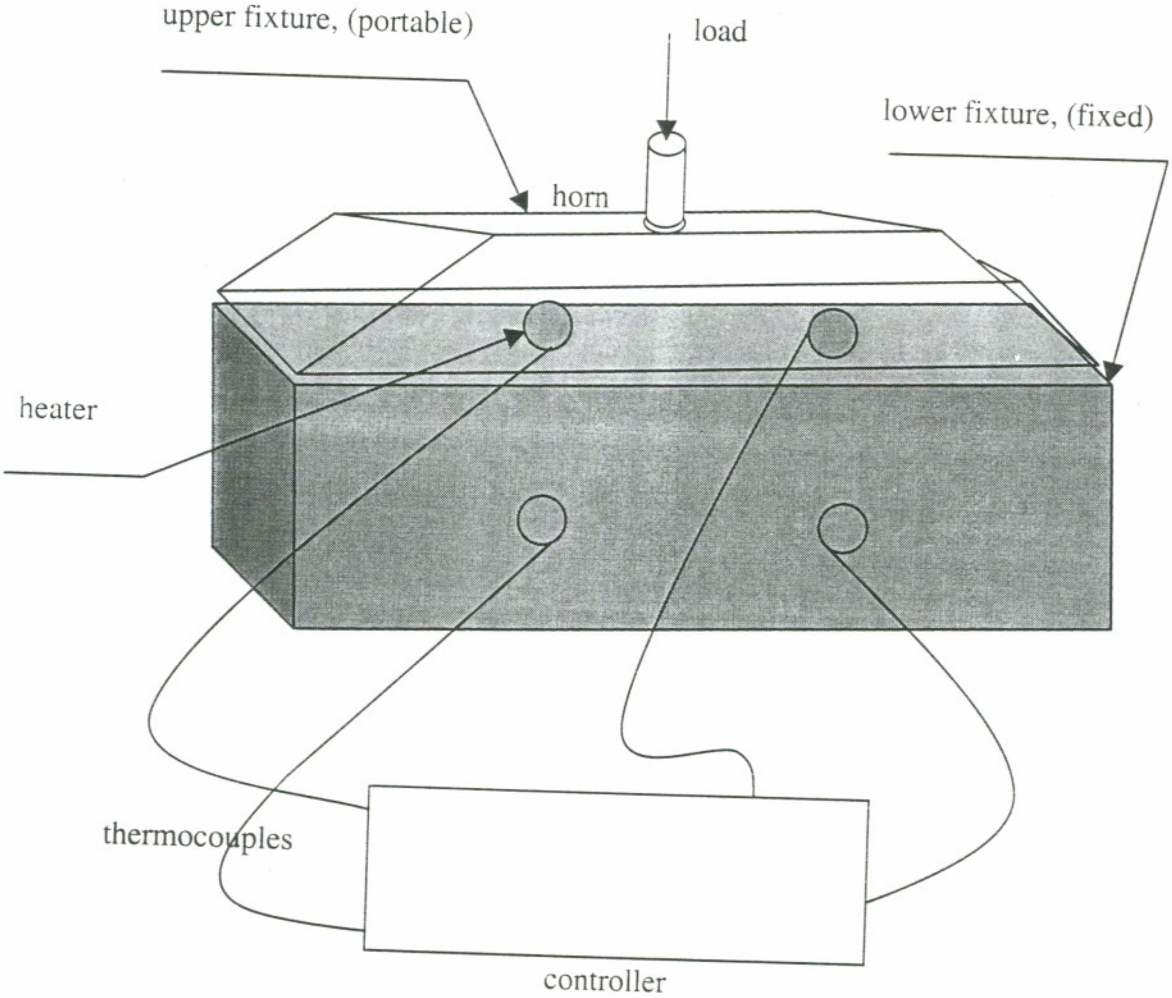

Figure 3.3 Schematic diagram of the flux-free ultrasonic soldering operation set up

The solder material was placed between the two coupons (as the coupons were placed between the upper and lower fixtures) before heating them and was melted when the sonic energy was applied. The output frequency of the sonic energy that was applied to the joint area and the molten solder as mechanical vibrations was 20 kHz. All ultrasonic tests were performed under a constant 50 psi pressure and held for 3 seconds. The ultrasonic soldering times were established for 2, 4, 8, and 12 seconds for different soldering operations and the cooling rates were kept approximately constant in the range of 5 °C/min. A 70Sn-30Pb solder alloy was used for the entire soldering operation.

In the process of ultrasonic soldering, mechanical vibrations (as the result of high frequency sonic energy) will be transferred to the molten solder through the work piece to create erosive forces. Not only these erosive forces, but also the coupling of sonic energy with the substrate affect the soldering operation and the joint integrity.

2024-T3 Alclad is an aluminum alloy claded with pure aluminum. The 2xxx series are heat treatable alloys, with copper as a major alloying element. In the T3 condition, the aluminum alloy will be quenched after a solution heat treatment. These alloys achieve a substantially stable condition as the results of a fairly fast natural aging after being cold worked. Another base material used in this work was a 304 stainless steel with enough alloying elements like Ni and Mn to stabilize its fully austenitic microstructure. The filler metal used was a near eutectic 70Sn-30Pb alloy. Its microstructure consisted of tin-rich proeutectic islands in a matrix of eutectic.

3.2 Ultrasonic Soldering Equipment

All ultrasonic soldering operations in this study were performed by a Branson Ultrasonic Plastic Welder, Model 8700. The principal components of this machine are: a power supply for converting a 50 to 60 Hz current to 20 kHz electrical energy; a converter that changes this electrical vibration to mechanical vibration at ultrasonic frequencies; a booster for establishing a modified amplitude at the face of the horn, a horn which transfers the ultrasonic vibrations to the work piece or molten solder. The major part of a converter is an element made of lead-zirconate-titanate, which expands or contracts at its resonant frequency when excited by electrical energy. The two ends of an excited horn at its resonant frequency are lengthening and shortening with no longitudinal motion at its center. The peak-to-peak displacement of the horn face is its amplitude, which can be changed by altering the input amplitude or the cross section area and its mass distribution. The ultrasonic horns are usually made of titanium or aluminum alloys because of their good acoustical properties and high strengths. Horns are made in several styles to meet the requirements of various applications. The horn used in this study was an exponential 20khz horn with a cross sectional area that follows an exponential equation. These types of horns are used mainly for application requiring high force and low amplitude. Figure 3.4 shows the principal components of an ultrasonic welder.

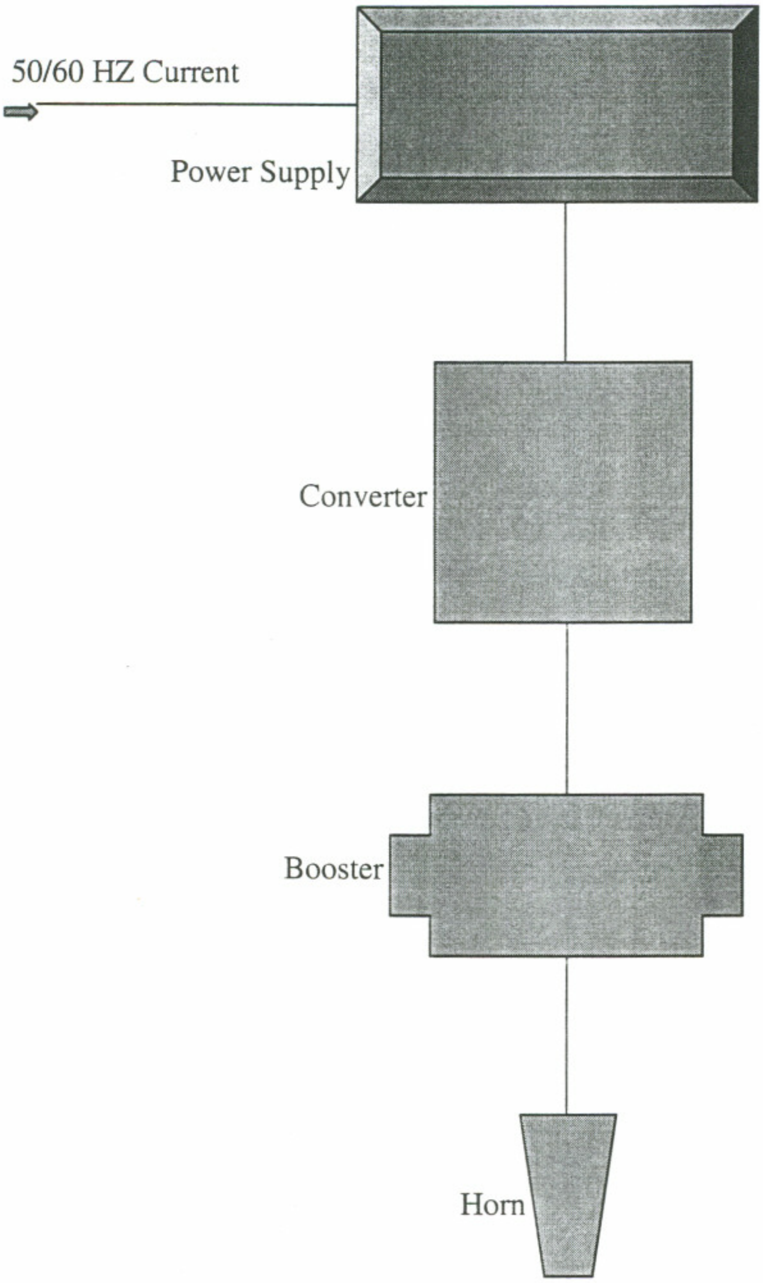

Figure 3.4 Principal component of an ultrasonic welder

3.3 Surface Preparation

All coupons for ultrasonic soldering tests were soap washed and then ultrasonically cleaned (degreased) in de-ionized water for 15 minutes at room temperature. Three different groups of coupons were used for the soldering operations. The first group was simply ultrasonically cleaned. The second group was tin-plated. The third group was chemically cleaned in alkaline or acid-cleaners. The aluminum coupons were immersed in an alkaline solution bath containing 75 grams of sodium hydroxide and 4 grams of sodium phosphate in 4 liters of de-ionized water. The stainless steel coupons were chemically cleaned in four different solutions.

First Cleaner: A dilute HCl, $H_2 SO_4$ solution.

Second Cleaner: A dilute HCl solution.

Third Cleaner: A reagent solution containing 7.45ml HCl, 15ml HNO_3, and 20ml of Methanol.

Fourth Cleaner: A reagent solution containing 75 parts of HCl, 5 parts of HNO_3, 25 parts of water, and 20 weight percent of $FeCl_3$.

3.4 Shear Strength Tests

All shear strength tests in this study were carried in stroke control mode, through an Instron Dynamic Testing Machine, Series 1330, derived by a servohydraulic control system with a feedback transducer, which can operate in three mode controllers, load, stroke, and strain. These mode controllers respond to the force applied by the actuator, the actuator movement or position, and the deformation of the test sample, respectively. Test parameters were defined and determined before translating the data into switch and control settings on the equipment. The shear strength for each test was obtained as the ratio of maximum load for breaking the joint over the shear joint area.

$$\text{Shear strength of the joint} = \frac{F_{MAX}}{A} \qquad (3.1)$$

Where F_{MAX} is the maximum force for breaking the specimen.

3.5 Non-Destructive Ultrasonic Evaluation

All non-destructive ultrasonic tests for evaluating the wetted area were performed on single joints as shown in Figure 3.2. The tests carried on aluminum samples, which were ultrasonically cleaned and ultrasonically soldered without flux at temperature ranges from 200 to 300°C. Pulse-echo methods were used to detect the pulses sent by a single element transducer, which works as an emitter receiver at the same time. Evaluations were based upon the response of the joint to an acoustic stimulus where the joint quality will be measured upon its acoustic impedance. A good joint, therefore, must show a different acoustic impedance from the defects, voids, inclusions, and dewetted or unsoldered area, simply by responding to the acoustic stimulus. The ultrasonic detector used in this study was calibrated before performing the non-destructive tests with the same aluminum used to prepare the soldered samples. The calibration was greatly simplified because the velocity of the test material (aluminum) was known. By knowing the velocity and choosing a proper transducer frequency which is usually marked on the probe, then the wavelength will be figured out according to Equation (3.2).

$$\lambda = \frac{V}{F} \qquad (3.2)$$

Where V is the velocity, F is the frequency and λ is the wavelength.

A Krautkramer USD-10 Portable Digital Ultrasonic Flaw Detector with a 1/8 inch diameter transducer (Sonopen 15Mhz Single-Element / Delay Line) was used to evaluate the percentage of the wetted areas throughout this study. The wetted area at each test-point was estimated by comparing the two pick signals separated from the initial signal, which is always located at the very left end of the monitor. These two signals were showing the lack of bonding at the interface and back reflection through the joint and both coupons respectively from left to right.

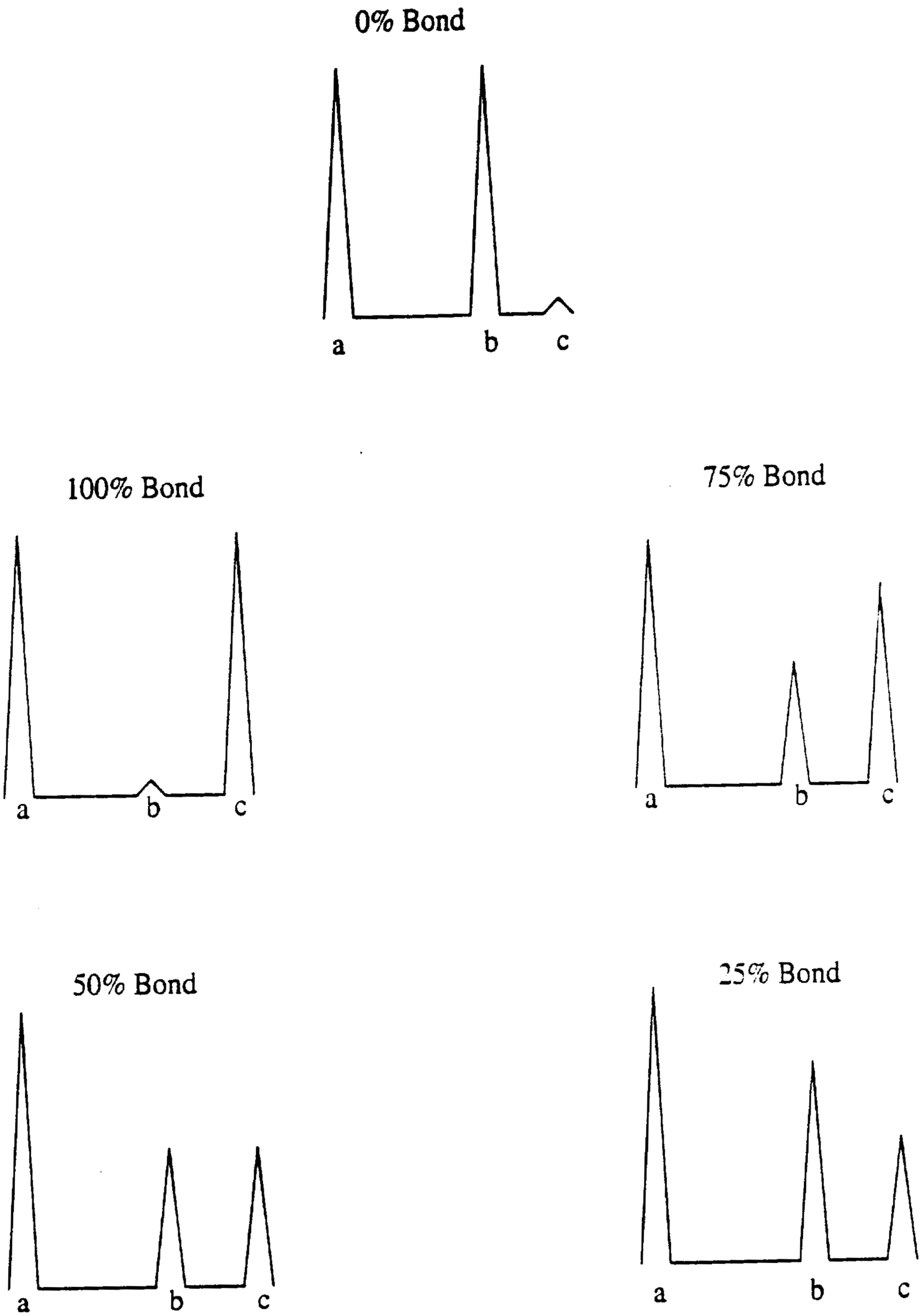

Figure 3.5 Schematic of some non-destructive ultrasonic signals

a: Initial signal

b: Lack of bonding signal

c: Reflection through signal

3.6 Specimens Preparation for SEM Analysis (Effect of Sonic Energy)

Two samples were used to investigate the effect of mechanical vibration on the microstructure of a solder joint during the solidification process. These samples are prepared by melting the fill metal (70tin-30lead) in two ceramic crucibles in a furnace, keeping them for a short period of time there, and solidifying them at a cooling rate similar to a solder joint cooling rate. During the solidification, the sonic energy (mechanical vibration) was applied into the molten solder on these crucibles. The solidified samples were then prepared for scanning electron microscopy to identify their microstructure and the effect of sonic energy on the as-solidified molten solder.

3.7 Specimen Preparation and Optical Microscopy

The nature of a soft solder joint, in combination with harder base materials such as aluminum alloy or stainless steel, in a mounted cross section make sample preparation very difficult. During grinding and polishing steps, the solder layer between the two base material coupons is easily scratched and also deformed plastically around the solder-substrate interface. Therefore, extreme caution must be applied during the specimen preparation for optical or scanning electron microscopy. All specimens were cold mounted with Epofix, a mixture of resin and hardener at a ratio of 15:2. Wet grinding and rough polishing of the mounted samples was conducted with 120, 240, 400, 600 and 800 grit silicon carbide papers. Tap water was used as the lubricant and the abrasion debris removal agent from the papers in each step of the operation. Wet grindings throughout this study were done by using a semi-automatic grinder to maintain a flat, polished surface for the cross section, having some phases or parts with different hardness. The speed of the lapping wheel was kept constant at the rate of 150rpm. A short polishing time and moderate pressure were applied to avoid excessive polishing effect or permanent deformation. After each grinding step, the specimens were washed by water. The final polishing was done either on high-nap or low-nap cloths and dried under high-pressure air, depending on the conditions of the surfaces to be polished. High-nap cloths were used for the fine polishing of the base materials or solder alloy surfaces and charged with a slurry of water containing 5, 1, and 0.05 micron alumina, respectively. Low-nap cloths were used for the fine polishing of the inhomogeneous ground cross-section surfaces and charged with the slurries of polishing oil containing 6 and 1 micro diamond pastes, respectively. The fine polishing steps were conducted at short polishing times under high polishing pressure. The speed of the lapping wheel remained under 300rpm. After each step, the specimens were water washed and dried. At the end of each final polishing, the lubricants were removed from the specimens' surface by washing with water, swabbing with alcohol, and dried with hot air. Aluminum alloy, stainless steel alloy and solder alloy specimens were etched by swabbing with the following etchants.

ALUMINUM ETCHANT:

- 1 gr. of NaOH, 100mL H_2O, swab for 5-10 seconds
- 100mL H_2O
- Swab for 5-10 second

STAINLESS STEEL ETCHANT: Used a dilute Aqua Regia

- 8.15mL HCl
- 5mL HNO_3
- 100mL H_2O

SOLDER MATERIAL ETCHANT:

- 2.2mL HCl
- 5mL HNO_3
- 93mL H_2O

All optical microscopy examinations were conducted on a Nikon system at different magnifications. The solder joint cross-sections and their interfaces were also investigated through this system. Optical microscopy of the solder joints was limited to a primary observation of the joints, because the maximum magnification was limited. Therefore only a percentage of the soldered area along the solder joint cross-section was estimated each time. A quantitative study of the wetted area for aluminum samples prepared at different soldering temperatures was done by Leco 2001 software. The samples used in this study were already evaluated by Krautkramer USD-10 ultrasonic detector. Two sides of a broken joint were qualified separately and the results were averaged. The contrast between the matrix and the soldered areas is large enough to avoid artificial effects on the wetted area percentage. Some simple operations, such as sharpening, histogram modification, and thresholding were employed during the image process. For each sample, the image processing was done at different locations and for two different magnifications, to improve the accuracy. The area fraction was determined for each specimen in image processing, then compared to the percentage of wetted area found by the ultrasonic detector. The results were matched.

3.8 Scanning Electron Microscopy

All the SEM studies were conducted in a Zeiss Digital 960 Scanning Electron Microscope at the range of 10 to 30 Kilo-volts. The composition of matrices and different phases were configured in a Link Energy Dispersive Spectrum System (EDS), using secondary and backscattered images and a beryllium window X-Ray Detector. All samples used in the scanning electron microscopy were fine-polished.

The SEM study on solder joint cross-sections included secondary imaging, backscattered imaging, electron dispersive spectrometry, and line-scan analysis.

- The secondary electron imaging of different solder joints prepared under various soldering conditions helped qualify the joint integrity. Also, most X-Ray analyses were done by using secondary electron images. The thickness of the solder joint layers were verified and measured through secondary images. The secondary images were taken to show the influence of cavitation erosion on the substrate surface and the morphology of the solder wetting pattern.

- Backscattered imaging was employed to investigate and determine the thickness and microstructures of different solder joints, as well as the solder-substrate interfaces. Also, the microstructure of the bulk solder was determined by backscattered imaging for further investigation of the effect of the solidification cooling rate on the microstructure of the solder joint. The backscattered images of the as-solidified bulk solder and as-solidified bulk solder under sonic energy were taken to compare their microstructures and configure the effect of sonic energy on the microstructure of the solder joint.

- X-ray analysis was used to identify the composition of the base materials, solder alloy, phases, and layers. X-Ray analysis was also used as a tool to investigate the possibility of diffusion of some elements from the base material into molten solder during the ultrasonic soldering operations.

- Line scan analysis was employed to investigate the condition of a protective layer such as Ni after soldering, the possibility of diffusion from the base material into molten solder, and the solder-substrate interface.

Chapter 4

Experimental Results and Analysis

Flux-free ultrasonic soldering of 2024 Alclad and 304 stainless steel was conducted to determine the conditions to produce the highest joint strength. Soldering was performed in air as well as in an argon atmosphere. The effect of surface preparation was investigated. Surface preparations included: (a) degreasing, (b) chemical cleaning, and (c) tin-plating with a nickel strike between the substrate and the tin. These surface preparations resulted in four case studies which include: (1) degreased specimens with 70Sn-30Pb filler metal, (2) chemically cleaned specimens with 70Sn-30Pb filler metal, (3) tin-plated without filler metal, and (4) tin-plated with 70Sn-30Pb filler metal. Other variables such as ultrasonic soldering time and temperature were investigated. In all cases, the solder alloy used in this study was the near-eutectic 70Sn-30Pb composition.

4.1 Shear Strength

Shear Strength of 2024 Alclad Lap Joints Soldered in Air

Alclad specimens were ultrasonically degreased in de-ionized water and then soldered at temperatures from 200 ° to 300 °C in air. Table 4.1.1 and Figure 4.1.1 show that increasing soldering temperature increased the joint shear strength up to a maximum of 2,260 psi at 300 °C which about half of bulk shear strength (5,500 psi) of the 70 Sn-30Pb filler metal. It is interesting to note that some joining did occur even at 200 °C despite the fact that the freezing range of the alloy is about 183 ° to 200 °C.

When the 2024 Alclad was only tin-plated prior to joining, significantly poorer joint strength resulted as shown in Table 4.1.2 and Figure 4.1.2, There was virtually no strength when the soldering temperature was only 200 °C. The reason for the poor strength of the tin-plated joints was because no solder (70Sn-30Pb) was added to reduce the melting point of the tin-plated filler metal. The melting temperature of the tin-plating (232 °C) exceeded the soldering temperature of only 200 °C. Thus, the tin-plated aluminum did not bond at 200 °C because the tin-plating did not liquefy at this low temperature. When the soldering temperature was raised to 230 °C, excellent joint strength resulted. However, unlike the degreased specimens in Figure 4.1.1, the tin-plated specimens exhibited decreasing strength with increasing temperature. For example, at a soldering temperature of 300 °C, the joint strength diminished to only 400 psi. The reason for the loss of strength at the elevated soldering temperatures was the dewetting which occurred due to the rapid oxidation of the tin plating.

Significantly improved shear strength resulted when the tin-plated 2024 Alclad was ultrasonically soldered with the 70Sn-30Pb filler metal in air. Since the liquidus and eutectic temperatures of the solder filler alloy were 200 °C and 183 °C, respectively, excellent joint strength was achieved without degradation due to oxidation, as shown in Table 4.1.3 and Figure 4.1.3. With increasing soldering temperature up to 300 °C, a gradual reduction in strength occurred as a result of oxidation of the solder.

For the chemically cleaned 2024 Alclad specimens soldered in air, the shear strength of the joint increased when the soldering temperature increased as shown in Table 4.1.4 and Figure4.1.4. The results also showed that the shear strengths of the chemically cleaned (deoxidized) joints were significantly improved for all soldering temperatures, specially at higher temperatures when the shear strength reached around 4,000 psi at 300 °C. This proves that the chemical cleaning (deoxidation) of substrate surfaces were successful. Although the oxide film was formed immediately on the 2024 Alclad deoxidized surface, it was not strong and thick enough to endure the cavitation produced by the ultrasonic vibrations. Therefore, during an ultrasonic soldering operation, the newly formed oxide layer on the substrate surface could be removed by the cavitation erosion action to created metallic surface with a much higher degree of wettability and solderability against the molten solder and consequently producing higher solder joint strength values.

Table 4.1.5 and Figure 4.1.5 present the shear strength values of degreased 2024 Alclad specimens soldered in air at 230 °C. The results show that increasing the soldering time from 2 to 4 seconds increased the joint strength from 330 psi to 1,080 psi. However, further increases in soldering time from 4 to 12 seconds had little effect on joint strength. The overall results suggested that the further increases in soldering time beyond 4 seconds was not able to break up more oxide from the joint surfaces. It could not expand the deoxidized metallic surface for more wetting and therefore a stronger joint.

When soldering tin-plated Alclad in air at 230 °C, increasing the soldering time increased the joint strength as shown in Table 4.1.6 and Figure 4.1.6. The results also show that for the tin-plated specimens without using filler metal, there is a significant improvement in strength from 970 psi to 1,830 psi (almost double) when the soldering time increases from 2 to 12 seconds. The results confirmed the steady increases in strength by increasing the ultrasonic soldering time. This is because increased ultrasonic energy created larger oxide-free areas to be wetted.

For the tin-plated specimens ultrasonically soldered using the 70Sn-30Pb filler metal, the results of shear tests shown in Table 4.1.7 and Figure 4.1.7 confirmed the previous outcomes for the tin-plated specimens (no solder added). There was an increase in the joint strength with increasing soldering time. The results also show that the shear strength of the joints for the tin-plated specimens (solder added) were higher than those without solder. This is because the shear strength of the bulk 70Sn-30Pn solder (around 5,500 psi) is greater than the strength of the pure tin (2,900 psi). Therefore, the shear strength of a solder joint very much depends on the filler metal used. The joint strength for the specimen soldered for the longest time

(12 seconds) was 2,220 psi. It was not as high as it was expected and the reason is that at the higher soldering times the tin-plating was further oxidized in air even at 230 °C and the ultrasonic vibration could not be able to remove the new formed oxide layers.

Significant improvements in shear strength resulted when the chemically cleaned 2024 Alclad specimens were soldered with the filler metal in air at different soldering times. As shown in Table 4.1.8 and Figure 4.1.8 the overall joint thickness increased for each individual sample compared to the results from the tin-plated specimens with and without filler metal. This shows that the deoxidizing operations were effective. At the same time, there was a significant increase in strength for the higher soldering times (8 and 12 seconds) where the shear strengths reached 6,000 psi. These outcomes again confirmed that in the absence of a thick oxide film, increasing the soldering time (increasing the time when the mechanical vibration was applied) was very beneficial to joint strength.

Shear Strength of 2024 Alclad Lap Joints Soldered in Argon

The overall results presented in Table 4.1.21 and Figure 4.1.21 through Table 4.1.28 and Figure 4.1.28 show that the strength of the solder joints, ultrasonically soldered (flux-free) at different soldering temperatures and times improved using an argon atmosphere. The reason is that the argon shielded the specimen surface and molten solder from further oxidation.

As for the degreased samples, soldered in argon, the joint strength increased when the soldering temperature increased. The results presented in Table 4.1.9 and Figure 4.1.9 show that at any soldering temperature the strength increased compared with the same operation performed in air. This confirmed that the quality of the soldering operation improved by using the argon atmosphere.

The results presented in Tables 4.1.(10 - 11) and Figures 4.1.(10 - 11) prove the significant effects of the argon shielded environments in an ultrasonic soldering operation. These results confirm that the oxidation of the tin-plating surfaces at higher soldering temperatures were the only reasons for the declining strength of the joints in Figures 4.1.(2 - 30) with increasing soldering temperature.

As for the chemically cleaned (degreased) 2024 Alclad specimens, soldering operation under argon gas protection was an adequate option at higher soldering temperatures. Table 4.1.12 and Figure 4.1.12 show that using argon protection was beneficial, especially for high temperatures. For example, the joint strength increased to around 5,000 psi for the shielded specimen soldered at 300 °C, compare to the unprotected sample. But, in the cases of protected and unprotected specimens soldered at 200 °C, the increased strength did not exceeded 100 psi as shown in Figures 4.1.(4 - 12). This is because oxidation did not affect wetting at such as low soldering temperature.

For the Alclad specimens soldered ultrasonically in argon at different soldering times with different surface preparations, the results show that the argon shielding was greatly beneficial. The effect of shielding was variable and depended on the severity of the oxidation during the soldering operation. For example, for the tin-plated and solder added specimens, the differences were quite large between the protected and unprotected specimens as shown in Table 4.1.27 and Figure 4.1.27. This was an indication that the tin-plating of the unshielded specimens were severely oxidized during the soldering operations. This was not the case for the chemically cleaned specimens soldered at different soldering times with or without the argon environment, as shown in Table 4.1.28 and Figure 4.1.28.

Shear Strength of 304 Stainless Steel Lap Joints in Air and in Argon

For the degreased and chemically cleaned stainless steel specimens, soldered with a flux-free ultrasonic operation, there was virtually no strength for the specimens soldered at different soldering temperatures or soldering times, as shown in Tables 4.1.(35 - 36) and Figures 4.1.(35 - 36). This was also true for the operations performed in an argon environment as shown in Tables 4.1.(37 - 38) and Figures 4.1.(37 - 38). In this case, the rate of re-formation of Cr_2O_3 apparently was so rapid after chemical cleaning that wetting by the molten solder was impossible. Thus, the ultrasonic energy was not able to prepare a pristine surface for wetting because it could not break the new chromium oxide layers formed on the surface after the chemical cleaning (deoxidization).

The tin-plated samples with nickel strike between the tin-plating and the 304 stainless steel, soldered ultrasonically with or without the filler metal in air at different temperatures, showed some strength particularly at the lower soldering temperatures, as presented in Tables 4.1.(29 - 30) and Figures 4.1.(29 - 30). For the tin-plated specimens (no solder added), there was virtually no strength for the sample prepared at 200 °C, because the tin-plating was not melted during soldering at this temperature. The severity of oxide formation and growth on the tin-plated surfaces caused some continuous reductions in strength of the joints with increasing soldering temperature. This was proved when the tin-plated specimens were soldered in argon, as shown in Tables 4.1.33 and Figures 4.1.33.

Tin-plated stainless steel specimens soldered without adding the filler metal at different soldering times in air also demonstrated some strength as shown in Table 4.1.31 and Figure 4.1.31. It was not expected to have a severe condition for the oxidation of the tin-plating, mostly because the soldering temperature was low (230 °C). But the overall results showed that a higher degree of oxidation occurred when the soldering time increased. For example the sample soldered for 12 seconds generated a joint strength of only 1,300 psi. Table 4.1.34 and Figure 4.1.34 show the results for similar soldering in a protected environment (argon). When protected with argon shielding, strength increased with increasing ultrasonic soldering time. At the longest ultrasonic soldering time of 12 seconds at 230 °C, the joint shear strength reached nearly 1,500 psi.

Comparison of the Strength of Ultrasonically Soldered Aluminum and Stainless Steel

The shear strength of tin-plated specimens ultrasonically soldered with addition of 70Sn-30Pb filler metal were higher than the tin-plated specimens without using solder for both the aluminum and stainless steel specimens. The reason was the difference between the strength of the tin-lead and the pure tin bulk materials. The shear strength of the bulk solder (70Sn-30Pb) was about 5,500 psi compared to the pure tin which was around 2,900 psi. The results also showed that the shear strength of the ultrasonically soldered tin-plated Alclad specimens were higher than the tin-plated stainless steels with or without using the 70Sn-30Pb filler metal. This was mainly because of the differences between the mechanical properties of the substrate materials. The 2024 Alclad alloy had a lower modulus of elasticity and strength than the 304 stainless steel. Experimental observations suggest that the efficiency of the ultrasonic activation for removing the oxide films depended as strongly upon the bulk properties of the substrate as on its surface conditions. The higher growth rate for the chromium oxide film was probably the most valid reason for explaining why the chemically cleaned stainless steel specimens which were joined using ultrasonic energy had virtually no strength. The opposite argument is also useful for explaining the very significant success when chemically cleaned Alclad specimens were ultrasonically soldered. The strengths of some joints for the Alclad specimens were even higher than the strength of the bulk solder as was the case for the specimen soldered at 230 °C for 12 seconds in air, as shown in Figure 4.1.8. This was also the case that the protective environment (argon gas) prevented further oxidation and thickening of the oxide layer on the substrate surface during the soldering operation. This is the reason behind the more successful wetting and higher strength when the argon gas was used. Therefore, breaking down the oxide layer, the strength of the bulk solder, and the shielding environment had significant effects on the solder joint strengths as shown through this study for both Alclad and stainless steel specimens.

The overall soldering results confirmed that the surface condition for 304 stainless steel specimens was more crucial than for 2024 Alclad. The results also showed that the oxide formation and growth was detrimental to soldering specially at high soldering temperatures. The soldering time in an ultrasonic soldering operation also affected the joint shear strength and wetting. Increasing the soldering time in general improved the quality of the joint and increased its strength. The ultrasonic soldering of the tin-plated 304 stainless steel specimens showed some achievable promise. The results confirmed that the tin-plating was a simple solution to an old problem of soldering of difficult-to-solder materials, especially when the flux was not used in the operation. The ultrasonic soldering also proved to be a doable method in a vast domain from microelectronics to refrigeration for coating and soldering. It is an easy and clean operation, which is even applicable for the complex geometries.

4.2 Metallography, Microanalysis, and Non-Destructive Evaluations

In a soldering operation, it is important to determine the compositions of the substrate and the bulk solder alloy, and evaluate their microstructures. Because the mechanical properties of the substrate and the bulk solder alloy and the compositions of their constituent elements affect the solder joint properties. Dissolution and diffusion of the elements mostly from the base material in to the molten solder and proportionally by lower amount from the molten solder into the substrate is proved to be essential and sometimes detrimental to soldering. However, it is always the case that even at the relatively lower soldering temperatures (maximum 400 ^{o}C), the element(s) from the substrate may be dissolved in or react with the molten solder at the interfaces. Although the compound formation at the joint interfaces is not the case for the aluminum substrates with the tin-lead filler metals, there could be a dissolution of the base metal into the molten solder. As in ultrasonic soldering in which the substrate surface can be eroded because of the cavitation action, it needs to be considered seriously, particularly for the aluminum substrate, because the melting temperature for aluminum and its alloys are not far from that of the molten solder (compared to stainless steel).

The metallography and microanalysis investigations presented in Table 4.2.1, Figure 4.2.1 and Table 4.2.2, Figure 4.2.2 respectively confirm that the substrates were; 2024 Alclad, and fully austenite 304 stainless steel. The Alclad layer shown in Figure 4.2.1 confirmed that a pure aluminum layer is claded on the 2024 Al alloy surface. The results of the electron dispersive spectrometry shown in Figures

4.2.(4 – 5) also confirmed that the compositions of both substrate alloys were matched with their nominal compositions. The bulk solder was a 70Sn-30Pb filler metal with a microstructure consisting of Sn-rich islands in a eutectic tin-lead matrix as shown in Table 4.2.3 and Figure 4.2.3.

A typical microstructure of an ultrasonically soldered joint deposited on 2024 Alclad is shown in Figure 4.2.7. The overall investigations suggested that the solder joint microstructure was independent of the soldering variables such as; soldering time, surface condition, and joint thickness. However, increasing the soldering temperature would coarsen the joint microstructure. Cooling rate was a major factor which had a significant effect on the joint microstructure as shown in Figures 4.2.(12 thru15). All the above solder joints have dendrite microstructures with proeutectic tin phase and eutectic matrix except for the Figure 4.2.15, which shows a eutecticlike structure. This is mainly caused by the dissolution of considerable amount of the aluminum substrate (compared to molten solder) into molten filler metal. It might also be affected by the solidification rate which was the same for the thicker joints, but for the very thin solder joint (the joint prepared at 300 °C), it was different and could not be kept the same as the others because of its small cross section. Expansion of the eutectic matrix which caused the proeutectic phase to be minimized can be explain in two steps. Primarily, a very large surface area (substrate material) compared to a thin solder joint may have increased the ratio of the temperature gradient and the growth velocity during the solidification. This higher value of G / R resulted a plane front solidification and minimized the proeutectic phase to create a eutectic microstructure. Secondly, there was some dissolution of the aluminum substrate into the molten solder at higher soldering temperature (300 °C). Dissolution of aluminum into tin-lead molten solder also helped a shift towards a fully eutectic structure. Becaue disolution of aluminum into molten solder could also change the G / R ratio by creating new nucleation sites, preventing a dendritic growth and in favor of a plane front solidification.

The effect of the ultrasonic energy on the solder joint microstructure was also investigated. The same quantities of molten bulk solder were prepared in two separated crucibles. Then the sonic energy (mechanical vibration) was applied to one as they solidified. The cooling rate was kept constant for both. The SEM backscattered images shown in Figure 4.2.10 and Figure 4.2.11 confirm that both samples have dendrite microstructures similar to the solder joints and the applied ultrasonic energy during the solidification had no noticible effect on the as solidified microstructures.

Thickness of solder joint

The influence of solder joint thickness on the joint strength has been the subject of many investigations. It is also important for this study, to determine its effect on the joint strength. A characteristic of ultrasonic soldering of lap joints is the change in joint gap thickness as a function of soldering temperature. This is mainly due to the changed in the fluidity of molten solder. The viscosity of molten solder can be controlled by temperature, and by increasing the temperature the viscosity is reduced exponentially. Lower viscosity increases the fluidity and improves the spreading of the molten solder on the substrate surface. An increase in the molten solder fluidity (resulted from the temperature change), not only affects the wetting but also the joint thickness as shown in Table 5.2.6 and Figure 5.2.16. These solder joint thickness changes which illustrated in the SEM backscattered images are shown in Figures 5.2.(12 – 13- 14- 15) for the chemically cleaned 2024 Alclad specimens, ultrasonically soldered for 4 seconds at different soldering temperatures in the ranges from 200 ° to 300 °C. It is also important here to cite that the reactivity of the Sn in the 70Sn-30Pb solder to form the stable compounds Ni_3Sn, Ni_3Sn_2, and Ni_3Sn played a definite role in wetting the tin-plated specimens with the nickel strikes.

Wetting of the substrate

Wetting of the substrate fundamentally controls the strength of the soldered joint. For example, when 2024 Alclad is chemically cleaned and then ultrasonically soldered at temperatures between 200 ° and 300 °C, both shear strength and percent of wetted area increase with increasing temperature as shown in Table 4.2.7 and Figure 4.2.17.

Figure 4.2.18 is a SEM secondary image as viewed looking down upon the fractured surface of a solder joint for an aluminum specimen, showing the annular morphology of the wetting pattern. During ultrasonic soldering, the mechanical vibrations had a turbulent effect in the molten solder and created an annular (donut) wetting pattern. These wetted, annular regions were the areas of the erosion on the substrate surface. In fact, the wetted areas separated by the non-wetted regions were the areas at the cavitation bubble walls which were preferentially attacked when the bubbles were collapsed as shown in Figure 4.2.19.

Erosion of Substrate during Ultrasonic Soldering

As discussed before, the constituent elements of a substrate material can be dissolved into molten solder. The amount of dissolution generally depends on, the solubility of these constituent elements, the phase diagram between reacting constituents, the soldering temperature, and the soldering time. But, in ultrasonic soldering, the dilution increased because of the erosive nature of the ultrasonic vibrations. Nickel was used as a barrier to prevent dissolution of the substrate as shown in Figure 4.2.22. The effectiveness of a nickel strike as a barrier and its presence on the joint interface was investigated. Figure 4.2.20 and Figure 4.2.21 show, the line scan microanalysis for two tin-plated specimens soldered ultrasonically without and with solder addition. The results confirm that the nickel strikes between the tin-plating and the substrate surface protected the substrate surfaces from oxidation and prevent the dissolution, as presented in Table 4.2.8. It was not the same for the chemically cleaned specimen. Table 4.2.9 presents a considerable amount of dissolution (1.00 wt%) for the aluminum in molten solder.

Non-destructive Test of Solder Joints

Ultrasonic non-destructive test was employed to evaluate the percentage of the wetted area for different specimens, which soldered (flux-free) at various soldering temperatures. In ultrasonic soldering, in the absence of a fluxing agent, the soldering temperature was one of the main variables affecting the spreading of molten solder on the substrate surface. Soldering temperature was exponentially and inversely related to the viscosity of molten solder. Therefore, increasing the soldering temperature greatly decreased the viscosity and increased the spreading. The chemically cleaned and ultrasonically soldered (at different temperatures) Alclad specimens were tested using a non-destructive ultrasonic instrument to measure the wetted area fractions. The results shown in Table 4.2.10 confirm that, soldering temperature was a crucial factor in an ultrasonic soldering operation and increasing the soldering temperature is beneficial to wetting.

Soldering Condition
Substrate: 2024-Alclad
Solder Alloy: 70Sn-30Pb
Soldering Time: 4s
Shielding Condition: Air

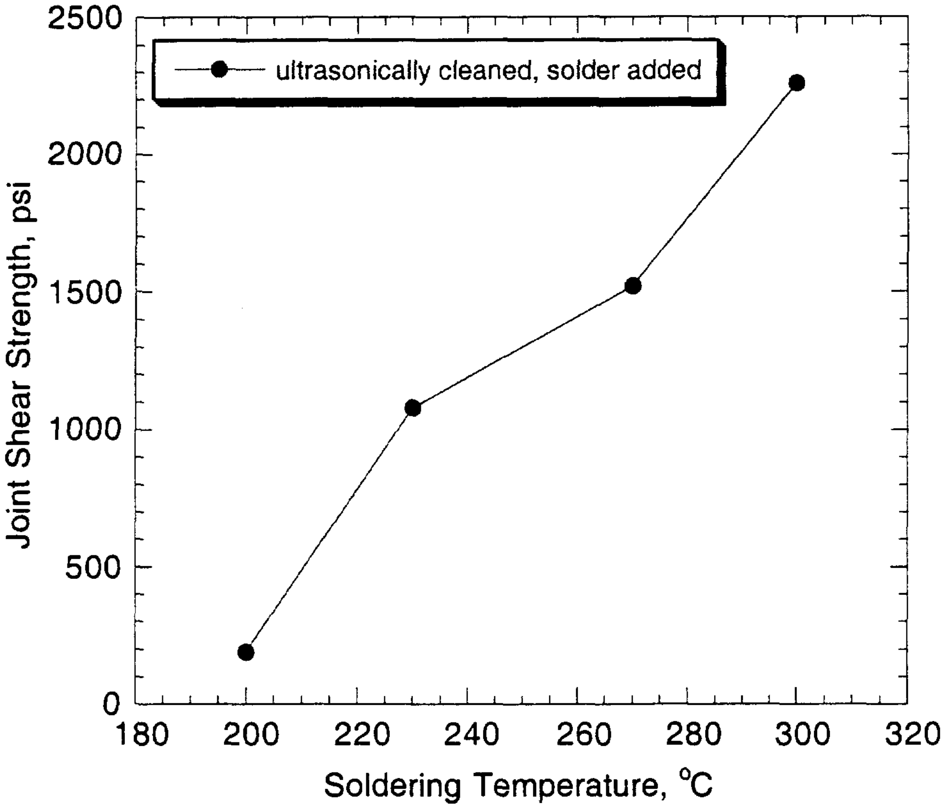

Figure 4.1.1 Shear strength of degreased 2024 Alclad, ultrasonically soldered with 70Sn-30Pb for 4 seconds in air, for different soldering temperatures.

Table 4.1.1 Shear strengths for the specimens, ultrasonically soldered at different temperatures.

Temperatre, °C	Shear Strength, psi
200	190
230	1080
270	1520
300	2270

Soldering Condition
Substrate: 2024-Alclad
Solder Alloy: 70Sn-30Pb
Soldering Time: 4s
Shielding Condition: Air

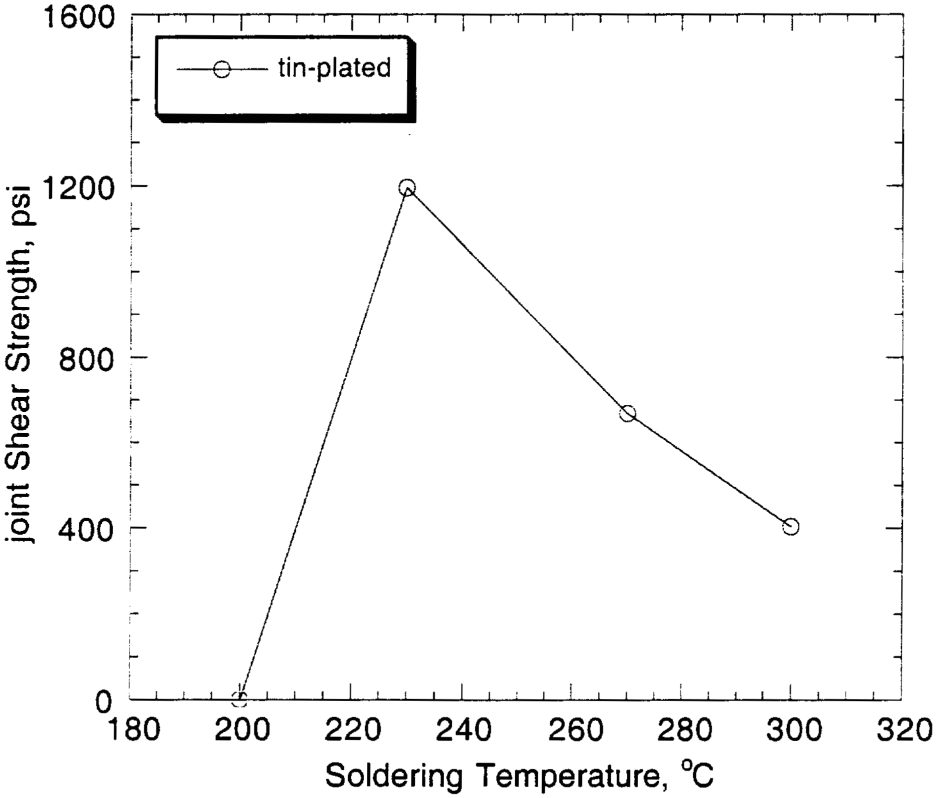

Figure 4.1.2 Shear strength of tin-plated 2024-Alclad, ultrasonically soldered for 4 seconds in air, for different soldering temperatures temperature.

Table 4.1.2 Shear strengths for the specimens, ultrasonically soldered at different temperatures.

Temperature, ^oC	Shear Strength, psi
200	-
230	1200
270	670
300	400

Soldering Condition

Substrate: 2024-Alclad
Solder Alloy: 70Sn-30Pb
Soldering Time: 4s
Shielding Condition: Air

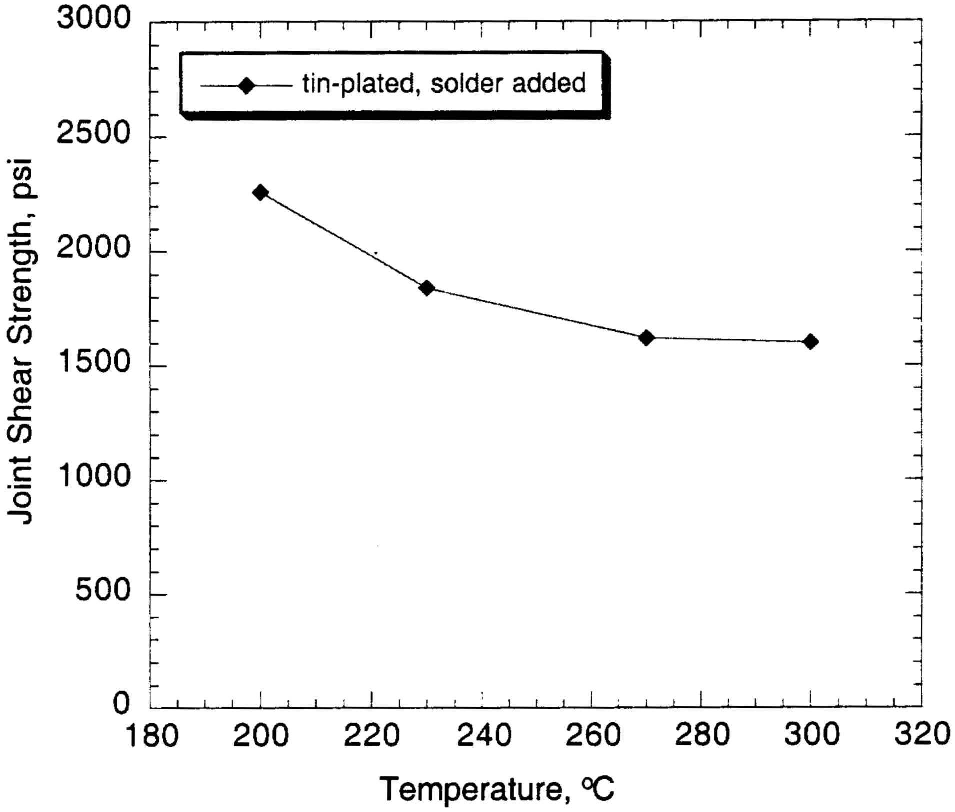

Figure 4.1.3 Shear strength of tin-plated 2024 Alclad, ultrasonically soldered with 70Sn-30Pb for 4 seconds in air, at different soldering temperatures.

Table 4.1.3 Shear strengths for the specimens, ultrasonically soldered at different soldering temperatures.

Temperature, ^{o}C	Shear Strength, psi
200	226o
230	1840
270	1620
300	1600

Soldering Condition
Substrate: 2024-Alclad
Solder Alloy: 70Sn-30Pb
Soldering Time: 4s
Shielding Condition: Air

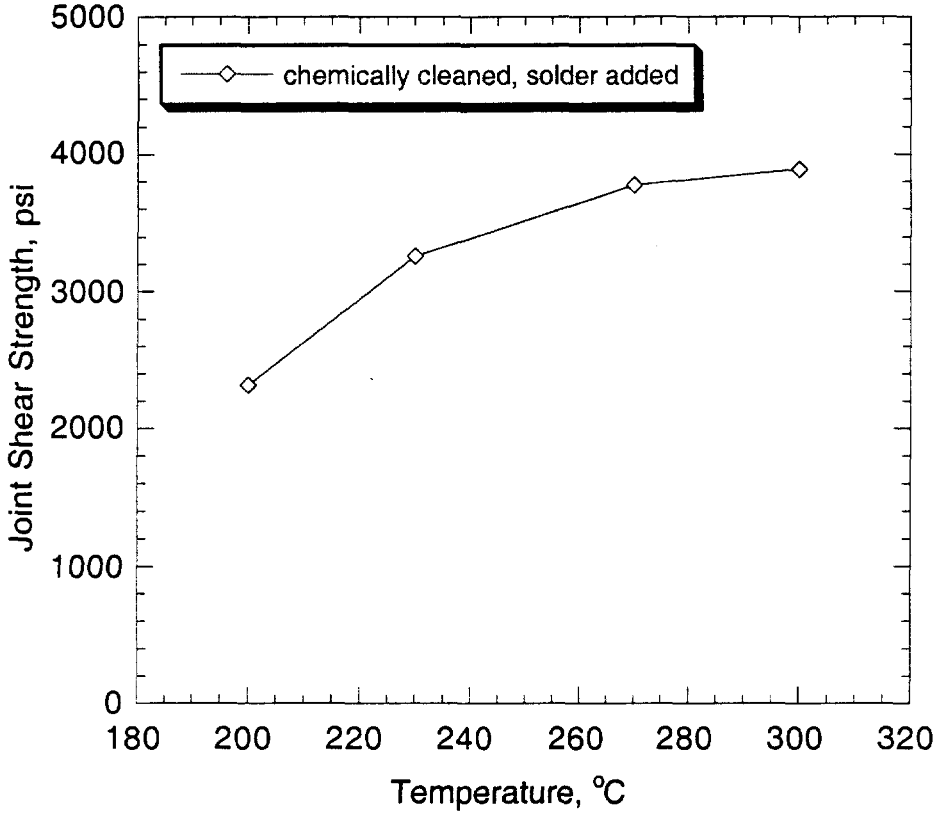

Figure 4.1.4 Shear strength of chemically cleaned 2024 Alclad, ultrasonically soldered with 70Sn-30Pb for 4 seconds in air, at different soldering temperatures.

Table 4.1.4 Shear strengths for the specimens, ultrasonically soldered at different soldering temperatures.

Temperature, °C	Shear Strength, psi
200	2320
230	3260
270	3780
300	3890

Soldering Condition
Substrate: 2024-Alclad
Solder Alloy: 70Sn-30Pb
Soldering Temperature: 230 °C
Shielding Condition: Air

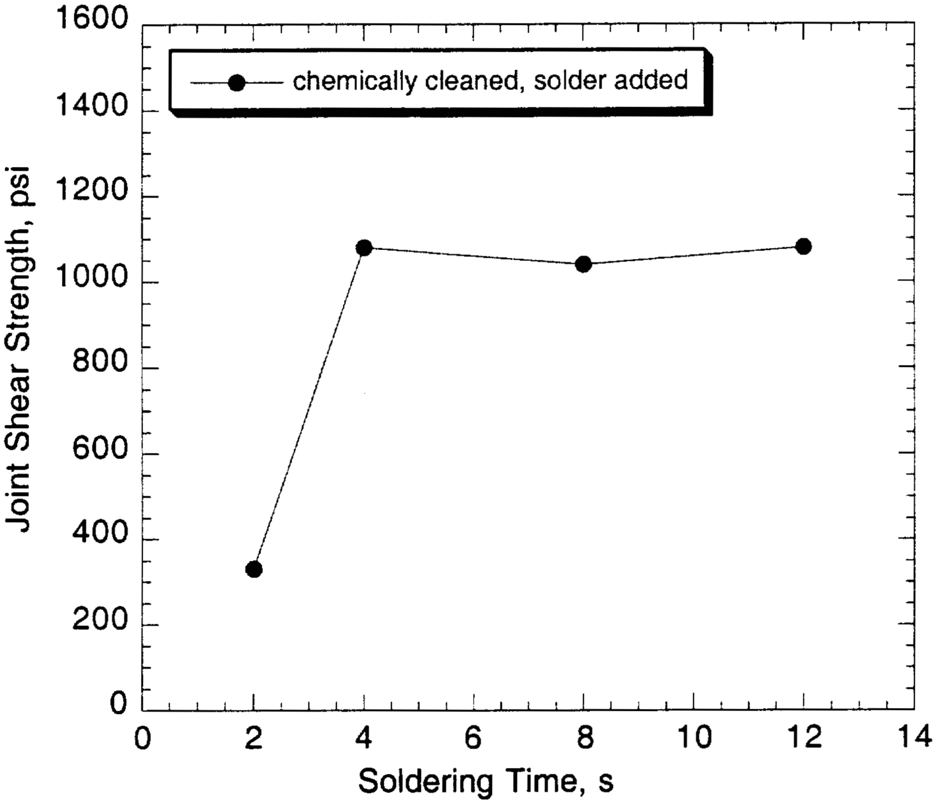

Figure 4.1. 5 Shear strength of degreased 2024 Alclad, ultrasonically soldered with 70Sn-30Pb at 230 °C in air, for different soldering times.

Table 4.1.5 Shear strengths for the specimens, ultrasonically soldered for different times.

Soldering Time, s	Shear Strength, psi
2	330
4	1080
8	1040
12	1080

Soldering Condition
Subatrate: 2024-Alclad
Solder Alloy: Non
Soldring Temperature: 230 °C
Shielding Condition: Air

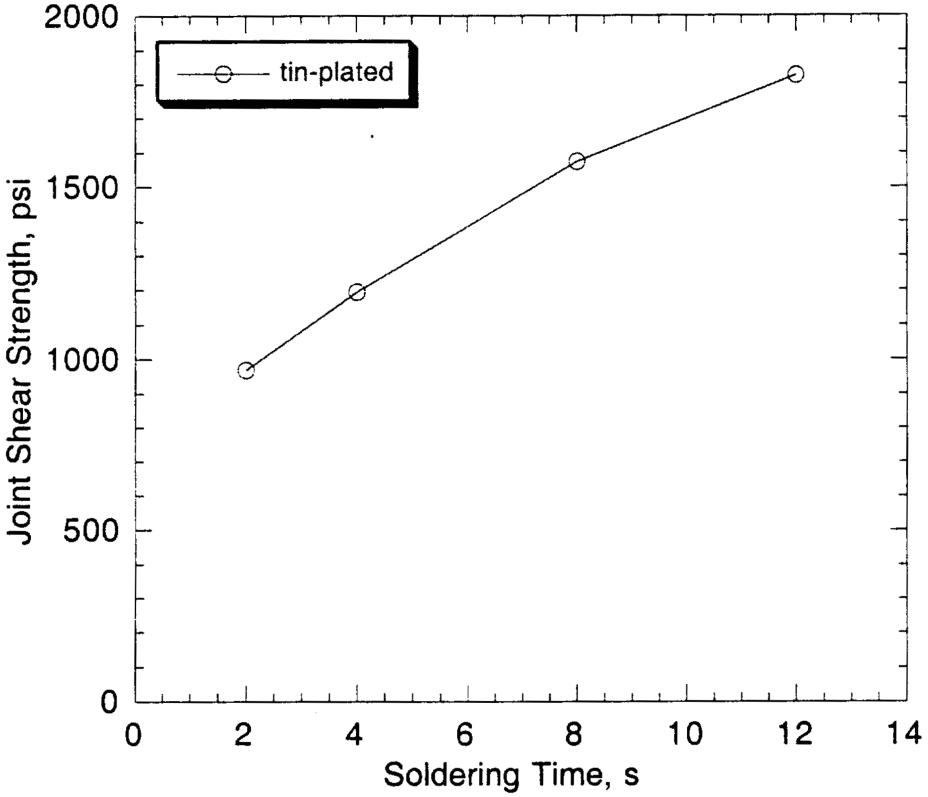

Figure 4.1.6 Shear strength of tin-plated 2024 Alclad, ultrasonically soldered at 230 °C in air, for different soldering times.

Table 4.1.6 Shear strengths for the specimens, ultrasonically soldered for different soldering times.

Soldering Time, s	Shear Strength, psi
2	970
4	1200
8	1570
12	1830

Soldering Condition
Substrate: 2024-Alclad
Solder alloy: 70Sn-30Pb
Soldering temperature: 230 °C
Shielding Condition: Air

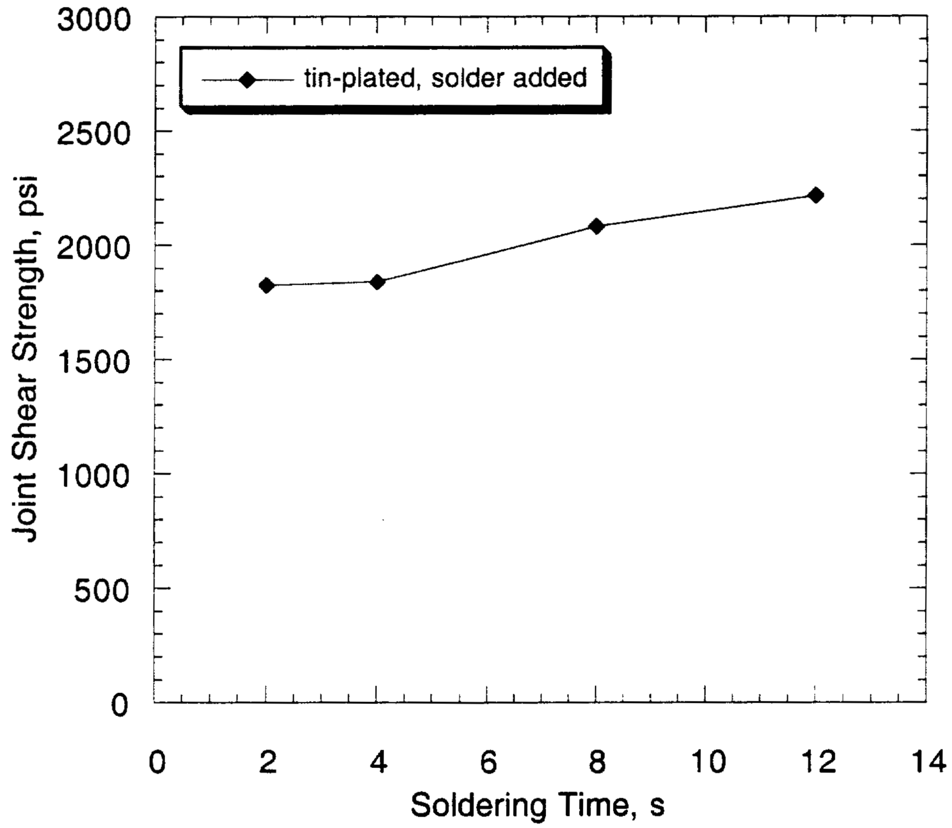

Figure 4.1.7 Shear strength of tin-plated 2024 Alclad, ultrasonically soldered with 70Sn-30Pb at 230 oC in air, for different soldering times.

Table 4.1.7 Shear strengths for the specimens, ultrasonically soldered for different times.

Soldering Time, s	Shear Strength, psi
2	1830
4	1840
8	2080
12	2220

Soldering Condition
Substrate: 2024-Alclad
Solder Alloy: 70Sn-30Pb
Soldering temperature, 230 °C
Shielding Condition: Air

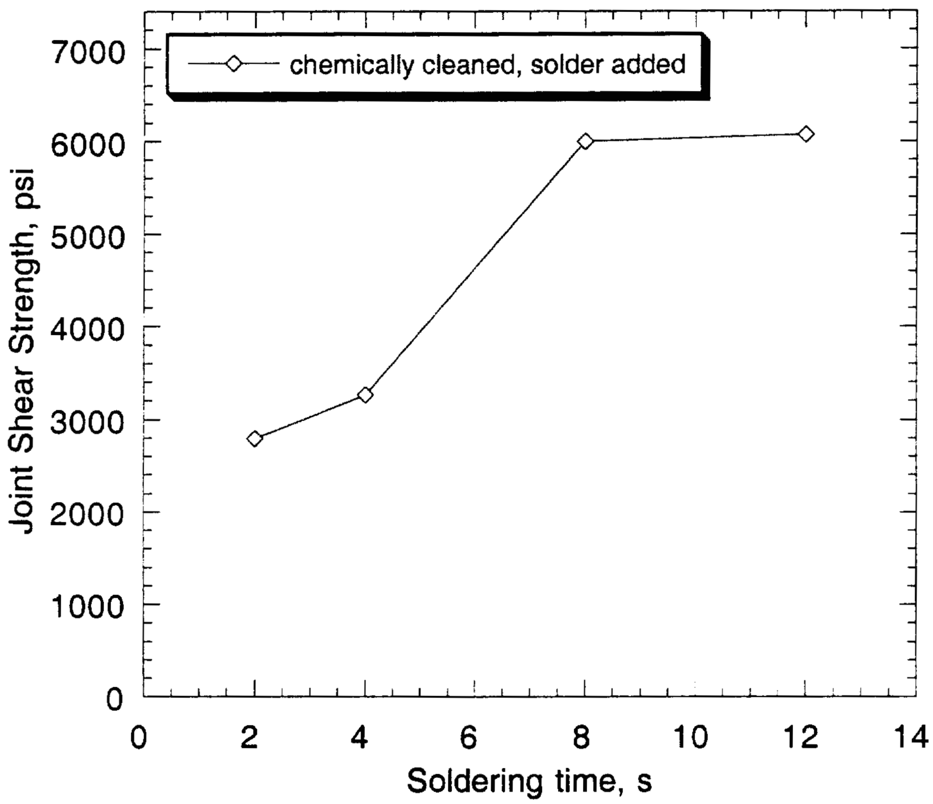

Figure 4.1.8 Shear strength of chemically cleaned 2024 Alclad, ultrasonically soldered with 70Sn-30Pb at 230 °C in air, for different soldering times.

Table 4.1.8 Shear strengths for the specimens, ultrasonically soldered for different soldering times.

Soldering Time, s	Shear Strength, psi
2	2790
4	3260
8	6000
12	6070

Soldering Condition
Substrate: 2024-Alclad
Solder Alloy: 70Sn-30Pb
Soldering Time: 4s
Shielding Condition: Argon

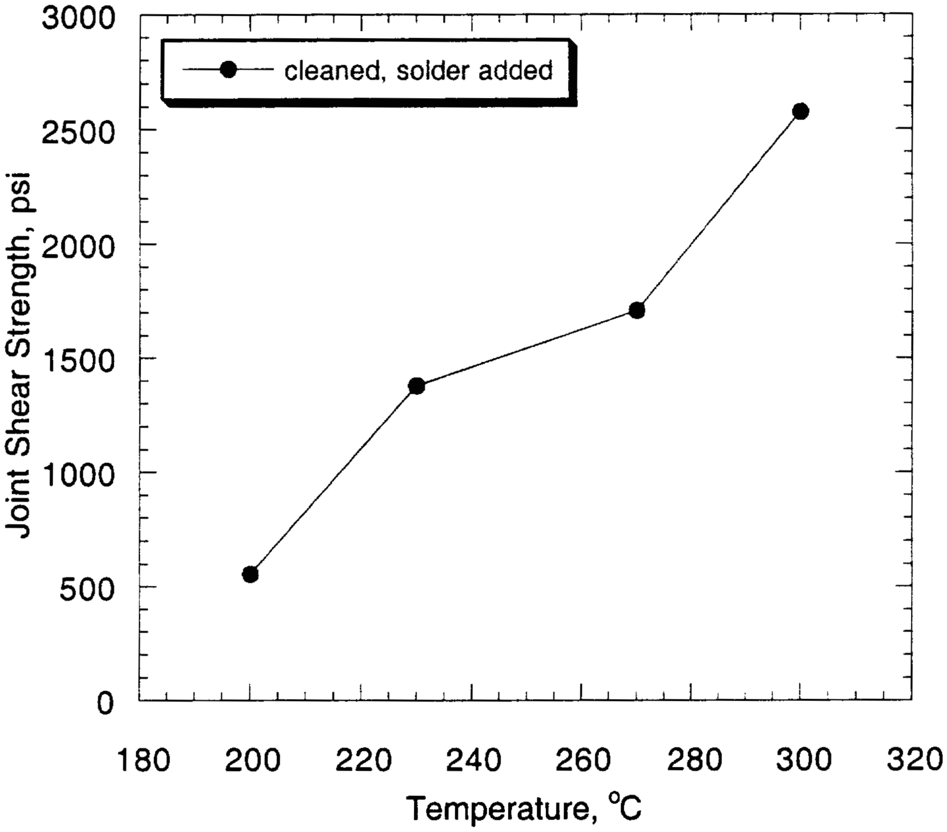

Figure 4.1.9 Shear strengths of degreased 2024 Alclad, ultrasonically soldered with 70Sn-30Pb for 4 seconds in argon, for different soldering temperatures.

Table 4.1.9 Shear strengths for the specimens, ultrasonically soldered at different termperatures.

Temperature, °C	Shear Strength, psi
200	560
230	1380
270	1710
300	2580

Soldering Condition
Substrate: 2024-Alclad
Solder Alloy: Non
Soldering Time: 4s
Shielding Condition: Argon

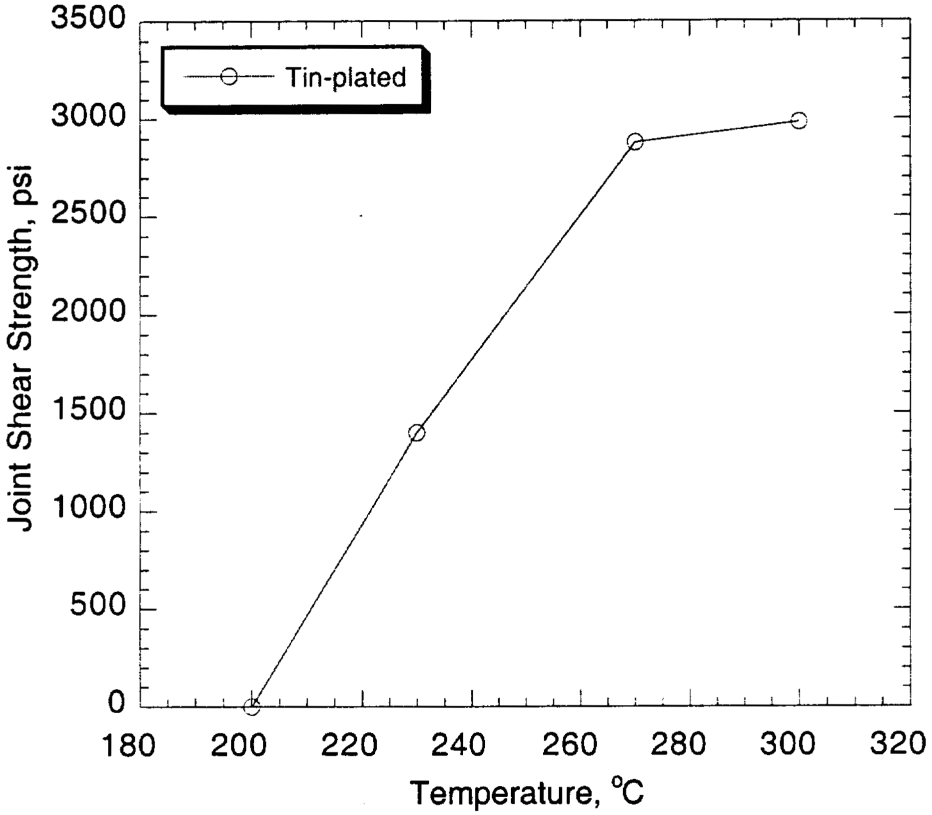

Figure 4.1.10 Shear strength of tin-plated 2024 Alclad, ultrasonically soldered for 4 seconds in argon, for different soldering temperatures.

Table 4.1.10 Shear strengths for the specimens, ultrasonically soldered at different soldering temperatures.

Temperature, °C	Shear Strength, psi
200	-
230	1400
270	2880
300	2980

Soldering Condition
Substrate: 2024-Alclad
Solder Alloy: 70Sn-30Pb
Soldering Time: 4s
Shielding Condition: Argon

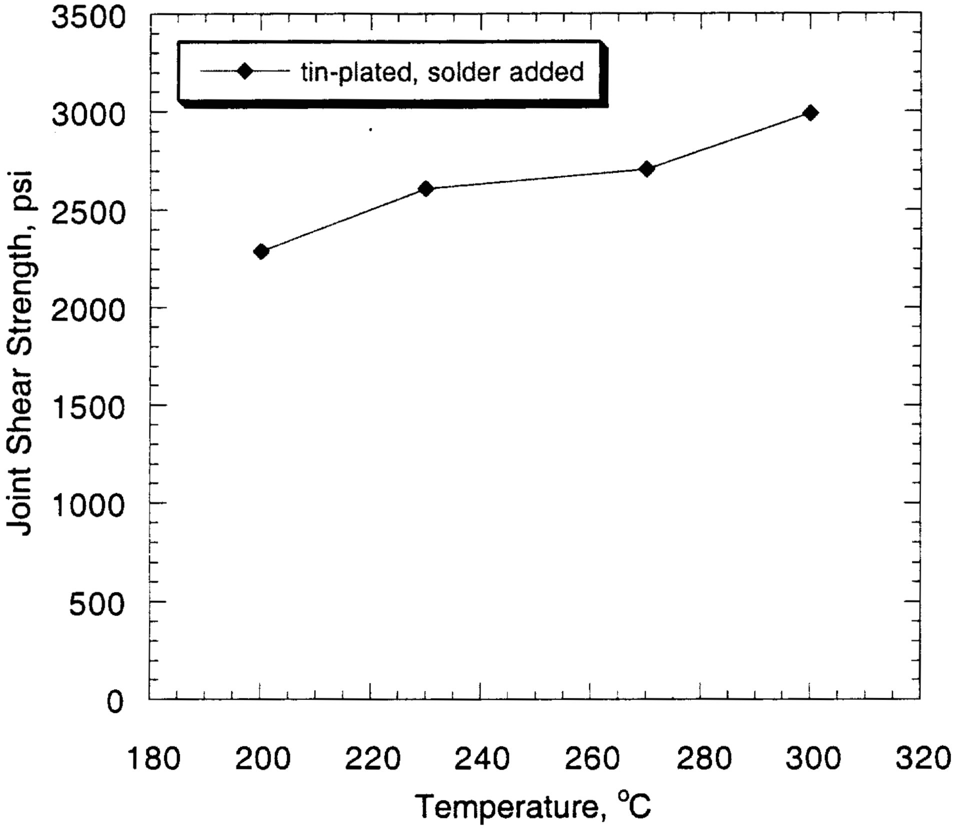

Figure 4.1.11 Shear strength of tin-plated 2024 Alclad, ultrasonically soldered with 70Sn-30Pb for 4 seconds in argon, for different soldering temperatures.

Table 4.1.11 Shear strengths for the specimens, ultrasonically soldered at different soldering temperatures.

Temperature, °C	Shear Strength, psi
200	2290
230	2610
270	2700
300	2990

Soldering Condition
Substrate: 2024-Alclad
Solder Alloy: 70Sn-30Pb
Soldering Time: 4s
Shielding Condition: Argon

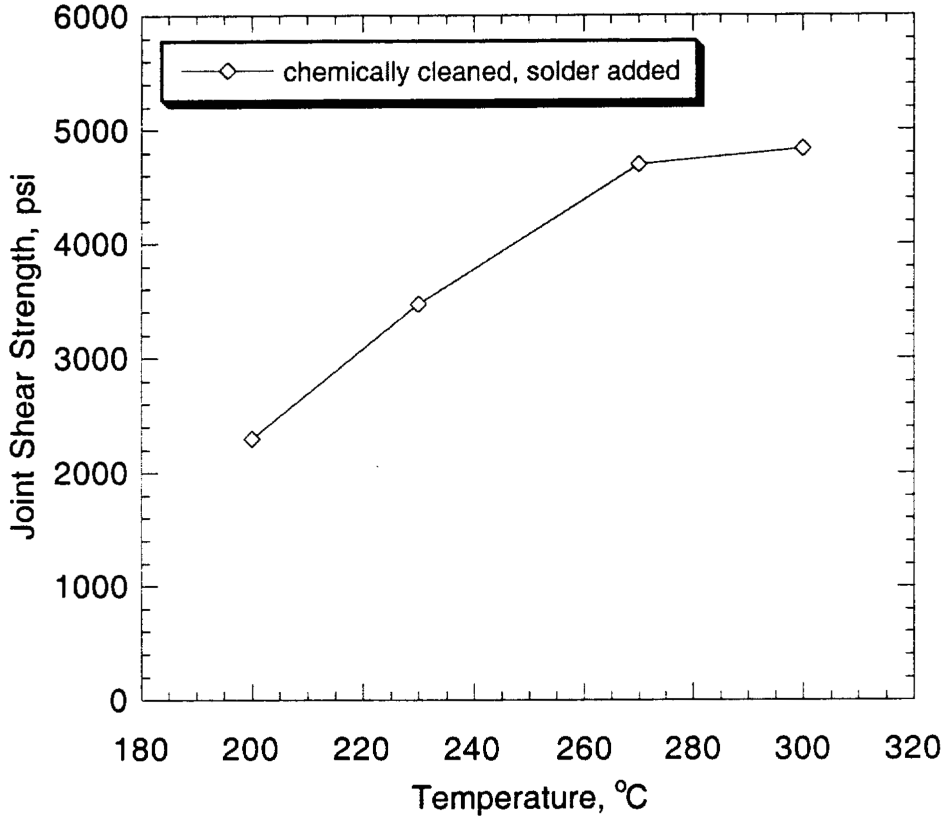

Figure 4.1.12 Shear strength of chemically cleaned 2024 Alclad, ultrasonically soldered with 70Sn-30Pb for 4 seconds in argon, for different temperatures .

Table 4.1.12 Shear strengths for the specimens, ultrasonically soldered at different soldering temperatures.

Temperature, ^oC	Shear Strength, psi
200	2300
230	3470
270	4700
300	4830

Soldering Condition
Substrate: 2024-Alclad
Solder Alloy: 70Sn-30Pb
Soldering Temperature: 230 °C
Shielding Condition: Argon

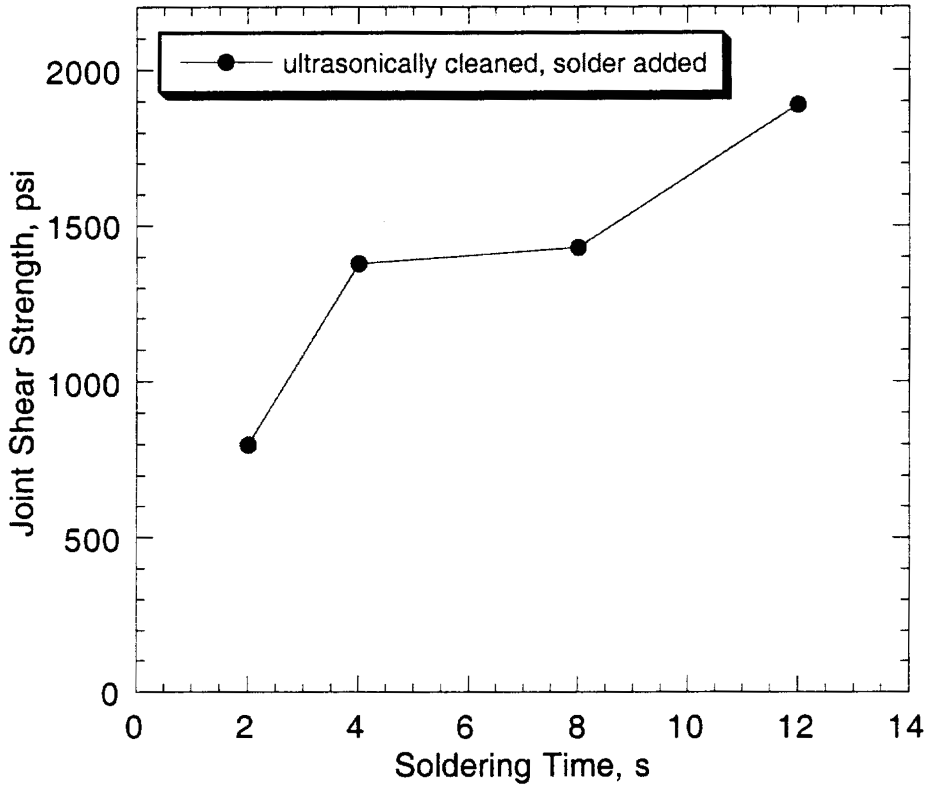

Figure 4.1.13 Shear strength for degreased 2024 Alclad, ultrasonically soldered with 70Sn-30Pb at 230 °C in argon, for differnt soldering times.

Table 4.1.13 Shear strengths for the specimens, ultrasonically soldered for different soldering times.

Soldering Time, s	Shear Strength, psi
2	800
4	1380
8	1430
12	1890

Soldering Condition

Substrate: 2024-Alclad
Solder Alloy: Non
Soldering Temperature: 230 ^{o}C
Shielding Condition: Argon

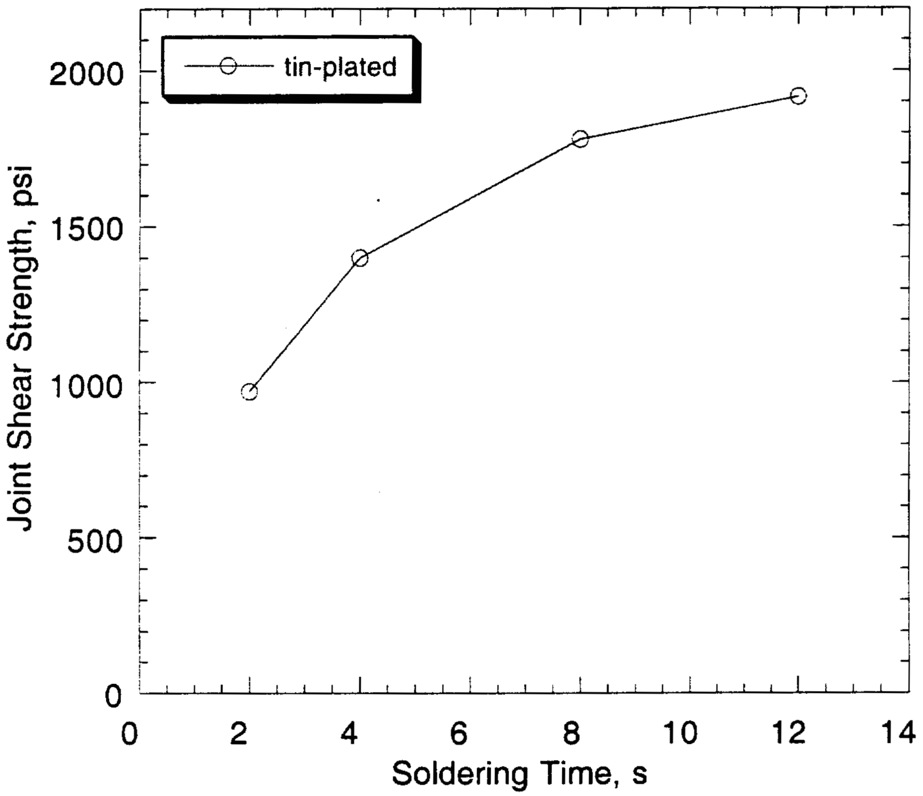

Figure 4.1.14 Shear strength of tin-plated 2024 Alclad, ultrasonically soldered at 230 ^{o}C in argon, for different soldering times.

Table 4.1.14 Shear strengths for the specimens, ultrasonically soldered for different soldering times.

Soldering Time, s	Shear Strength, psi
2	970
4	1400
8	1780
12	1920

Soldering Condition
Substrate: 2024-Alclad
Solder Alloy: 70Sn-30Pb
Soldering Temperature: 230 °C
Shielding Condition: Argon

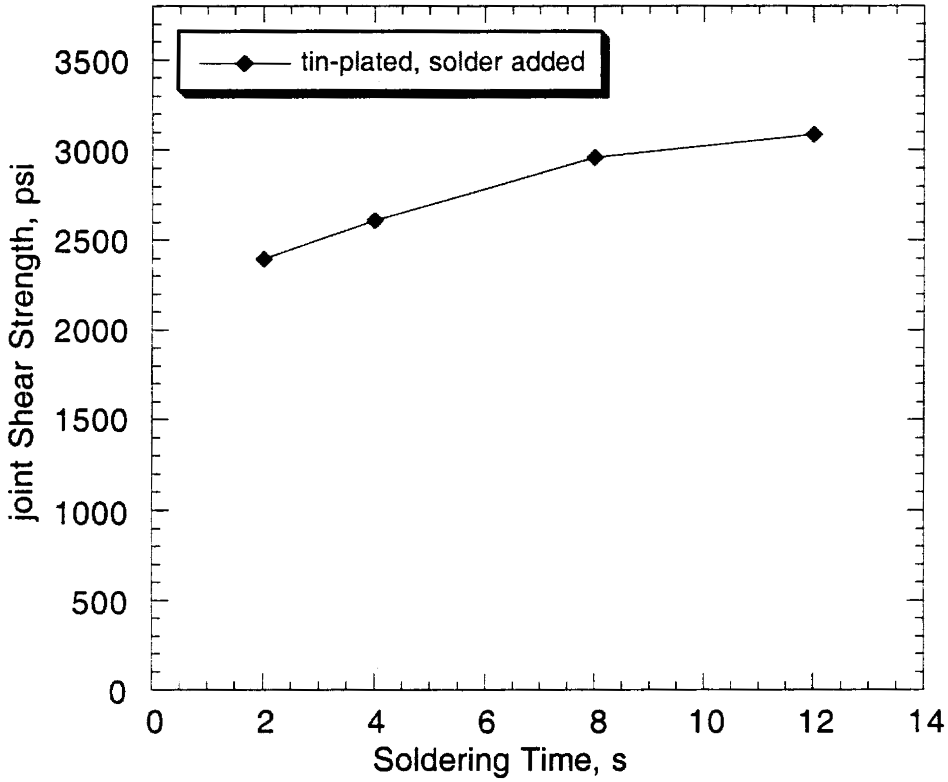

Figure 4.1.15 Shear strength for tin-plated 2024 Alclad, ultrasonically soldered with 70Sn-30Pb at 230 oC in argon, for different soldering times.

Table 4.1.15 Shear strengths for the specimens, ultrasonically soldered for different soldering times .

Soldering Time, s	Shear Strength, psi
2	2390
4	2610
8	2960
12	3090

Soldering Condition
Substrate: 2024-Alclad
Solder Alloy: 70Sn-30Pb
Soldering Temperature: 230 °C
Shielding Condition: Argon

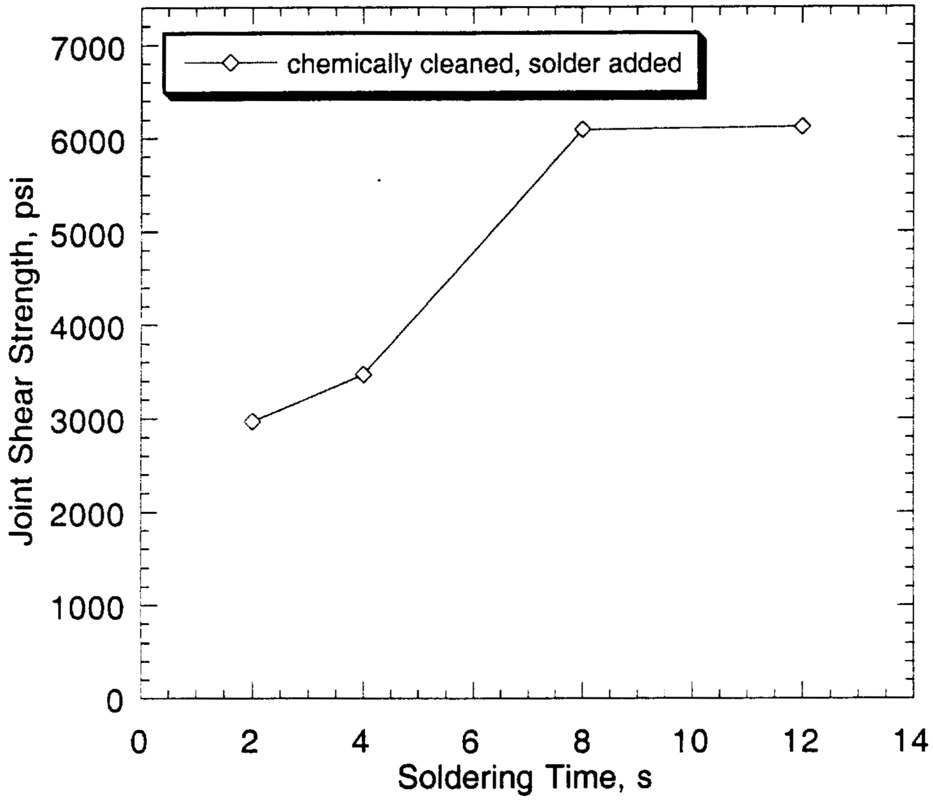

Figure 4.1.16 Shear strength of chemically cleaned 2024 Alclad, ultrasonically soldered with 70Sn-30Pb at 230 °C in argon, for different soldering times.

Table 4.1.16 Shear strengths for the specimens, ultrasonically soldered for different soldering times.

Soldering Time, s	Shear Strength, psi
2	2970
4	3470
8	6090
12	6120

Soldering Condition
Substrate: 2024-Alclad
Solder Alloy: 70Sn-30Pb
Soldering Time: 4s
shielding Condition: Air

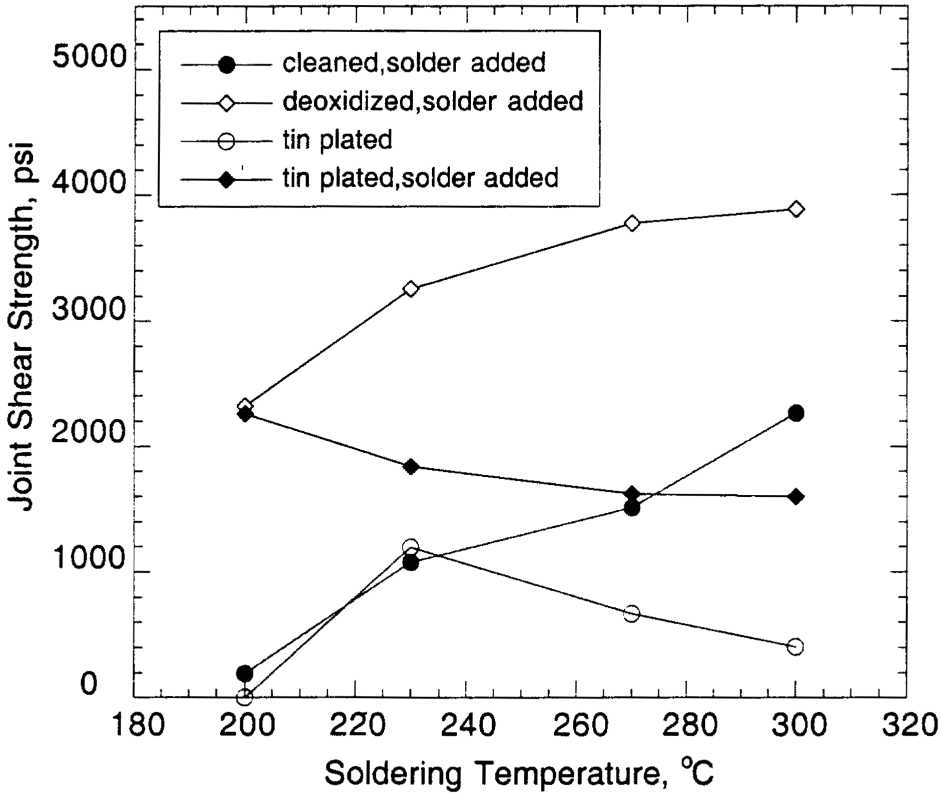

Figure 4.1.17 Comparison the shear strengths of 2024 Alclad specimens, ultrasonically soldered at different temperatures in air, with different surface conditions.

Table 4.1.17 Shear strengths for the specimens, ultrasonically soldered with different surface conditions.

Temperature, °C	Shear Strength, psi (cleaned+solder)	Shear Strength, psi (tin-plated)	Shear Strength, psi (tin-plated+solder)	Shear Strength, psi (deoxidized+solder)
200	190	-	2260	2320
230	1080	1200	1840	3260
270	1520	670	1620	3780
300	2260	400	1600	3890

Soldering Condition
Substrate: 2024-Alclad
Solder Alloy: 70Sn-30Pb
Soldering Time: 4s
Shielding Condition: Argon

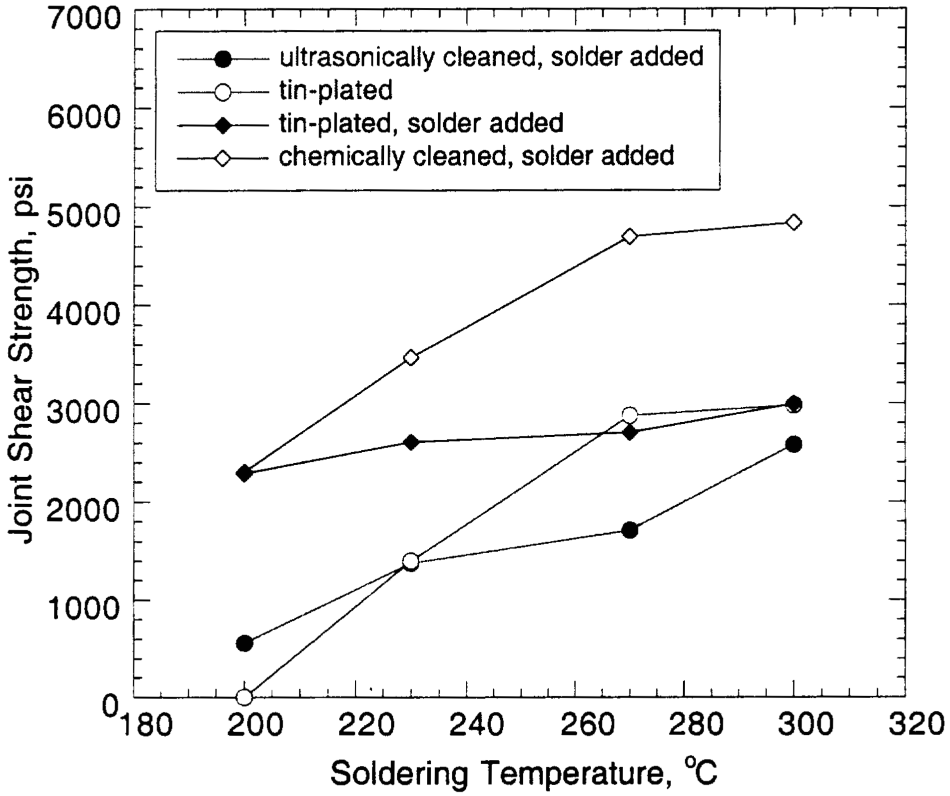

Figure 4.1.18 Comparison the shear strengths of 2024 Alclad specimens, ultrasonically soldered at different temperatures in argon, with different surface conditions.

Table 4.1.18 Shear strengths for the specimens, ultrasonically soldered with different surfcae conditions.

Temperature, °C	Shear Strength, psi (cleaned+solder)	Shear Strength, psi (tin-plated)	Shear Strength, psi (tin-plated+solder)	Shear Strength, psi (deoxidized)
200	560	-	2290	2300
230	1380	1400	2610	3470
270	1710	2880	2700	4700
300	2580	2990	2990	4830

Soldering Condition
Substrate: 2024-Alclad
Solder Alloy: 70Sn-30Pb
Soldering Temperature: 230 ^{o}C
Shielding Condition: Air

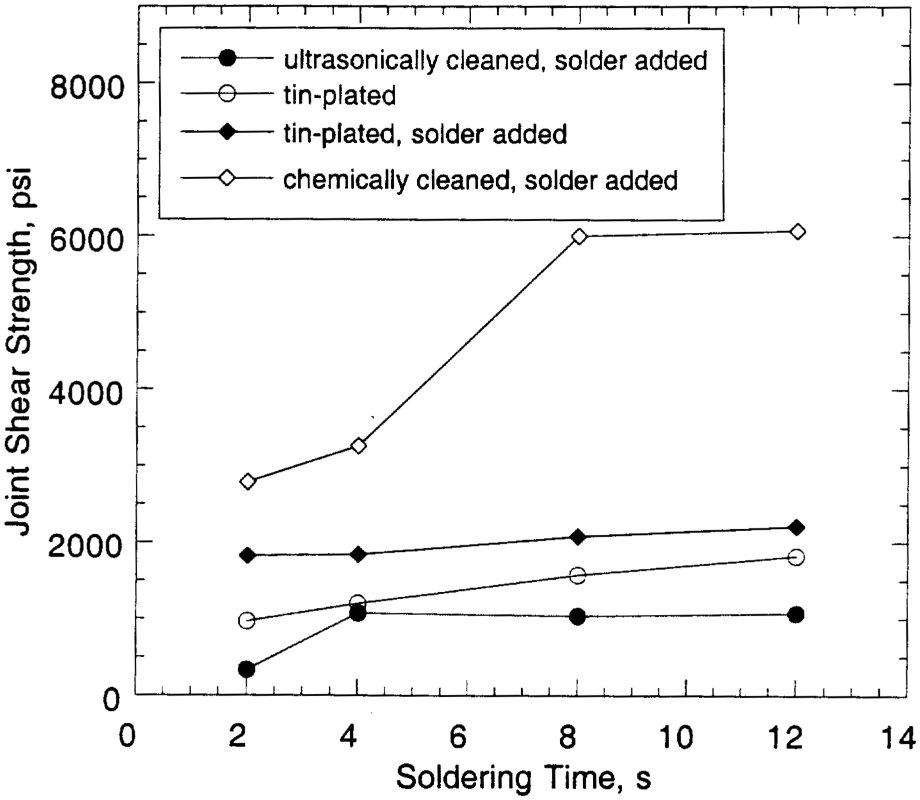

Figure 4.1.19 Comparison the shear strengths of 2024 Alclad specimens, ultrasonically soldered for different times in air, with different surface conditions.

Table 4.1.19 Shear strengths for the specimens, ultrsonically soldered with different surfcae conditions.

Time, s	Shear Strength, psi (cleaned+solder)	Shear Strength, psi (tin-plated)	Shear Strength, psi (tin-plated+solder)	Shear Strength, psi (deoxidized_solder)
2	330	970	1830	2790
4	1080	1200	1840	3260
8	1040	1570	2080	6000
12	1080	1830	2220	6070

Soldering Condition

Substrate: 2024-Alclad
Solder Alloy: 70Sn-30Pb
Soldering Temperature: 230 °C
Shielding Condition: Argon

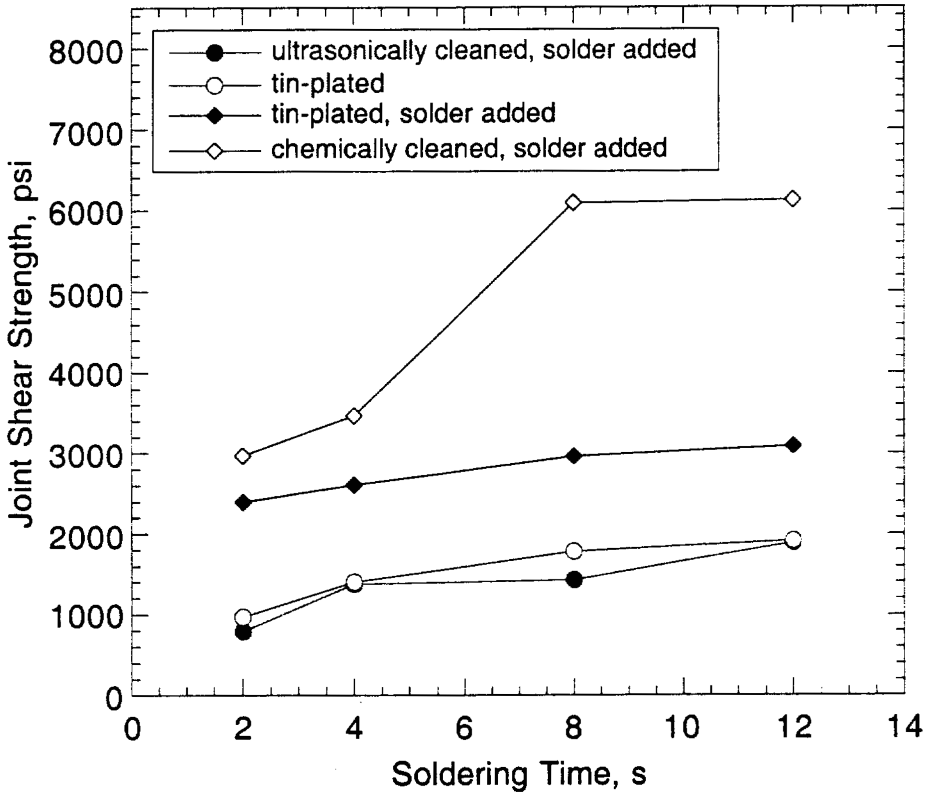

Figure 4.1.20 Comparison the shear strengths of 2024 Alclad specimens, ultrasonically soldered for different times in argon, with different surface conditions.

Table 4.1.20 Shear strengths for the specimens, ultrasonically soldered with different surface conditions.

Time, s	Shear Strength, psi (cleaned+solder)	Shear Strength, psi (tin-plated)	Shear Strength, psi (tin-plated+solder)	Shear Strength, psi (deoxidized+solder)
2	800	970	2390	2970
4	1380	1400	2610	3470
8	1430	1780	2960	6090
12	1890	1920	3090	6120

Soldering Condition
Substrate: 2024-Alclad
Solder Alloy: 70Sn-30Pb
Soldering Time: 4s
Surface Condition: Ultrasonically cleaned (degreased)

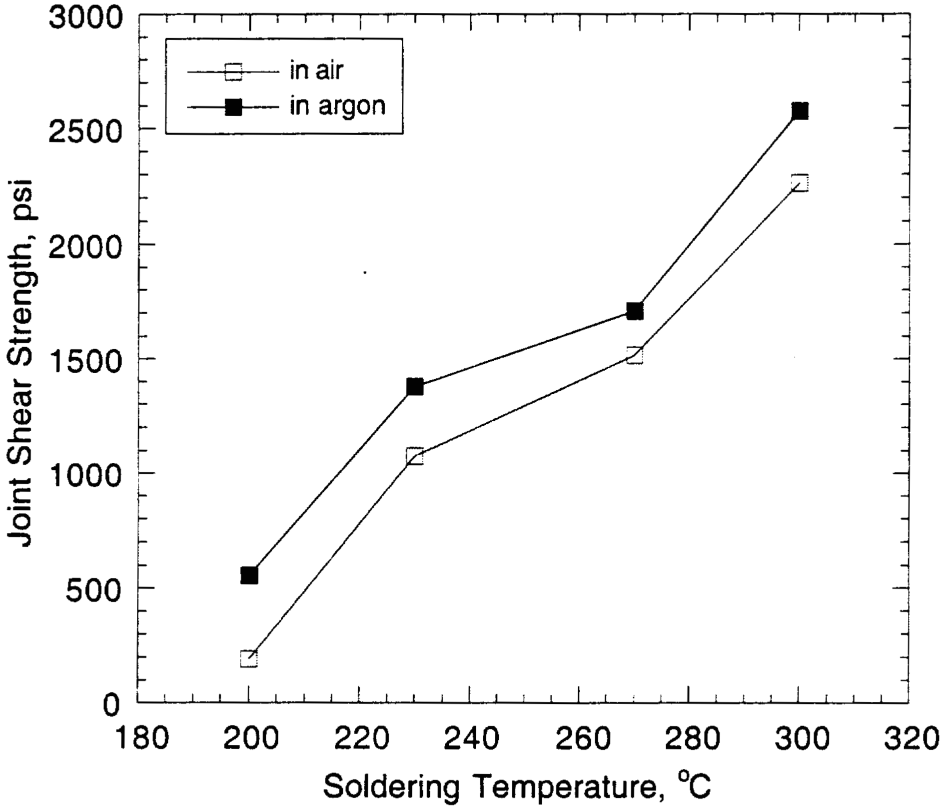

Figure 4.1.21 Shear strengths vs soldering temperature for 2024 Alclad specimens, ultrasonically soldered in air and in argon.

Table 4.1.21 Shear strengths for the specimens, ultrasonically soldered at different temperatures, in air and in argon.

Temperature, ^{o}C	Shear Strength, psi (in air)	Shear Strength, psi (in argon)
200	190	560
230	1080	1380
270	1520	1710
300	2260	2580

Soldering Condition
Substrate: 2024-Alclad
Solder Alloy: Non
Soldering Time: 4s
Surface Condition: Tin-plated

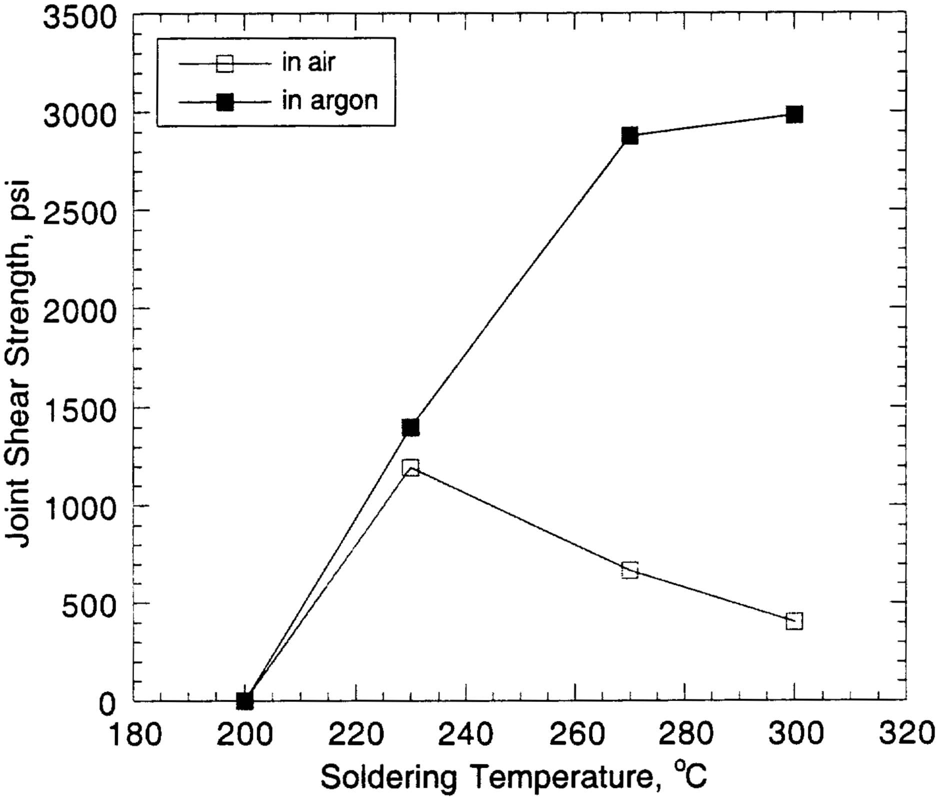

Figure 4.1.22 Shear strength vs soldering temperature for 2024 Alclad specimens, utrasonically soldered in air and in argon.

Table 4.1.22 Shear strengths for the specimens, ultrasonically soldered at different temperatures, in air and in argon.

Temperature, °C	Shear Srength, psi (in air)	Shear Strength, psi (in argon)
200	-	-
230	1200	1400
270	670	2880
300	400	2980

Soldering condition
Substrate: 2024-Alclad
Solder Alloy: 70Sn-30Pb
Soldering Time: 4s
Surface Condition: Tin-plated, Solder Added

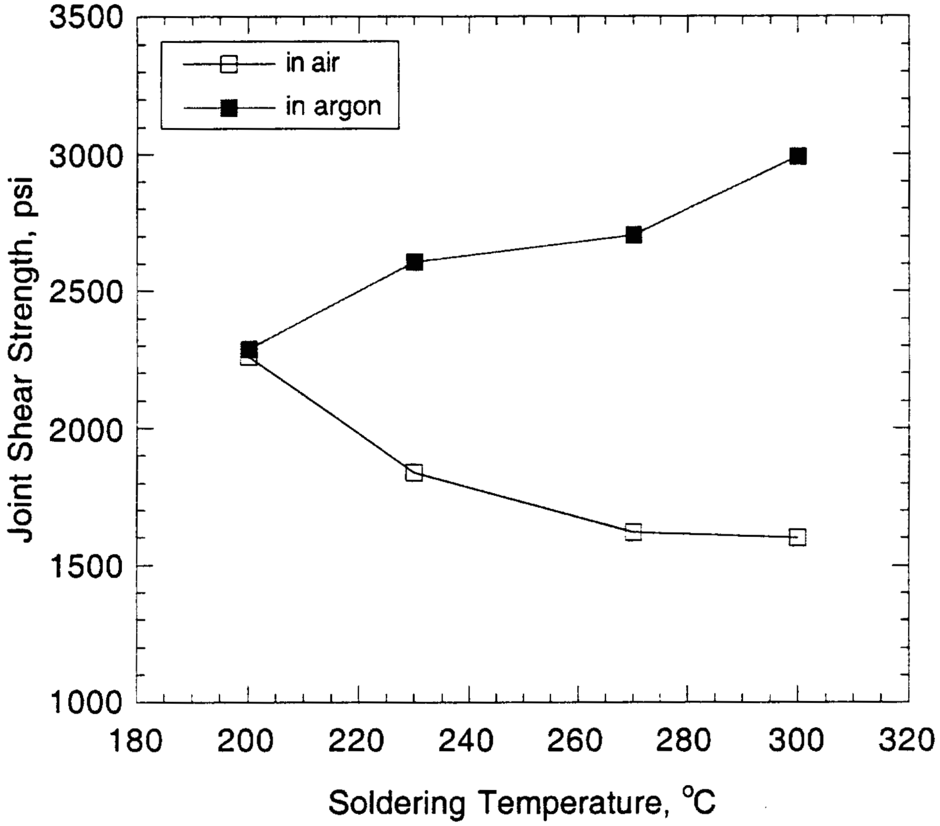

Figure 4.1.23 Shear strength vs soldering temperature for 2024 Alclad specimens, ultrasonically soldered in air and in argon.

Table 4.1.23 Shear strengths for the specimens, ultrasonically soldered at different temperatures, in air and in argon.

Temperature, °C	Shear Strength, psi (in air)	Shear Strength, psi (in argon)
200	2260	2290
230	1840	2610
270	1620	2700
300	1600	2990

Soldering Condition
Substrate: 2024-Alclad
Solder Alloy: 70Sn-30Pb
Soldering Time: 4s
Surface Condition: Chemically Cleaned (deoxidized)

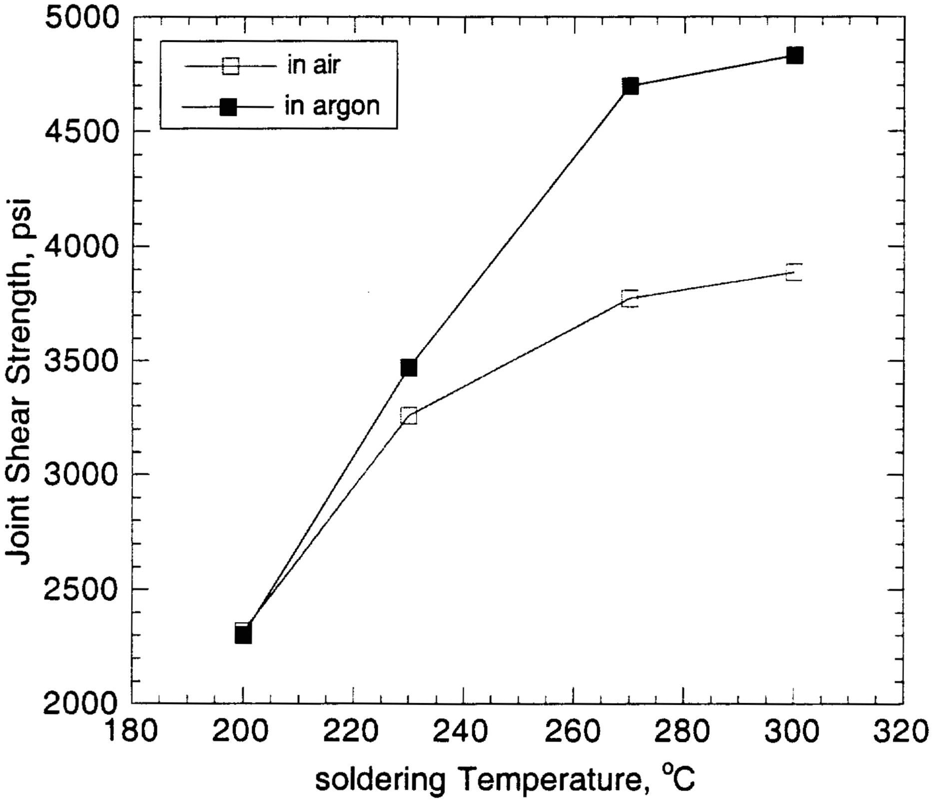

Figure 4.1.24 Shear strength vs soldering temperature for 2024 Alclad specimens, ultrasonically soldered in air and in argon.

Table 4.1.24 Shear strengths for the specimens, ultrasonically soldered at different temperatures, in air and in argon.

Temperature, °C	Shear Strength, psi (in air)	Shear Strength, psi (in argon)
200	2320	2300
230	3260	3470
270	3780	4700
300	3890	4830

Soldering Condition
Substrate: 2024-Alclad
Solder Alloy: 70Sn-30Pb
Soldering temperature: 230 °C
Surface Condition: ultrasonically cleaned (degreased)

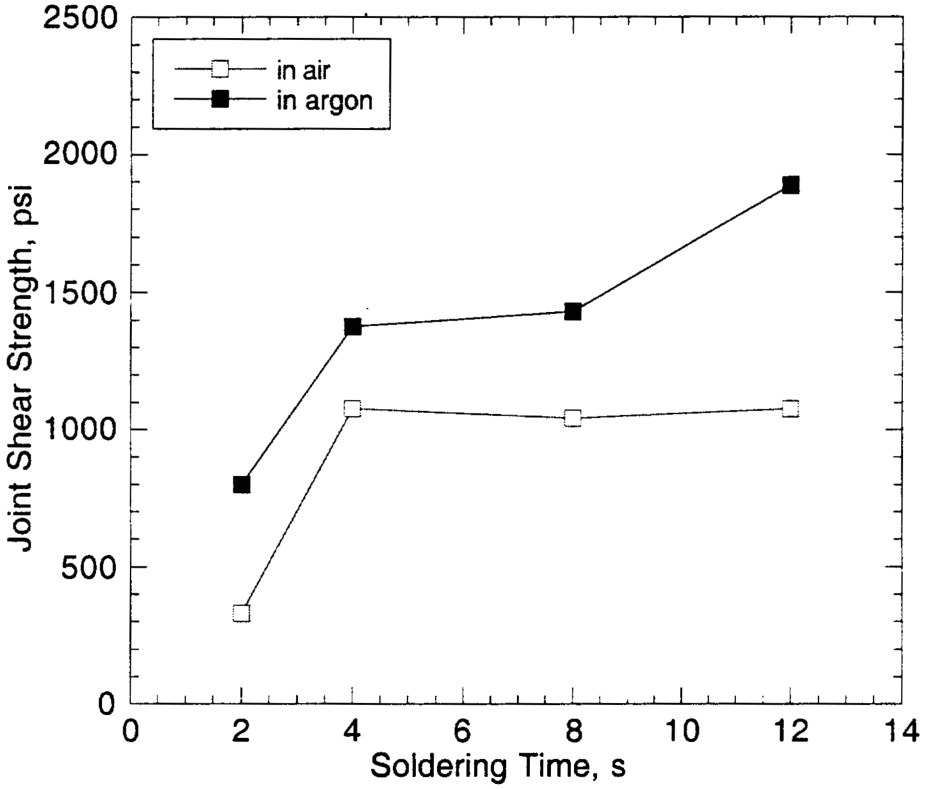

Figure 4.1.25 Shear strength vs soldering time for 2024 Alclad specimens, ultrasonically soldered in air and in argon.

Table 4.1.25 Shear strengths for the specimens, ultrasonically soldered for different times, in air and in argon.

Time, s	Shear Strength, psi (in air)	Shear Strength, psi (in argon)
2	330	790
4	1080	1380
8	1040	1430
12	1080	1890

Soldering Condition

Substrate: 2024-Alclad
Solder Alloy: Non
Soldering Temperature: 230 ^oC
Surface Condition: Tin-plated

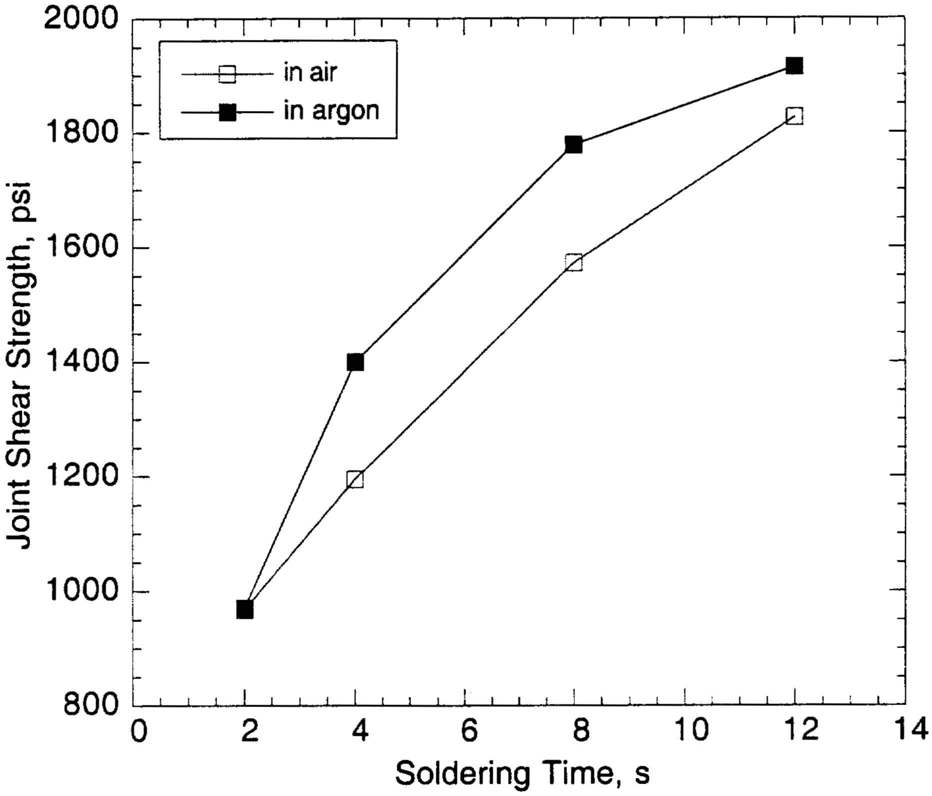

Figure 4.1.26 Shear strength vs soldering time for 2024 Alclad specimens, ultrasonically soldered in air and in argon.

Table 4.1.26 Shear strengths for the specimens, ultrasonically soldered at different times, in air and in argon.

Time, s	Shear Strength, psi (in air)	Shear Strength, psi (in argon)
2	970	970
4	1200	1400
8	1570	1780
12	1830	1920

Soldering Condition

Substrate: 2024-Alclad
Solder Alloy: 70Sn-30Pb
Soldering Temperature: 230 ^oC
Surface Condition: Tin-plated, Solder Added

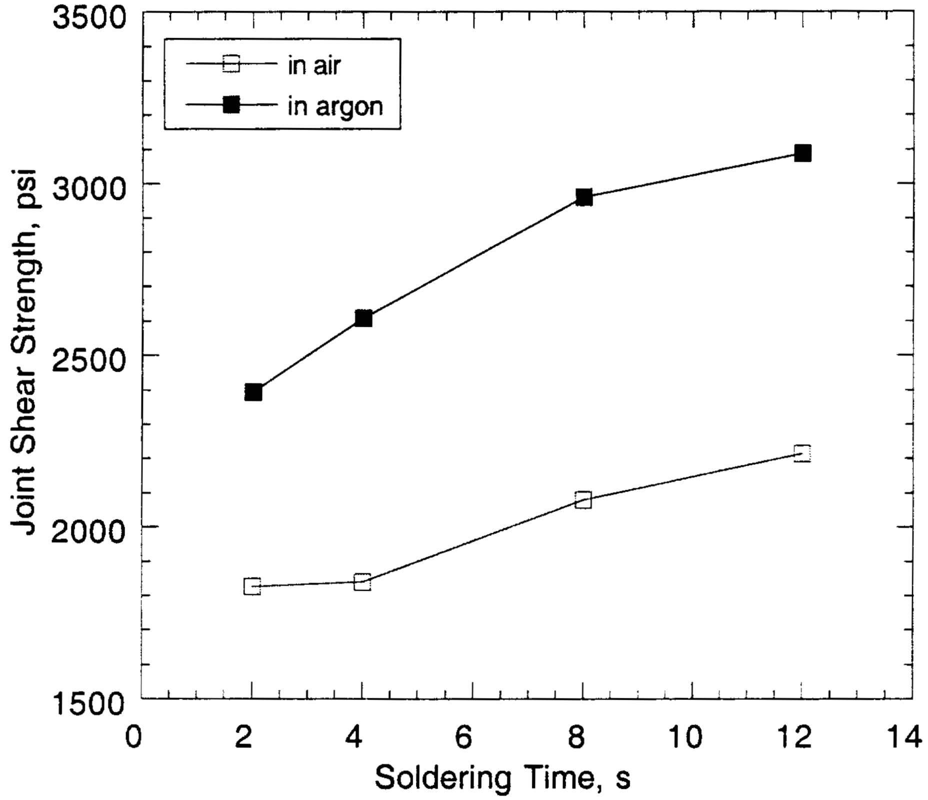

Figure 4.1.27 Shear strength vs soldering time for 2024 Alclad specimens, ultrasonically soldered in air and in argon.

Table 4.1.27 Shear strengths for the specimens, ultrasonically soldered at different times, in air and in argon.

Time, s	Shear Strength, psi (in air)	Shear Strength, psi (in argon)
2	1830	2390
4	1840	2610
8	2080	2960
12	2220	3090

Soldering Condition

Substrate: 2024-Alclad
Solder Alloy: 70Sn-30Pb
Soldering Temperature: 230 °C
Surface Condition: Chemically Cleaned (deoxidized)

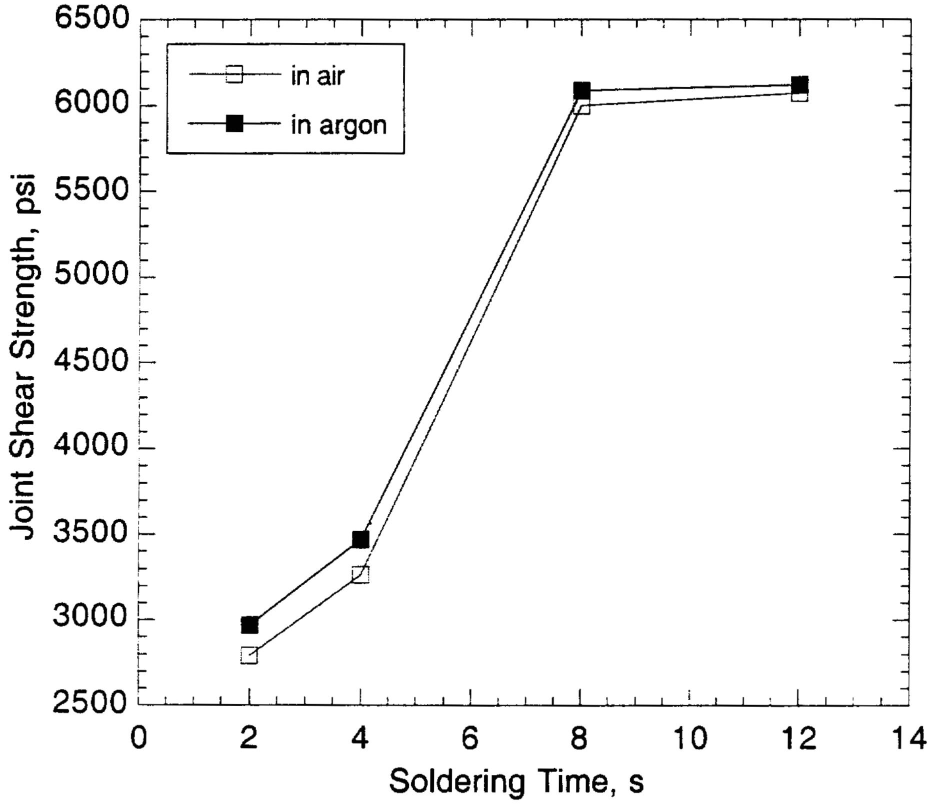

Figure 4.1.28 Shear strength vs soldering time for 2024 Alclad specimens, ultrasonically soldered in air and in argon.

Table 4.1.28 Shear strengths for the specimens, ultrasonically soldered at different times, in air and in argon.

Time, s	Shear Strength, psi (in air)	Shear Strength, psi (in argon)
2	2790	2970
4	3290	3470
8	6000	6090
12	6070	6120

Soldering Condition
Substrate: Stainless Steel
Solder Alloy: Non
Soldering Time: 4s
Shielding Condition: Air

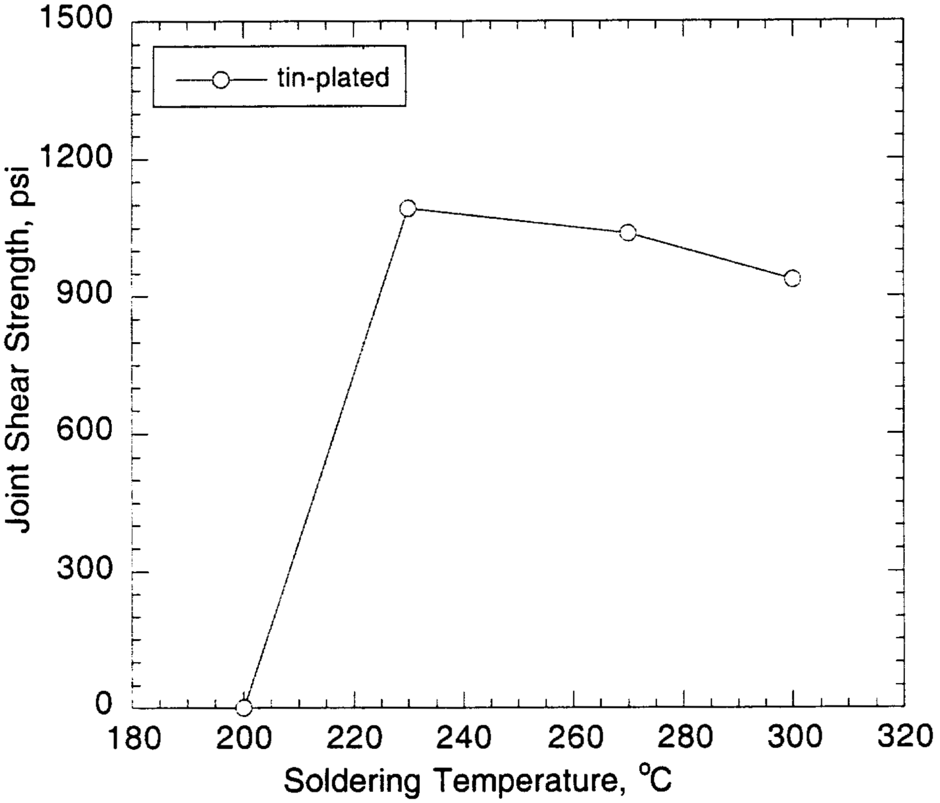

Figure 4.1.29 Shear strength of 304 stainless steel specimens, ultrasonically soldered for 4 seconds in air, for different soldering temperatures.

Table 4.1.29 Shear strengths for the specimens, ultrasonically soldered at different soldering temperatures.

Temperature, ^oC	Shear Strength, psi
200	-
230	1090
270	1040
300	940

Soldering Condition
Substrate: Stainless Steel
Solder alloy: 70Sn-30Pb
Soldering Time: 4s
Shielding Condition: Air

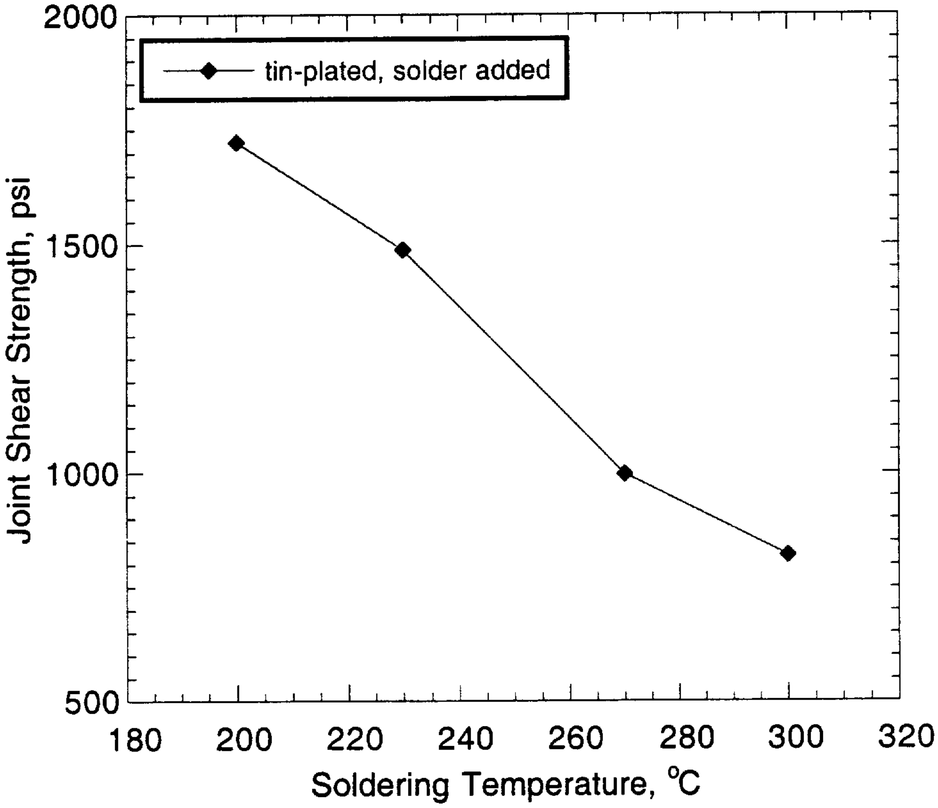

Figure 4.1.30 Shear strength vs soldering temperature for 304 stainless steel specimens, ultrasonically soldered for 4 seconds in air, for different soldering temperatures.

Table 4.1.30 Presents shear strengths for the specimens, ultrasonically soldered at different temperatures.

Temperature, ^{o}C	Shear Strength, psi
200	1720
230	1490
270	1000
300	820

Soldering Condition
Substrate: Stainless Steel
Solder Alloy: Non
Soldering temperature: 230 °C
Shielding Condition: Air

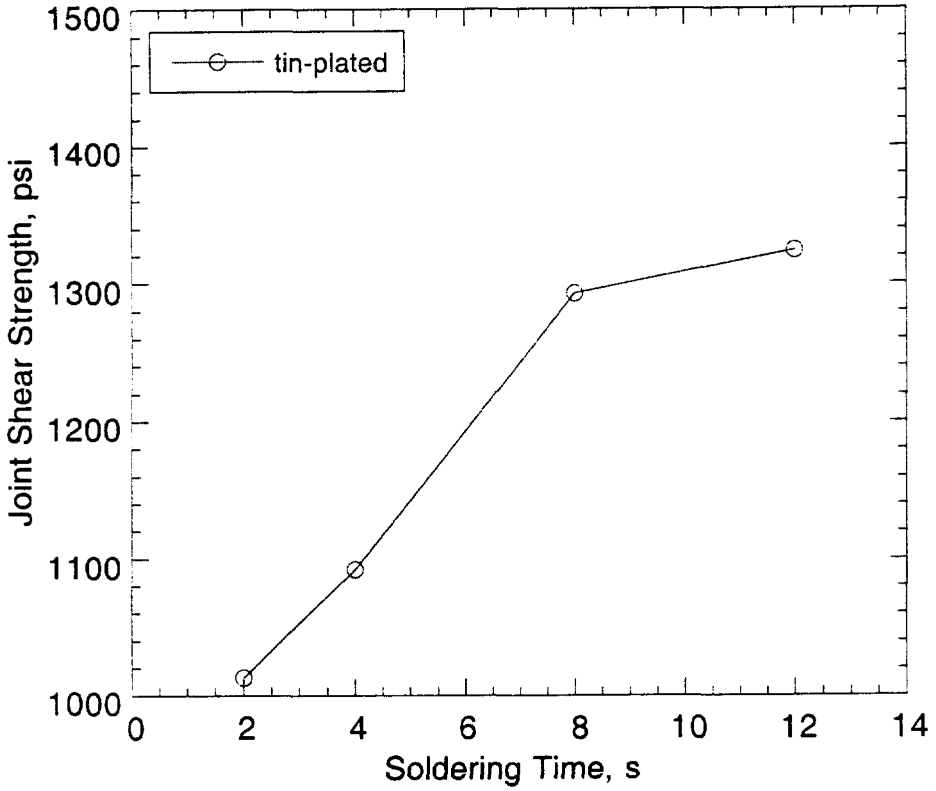

Figure 4.1.31 Shear strength vs soldering time for 304 stainless steel specimens, ultrasonically soldered at 230 °C in air, for different soldering times.

Table 4.1.31 Shear strengths for the specimens, ultrasonically soldered for different soldering times.

Time, s	Shear Strength, psi
2	1010
4	1090
8	1290
12	1320

Soldering Condition

Substrate: Stainless Steel
Solder Alloy: 70Sn-30Pb
Soldering temperature: 230 °C
Shielding Condition: Air

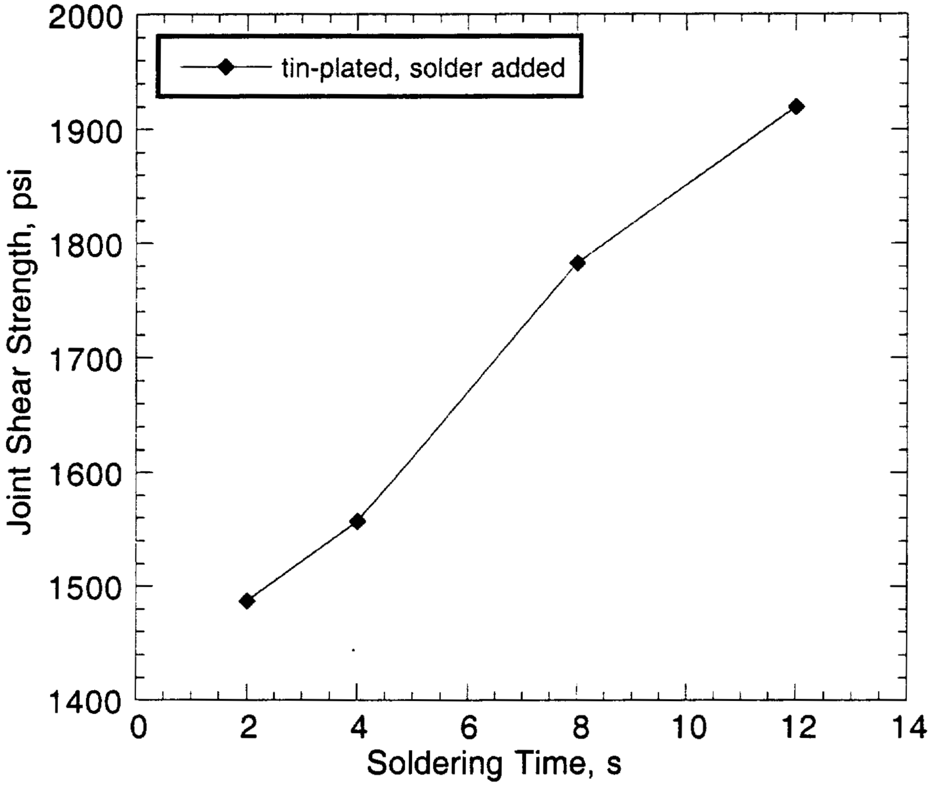

Figure 4.1.32 Shear strength vs soldering time for 304 stainless steel specimens, ultrasonically soldered with 70Sn-30Pb at 230 °C in air, for different soldering times.

Table 4.1.32 Presents shear strengths for the specimens, ultrasonically soldered in different times.

Time, s	Shear Strength, psi
2	1560
4	1490
8	1780
12	1920

Soldering Condition
Substrate: Stainless Steel
Solder Alloy: Non
Soldering Time: 4s
Shielding Condition: Argon

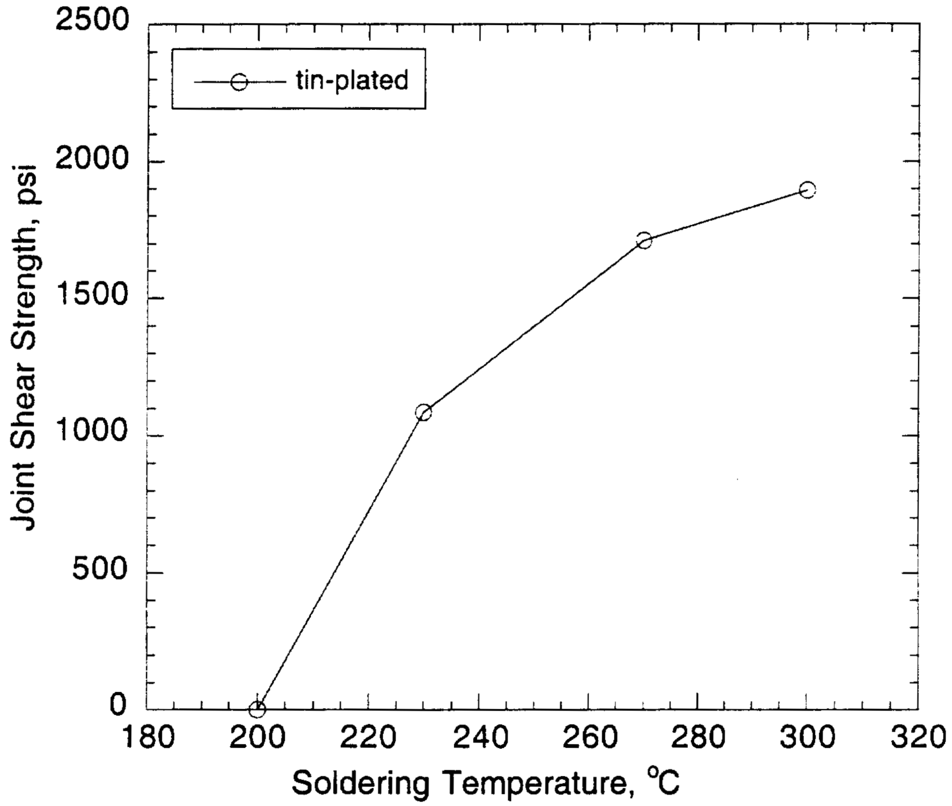

Figure 4.1.33 Shear strength vs soldering temperature for 304 stainless steel specimens, ultrasonically soldered for 4 seconds in argon, for different soldering temperatures.

Table 4.1.33 Shear strengths for the specimens, ultrasonically soldered at different soldering temperatures.

Temperature, ^oC	Shear Strength, psi
200	-
230	1090
270	1710
300	1900

Soldering Condition
Substrate: Stainless Steel
Solder Alloy: Non
Soldering Temperature: 230 ^{o}C
Shielding Condition: Argon

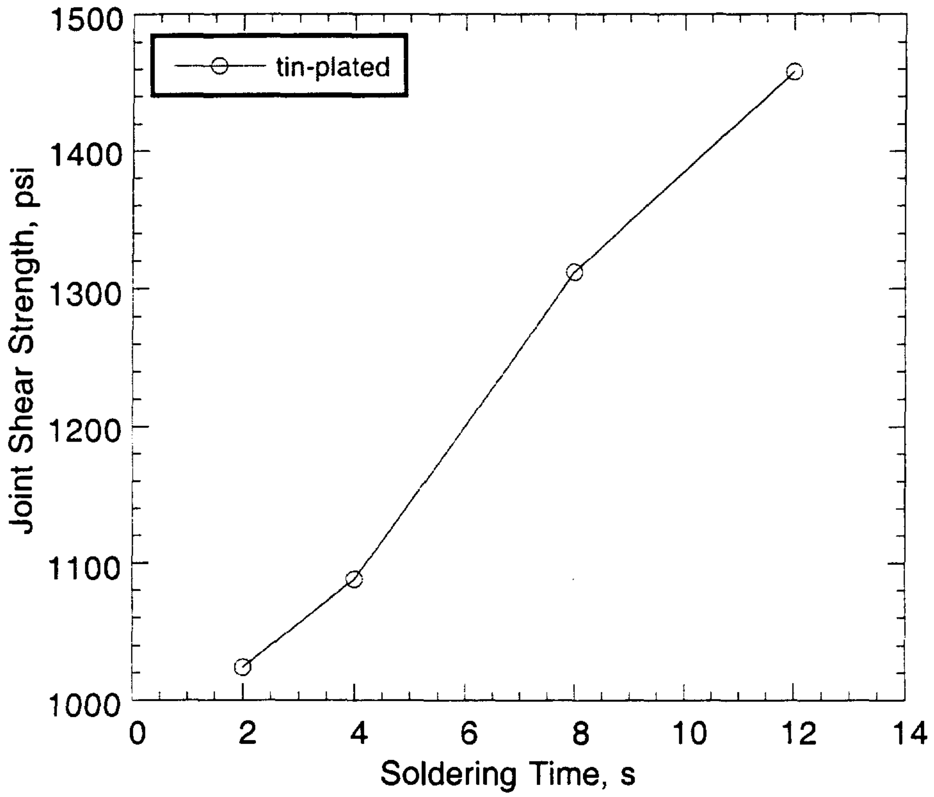

Figure 4.1.34 Shear strength vs soldering time for 304 stainless steel specimens, ultrasonically soldered at 230 ^{o}C in argon, for different soldering times.

Table 4.1.34 Shear strengths for the specimens, ultrasonically soldered in different soldering times.

Time, s	Shear Strength, psi
2	1020
4	1090
8	1310
12	1460

Soldering Condition
Substrate: Stainless Steel
Solder Alloy: 70Sn-30Pb
Soldering Time: 4s
Shielding Condition: Air

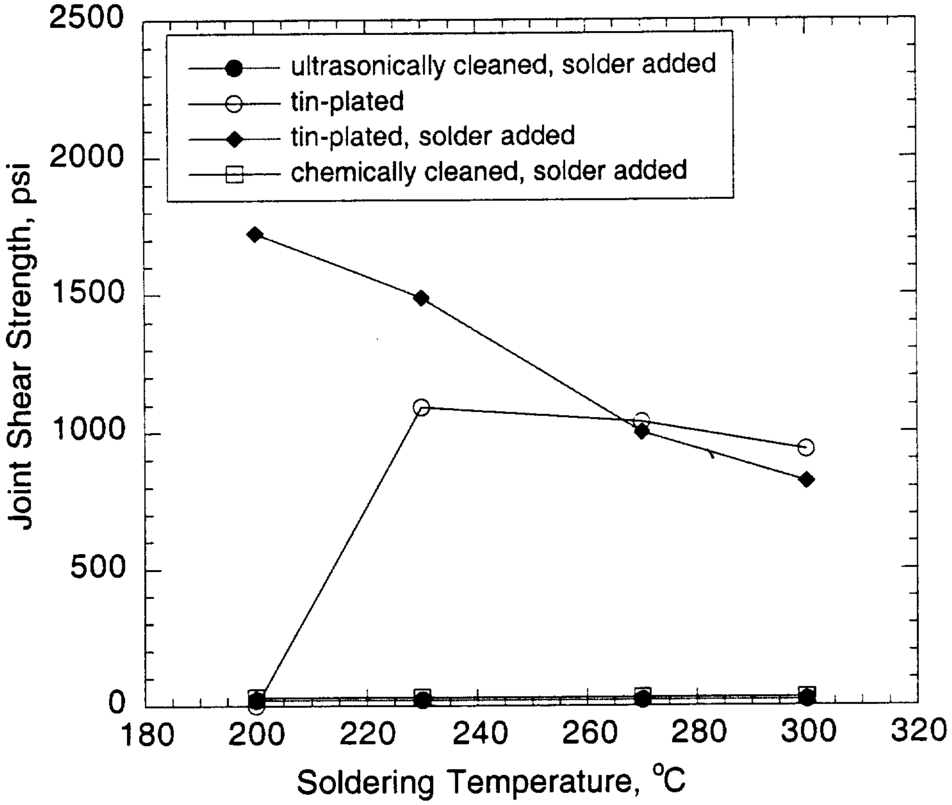

Figure 4.1.35 Comparison the shear strengths of 304 stainless steel specimens, ultrasonically soldered for 4 seconds in air, with different surface conditions.

Table 4.1.35 Shear strengths for different specimens, ultrasonically solderedwith various surface conditions.

Temperature, ^{0}C	Shear Strength, psi (degreased+solder)	Shear Strength, psi (tin-plated)	shear Strength, psi (tin-plated+solder)	Shear Strength, psi (deoxidized+solder)
200	20	-	1720	30
230	20	1090	1490	30
270	20	1040	1000	30
300	20	940	820	30

Soldering Condition

Substrate: Stainless Steel
Solder Alloy: 70Sn-30Pb
Soldering Temperature: 230 °C
Shielding Condition: Air

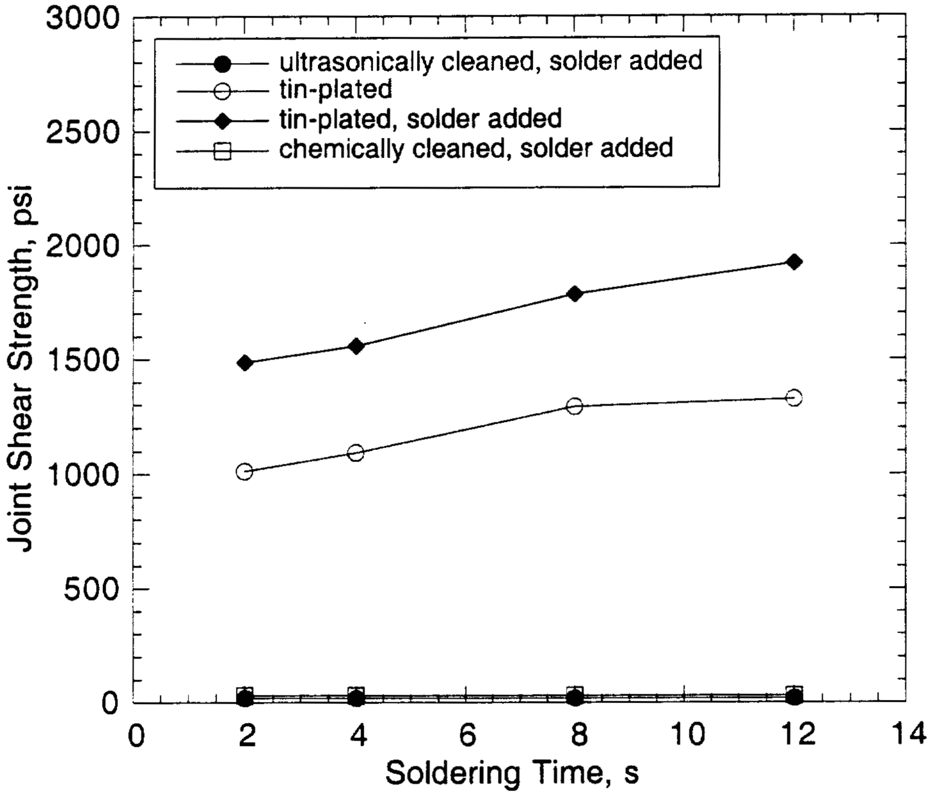

Figure 4.1.36 Comparison the shear strengths of 304 stainless steel specimens, ultrasonically soldered at 230 °C in air, with different surface conditions.

Table 4.1.36 Shear strength for the specimens, ultrasonically soldered with different surface conditions.

Time, s	Shear Strength, psi (degreased+solder)	Shear Strength, psi (tin-plated)	Shear strength, psi (tin-plated+solder)	Shear Strength, psi (deoxidized+solder)
2	20	1010	1560	30
4	20	1090	1490	30
8	20	1290	1780	30
12	20	1320	1920	30

Soldering Condition
Substrate: Stainless Steel
Solder Alloy: 70Sn-30Pb
Soldering Time: 4s
Shielding Condition: Argon

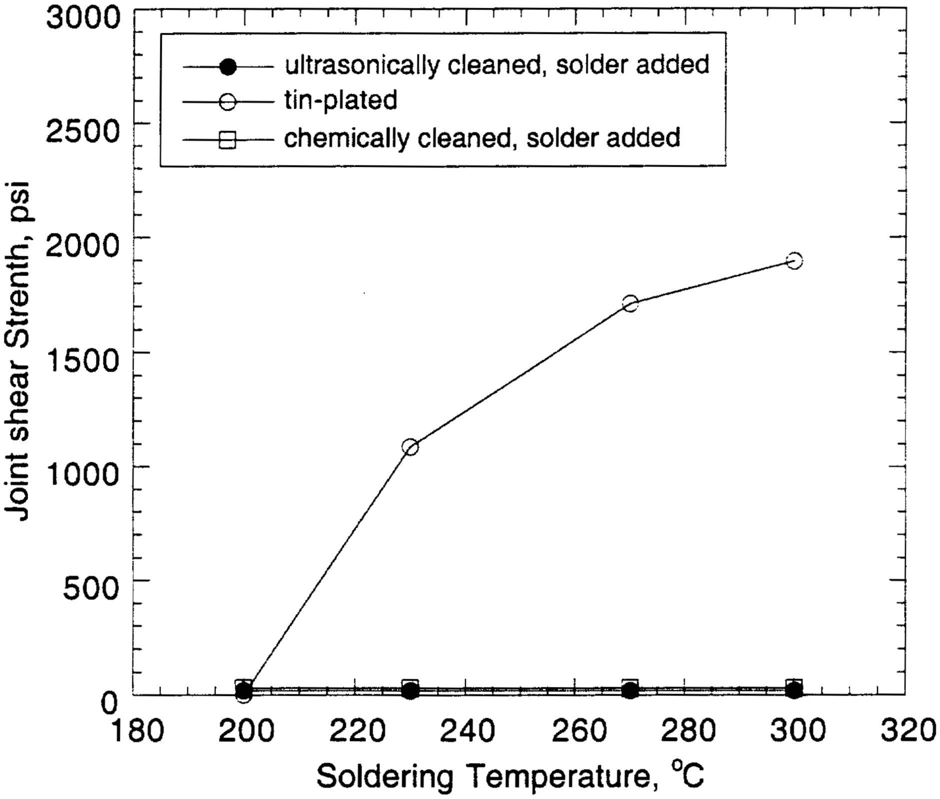

Figure 4.1.37 Comparison the shear strengths of 304 stainless steel specimens, ultrasonically soldered for 4 seconds in argon, with different surface conditions.

Table 4.1.37 Presents the shear strength for different specimens, ultrasonically soldered with various surface conditions.

Temperature, °C	Shear Strength, psi (degreased+solder)	Shear Strength, psi (tin-plated)	Shear Strength, psi (deoxidized+solder)
200	20	-	30
230	20	1090	30
270	20	1710	30
300	20	1900	30

Soldering Condition
Substrate: Stainless Steel
Solder Alloy: 70Sn-30Pb
Soldering Temperature: 230 °C
Shielding Condition: Argon

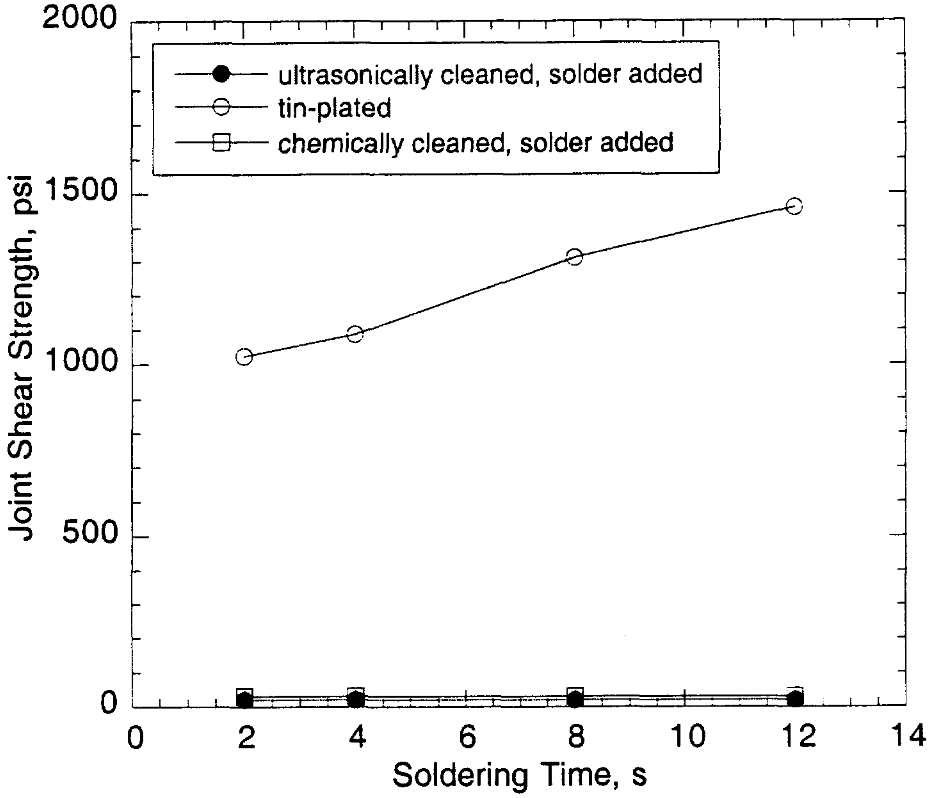

Figure 4.1.38 Comparison the shear strengths of 304 stainless steel specimens, ultrasonically soldered at 230 °C in argon, with different surface conditions.

Table 4.1.38 Shear strength for different specimens, ultrasonically soldered with different surface conditions.

Time, s	Shear Strength, psi (clened+solder)	Shear Strength, psi (tin-plated)	Shear Strength, psi (deoxidized+solder)
2	20	1020	30
4	20	1090	30
8	20	1310	30
12	20	1460	30

Soldering Condition

Substrate: Stainless Steel
Solder Alloy: Non
Soldering Time: 4s
Surface Condition: Tin-plated

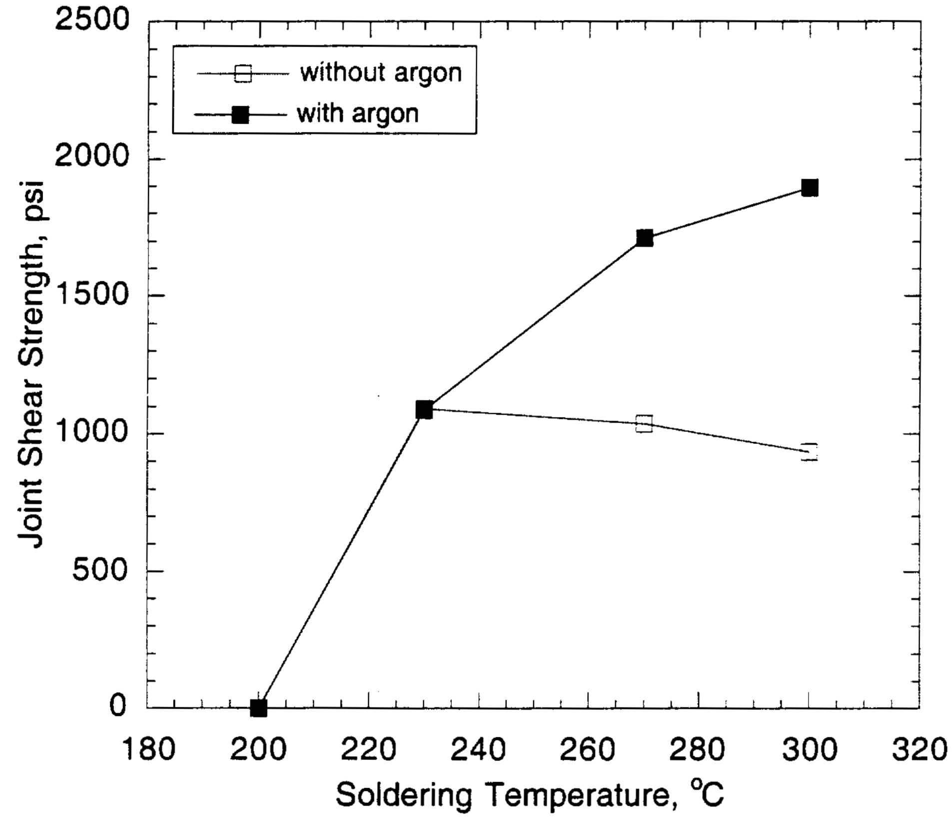

Figure 4.1.39 Shear strength vs soldering temperature for 304 stainless steel specimens, ultrasonically soldered for 4 seconds in air and in argon.

Table 4.1.39 Shear strengths for 304 stainless steel specimens, ultrasonically soldered in air and in argon.

Temperature, °C	Shear Strength, psi (in air)	Shear Strength, psi (in argon)
200	-	-
230	1090	1090
270	1040	1710
300	940	1900

Soldering Condition
Substrate: Stainless Steel
Solder Alloy: Non
Soldering Temperature: 230 °C
Surface Condition: Tin-plated

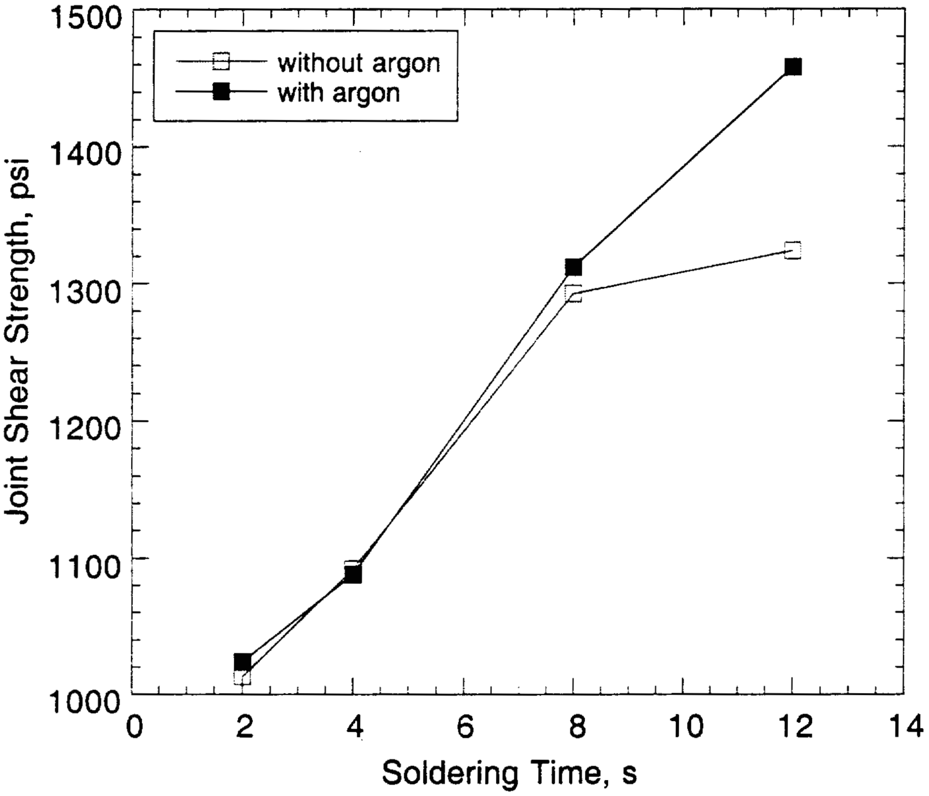

Figure 4.1.40 Shear strength vs soldering time for 304 stainless steel specimens, ultrasonically soldered at 230 °C in air and in argon.

Table 4.1.40 Shear strengths for 304 stainless steel specimens, ultrasonically soldered in air and in argon.

Time, s	Shear Strength, psi (in air)	Shear Strength, psi (in argon)
2	1010	1020
4	1090	1090
8	1290	1310
12	1320	1460

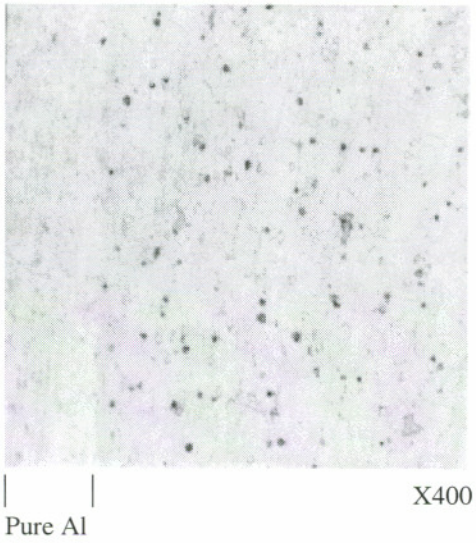

Figure 4.2.1 Optical image for 2024-Alclad, left side surface is commercial pure aluminum and right side is 2024 aluminum alloy.

Table 4.2.1 EDS results and the nominal composition for 2024-Al alloy.

Elements	Al	Cu	Mg	Mn
Nominal Composition, W%	93.5	4.4	1.5	0.6
EDS Results	93.4	5.1	1	0.5

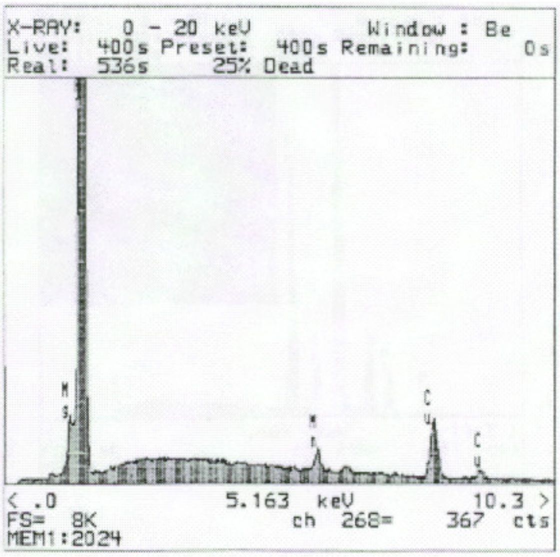

Figure 4.2.4 X-ray spectrum for the aluminum alloy substrate.

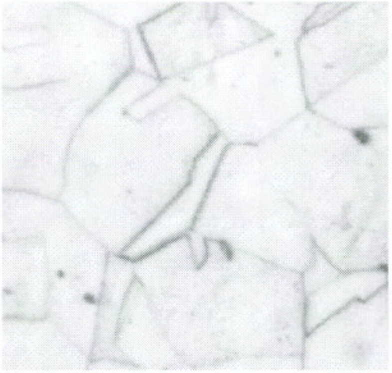

Optical Image X800

Figure 4.1.2 304 stainless steel substrate microstructure (Fully Austenite).

Table 4.2.2 Composition of 304 stainless steel substrate, compare to its nominal composition.

Elements	Fe	Cr	Ni	Mn	Si	C
Nominal Composition, W%	-	18-20	8-10	2	1	0.08
EDS Results	70.2	19	6.6	3.85	0.42	-

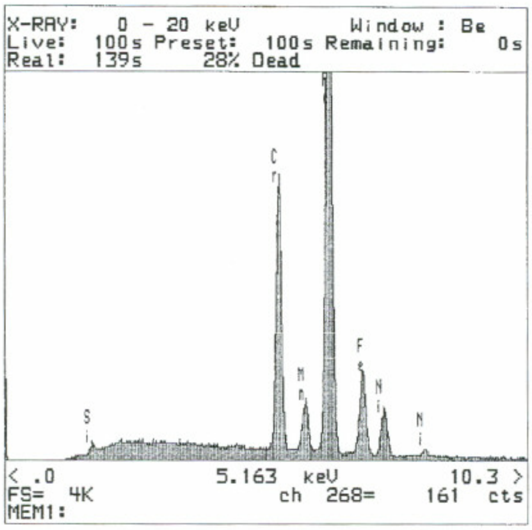

```
X-RAY:    0 - 20 keV              Window : Be
Live:   100s Preset:  100s Remaining:     0s
Real:   139s      28% Dead
```

```
< .0               5.163  keV          10.3 >
FS=  4K                ch  268=     161  cts
MEM1:
```

Figure 4.2.5 X-ray spectrum for the 304 stainless steel substrate.

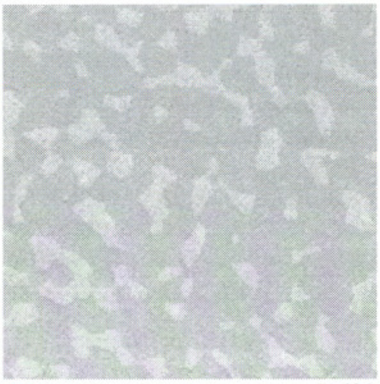

Figure 4.2.3 Microstructure of the 70Sn-30Pb bulk solder.

Table 4.2.3 EDS results for the bulk solder alloy, compare to its nominal composition.

Elements	Sn	Pb
Nominal Composition, W%	70	30
EDS Results	69	31

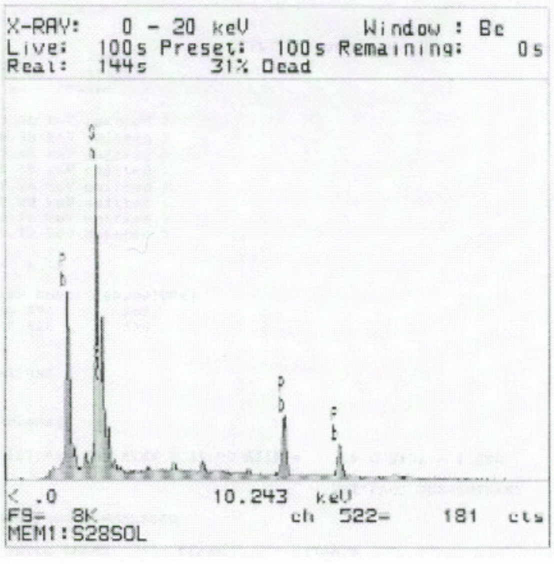

Figure 4.2.6 X-ray spectrum for the bulk solder.

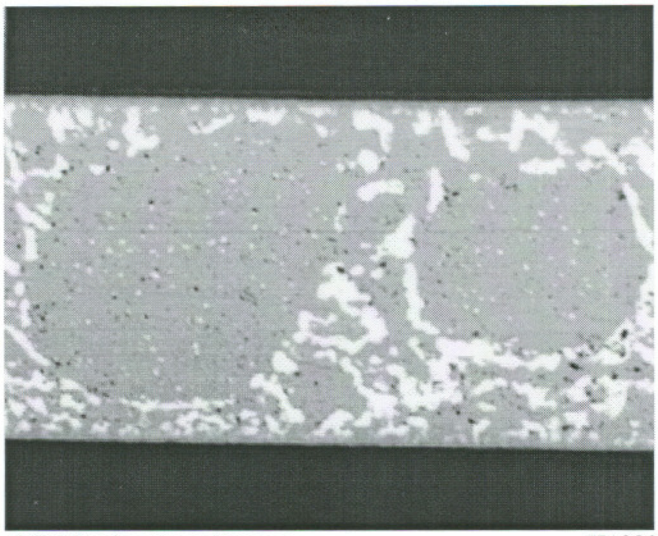

Figure 4.2.7 Microstructure of an ultrasonically soldered joint deposited on tin-plated 2024 Alclad using 70Sn-30Pb in air at 300 °C.

Tables 4.2.(4-5) EDS results for tin-rich and lead-rich areas.

Elements	Sn	Pb
W%, Tin-rich, (dark area)	97.26	2.74

Table 4.2.4

Elements	Sn	Pb
W%, Lead-rich, (white area)	4.25	95.75

Table 4.2.5

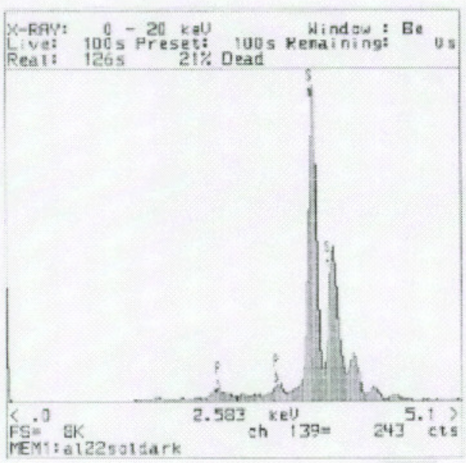

Figure 4.2.8

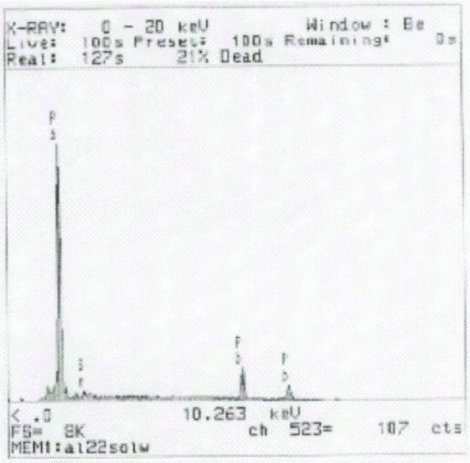

Figure 4.2.9

Figures 4.2.(8-9) X-ray spectrum for tin-rich and lead-rich areas on the joint, absent from this spectrum is the aluminum substrate dilution.

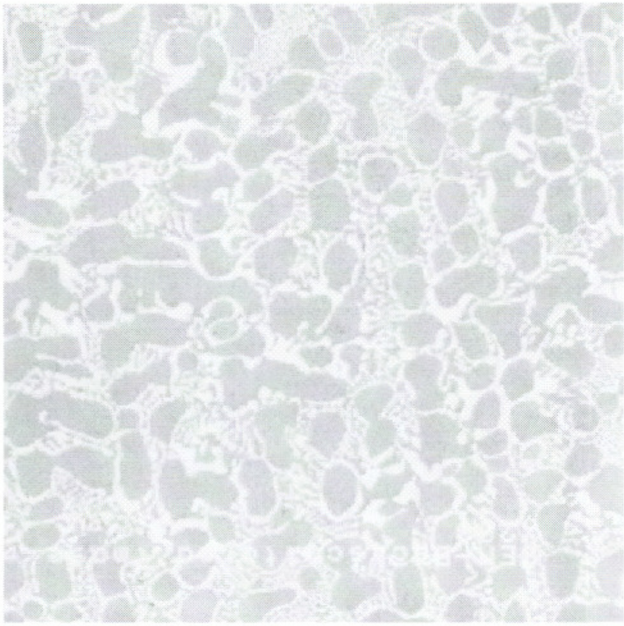

SEM Backscattered Image X200

Figure 4.2.10 Microstructure of as-solidified molten bulk 70Sn-30Pb solder.

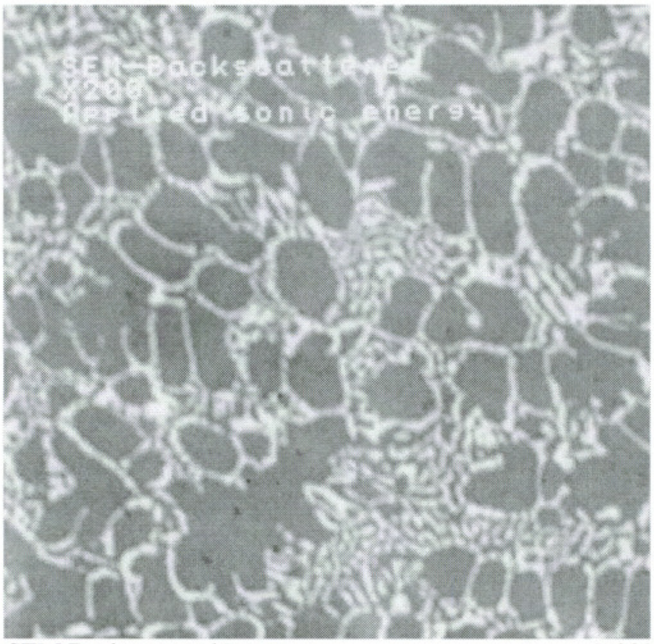

SEM Backscattered Image X200

Figure 4.2.11 Microstructure of as-solidified molten bulk 70Sn-30Pb solder (solidified with applying the ultrasonic vibrations).

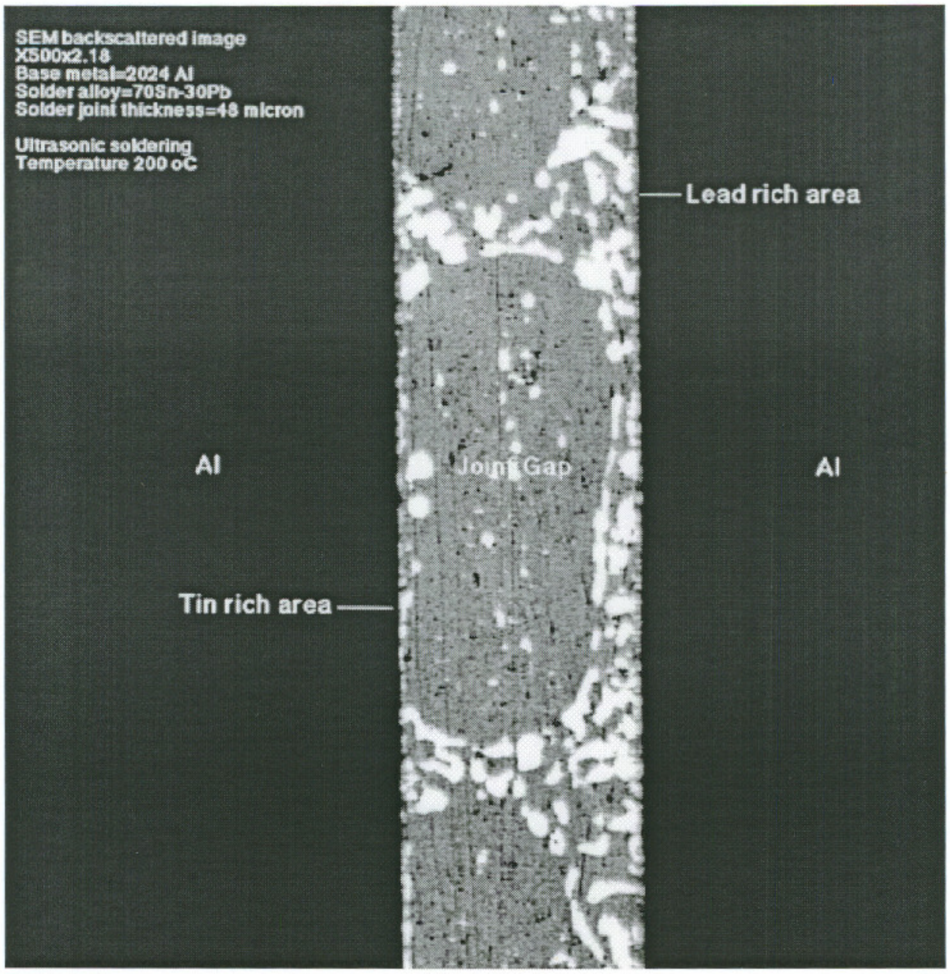

SEM Backscattered Image **48 microns** X1090

Figure 4.2.12 Solder joint microstructure and its thickness.

Substrate: 2024-Alclad
Solder Alloy: 70Sn-30Pb
Soldering Type: Flux-free Ultrasonic
Soldering Temperature: 200 ^{o}C
Solder Joint Thickness: 48 microns

SEM Backscattered Image **17 microns** X1635

Figure 4.2.13 Solder joint microstructure and its thickness.

Substrate: 2024-Alclad
Solder Alloy: 70Sn-30Pb
Soldering Type: Flux-free Ultrasonic
Soldering Temperature: 230 ^{o}C
Solder Joint Thickness: 17 microns

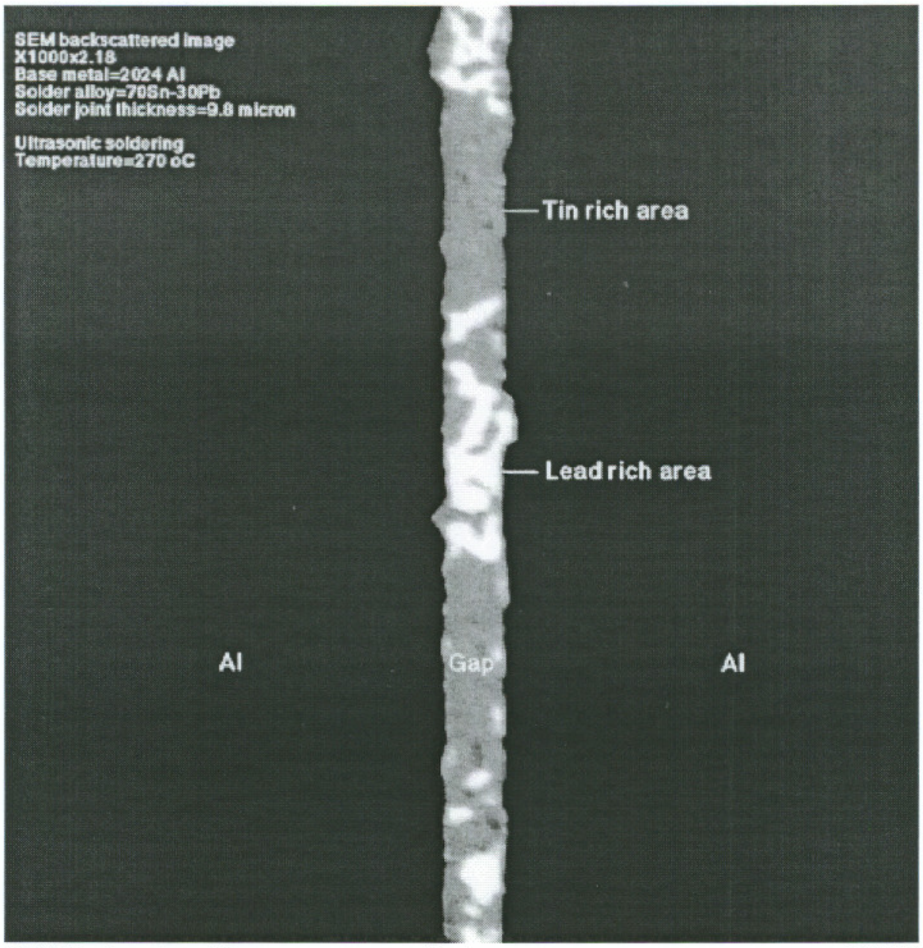

SEM Backscattered Image **9 microns** X2180

Figure 4.2.14 Solder joint microstructure and its thickness.

Substrate: 2024-Alclad
Solder Alloy: 70Sn-30Pb
Soldering Type: Flux-free Ultrasonic
Soldering Temperature: 270 ^{o}C
Solder Joint Thickness: 9 microns

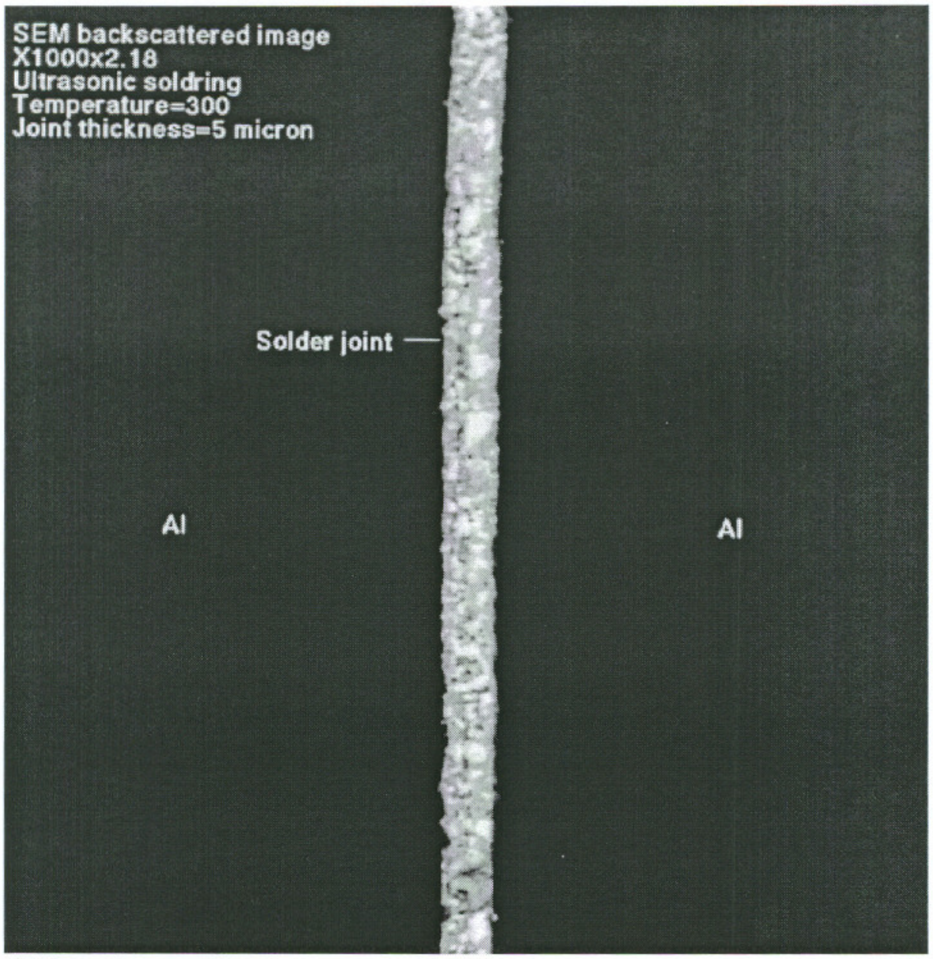

SEM Backscattered Image **5 microns** X2180

Figure 4.2.15 Shows the solder joint microstructure and its thickness.

Substrate: 2024-Alclad
Solder Alloy: 70Sn-30Pb
Soldering Type: Flux-free Ultrasonic
Soldering Temperature: 300 ^{o}C
Solder Joint Thickness: 5 microns

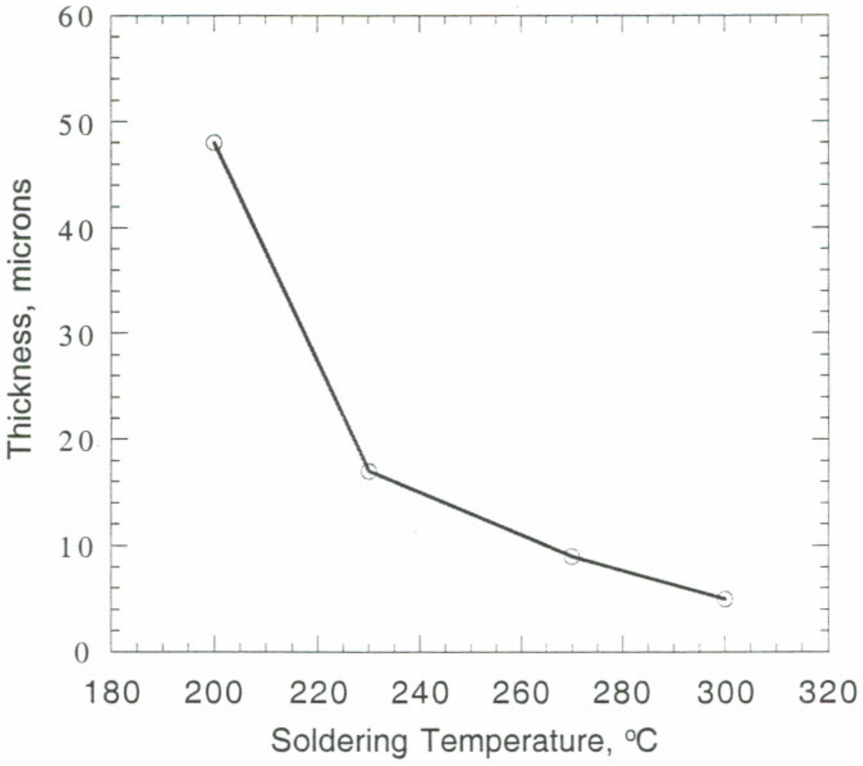

Figure 4.2.16 Thickness of the joints for chemically cleaned 2024 Alclad specimens, ultrasonically soldered at different temperatures.

Table 4.2.6 Solder joint thickness versus soldering temperature.

Soldering Temperature, °C	Solder Joint Thickness, microns
200	48
230	17
270	9
300	5

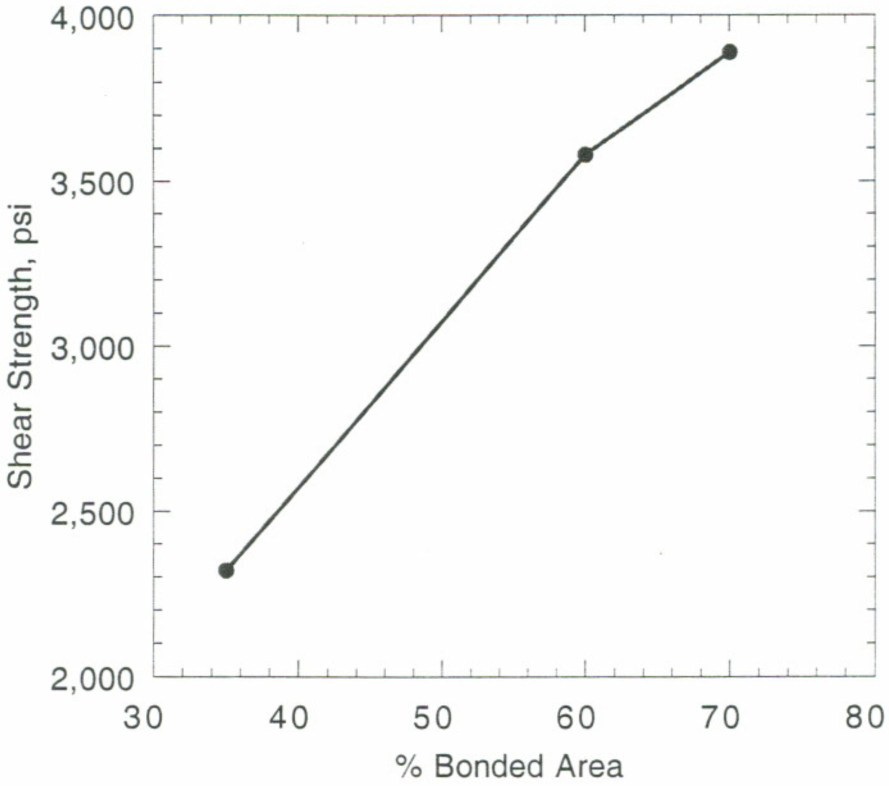

Figure 4.2.17 Shear strength vesus percentage bonded area for chemically cleaned 2024 Alclad specimens, ultrasonically soldered at different soldering temperatures.

Table 4.2.7 Percentage bonded area versus shear strength.

Percentage Bonded Area	Shear Strength, psi
35	2320
60	3580
70	3890

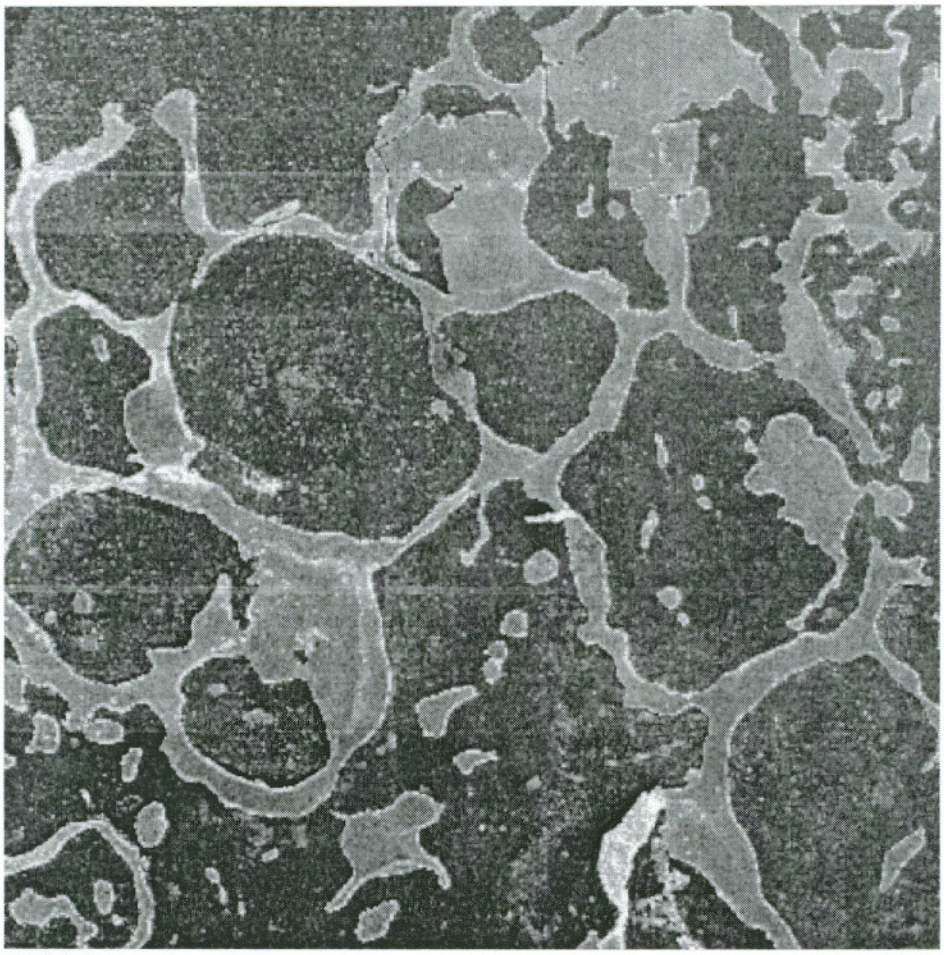

Figure 4.2.18 Fracture surface of 2024 alclad solder joint showing annular morphology of the solder wetting pattern.

Substrate: 2024-Alclad
Solder Alloy: 70Sn-30Pb
Soldering Type: Flux-free Ultrasonic

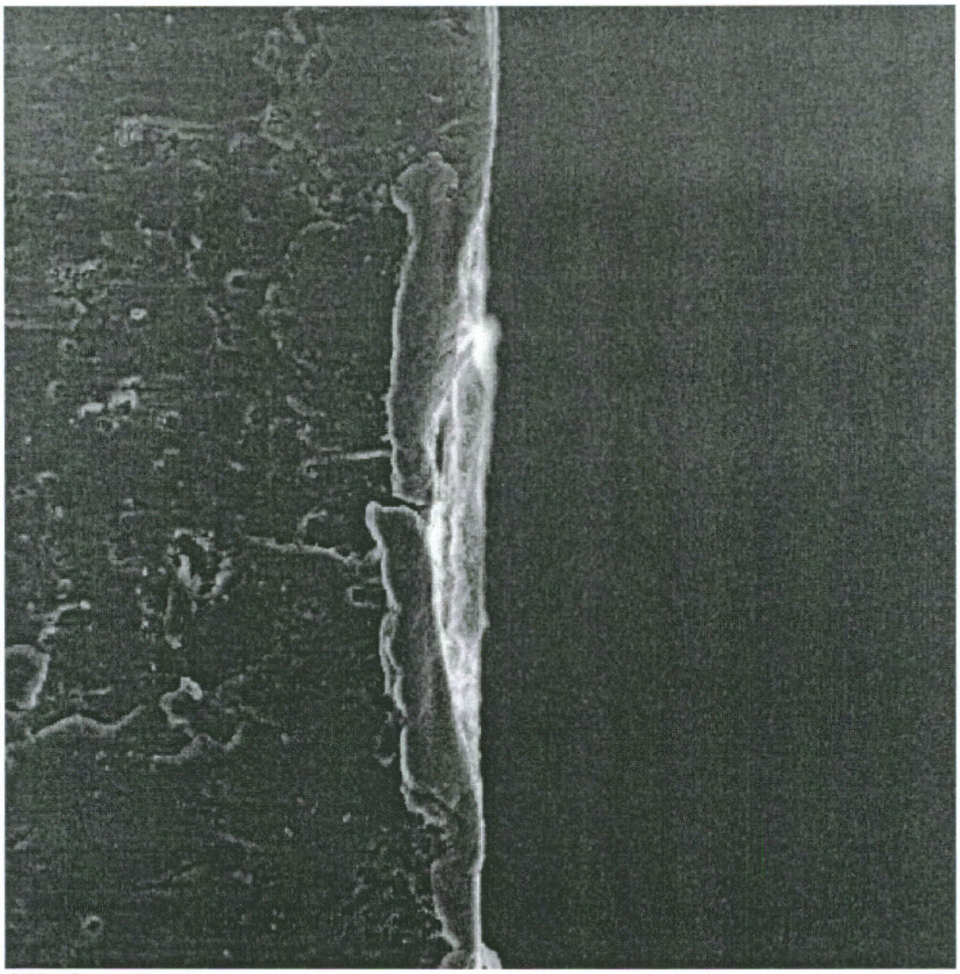

Figure 4.2.19 Effect of cavitation erosion on 2024 Alclad substrate surface.

Substrate: 2024-Alclad
Solder Alloy: 70Sn-30Pb
Soldering Type: Flux-free Ultrasonic

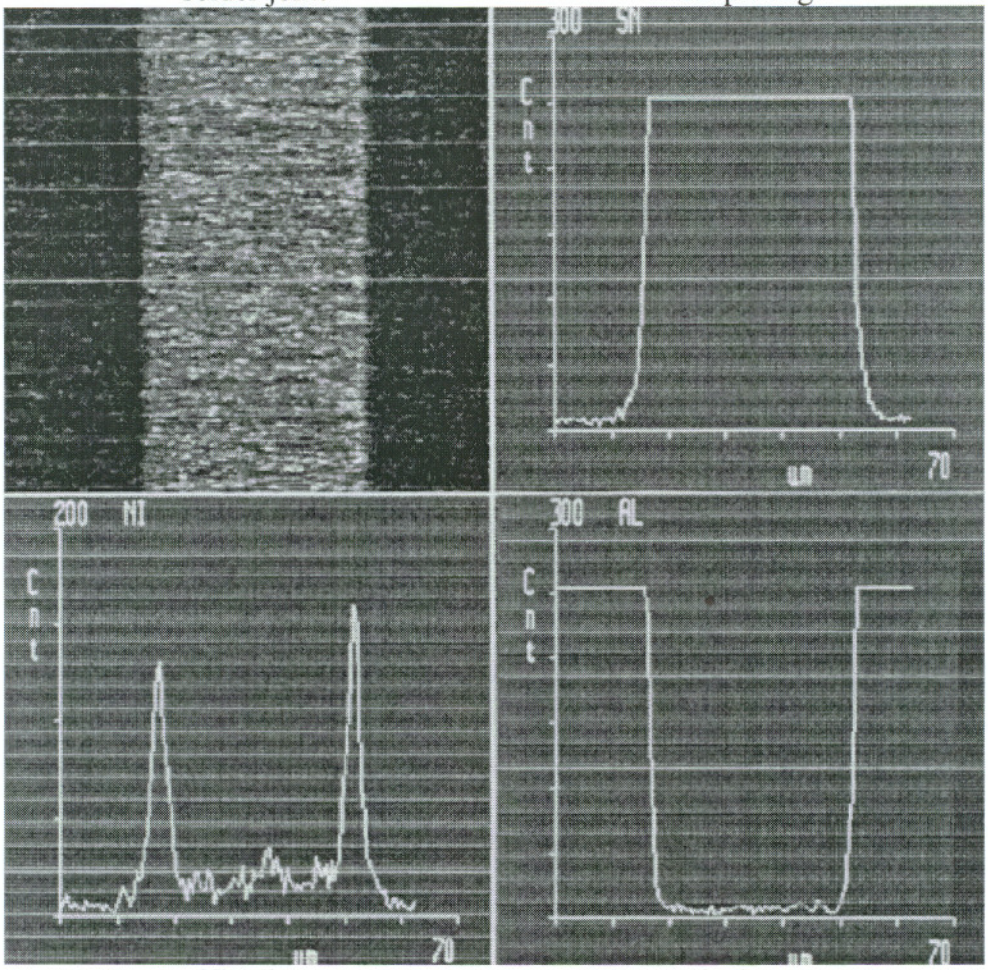

solder joint

Sn-plating

Ni strike

Al substrate

Figure 4.2.20 Line scan x-ray analysis of a solder joint (tin-plated specimen).

Substrate: 2024-Alclad
Solder Alloy: None
Surface Condition: Tin-plated with Nickel Strike
Soldering Type: Flux-free Ultrasonic

Al substrate

Sn-rich area

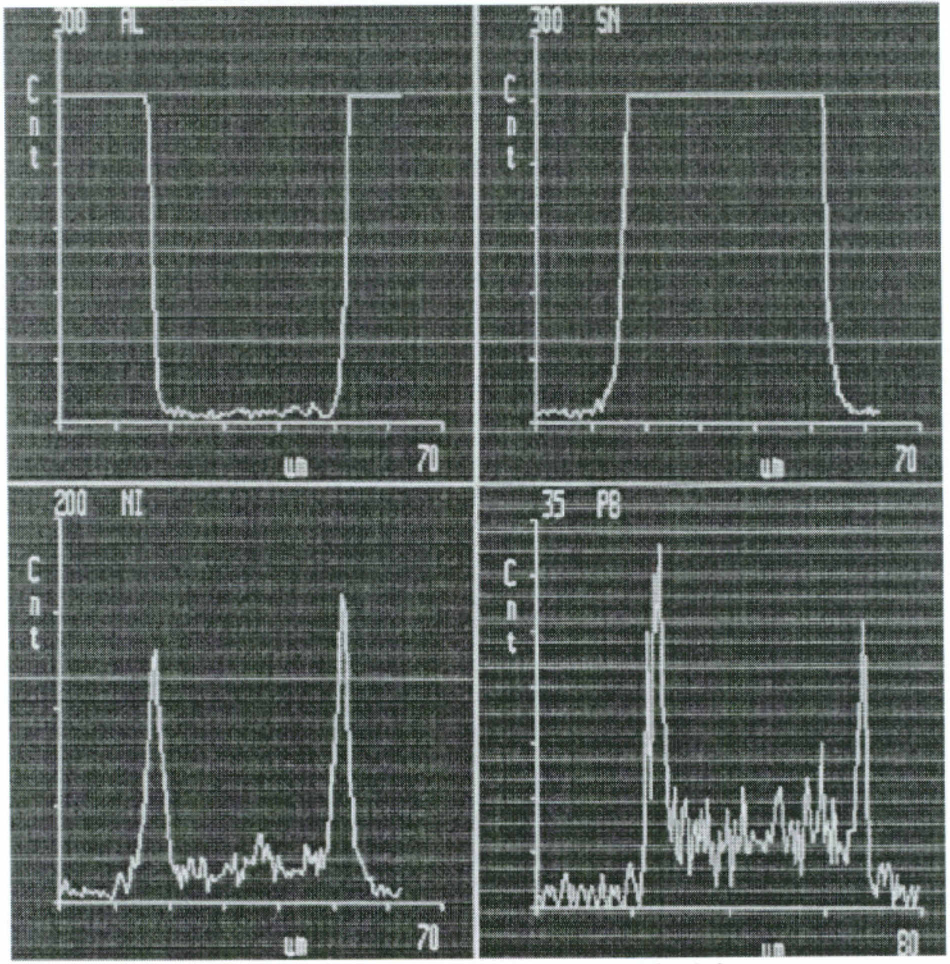

Ni strike

Pb-rich area

Figure 4.2.21 Line scan x-ray analysis for a solder joint (tin-plated, solder added).

Substrate: 2024-Alclad
Solder Alloy: 70Sn-30Pb
Surface Condition: Tin-plated with Nickel Strike
Soldering Type: Flux-free Ultrasonic

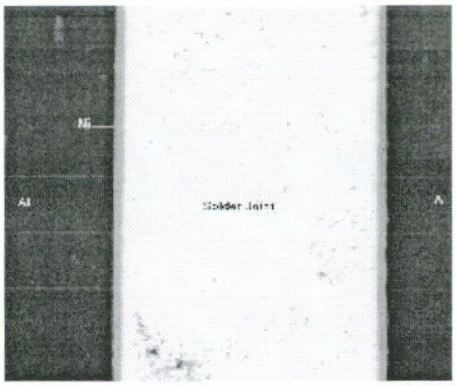

SEM Backscattered Image X2180

Figure 4.2.22 Micrograph showing the nickel strike (prior to tin-plating) at the substrate and solder joint interface for the tin-plated 2024 Alclad solder joint using 70Sn-30Pb filler.

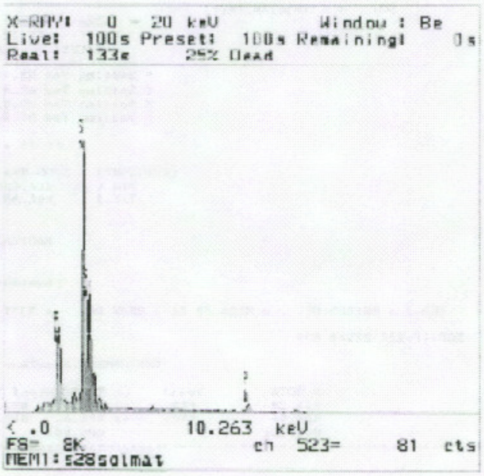

Figure 4.2.23 X-ray analysis spectrum of the joint.

Table 4.2.8 Composition of the solder joint.

Elements	Sn	Pb
EDS Results, W%	73.2	26.8

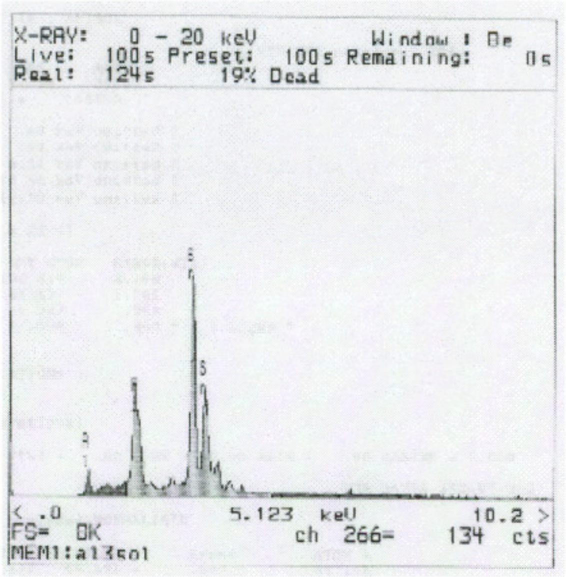

Figure 4.2.24 X-ray analysis spectrum of 2024 Alclad solder joint without nickel strike.

Table 4.2.9 Composition of the solder joint.

Elements	Sn	Pb	Al
EDS Results, W%	66.2	32.8	1

Table 4.2.10 Average wetted area evaluated by the ultrasonic non-destructive tests for 2024 Alclad solder joints soldered at different temperatures.

Soldering Temperature, ^{o}C	Average Wetted Area, %
200	35
220	40
240	50
260	60
280	65
300	70

Soldering Condition

Substrate: 2024-Alclad
Solder Alloy: 70Sn-30Pb
Soldering Time: 4s
Surface Condition: Deoxidized
Shielding Condition: Air

Chapter 5

Numerical Modeling

5.1 Introduction

Solder is a viscoplastic material which undergoes a complicated load history when used as interconnect for joining the devices or the microelectronic components. The strength of a solder joint is quite different from its bulk filler material. For the tin-lead alloys the maximum in tensile and shear strengths exist for the near eutectic alloys as well, the shear strength is lower than tensile as well. It is also noticeable that the strength of the pure lead and the pure tin is lower than the strength of tin-lead alloys. Open literature data confirms that the elastic modulus of pure tin is higher than pure lead and they are different from the elastic modulus of tin-lead alloys. However, the elastic modulus of a tin-lead alloy is not greatly influenced by its compositions[8].

The mechanical properties of solder joints are generally influenced by the joint geometry, the soldering time and temperature, the substrate material, the flux and the modes of heating and cooling. Another factor affecting the strength of a solder joint is its thickness. There is an optimum joint thickness at which the strength is at a maximum. It is reported that when the solder joint thickness is around 0.003 inches, the molten solder can flow easily into the joint area and the result is a uniform wetting with the highest strength. With narrower gap, gases and flux residues can be trapped to create voids. With larger gap, a decrease in capillary force reduces the wetting. Both cases result in a decrease in the joint strength. Dissolution of the base material into molten solder also strengthens the joint, but it does not have a significant effect on the maximum strength in relation with the joint thickness[8, 114, 115].

Soldering temperature definitely affects the joint thickness, because the viscosity of molten solder changes exponentially in relation with the temperature. The higher the temperature of the molten solder, the lower is the thickness of the joint. Nightingale and Hudson[115] concluded their work on the relationship between the soldering temperature and the solder joint thickness by the following empirical formula:

$$(T - t)\,S = K \qquad (5.1\text{-}1)$$

Where; T is the soldering temperature in °C, t is the eutectic temperature of tin-lead solder alloy in °C, S is the joint thickness in inches and K is a constant found empirically equal to 0.34.

A solder joint behaves differently in shear and in tensile. The shear strength of a solder joint (sensitive to the composition, microstructure and testing condition) is quite similar to its ultimate tensile strength, except that because the test is carried out in shear, plastic instability does not intercede. Depending on the joint geometry and its simplicity, the stress distribution and concentration may be analyzed quite readily. For a single lap joint under a tensile load, the differential straining between the substrate and solder joint and eccentricity of the loading path cause a stress concentration. In contrast with tensile strength, increasing the joint area or the joint length does not augment the shear strength and there is an optimum value for the joint length where the shear strength is at maximum. The reason behind this anomaly is that the shear stress is at maximum toward the ends of the joint and the joint at its central portion carries a little or no load. Figures 5.1.(a - b) and 5.1.(c - d) illustrate the stress distribution for the long and short single lap joints.

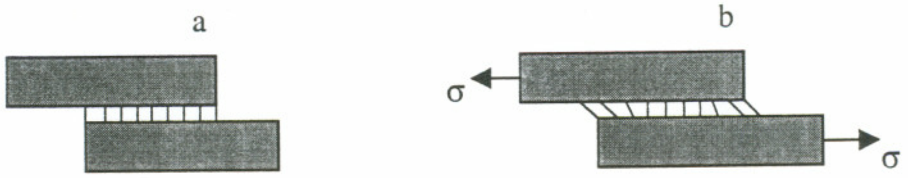

Figures 5.1.1(a-b) A long overlap joint, before and after shear loading

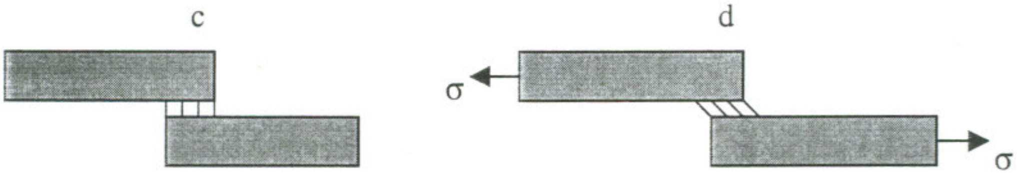

Figures 5.1.1(c-d) A short overlap joint, before and after shear loading

The stress concentration in a solder joint (as the results of applied shear) is inversely proportional to the joint thickness and directly proportional to the joint length. Therefore, stress concentration is at a minimum, when the joint is short and thin. For a lap joint with a simple geometry, the stress concentration factor K_t is relatively low.

$K_t < 2$ (stress concentration factor for a simple lap joint)

Figure 5.1.2 shows the tensile stresses at both ends of a single lap joint caused by the eccentricity of shear load path. This tensile stress is approximately four times magnitude of the shear and is perpendicular to the joint. For a short single overlap joint the mode of failure is shear, as the length increases, the failure occurs in tensile (peeling) stress[8, 114 - 118].

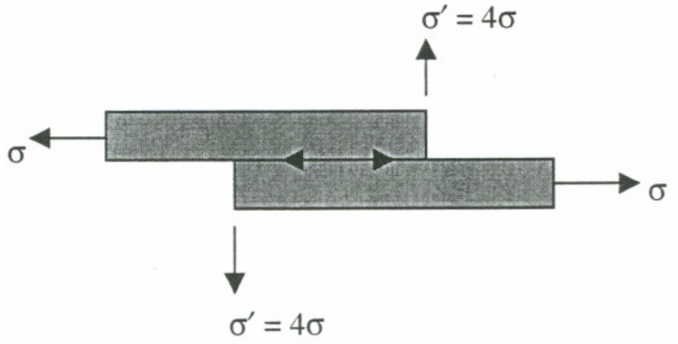

Figure 5.1.2 Stress concentration or peeling stress for a single lap joint loaded in tension

Computer simulation is a powerful tool that can provide approximate numerical solutions for a wide range of engineering problems. For example, finite element analysis (FEA) can provide a reasonable description of solder stress/strain distribution under different loading conditions. A finite element method also offers convenient ways to perform design optimization and parametric studies. All the above evaluations and design optimization can be done experimentally, but it requires precise test equipment and special test samples. Design, preparation and optimization of sample/equipment and performing the tests are usually the time consuming operations and generally quite costly.

The finite element method is applied to transform an engineering system with infinite number of unknowns (degree of freedoms) to a discrete system with finite number of unknowns represented by the interconnected pieces of finite size sub-domains called elements. The elements establish how the unknowns are coupled and how they respond to the applied actions. Each element has one or more nodes along its boundary. These nodal points create a system for passing the information from one element to the others. For example, in structural applications, the displacement (unknown) response to the force (applied action). These unknowns and the actions are related by a set of equilibrium equations. A finite element method is a common tool of choice for solving these equations[119 - 123].

The finite element method can be applied to evaluate the stress distribution and stress concentration of a longitudinally loaded lap joint. This three dimensional problem will be further reduced to a plane strain or plane stress two dimensional problems, by recognizing that the essential descriptions of the geometry of sample and the loading require only two independent coordinates. For the plane strain approach, the component of displacement along "z" direction or normal to "x-y" plane is zero, while for plane stress the component of stress perpendicular to "x-y" plane is zero[124, 125].

For the plane strain case, the preceding equations of elasticity theory can be simplified and written as:

Stress components:

$$[\sigma] = [\sigma_x \quad \sigma_y \quad \sigma_{xy}] \tag{5.1-2}$$

$$\sigma_z = \upsilon(\sigma_x + \sigma_y) \tag{5.1-3}$$

Strain components:

$$[\varepsilon] = [\varepsilon_x \quad \varepsilon_y \quad \gamma_{xy}] \tag{5.1-4}$$

Hooke's law:

$$\{\sigma\} = [C]\{\varepsilon\} \tag{5.1-5}$$

Where:

$$[C] = (E/(1+\upsilon)(1-2\upsilon)) \begin{bmatrix} 1-\upsilon & \upsilon & 0 \\ \upsilon & 1-\upsilon & 0 \\ 0 & 0 & (1-2\upsilon)/2 \end{bmatrix} \tag{5.1-6}$$

Static equilibrium:

$$d\sigma_x / dx + d\tau_{xy} / dy + X = 0 \quad (5.1\text{-}7)$$

$$d\tau_{xy} / dx + d\sigma_y / dy + Y = 0 \quad (5.1\text{-}8)$$

$$d\sigma_z / dz + Z = 0 \quad (5.1\text{-}9)$$

Compatibility:

$$d^2 \varepsilon_x / dy^2 + d^2 \varepsilon_y / dx^2 = d^2 \gamma_{xy} / dx\, dy \quad (5.1\text{-}10)$$

Differential equations for displacements are:

$$\nabla^2 u + (1/1\text{-}2\upsilon)\, (d\, (du/dx + dv/dy) / dx) + X/\mu = 0 \quad (5.1\text{-}11)$$

$$\nabla^2 u + (1/1\text{-}2\upsilon)\, (d\, (du/dx + dv/dy) / dy) + Y/\mu = 0 \quad (5.1\text{-}12)$$

Where:

$$\nabla^2 = d^2 / dx^2 + d^2 / dy^2 \quad (5.1\text{-}13)$$

For a plane stress case, the preceding equations of elasticity theory can be simplified and written as:

Stress components:

$$[\, \sigma \,] = [\, \sigma_x \quad \sigma_y \quad \tau_{xy} \,] \quad (5.1\text{-}14)$$

$$\sigma_z = 0 \quad (5.1\text{-}15)$$

Strain components:

$$[\, \varepsilon \,] = [\, \varepsilon_x \quad \varepsilon_y \quad \gamma_{xy} \,] \quad (5.1\text{-}16)$$

$$\varepsilon_z = (-\upsilon / 1\text{-}\upsilon)\, (\varepsilon_x + \varepsilon_y) \quad (5.1\text{-}17)$$

Hooke's law: $$\{ \sigma \} = [C] \{ \varepsilon \} \tag{5.1-18}$$

$$[C] = (E / (1-\upsilon^2)) \begin{bmatrix} 1 & \upsilon & 0 \\ \upsilon & 1 & 0 \\ 0 & 0 & (1-\upsilon)/2 \end{bmatrix} \tag{5.1-19}$$

Static equilibrium: $$d\sigma_x / dx + d\tau_{xy} / dy + X = 0 \tag{5.1-20}$$

$$d\tau_{xy} / dx + d\sigma_y / dy + Y = 0 \tag{5.1-21}$$

Compatibility: $$d^2 \varepsilon_y / dz^2 + d^2 \varepsilon_z / dy^2 = 0 \tag{5.1-22}$$

$$d^2 \varepsilon_z / dx^2 + d^2 \varepsilon_x / dz^2 = 0 \tag{5.1-23}$$

$$d^2 \varepsilon_x / dy^2 + d^2 \varepsilon_y / dx^2 = d^2 \gamma_{xy} / dx\, dy \tag{5.1-24}$$

$$2\, d^2 \varepsilon_x / dy\, dz = d^2 \gamma_{xy} / dx\, dz \tag{5.1-25}$$

Differential equations for displacements are:

$$\nabla^2 u + (1+\upsilon)/(1-\upsilon)\ (d\ (du/dx + d\upsilon/dy) / dx) + X/\mu = 0 \tag{5.1-26}$$

$$\nabla^2 \upsilon + (1+\upsilon)/(1-\upsilon)\ (d\ (du/dx + d\upsilon/dy) /dy) + Y/\mu = 0 \tag{5.1-27}$$

Then the principal stresses can be calculated from the stress components by the cubic equation:

$$\begin{bmatrix} \sigma_x - \sigma_o & \sigma_{xy} & \sigma_z \\ \sigma_{xy} & \sigma_y - \sigma_o & \sigma_{yz} \\ \sigma_{xz} & \sigma_{yz} & \sigma_z - \sigma_o \end{bmatrix} = 0 \qquad (5.1\text{-}28)$$

σ_o is the normal stress (hydrostatic)
σ_i is the principal stress (three values)
The three principal stresses are labeled as "σ_1 , σ_2 , σ_3" where:

$$\sigma_1 > \sigma_2 > \sigma_3$$

Or:

$$\sigma_1 = \mathrm{MAX}\,(\,|\,\sigma_1 - \sigma_2\,|\,,\,|\,\sigma_2 - \sigma_3\,|\,,\,|\,\sigma_3 - \sigma_1\,|\,) \qquad (5.1\text{-}29)$$

The von Mises or equivalent stress "σ_e" is computed as:

$$\sigma_e = (\,\tfrac{1}{2}\,\{(\,\sigma_1 - \sigma_2\,)^2 + (\,\sigma_2 - \sigma_3\,)^2 + (\,\sigma_3 - \sigma_1\,)^2\,\}\,)^{1/2} \qquad (5.1\text{-}30)$$

The equivalent stress is related to the equivalent strain through:

$$\sigma_e = 2\,G\,\varepsilon_e \qquad (5.1\text{-}31)$$

Where the shear modulus is:

$$G = E\,/\,2(1+\upsilon) \qquad (5.1\text{-}32)$$

5.2 Finite Element Analysis

In this study, a two-dimensional finite element analysis was conducted using the ANSYS program to determine the stress distributions and locate the maximum stress concentration along a longitudinally loaded single lap joint. Maximum stresses, concentrating along the solder joints were simulated by changing the joint thickness. The FEA simulations were conducted in both linear elastic and elasto-plastic regimes assuming a plane strain condition. In the elasto-plastic model, only the solder joint has non-linear material properties and a Classical Bilinear Kinematic Hardening approach was used to define the stress-strain curve. This option is initially used for isotropic materials includes most metals which obey the von Mises yield criterion. The stress-strain curve represented by the Bilinear Kinematic Hardening consists an elastic slope "E" and a plastic slope "E_T" shown in Figure 5.2.1.

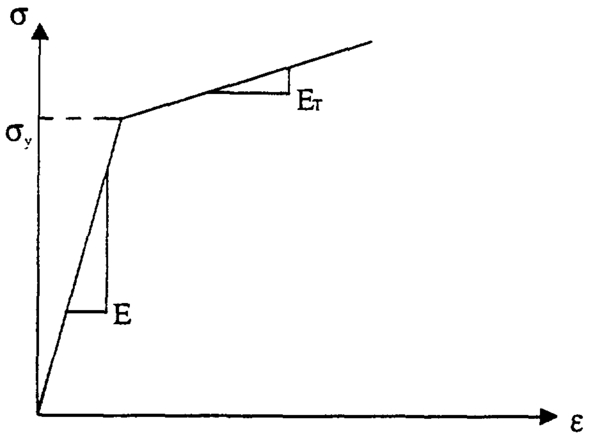

Figure 5.2.1 Stress-strain curve represented by Bilinear Kinematic Hardening.

Table 5.2.1 Material properties of the substrate and the solder joint.

Material	Young's modulus E, GPa	Poisson's Ratio at 20 °C	Density D, gr/cm^3 at 20 °C	Yield Strength MPa	Tensile Strength MPa
Substrate 2024-Alclad	72.4	0.33	2.77	290	440
Solder Alloy 70Sn-30Pb	30	0.4	8.3	36.7	46.9

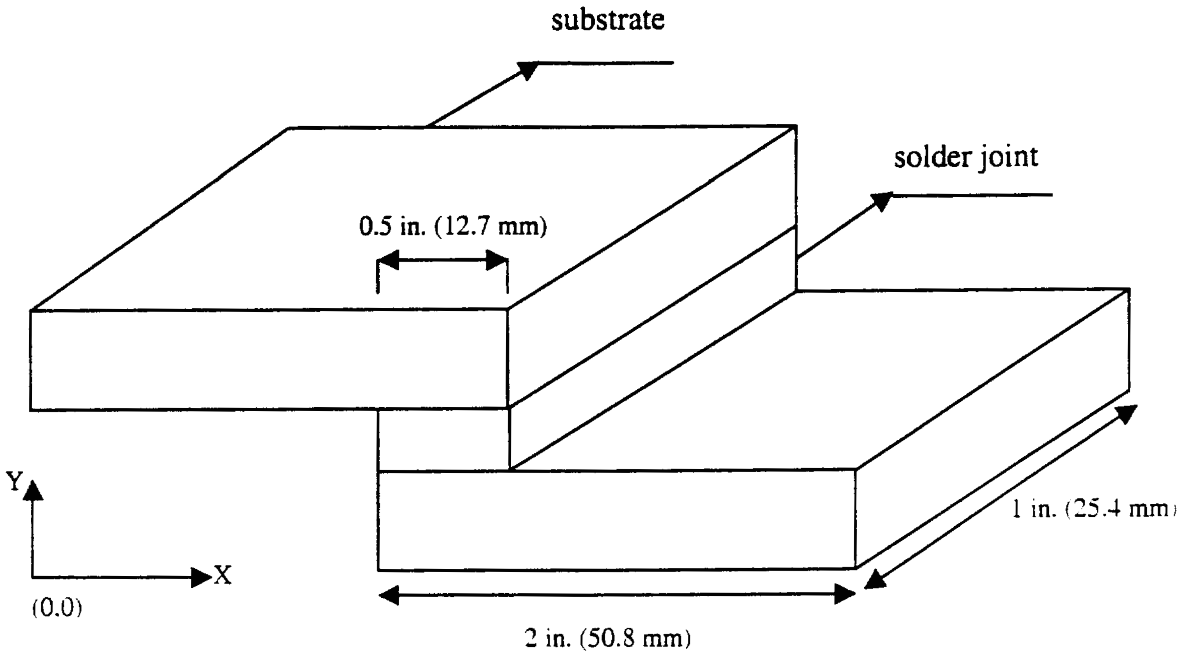

Figure 5.2.2 Single overlap joint model and its dimensions.

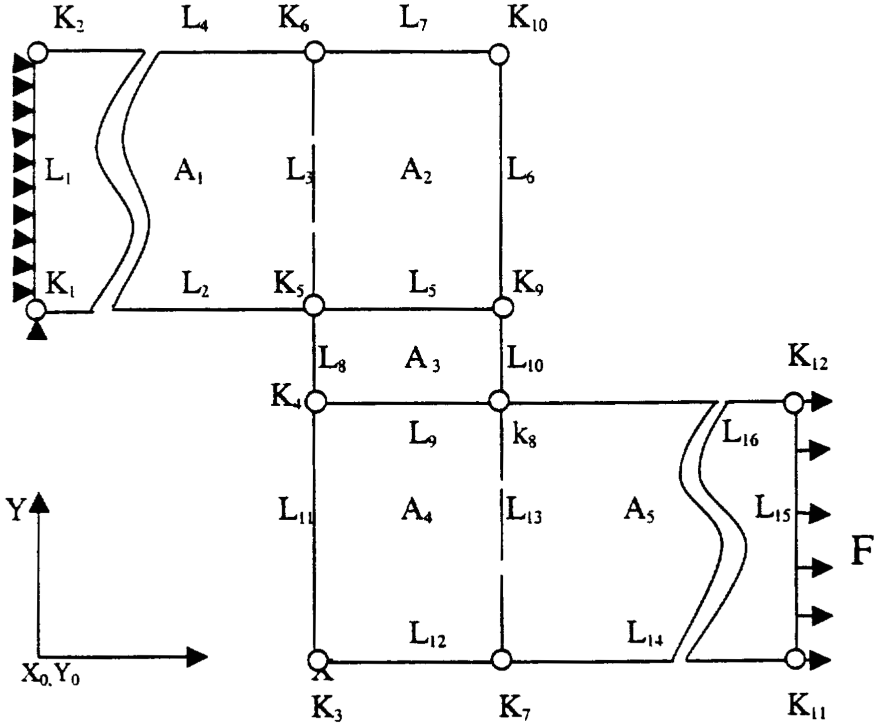

Figure 5.2.3 A two-dimensional model outlining the geometry, applied load and boundary condition.

The following assumptions were considered throughout the numerical simulations:

- Solder Joint: 100% wetting (perfect joint without voids or inclusions)
- Joint Interface: Metallurgical Bonding (no compounds formed at the interfaces)
- Applied Load: Constant
- Elastic Model: Elastic deformation for both substrate and the joint.
- Elasto-plastic Model: plastic deformation only for the joint.

5.3 Modeling Results and discussions

One of the factors influencing solder joint strength is the joint gap, as reported by Manko[8] and Nightingale[115] for the copper alloys and mild steel using traditional soldering operations with activated fluxing agents. Manko[8] and Nightingale[115] stated that there is an optimum joint thickness for which the joint strength is maximum. It is very important to bear in mind that, in traditional soldering or even in wave soldering and re-flow soldering (used in microelectronic industry), the fluxing agent is an integrated part of the soldering operation. The flux plays very important roles such as; removing the oxide films or other corrosion products from the surfaces and protecting the joint interfaces from re-oxidation. Using a suitable and strong fluxing agent is usually helpful in maximizing the wetted area and the joint strength. This is generally not the case for the flux-free ultrasonic soldering operations used in this study because the wetting percentages for the joints, soldered at different temperatures, were relatively low. Also, the wetting percentage was the highest for the lowest joint gap only because it was prepared at the highest soldering temperature (300 °C). It means that in the absence of the flux, besides ultrasonic energy, soldering temperature was the key factor controlling the wetting and spreading of the molten solder on the substrate surfaces and consequently the joint gap. Experimental results and conclusions drawn from this study concerning the relationship between the joint thickness and its strength can therefore not be compared with the results from Manko[8] or Nightingale[115].

From a metallurgical point of view, it is quite noticeable that the mechanical properties of a solder joint can be affected by its gap size. As the gap size decreases, there is a higher possibility for the gases or air and the flux residues to be trapped in molten solder during the solidification process. Bubbles form as result of trapped gases or air. These bubbles create voids in the solder joint or at the joint interfaces. It would be expected the increasing the number and the size of the voids caused by solidification shrinkage and trapped gas, and the inclusions resulting from the flux residues will affect the mechanical properties of the joint and its lifetime in service.

When the joint gap size increases, the probability of gas trapping decreases, but a large gap causes capillary forces to be reduced, which in turn result in decreasing the wetting percentage. At the same time the mechanical properties of a large joint is similar to the bulk solder. In both cases, the strength of a solder joint expected to decrease and there must exist an optimum joint thickness at which the strength is at maximum. This optimum joint thickness would vary, depending on the base material, the filler metal, the fluxing agent, and the factors involved in the soldering operation.

From a mechanical point of view, for a single lap joint without any defects (ideal joint), the shear stress concentration in the filler is inversely proportional to its thickness and directly proportional to its length. This statement implies that the joint strength is higher for a thin joint of short overlap. Stress concentration along a single lap joint loaded in tension is caused by the differential straining between the solder - base material and the eccentricity of the loading path. This eccentricity of the loading path is the major factor leading to peeling stresses (stress concentration) that act normal to the joint. The amount of the stress concentrated along the joint is directly related to the length of the joint. As mentioned before, increasing the joint length increases the stress concentration, which is mainly located at the ends of the joint. It is possible to reduce the stress by using different joint configurations that distribute the load away from the joint. It may also be possible to redistribute the stress pattern and relocate the maximum stress concentration along the joint and in the substrate by changing the joint gap, because the major factor contributing the stresses is the eccentricity loading path (tensile or peeling stresses) which are perpendicular to the joint[114]. Therefore, it is normal to expect that a change in the joint length or the joint spacing, results in the redistribution of the stresses along the joint and in the base material.

The simulation results confirm that the stress distribution pattern and the location of the maximum stress concentration change when the gap of the joint changes as shown in Figures 5.3.(2 - 4). Changing the location of the maximum stress thus affects the joint strength, because this is the peeling load (maximum stress concentrated) that is moving away from the joint.

Maximum shear stresses and von Mises stresses are simulated for the joints with different gaps in both elastic and elasto-plastic approaches by assuming that the joints have no metallurgical or mechanical defects. For the elastic approach, the results show that the maximum shear stress concentration along the joint is decreasing as the joint gap increases. The results are shown in Figures 5.3.(5 – 8 - 11) for the 500, 1000, and 2000 lbs of constant applied loads. These results confirm the previous statement that the maximum shear stress concentration along the solder joint is inversely proportional to the joint thickness.

For the elasto-plastic approach, the results are quite similar to the elastic approach as long as the elastic domain is preserved as shown in Figure 5.3.6 and Figure 5.3.9. When the applied load increases to 2000 lbs, then at some point (spacing), the maximum stress concentration increases as the gap increases as shown in Figure 5.3.12. This is because we are entering in to the plastic domain according to the properties data used in the simulation program concerning the yield strength and the ultimate tensile strength of the bulk solder.

The results are quite different as it would be expected for the maximum von Mises stresses obtained in both elastic and elasto-plastic approaches. Because the von Mises stress does not depend on normal stress and shear stress. Since the von Mises yield criterion is based on the differences of principal stresses with the square terms as shown in equation (5.1-30). Therefore the criterion is independent of the component of the hydrostatic stress, and the sign of the individual stresses. For both elastic and elasto-plastic approaches under different constant tension loads, there is an optimum joint thickness in which the maximum stress concentration, (the peeling load) along the joint is at minimum as shown in Figure 5.3.14 through Figure 5.3.22. It means that a solder joint demonstrates its maximum strength depends only on its joint spacing. The strength of a solder joint with a particular gap size is at a maximum, not because the peeling stress normal to the joint is reduced. But, because the location of the maximum stress concentration is changed from the ends of the joint to other areas located along the joint or possibly on the substrate. The shear strength and von- Mises results simulated in elastic and elasto-plastic regimes under the 500, 1000, and 2000 lbs applied loads are compared and shown in Figures 5.3.(23 – 24 – 25 - 26).

Figure 5.3.27 presents the average strengths simulated for solder joints with different gaps, compared to the experimental results obtained from Manko[8] and ultrasonically soldered specimens prepared in this study. The strengths simulated for the joints with different thickness and the results from Manko[8] confirm that there is an optimum joint spacing in which the joint strength is at a maximum, however, this is not matched with the experimental results found through this study. It was explained earlier that, not using a fluxing agent introduced another factor into the equation. This new factor is the total wetted area for each specimen. The wetting percentages were assumed to be 100% for the simulations. The high percentages of wetting must be the fact for the specimens prepared by Manko[8], because of using strong flux to prepare them with different spacings. Therefore, the thickness of the joint was the only variable affecting the joint strength for the simulation and the experiment results reported by Manko[8].

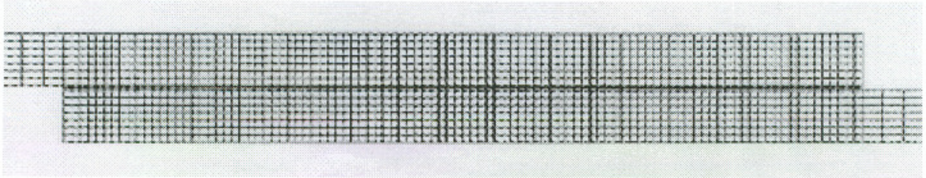

Figure 5.3.1 Two-dimensional finite element model for a single lap joint to simulate ultrasonically soldered specimens.

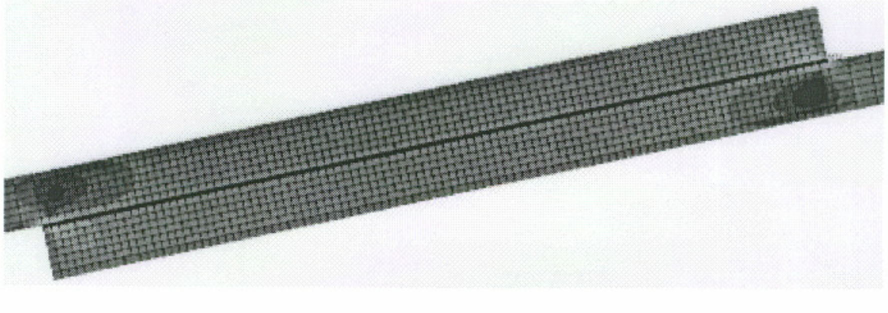

Figure 5.3.2 Stress distribution along the joint and the base material for a two-dimensional model. The joint thickness is 0.002 inches and stressed under 2000 pounds load.

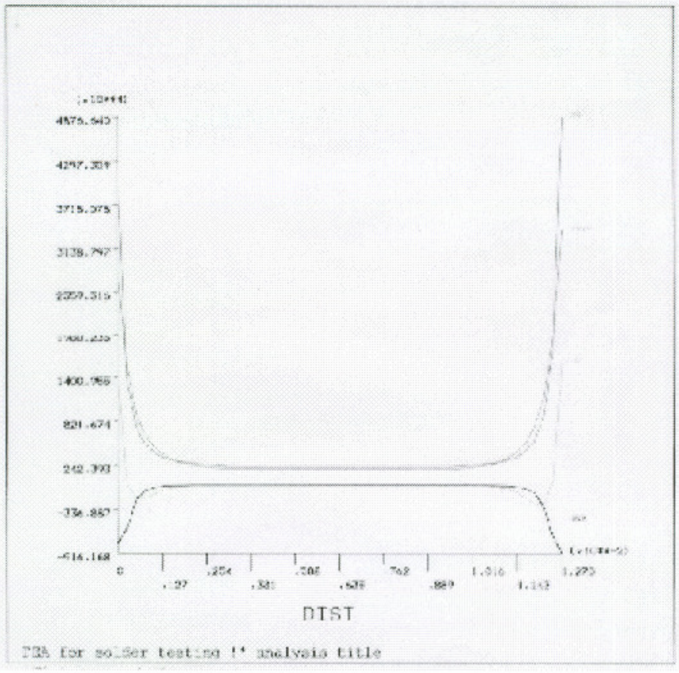

Figure 5.3.3 Plots the S_x, S_y, S_{xy}, and von Mises stress, distributed along the joint.

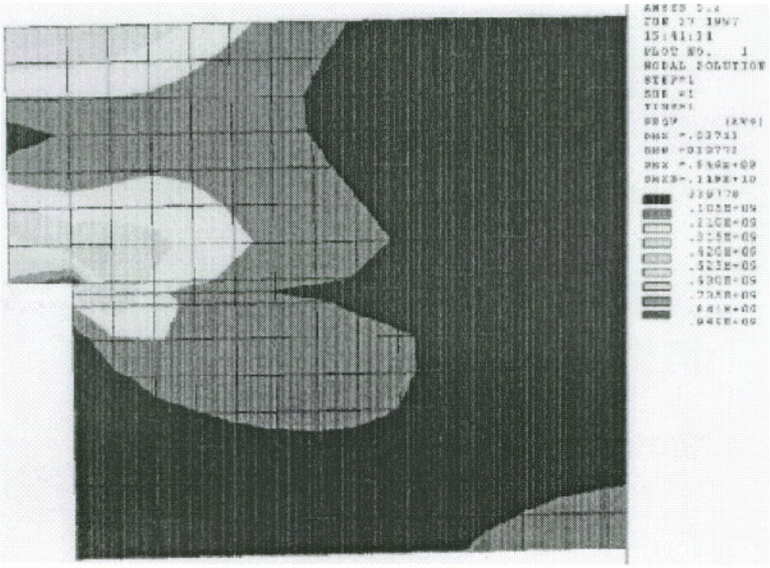

Figure 5.3.4 Stress concentration at a joint end for a two-dimensional model.

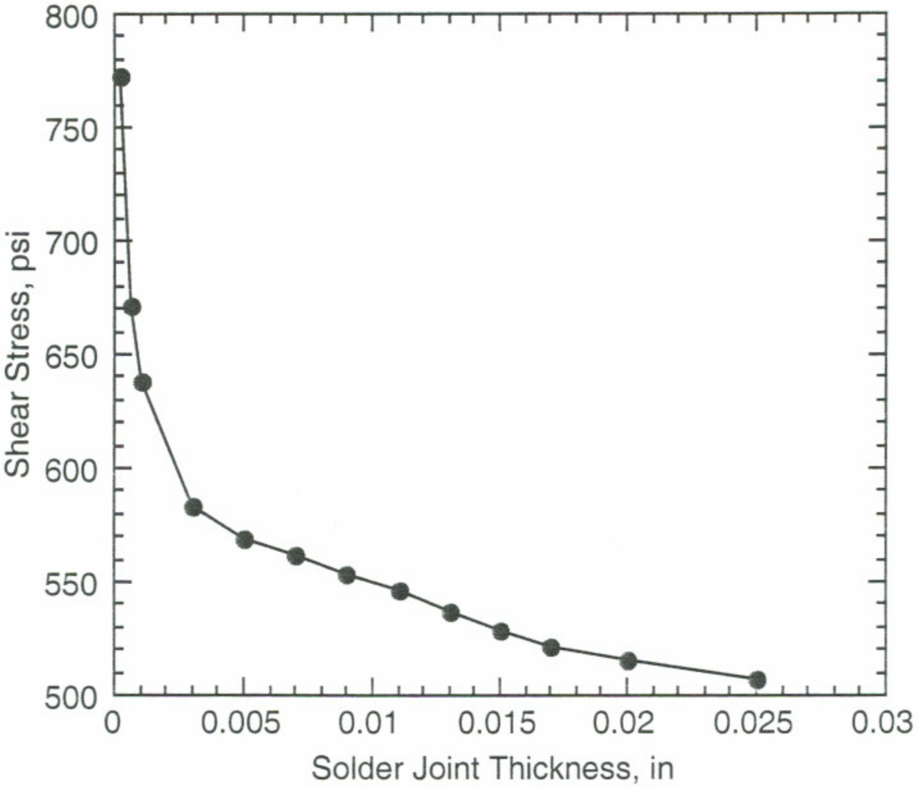

Figure 5.3.5 Maximum shear stress simulated for different joint spacings under 500 pounds applied load for a linear elastic approach.

Table 5.3.1 Maximum shear stress for different spacings.

Joint Thickness, in	Max. Shear Stress, psi
0.0002	773
0.0006	672
0.0010	638
0.0030	583
0.0050	569
0.0070	562
0.0090	554
0.0110	546
0.0130	537
0.0150	529
0.0170	522
0.0200	515
0.0250	507

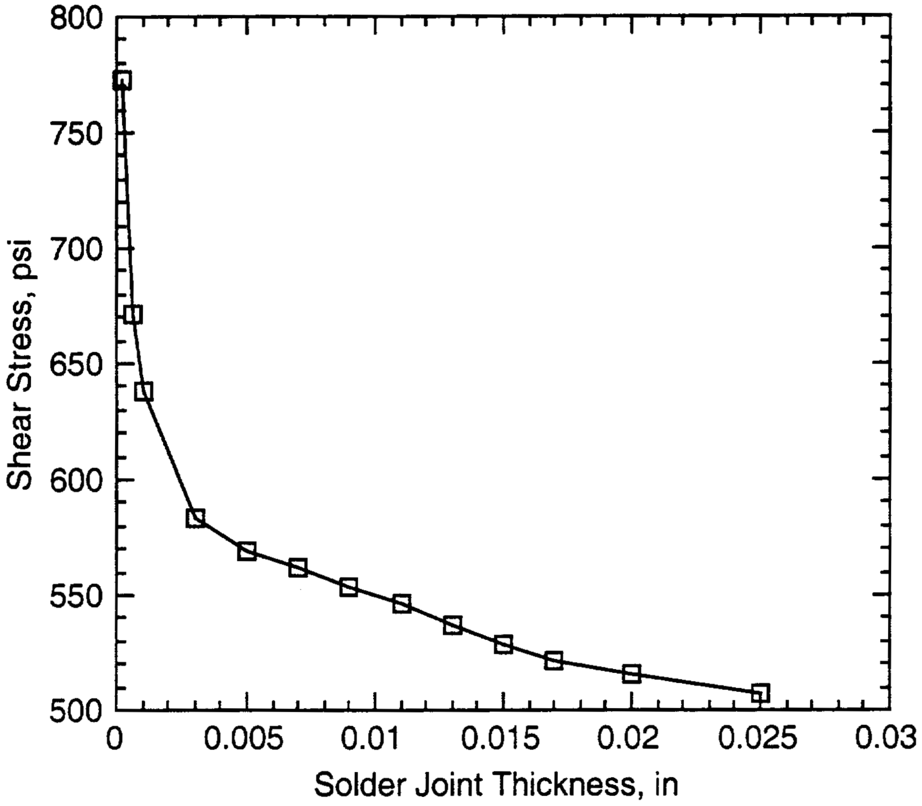

Figure 5.3.6 Maximum shear stress simulated for different joint spacings under 500 pounds applied load for a plastic approach.

Table 5.3.2 Maximum shear stress for different spacings.

Joint Thickness, in	Max. Shear stress, psi
0.0002	773
0.0006	672
0.0010	638
0.0030	583
0.0050	569
0.0070	562
0.0090	554
0.0110	546
0.0130	537
0.0150	529
0.0170	522
0.0200	515
0.0250	507

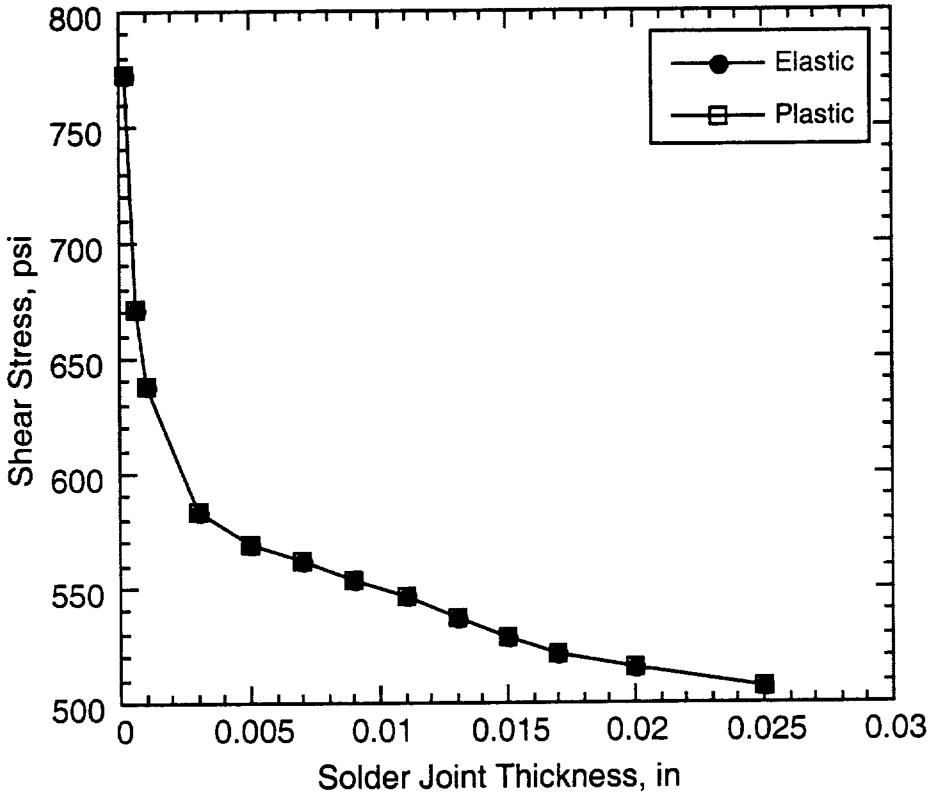

Figure 5.3.7 Maximum shear stress vs joint spacings, F=500 lbs.

Figure 5.3.3 Maximum shear stress for different spacings.

Joint Thickness, in	Max. Shear Stress, psi (Elastic)	Max. Shear Stress, psi (Plastic)
0.0002	773	773
0.0006	672	672
0.0010	638	638
0.0030	583	583
0.0050	569	569
0.0070	562	562
0.0090	554	554
0.0110	546	546
0.0130	537	537
0.0150	529	529
0.0170	522	522
0.0200	515	515
0.0250	507	507

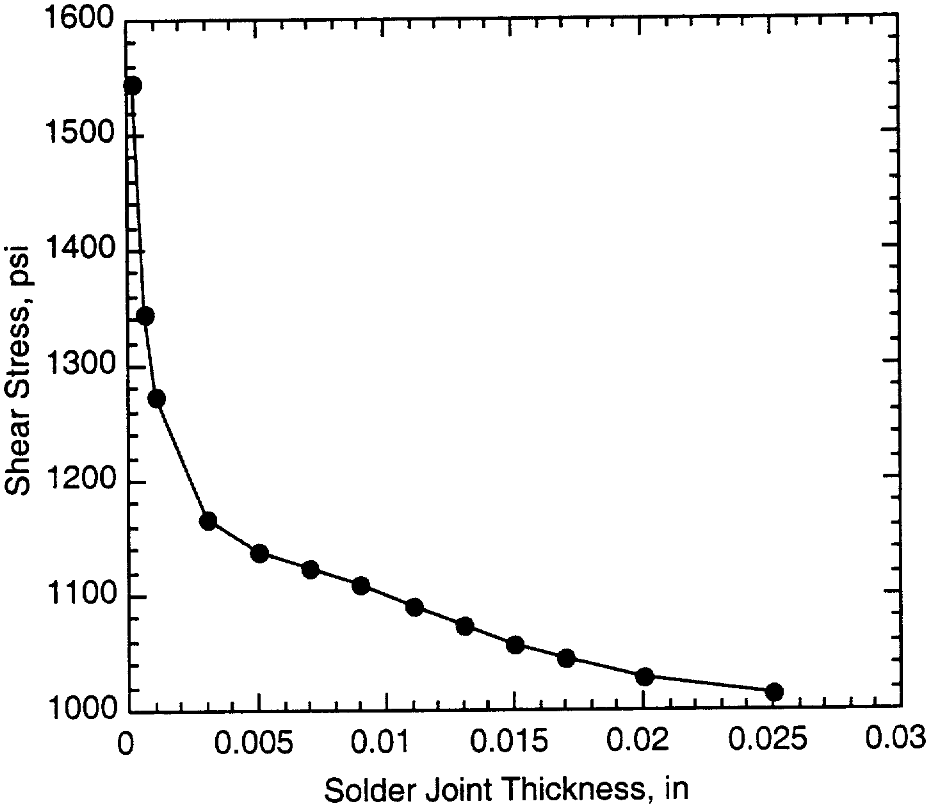

Figure 5.3.8 Maximum shear stress simulated for different joint spacings, under 1000 pounds applied load for a linear elastic approach.

Table 5.3.4 Maximum shear stress for different spacings.

Joint Thickness, in	Max. Shear Stress, psi
0.0002	1545
0.0006	1345
0.0010	1275
0.0030	1167
0.0050	1138
0.0070	1124
0.0090	1109
0.0110	1091
0.0130	1074
0.0150	1058
0.0170	1045
0.0200	1029
0.0250	1014

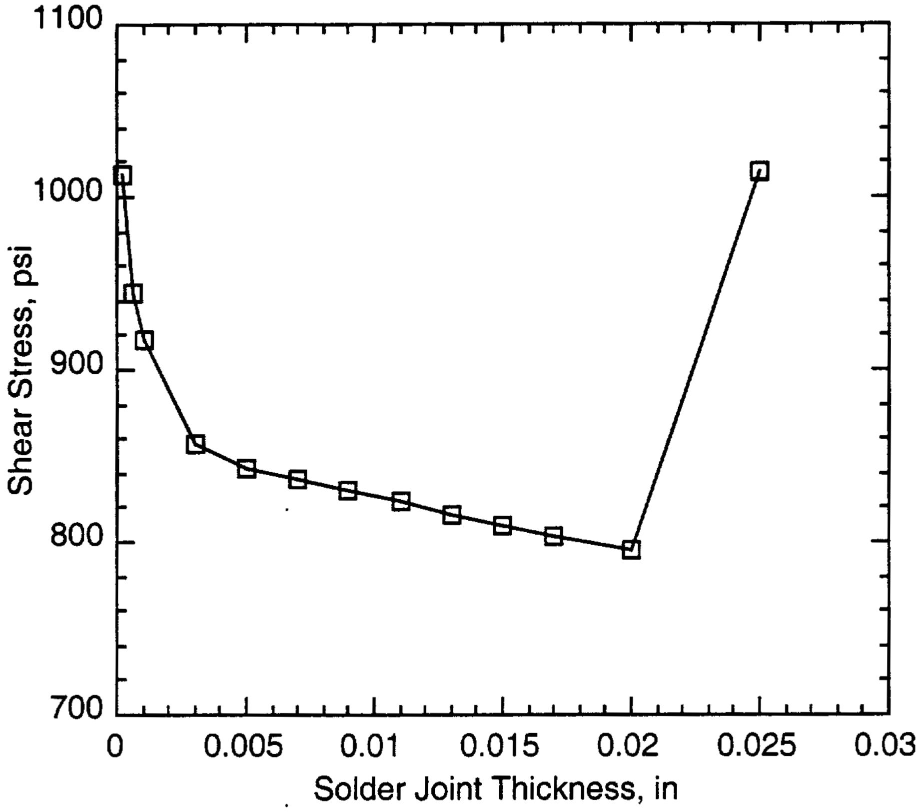

Figure 5.3.9 Maximum Shear stress simulated for different joint spacings, under 1000 pounds applied load for a plastic approach.

Table 5.3.5 Maximum shear stress for different spacings.

Joint Thickness, in	Max. Shear Stress, psi
0.0002	1013
0.0006	945
0.0010	917
0.0030	857
0.0050	843
0.0070	837
0.0090	830
0.0110	824
0.0130	816
0.0150	809
0.0170	803
0.0200	796
0.0250	1014

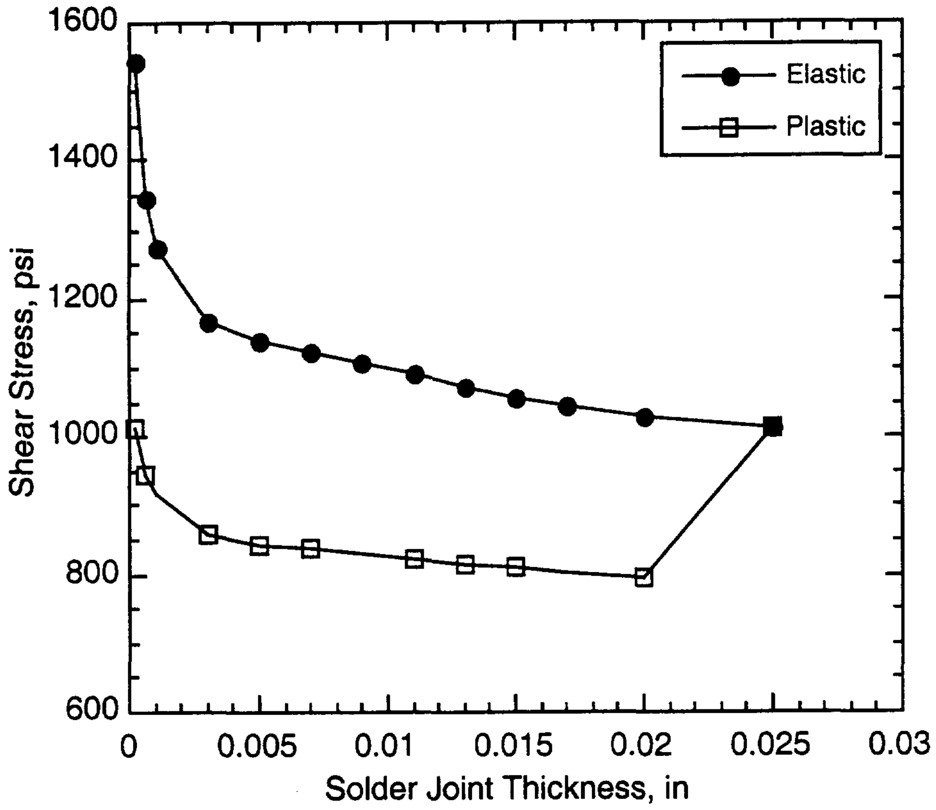

Figure 5.3.10 Maximum shear stress vs joint spacing, F=1000 lbs.

Table 5.3.6 Maximum shear stress for different spacings.

Joint Thickness, in	Max. Shear Stress, psi (Elastic)	Max. Shear Stress, psi (Plastic)
0.0002	1545	1013
0.0006	1345	945
0.0010	1275	917
0.0030	1167	857
0.0050	1138	843
0.0070	1124	837
0.0090	1109	830
0.0110	1091	824
0.0130	1074	816
0.0150	1058	809
0.0170	1045	803
0.0200	1029	796
0.0250	1014	1014

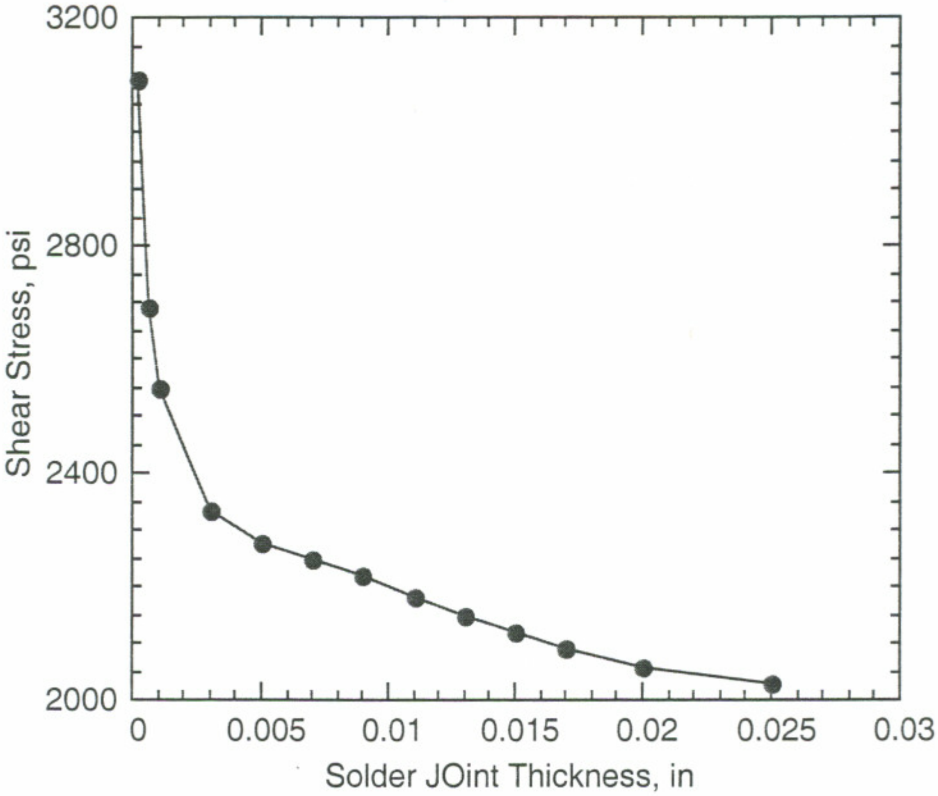

Figure 5.3.11 Maximum shear stress simulated for different joint spacings, under 2000 pounds applied load for a linear elastic approach.

Table 5.3.7 Maximum shear stress for different spacings.

Joint Thickness, in	Max. Shear Stress, psi
0.0002	3090
0.0006	2690
0.0010	2550
0.0030	2333
0.0050	2277
0.0070	2249
0.0090	2218
0.0110	2183
0.0130	2149
0.0150	2117
0.0170	2090
0.0200	2058
0.0250	2028

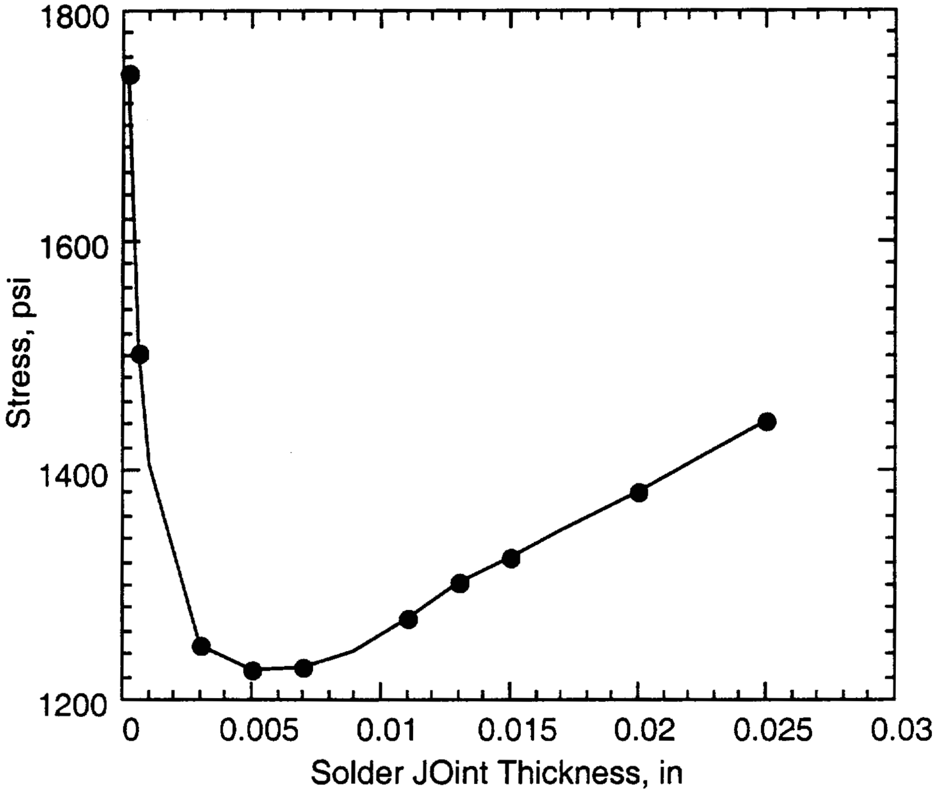

Figure 5.3.12 Maximum shear stress simulated for different joint spacings, under 2000 pounds applied load for a plastic approach.

Table 5.3.8 Maximum shear stress for different spacings.

Joint Thickness, in	Max. Shear Stress, psi
0.0002	1746
0.0006	1503
0.0010	1405
0.0030	1248
0.0050	1227
0.0070	1228
0.0090	1244
0.0110	1272
0.0130	1302
0.0150	1324
0.0170	1347
0.0200	1381
0.0250	1443

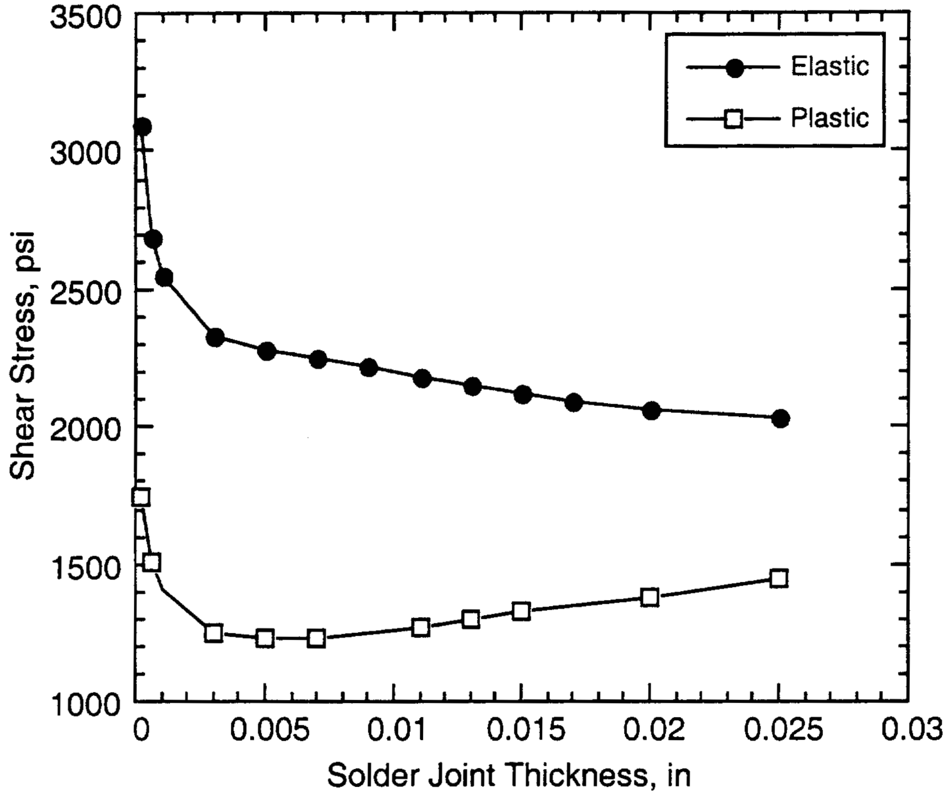

Figure 5.3.13 Maximum shear stress vs joint spacings, F=2000 lbs.

Table 5.3.9 Maximum shear stress for different spacings.

Joint Thickness, in	Max. Shear Stress, psi (Elastic)	Max. Shear Stress, psi (Plastic)
0.0002	3090	1746
0.0006	2690	1503
0.0010	2550	1405
0.0030	2333	1248
0.0050	2277	1227
0.0070	2249	1228
0.0090	2218	1244
0.0110	2183	1272
0.0130	2149	1302
0.0150	2117	1324
0.0170	2090	1347
0.0200	2058	1381
0.0250	2028	1443

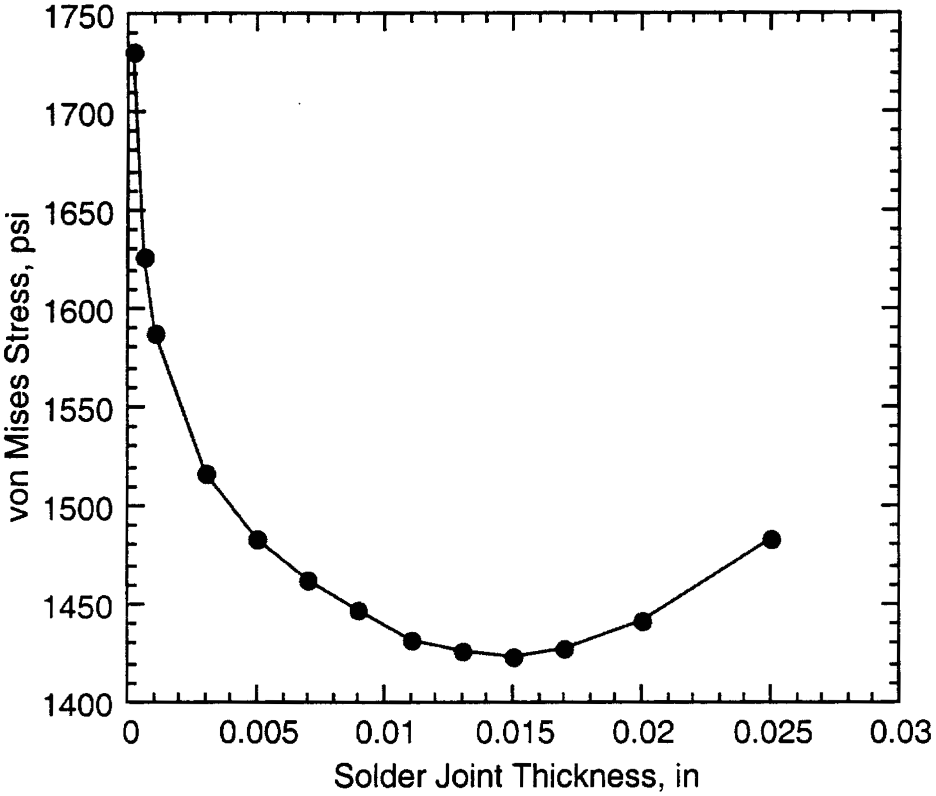

Figure 5.3.14 Maximum von Mises stress simulated for different joint spacings, under 500 pounds applied load for a linear elastic approach.

Table 5.3.10 Maximum von Mises stress for different spacings.

Joint Thickness, in	Max. von Mises Stress, psi
0.0002	1731
0.0006	1627
0.0010	1588
0.0030	1517
0.0050	1484
0.0070	1462
0.0090	1448
0.0110	1432
0.0130	1426
0.0150	1424
0.0170	1428
0.0200	1442
0.0250	1483

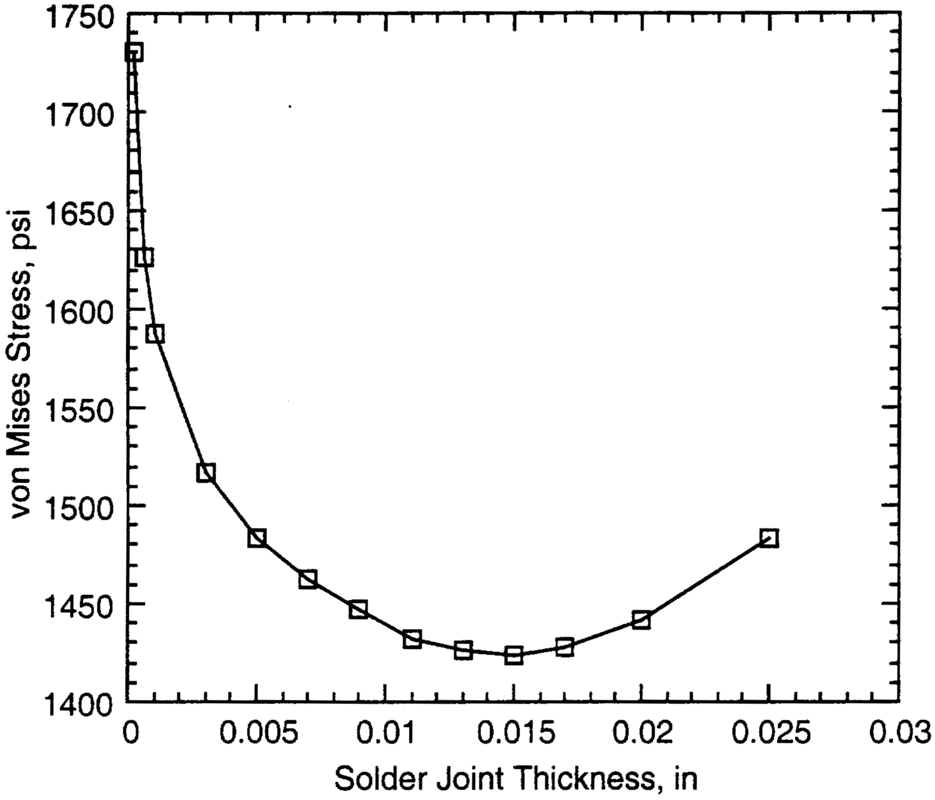

Figure 5.3.15 Maximum von Mises stress simulated for different joint spacings, under 500 pounds applied load for a plastic approach.

Table 5.3.11 Maximum von Mises stress for different spacings.

Joint Thickness, in	**Max. von Mises Stress, psi**
0.0002	1731
0.0006	1627
0.0010	1588
0.0030	1517
0.0050	1484
0.0070	1462
0.0090	1448
0.0110	1432
0.0130	1426
0.0150	1424
0.0170	1428
0.0200	1442
0.0250	1483

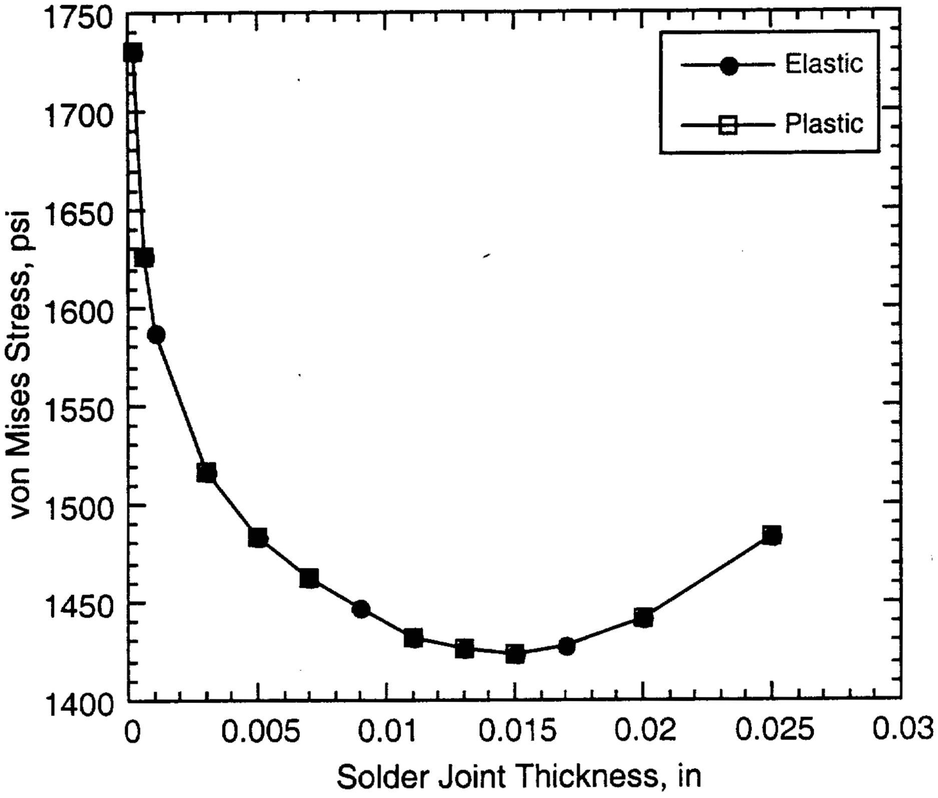

Figure 5.3.16 Maximum von Mises stress vs joint spacings, F=500 lbs.

Table 5.3.12 Maximum von Mises stress for different spacings.

Joint Thickness, in	Max. von Mises Stress,psi (Elastic)	Max. von Mises stress, psi (Plastic)
0.0002	1731	1731
0.0006	1627	1627
0.0010	1588	1588
0.0030	1517	1517
0.0050	1484	1484
0.0070	1462	1462
0.0090	1448	1448
0.0110	1432	1432
0.0130	1426	1426
0.0150	1424	1424
0.0170	1428	1428
0.0200	1442	1442
0.0250	1483	1483

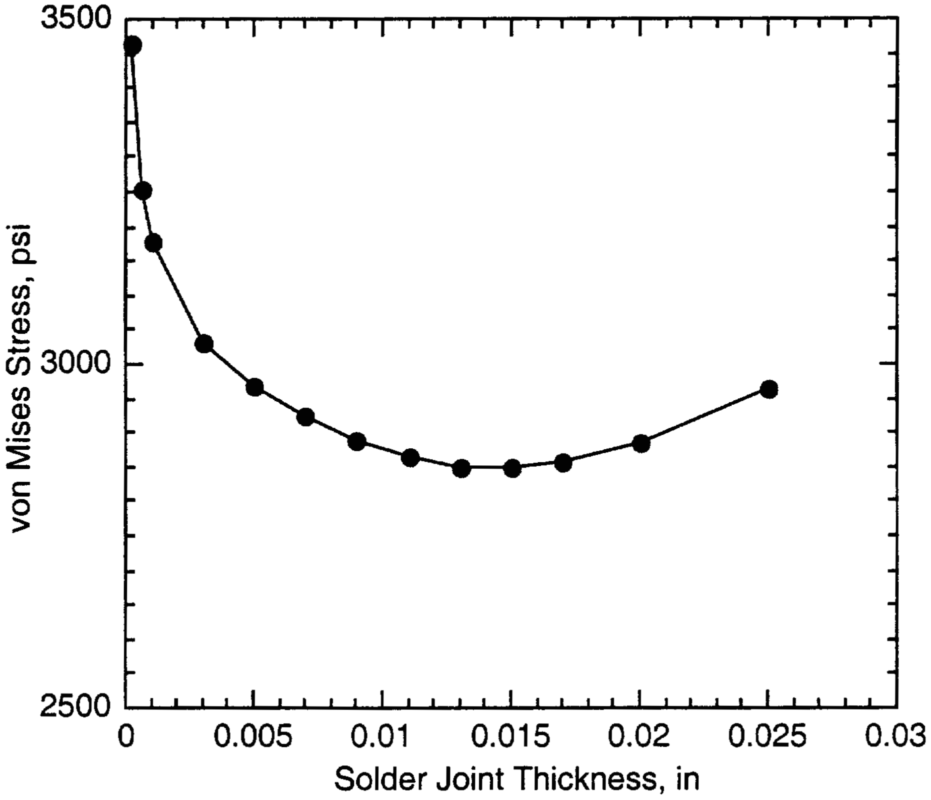

Figure 5.3.17 Maximum von Mises stress simulated for different joint spacings, under 1000 pounds applied load for a linear elastic approach.

Table 5.3.13 Maximum von Mises stress for different spacings.

Joint Thickness, in	Max. von Mises Stress, psi
0.0002	3463
0.0006	3253
0.0010	3177
0.0030	3033
0.0050	2968
0.0070	2924
0.0090	2889
0.0110	2865
0.0130	2851
0.0150	2849
0.0170	2856
0.0200	2884
0.0250	2966

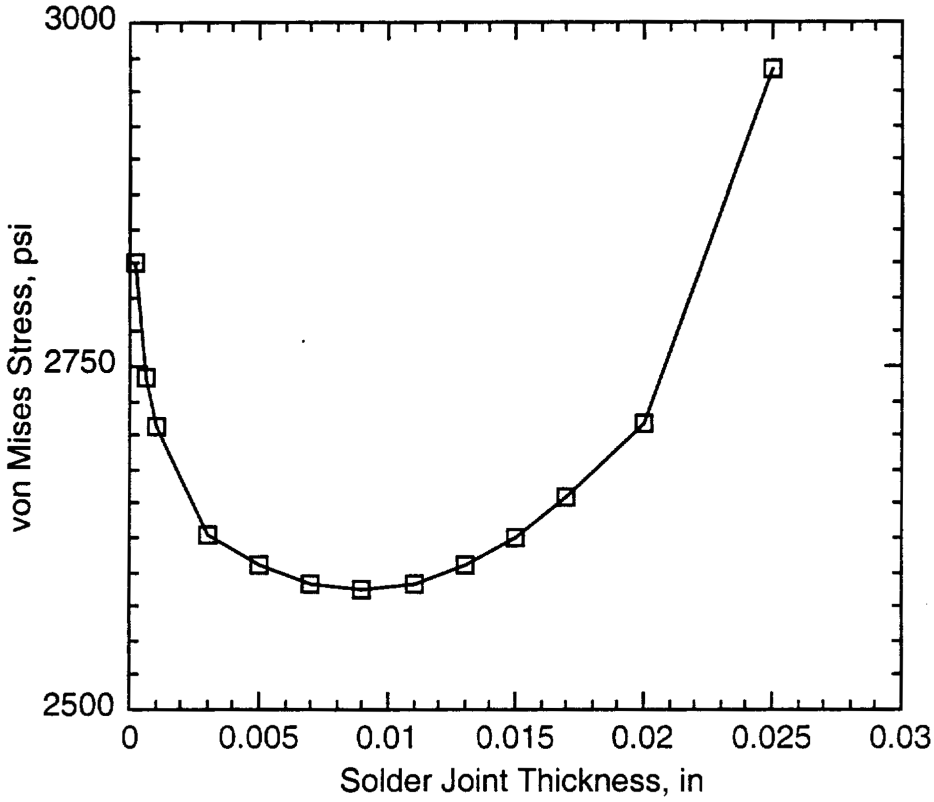

Figure 5.3.18 Maximum von Mises stress simulated for different joint spacings, under 1000 pounds applied load for a plastic approach.

Table 5.3.14 Maximum von Mises stress for different spacings.

Joint Thickness, in	Max. von Mises Stress, psi
0.0002	2826
0.0006	2742
0.0010	2706
0.0030	2628
0.0050	2605
0.0070	2592
0.0090	2588
0.0110	2592
0.0130	2605
0.0150	2626
0.0170	2655
0.0200	2709
0.0250	2966

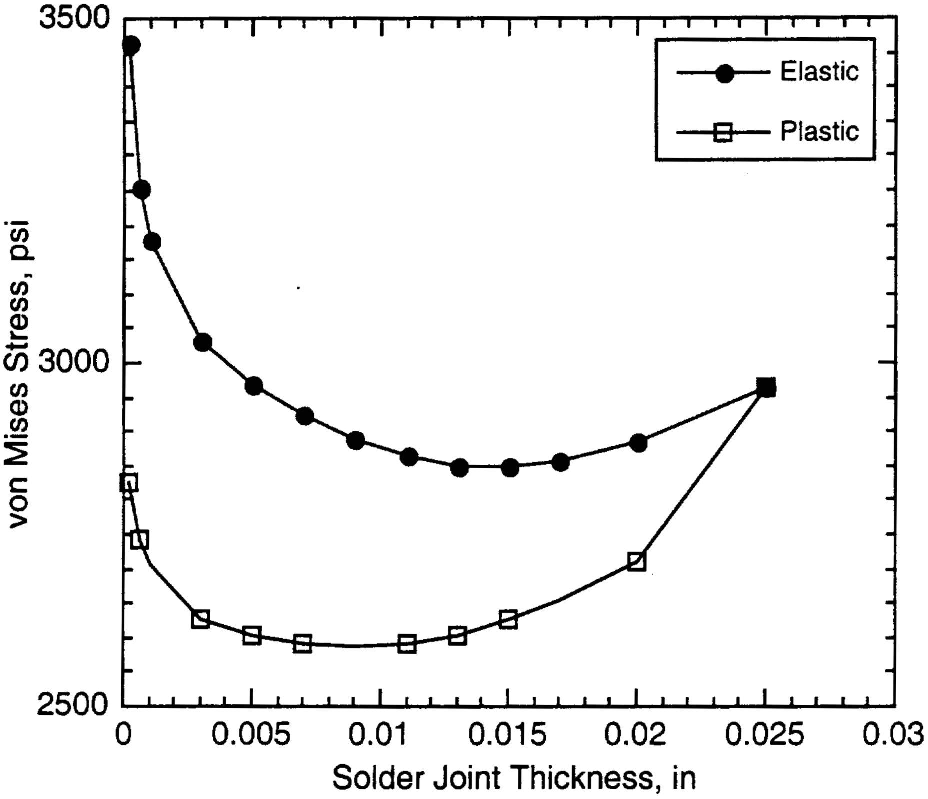

Figure 5.3.19 Maximum von Mises stress vs joint spacings, F=1000 lbs.

Table 5.3.15 Maximum von Mises stress for different spacings.

Joint Thickness, in	Max. von Mises Stress, psi (Elastic)	Max. von Mises Stress, psi (Plastic)
0.0002	3463	2826
0.0006	3253	2742
0.0010	3117	2706
0.0030	3033	2628
0.0050	2968	2605
0.0070	2924	2592
0.0090	2889	2588
0.0110	2865	2592
0.0130	2851	2605
0.0150	2849	2626
0.0170	2856	2655
0.0200	2884	2709
0.0250	2966	2966

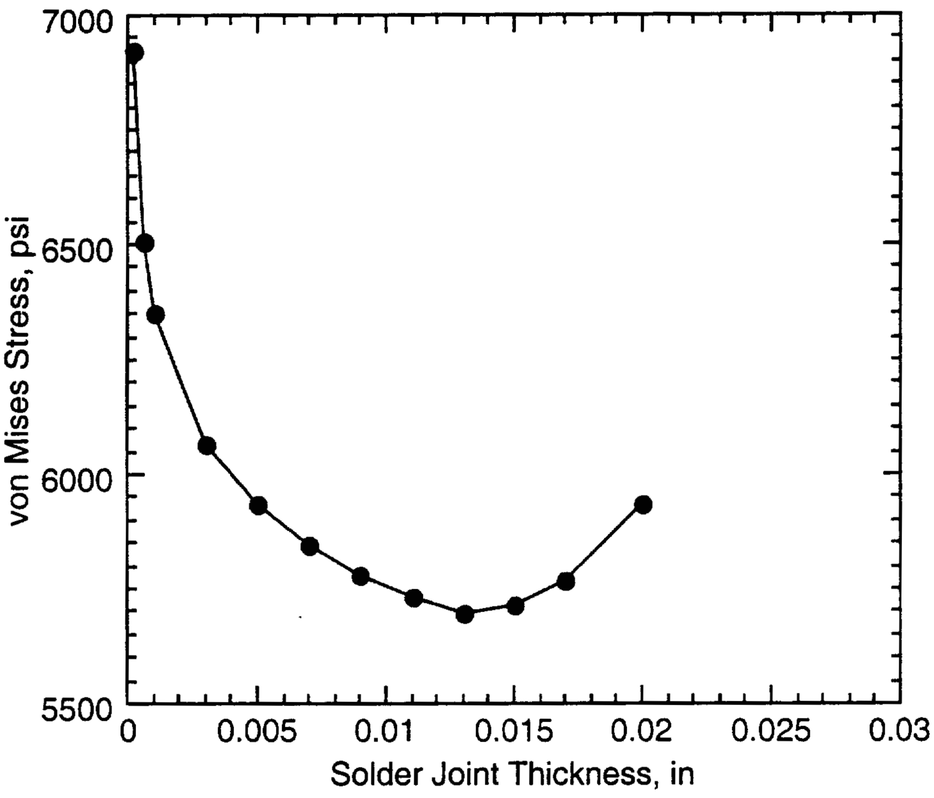

Figure 5.3.20 Maximum von Mises stress simulated for different joint spacings, under 2000 pounds applied load for a linear elastic approach.

Table 5.3.16 Maximum von Mises stress for different spacings.

Joint Thickness, in	Max. von Mises Stress, psi
0.0002	6925
0.0006	6506
0.0010	6353
0.0030	6067
0.0050	5936
0.0070	5848
0.0090	5779
0.0110	5730
0.0130	5730
0.0150	5697
0.0170	5712
0.0200	5768
0.0250	5932

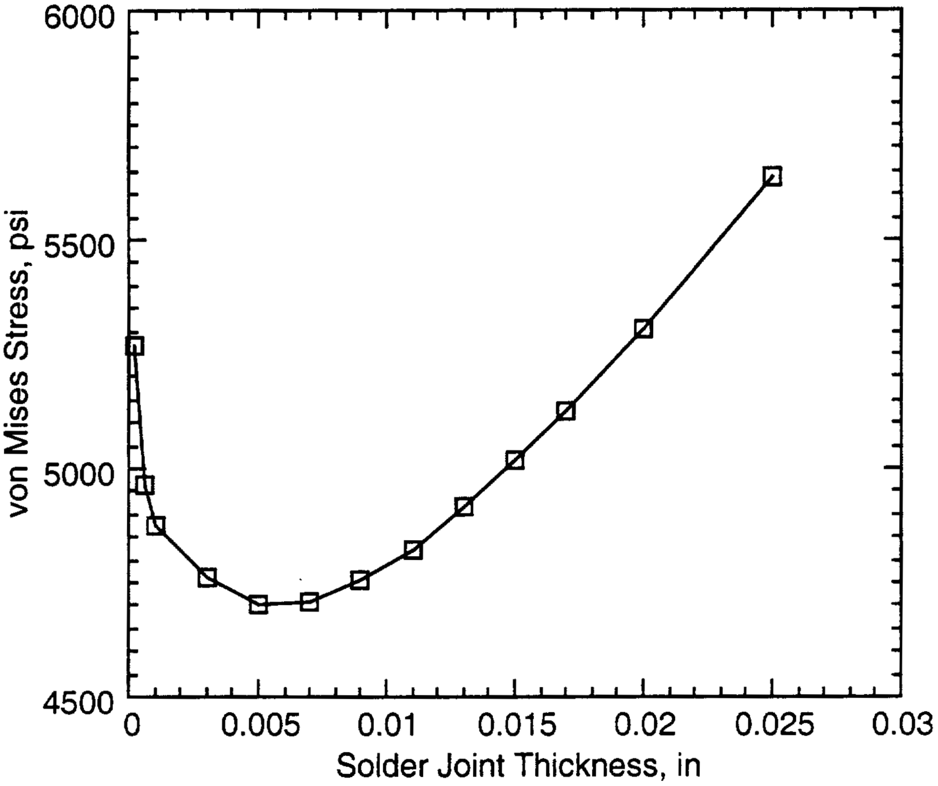

Figure 5.3.21 Maximum von Mises stress simulated for different joint spacings, under 2000 pounds applied load for a plastic approach.

Figure 5.3.17 Maximum von Mises stress for different spacings.

Joint Thickness, in	Max. von Mises Stress, psi
0.0002	5270
0.0006	4964
0.0010	4876
0.0030	4762
0.0050	4700
0.0070	4708
0.0090	4755
0.0110	4824
0.0130	4916
0.0150	5016
0.0170	5128
0.0200	5306
0.0250	5635

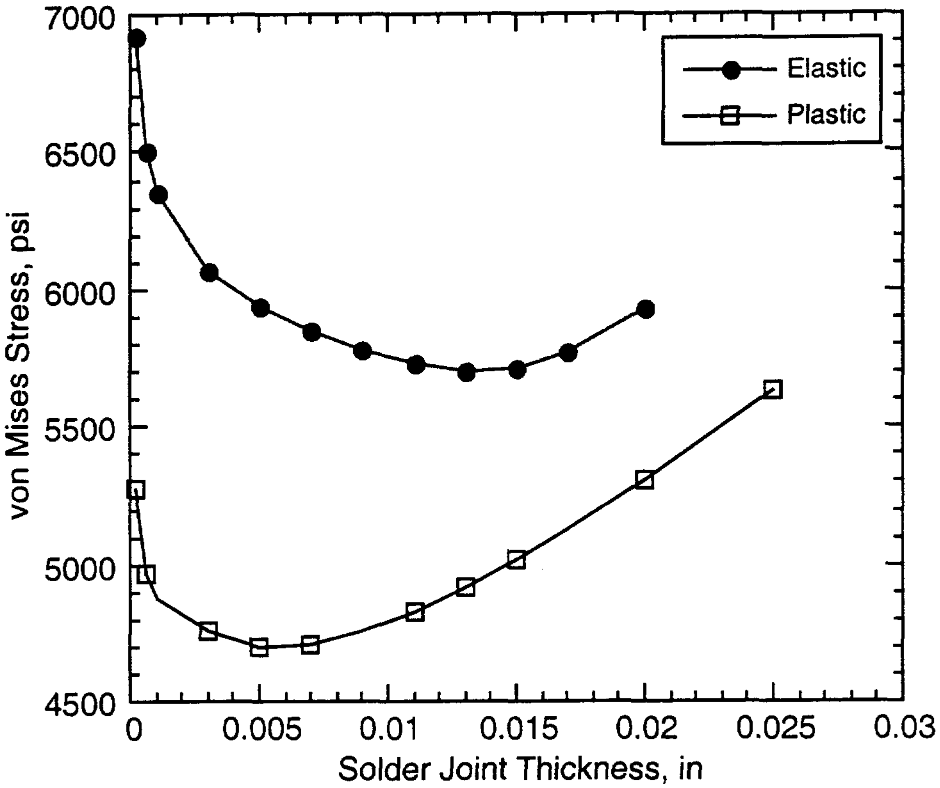

Figure 5.3.22 Maximum von Mises stress vs joint spacings, F=2000 lbs.

Table 5.3.18 Maximum von Mises stress for different spacings.

Joint Thickness, in	Max. von Mises Stress, psi (Elastic)	Max. von Mises Stress, psi (Plastic)
0.0002	6925	5270
0.0006	6506	4964
0.0010	6353	4876
0.0030	6067	4762
0.0050	5936	4700
0.0070	5848	4708
0.090	5779	4755
0.0110	5730	4824
0.0130	5730	4916
0.0150	5697	5016
0.0170	5712	5128
0.0200	5768	5306
0.0250	5932	5635

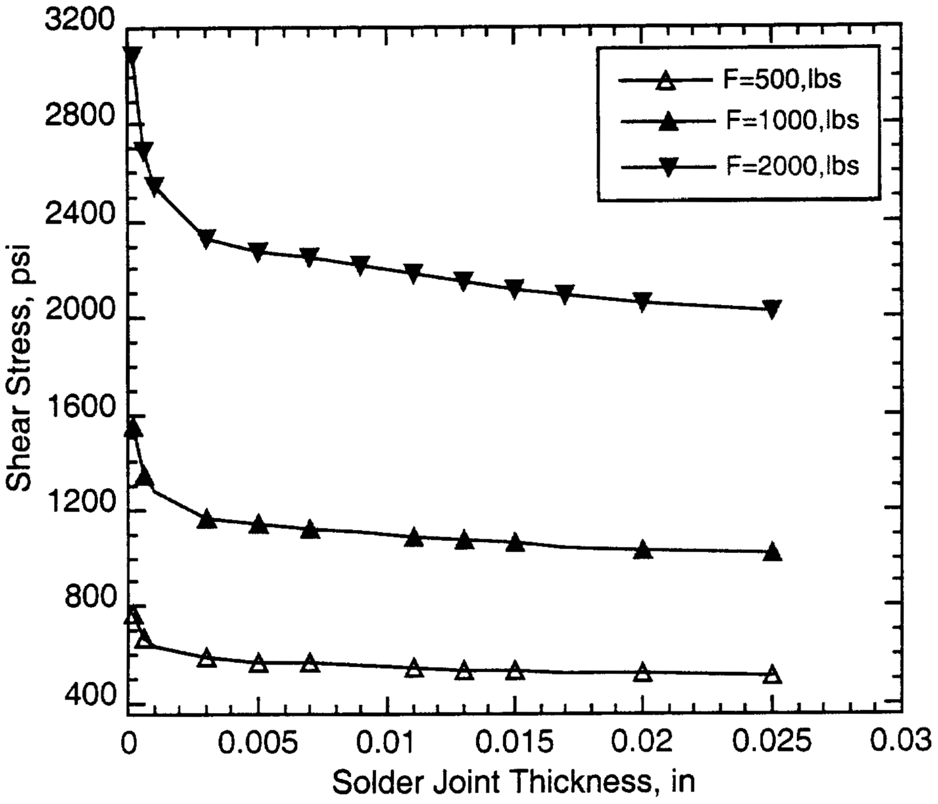

Figure 5.3.23 Maximum shear stress simulated vs joint gap for the linear elastic approaches. Applied loads; 500, 1000 and 2000 lbs.

Table 5.3.19 Maximum shear stress for different spacings.

Joint Thickness, in	**Max. Shear Stress, psi (F=500 lbs)**	**Max. Shear Stress, psi (F=1000 lbs)**	**Max. Shear Stress, psi (F=2000 lbs)**
0.0002	773	1545	3090
0.0006	672	1345	2690
0.0010	638	1275	2550
0.0030	583	1167	2333
0.0050	569	1138	2277
0.0070	562	1124	2249
0.0090	554	1109	2218
0.0110	546	1091	2183
0.0130	537	1074	2149
0.0150	529	1058	2117
0.0170	522	1045	2090
0.0200	515	1029	2058
0.0250	507	1014	2028

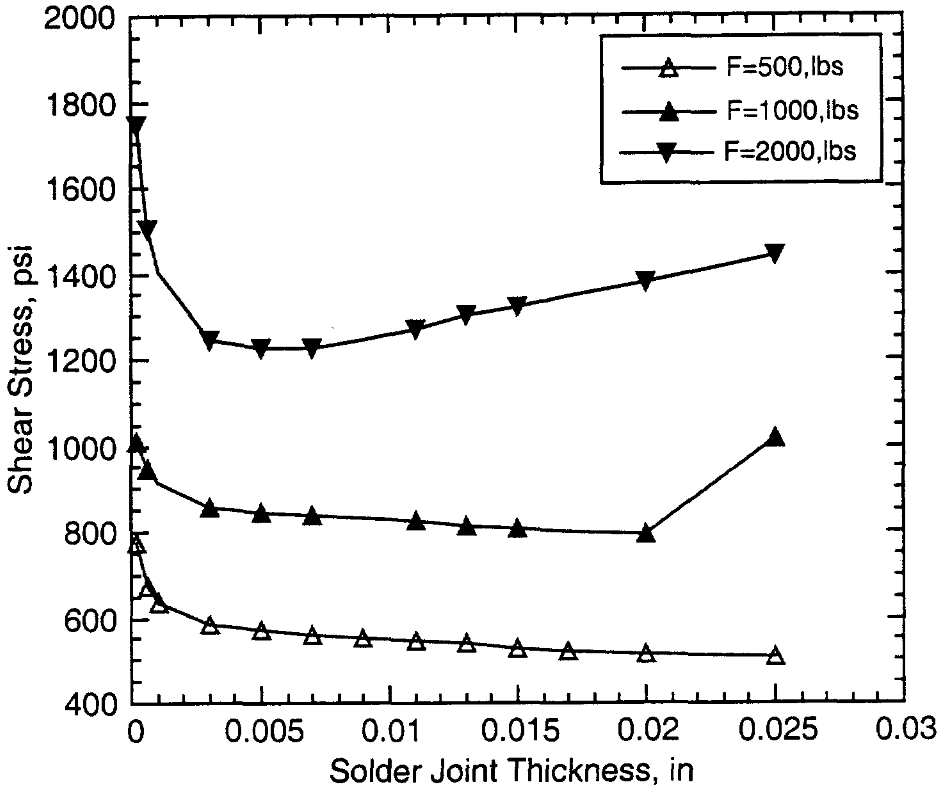

Figure 5.3.24 Maximum shear stress simulated vs joint gap for the plastic approaches. Applied loads; 500, 1000, 2000 lbs.

Table 5.3.20 Maximum shear stress for different spacings.

Joint thickness, in	**Max. Shear Stress, psi (F=500 lbs)**	**Max. Shear Stress, psi (F=1000 lbs)**	**Max. Shear Stress, psi (F=2000 lbs)**
0.0002	773	1013	1746
0.0006	672	945	1503
0.0010	638	917	1405
0.0030	583	857	1248
0.0050	569	843	1227
0.0070	562	837	1228
0.0090	554	830	1244
0.0110	546	824	1272
0.0130	537	816	1302
0.0150	529	809	1324
0.0170	522	803	1347
0.0200	515	796	1381
0.0250	507	1014	1443

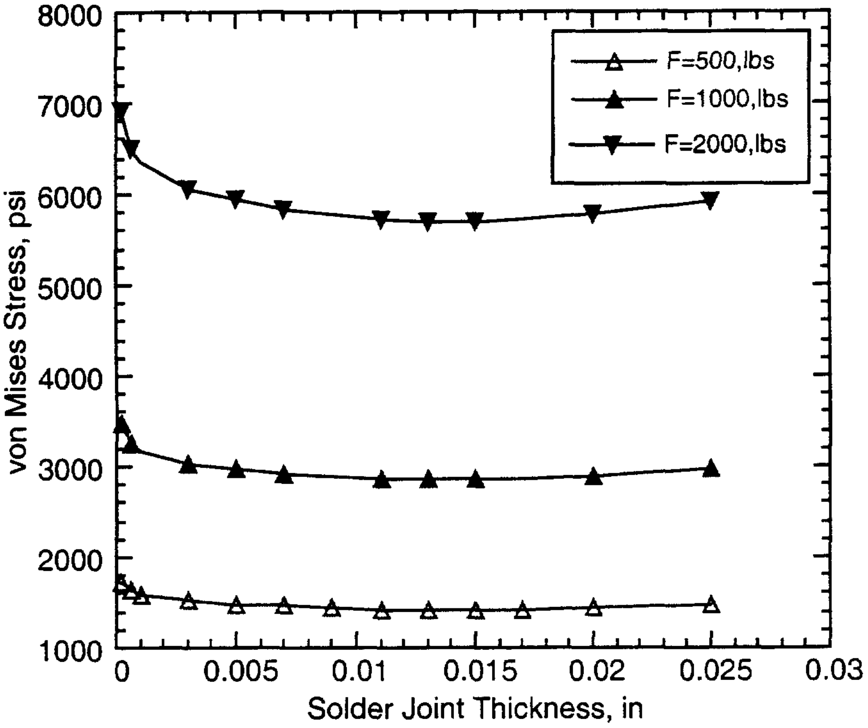

Figure 5.3.25 Maximum von Mises stress simulated vs joint gap for the linear elastic approaches. Applied loads; 500, 1000 and 2000 lbs.

Table 5.3.21 Maximum von Mises stress for different spacings.

Joint Thickness, in	**Max. von Mises Stress, psi (F=500 lbs)**	**Max. von Mises stress, psi (F=1000 lbs)**	**Max. von Mises Stress, psi (F=2000)**
0.0002	1731	3463	6925
0.0006	1627	3253	6506
0.0010	1588	3177	6353
0.0030	1517	3033	6067
0.0050	1484	2968	5936
0.0070	1462	2924	5848
0.0090	1448	2889	5779
0.0110	1432	2865	5730
0.0130	1426	2851	5703
0.0150	1424	2849	5697
0.0170	1428	2856	5712
0.0200	1442	2884	5768
0.0250	1483	2966	5932

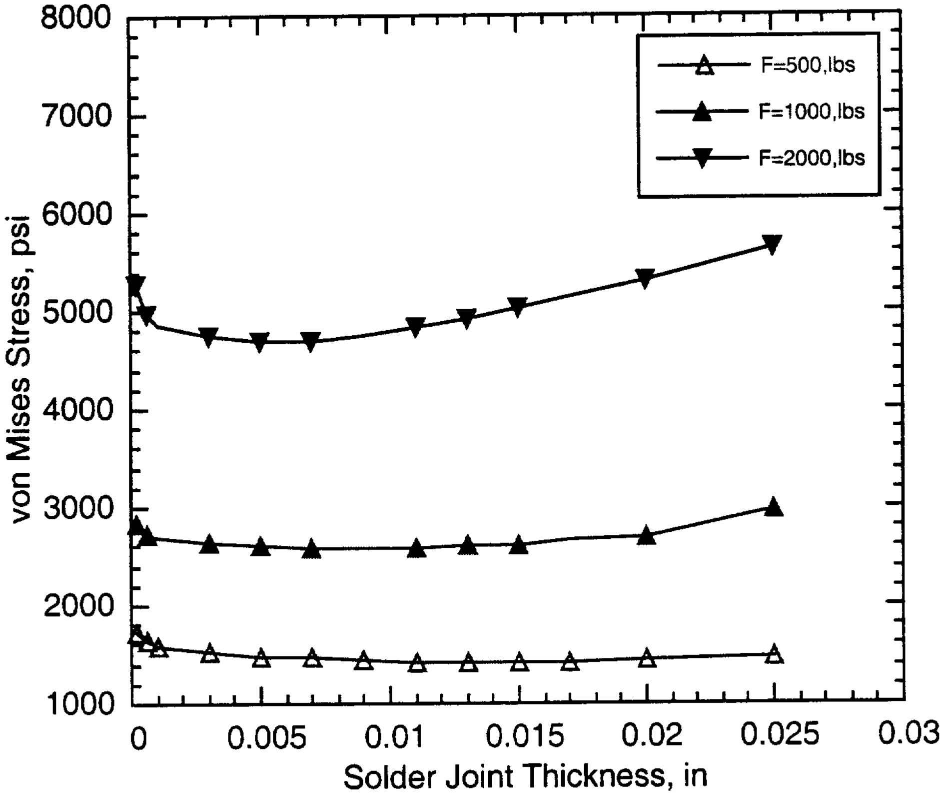

Figure 5.3.26 Maximum von Mises stress simulated vs joint gap for the plastic approaches. Applied loads; 500, 1000 and 2000 lbs.

Table 5.3.22 Maximum von Mises stress for different spacings.

Joint Thickness, in	**Max. von Mises Stress, psi (F=500 lbs)**	**Max. von Mises stress, psi (F=1000 lbs)**	**Max. von Mises Stress, psi (F=2000 lbs)**
0.0002	1731	2826	5270
0.0006	1627	2724	4964
0.0010	1588	2706	4876
0.0030	1517	2628	4762
0.0050	1484	2605	4700
0.0070	1462	2592	4708
0.0090	1448	2588	4755
0.0110	1432	2592	4824
0.0130	1426	2605	4916
0.0150	1424	2626	5016
0.0170	1428	2655	5128
0.0200	1442	2709	5306
0.0250	1483	2966	5635

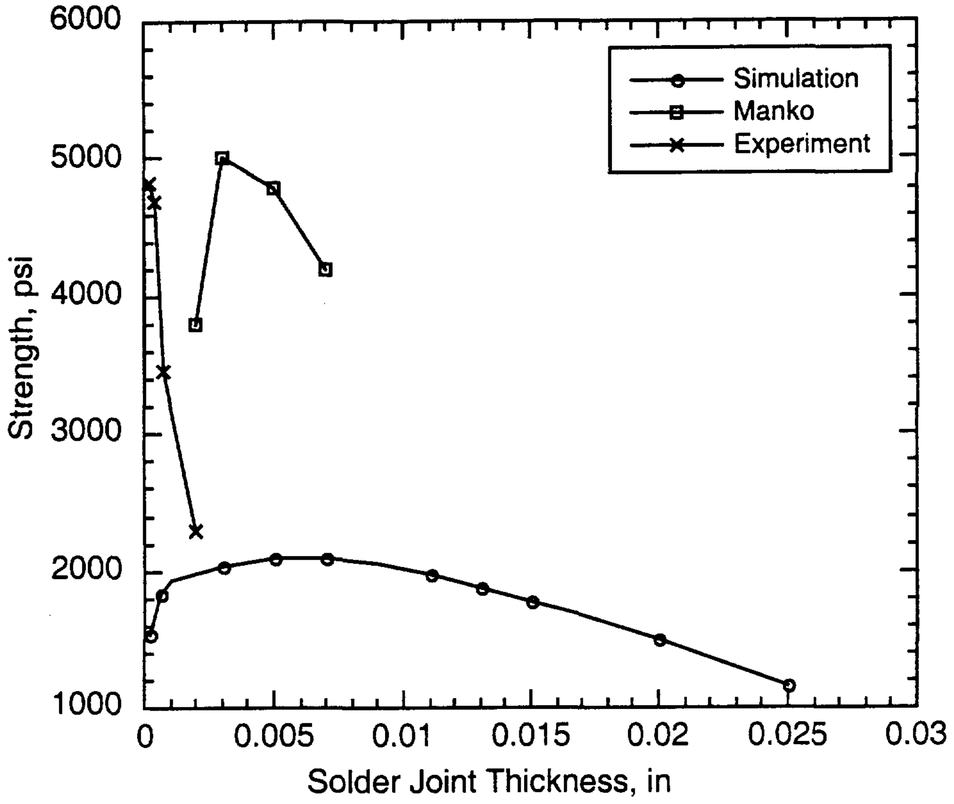

Figure 5.3.27 Average strength simulated for the solder joints vs joint spacings, compare with the experimental results.

Figure 5.3.23 Strength of the joints for different spacings.

Joint Thickness, in	Average von Mises Strength , psi (Simulated)	Shear Strength, psi (Manko)	Shear Strength, psi (Experiment)
0.0002	1530		4832
0.0004			4696
0.0006	1836		
0.0007			3470
0.0010	1924		
0.0020		3800	2300
0.0030	2038	5000	
0.0050	2100	4800	
0.0070	2092	4200	
0.0090	2045		
0.0110	1976		
0.0130	1884		
0.0150	1784		
0.0170	1672		
0.0200	1492		
0.0250	1165		

Chapter 6

Discussion

The strength of an ultrasonically soldered joint is always a useful value to determine in order to predict the joint's reliability and durability in service. As with any soldering process, there are some essential factors such as; substrate surface condition, soldering temperature, ultrasonic soldering time and shielding environment that affect the mechanical properties of the solder joint and its integrity. These factors were the major variables in this study to prepare different specimens for shear testing. The first and foremost factor is the substrate surface condition. Any contamination or oxide film (corrosion products) existence or formation on the substrate surface will strictly deteriorate the solder joint properties and its predicted lifetime. The results throughout this study showed that the substrate surface must be clean, deoxidized and the soldering operation should be performed in a neutral environment.

For both aluminum and stainless steel specimens, the overall results indicate that the ultrasonic solderability of the substrate materials and the quality of the joints improve when the substrate surfaces are properly cleaned and degreased by washing in solvent and air drying. This is a simple and efficient method to degrease the parts to be soldered without damaging the surface. Using ultrasonic vibration is also a fast and reliable method of cleaning (degreasing) the specimens to be soldered. Experimental results through out this study showed that, the ultrasonic cleaning operations must be optimized. Because the process depends on the intensity of the applied sonic energy, type of the cleaning solution (water, alcohol, etc.), the bath temperature and the operation time and the substrate surface can be damaged if a proper procedure is not followed.

For the aluminum specimens, the shear test results indicate that the strength of a solder joint depends strongly on its surface condition. The solder joints of deoxidized surfaces (chemically cleaned specimens which were ultrasonically soldered at different temperatures and times) showed the highest strengths as presented in Figures (4.1.4) and (4.1.8). These results confirm that a metallic surface exposed by chemical cleaning in NaOH has strong tendency to be wetted by the molten solder. Although a thin oxide film formed rapidly on the surface after deoxidization, the sonic energy was able to break it off from the surface to demonstrate a clean metallic surface against the molten solder. This is also true for the ultrasonically cleaned (degreased) specimens. However, during the soldering of degreased samples, the ultrasonic vibrations were not able to break the oxide films completely and the oxide layers remained intact on some parts of the substrate surface. These remaining oxide films prevented the molten solder to contact the metallic surfaces and the results were poor wetting and low shear strength as shown in Figures (4.1.1) and (4.1.5).

For the tin plated specimens, the strengths of the joints are acceptable for the specimens prepared at lower soldering temperatures but not acceptable for higher temperatures. This is an indication that a metallic surface can be protected from oxidation during a soldering process by tin-plating. But at higher soldering temperatures, the molten tin layers are oxidized themselves, showing poor wetting and much lower strength as illustrated in Figures (4.1.2) and (4.1.3). Similar test results, performed under an argon shielding environment, presented in Figures (4.1.10) and (4.1.11), show an increase in strength as soldering temperature increases. The results suggest that the tin-plated specimens were greatly tarnished at higher temperatures in a non-shielded environment. The plotted shear strength results shown in Figures (4.1.6) and (4.1.7) also show that a plated tin layer can protect the substrate surface only at lower soldering temperatures and soldering times. The work performed by Manko[8] on tin-plated copper and brass specimens demonstrate that the joint shear strength decreases for the solder joints prepared at higher temperatures with fixed joint thickness even in the presence of a strong fluxing agent. He suggested that, this was caused by the higher degree of tarnishing at elevated temperatures.

The overall shear strength results throughout this study showed that the ultrasonic soldering temperature has a great influence on the joint strength. This is because the viscosity of molten solder will decrease exponentially as the soldering temperature increases. Equation (6.1) shows that the viscosity is inversely proportional to the temperature[125]. A reduction in the viscosity will affect the spreading of the molten solder on the substrate surface and improves the wettability to accomplish a stronger joint. As illustrated in Figure (4.1.18), in the absence of an oxide film, the strength of a joint will increase if the soldering temperature increases for a fixed soldering time. Equation (6.1) shows that the viscosity changes exponentially if the temperature changes.

$$\eta \propto \exp E_\eta / RT \qquad (6.1)$$

where: $\eta$is the viscosity, E_η is the activation energy, R is the universal constant, and T is the temperature in Kelvin.

Soldering time also showed a dominant influence on the joint strength, as presented in Figures (4.1.19) and (4.1.20). At a constant soldering temperature, the joint strength increases when the soldering time increases. This is mainly because, the longer the sonic energy applied, the greater is the cavitation effects on the substrate surface. Ultrasonic soldering technique is an alternative to flux. In this method, the mechanical vibration caused the oxide film to break down and creates a metallic surface against the molten solder. The ultrasonic energy in the form of sound waves forces the liquid filler metal to cavitate. This cavitation action as the result of collapsing bubbles on the substrate surface erodes the surface preferentially at the bubble wall. Therefore, increasing the soldering time increases the effectiveness of cavitation, which is strictly related to the number of bubbles formed in the molten solder and subsequently collapsed on the substrate surface.

A shielding argon environment is proved to be effective in protecting the specimens and also the molten solder from oxidation. The results of the shear tests for the 2024 Alclad specimens, which were ultrasonically soldered at different temperatures and for different times as shown in Figures 4.1.(21 to 28), confirm that the argon shielding was effective in protecting the specimens from further oxidation resulting in strengthened joints.

For the stainless steel specimens, which were ultrasonically soldered with and without adding filler metal, the shear test results showed that the protective tin layers on the substrate surfaces were also oxidized at elevated temperatures. Formation and growth of the tin oxide layer at the joint interfaces during the ultrasonic operation will affect the wetting and decreases the joint strength as presented in Figures (4.1.29) and (4.1.30). A shielding environment such as argon will improve the soldering condition, especially at elevated temperatures and protects the tin layer from oxidation. Figures (4.1.33) and (4.1.34) show the effect of argon shielding on the joint strength.

Figures (4.1.31) and (4.1.32) present the joint strengths for the tin-plated stainless steel specimens which were ultrasonically soldered at different soldering times at 230 °C. These results also confirm that the protective tin layers work well at lower soldering temperatures; and, increasing soldering time will improve the quality of the joint and its strength. Figures (4.1.33) and (4.1.34) prove again the positive role of using an argon shielding environment in a soldering operation.

The shear test results shown in Figure (4.1.38) for the degreased and chemically cleaned stainless steel specimens (ultrasonically soldered without flux) demonstrate a non-wetting condition. This is not the case for either degreased or chemically cleaned 2024 Alclad specimens. In fact, the shear strength of the solder joints for chemically cleaned Alcald samples which were ultrasonically soldered at 300 °C for 4 second or at 230 °C for 12 seconds were around 6,000 psi, which is even higher than the shear strength of the bulk 70Sn-30Pb filler metal (5,500 psi).

- For the degreased stainless steel specimens, the question is why could the ultrasonic vibration break the oxide film from the degreased aluminum substrate surfaces but not from the stainless steels. The answer to this question can be related to two different factors.
  - The mechanical properties of 304 stainless steel, such as its modulus of elasticity, are different from the 2024 Alclad alloy.
  - The thickness and adhesivity of the chromium oxide on the stainless steel substrate surface is higher than the aluminum oxide on aluminum.

The experimental observations obtained by Vianco, et al[32] showed that the effectiveness of the erosion force (cavitation action) depends as strongly upon the material properties of the bulk substrate as on the soldering operation and its surface condition. Therefore the oxide removal from the substrate surface, for generating a pristine metallic surface against the molten solder, is not due entirely to the erosive action of the ultrasonic vibrations. Rather the sonic energy that is available to the whole surface if it couples to the substrate. This is the reason why the thickness and the properties of the substrate material are important as much as the tenacity of the oxide film.

Both aluminum oxide and chromium oxide form immediately after deoxidizing the surfaces. They are strong and protective passive layers which preventing the aluminum and stainless steel substrate surfaces from corrosion. The following chemical formulas show the reactions between chromium and aluminum with oxygen.

$$2Cr + 3/2O_2 = Cr_2O_3 \qquad (6.2)$$

$$2Al + 3/2O_2 = Al_2O_3 \qquad (6.3)$$

The reactions (6.2) and (6.3) are characterized by their standard free-energy changes (ΔG^o). The standard free-energy changes must be negative in order for the reactions to proceed spontaneously from left to right. The standard free-energy changes for the aluminum oxide and the chromium oxide formations can be calculated as:

$$\Delta G^o = \Delta G^o\,(\text{products}) - \Delta G^o\,(\text{reactants}) \qquad (6.4)$$

$\Delta G^o\,(O_2) = 0$

$\Delta G^o\,(Al) = 0$

$\Delta G^o\,(Cr) = 0$

$\Delta G^o\,(Al_2O_3) = -\ 1582.3$ kJ/mol

$\Delta G^o\,(Cr_2O_3) = -\ 1058.1$ kJ/mol

The standard free-energy of formation for Equation (6.2) is:

$$\Delta G^o = \Delta G^o\,(Al_2O_3) - \{\ [\Delta G^o\,(Al)]^2 + [\Delta G^o\,(O_2)]^{3/2}\ \}$$

$$\Delta G^o = -\ 1582.3 - (\ 0 + 0\ ) = -\ 1582.3 \text{ kJ/mol} \qquad (6.5)$$

The standard free-energy of formation for Equation (6.3) is:

$$\Delta G^o = \Delta G^o\,(Cr_2O_3) - \{\ [\Delta G^o\,(Cr)]^2 + [\Delta G^o\,(O_2)]^{3/2}\ \}$$

$$\Delta G^o = -\ 1058.1 - (\ 0 + 0\ ) = -\ 1058.1 \text{ kJ/mol} \qquad (6.6)$$

A departure from standard condition is shown as followed:

$$\Delta G = \Delta G^o + RT \ln a_{(\text{oxide})} \,/\, (a_{(\text{metal})}{}^2)(PO_2{}^{3/2}) \qquad (6.7)$$

Where:

- R is the universal gas constant: 8.314 J/mol.k
- T is the absolute temperature: 298 °K at room temperature

- a is the activity: activity of pure solid in the stable form is equal to 1.00
- PO_2 is the partial pressure of oxygen: 0.2 atmosphere

Therefore the free-energy of formation for the aluminum oxide and chromium oxide can be calculated as followed:

$$\Delta G_{(Al2O3)} = -\ 1582.3\ \text{kJ/mol} - \{1.5(0.008314\ \text{kJ/mol.K})(298\text{K})\}\ \ln 0.2$$

$$\Delta G_{(Al2O3)} = -\ 1576.3\ \text{kJ/mol} \qquad (6.8)$$

$$\Delta G_{(Cr2O3)} = -\ 1058.1\ \text{kJ/mol} - \{1.5(0.008314\ \text{kJ/mol.K})(298\text{K})\}\ \ln 0.2$$

$$\Delta G_{(Cr2O3)} = -\ 1052.1\ \text{kJ/mol} \qquad (6.9)$$

The calculation results from (6.8) and (6.9) show that the ΔG (free-energy of formation) for the aluminum oxide is more negative. Therefore, the aluminum oxide is more stable[126 - 128].

Although, aluminum oxide forms more readily than chromium oxide, the shear test results of the solder joints from degreased specimens showed that the ultrasonic vibrations were able to break and remove the Al_2O_3 layers but not the Cr_2O_3 layers. It appears that, for the stainless steel specimens, there is a thicker chromium oxide layer, which strongly adheres to the substrate surfaces as well.

• A similar problem also exists for the chemically cleaned (deoxidized) specimens, as shown in Figures (4.1.12) and (4.1.16) for the Alclad specimens and Figures (4.1.35) and (4.1.36) for the stainless steel. Although the free-energy of oxide formation show that the Al_2O_3 oxidation reaction is far more stable than the Cr_2O_3 reaction, no chemical cleaning process used in this study could be found to permit wetting of the 304 stainless steel substrates. This may be due to the reaction kinetics of oxide formation.

The kinetics of oxide formation and growth is logarithmic, either direct or inverse for low temperature oxidation. The velocity of the oxide growth is expressed by Cabrera-Mott[129] as written in Equation (6.10).

$$dx / dt = N\Omega\nu \exp\{-(W-qaE) / KT\} \qquad (6.10)$$

Where: dx/dt is the reaction rate, N is the number of mobile ions that assumed to pass the passive layer once they entered into the oxide, Ω is the oxide volume, ν is the atomic vibration frequency, W is the energy barrier to the ion movement into the oxide layer, q is the ionic charge, a is the half of the ion jump distance, E is the electric field across the oxide layer, k is the Boltzmann's constant, and T is the absolute temperature. Ghez[130] has integrated the equation (6.10) to demonstrate the inverse logarithmic law:

$$x_1 / x = -\ln(t+\tau) / x^2 - \ln x_1 N\Omega\nu \exp(-W / KT) \qquad (6.11)$$

Where:

$$x_1 = \left| qv / KT \right|$$

$$v = E / x$$

The logarithmic and inverse logarithmic empirical oxidation rate laws are shown in Equations (6.12) and (6.13) respectively[131].

$$w = k_e \log(C\,t + A) \qquad (6.12)$$

$$1/w = C - k_i \log t \qquad (6.13)$$

where: w is the weight gain per unit area, k_e, C, A, and k_i are constants. The logarithmic behaviors are observed for the thin oxide layers (less than 0.1 micron) of aluminum, copper, iron, and some other metals at low temperature oxidation. This is generally explained by the fact that the ions transport across a thin oxide layer as the result of an electrical potential gradient. The parabolic rate laws are usually expected for high temperature oxidation. The mechanism of oxide film formation on a metallic surface can be explained in two steps. Adsorption of a two-dimensional oxygen layer on the metallic surface and nucleation and growth of three-dimensional islands of the oxide layers. The model of thin oxide film growth on low-temperature oxidation was also discussed by Fehlner[132]. The model is based on the electron tunneling. As soon as an oxide layer forms on the metallic surface, without thermal activation, the adsorbed oxygen atoms on the oxide surface will capture the electrons, which pass through the oxide layer, and create an electric field across the oxide film. This electric field decreases the activation energy for ion movement within the oxide layer and allows the oxide film to grow thicker. This must be a self-limiting process. Because the amount of electric charge is fixed, therefore the electric field across the oxide layers decreases when the oxide layer thickens. According to Fehlner[132], the kinetics of oxidation at low temperature depends on the structure of the oxide, which is considered as a network-former or a modifier. In network-forming oxides such as Al_2O_3, covalent bonds connect its atoms in a three-dimensional structure. The modifiers such as Cr_2O_3 have ionic bonding. Inverse logarithmic kinetics is usually expected for the network formers with a bond strength over 75 kcal/mol. The modifiers seem to follow the direct logarithmic kinetics law and their bond strength is below 50 kcal/mol. Figure 6.1 presents different oxidation rate laws. Where w is the weight gain per unit area, and t is time.

According to Kingery[133], the rate of diffusion of copper in Cu_2O, which is a modifier is six times bigger than that of aluminum in Al_2O_3, a network-forming oxide. This could be true for the rate of diffusion of Cr in Cr_2O_3 , which is also a modifier oxide. Therefore the velocity of oxidation for the chromium oxide as a modifier could be far higher than that for the aluminum oxide. In fact, this literature survey supports the idea that the rate of oxide growth after chemical cleaning of stainless steel is far faster than that of the aluminum and from a practical point of view, it may impractical to chemically clean stainless steel and expect any wetting by molten 70Sn-30Pb solder. Although Sn can react with Fe and Ni in the stainless steel to form intermetallic compounds, the Cr_2O_3 layer prevents any contact or wetting between the substrate and the molten solder. Therefore, practical soldering of stainless steel can only be achieved by plating the stainless steel substrate with Sn or other solder-compatible coating. The Sn-plating is always preceded by a Ni strike which replaces the Cr_2O_3 layer with a thin film of Ni which not only bonds the stainless steel to the Sn-plating but also provides a diffusion barrier during the subsequent soldering reactions.

The microstructure of the 70Sn-30Pb solder joints deposited on 2024 Alclad is typically a mixture of proeutectic Sn surrounded by eutectic Sn-Pb structure as shown in Figure (4.2.7). For further investigation concerning the effect of ultrasonic energy on the solder joint microstructure, two crucibles containing molten bulk solder were solidified with and without applying sonic energy. The results presented in Figures (4.2.10) and (4.2.11) confirm a dendrite microstructure for both cases with no effect on the microstructure as the result of applying the ultrasonic energy. For the chemically cleaned Alclad specimens, ultrasonically soldered at different temperatures, as shown in Figures 4.2.(12 to 15), dendritic microstructures with a mixture of proeutectic Sn surrounded by eutectic Sn-Pb structure are observed. Only in the thinnest joint, (which was ultrasonically soldered at 300 ^{o}C), the proeutectic Sn phase disappeared and a eutecticlike structure was maintained as shown in Figure (4.2.16). This may be due to the influence of the aluminum erosion on the Sn-Pb-Al ternary system, which caused the solidification parameter G/R to be changed. G is the temperature gradient and R is the growth velocity. A eutectic or eutecticlike microstructure can be obtained for the alloys with off-eutectic compositions (such as the 70Sn-30Pb solder alloy), if during the solidification, the stability of the solid-liquid interface in the plane front configuration is maintained. When the interface breaks down (instable interface), a dendrite structure will form as shown for the larger solder joint gaps. High values of G/R are necessary for the alloys with compositions far from their eutectic composition as shown in Figure (6.2), which is a plot of experimental results of Mollard and Fleming[134], on tin-lead alloys. These experimental results also show that, low values of G/R are sufficient to stabilize the solid-liquid interfaces for the alloys with compositions, that are close to their eutectic composition.

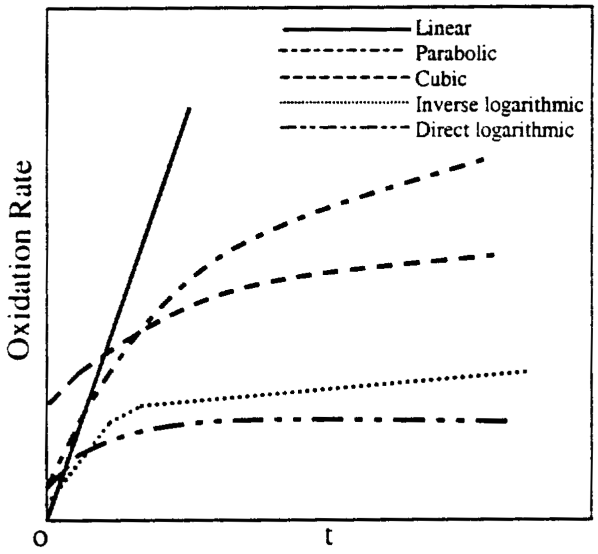

Figure 6.1 Oxidation rate laws for metals and alloys.

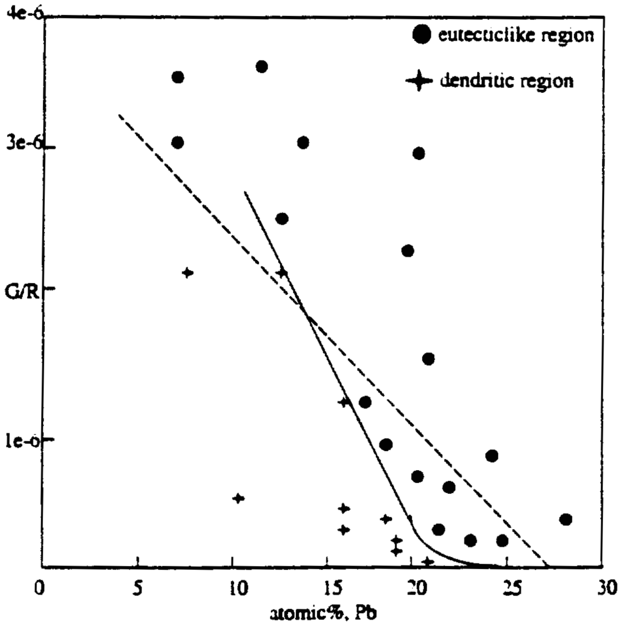

Figure 6.2 Plane front stability in Sn-Pb alloys.

It is true that increasing the temperature of a liquid will change its viscosity. For a molten solder, the viscosity changes would affect the joint thickness. The SEM secondary images of different solder joint microstructures which are ultrasonically soldered without flux at different temperatures, presented in Figures 4.2.(12 to 15), confirm that the thickness of the joint decreases when the soldering temperature increases as also shown in Fgiure (4.2.16).

The results on flux-free ultrasonic tinning by Hosking et al[20] indicate that the solder wetting pattern has the annular morphology and the substrate surface will be eroded by the cavitation erosion action accordingly. The same results concluded in this study confirms the annular morphology of the solder wetting pattern. The cavitation action causes erosion on the substrate surface where the bubbles are collapsed. Figures (4.2.18) and (4.2.19) show the results.

Dissolution of the base material into the molten solder during a soldering operation is a factor affecting the wetting and consequently the joint mechanical properties. The amount of the dissolution depends on the solubility of the base material's constituents into molten solder according to their binary and ternary phase diagrams. In the ultrasonic soldering operation, the substrate surface could be also eroded as a result of the cavitation action and the severity of the erosion. The amount of dissolution depends on the soldering time in which the ultrasonic energy is applied. Work done by Fujii[65] for joining copper pipes to aluminum pipes using ultrasonic soldering indicates that if ultrasonic vibration continued too long, then the end portion of the aluminum pipe could dissolve into molten solder. The x-ray microanalysis results in this study also showed that the aluminum substrate dissolved into molten solder in the absence of the nickel strike. Figure (4.2.22) is the micrograph of the nickel strike, which is usually plated before the tin-plating. Figures 4.2.(23-24) and their related Tables (4.2.8) and (4.2.9) present the compositions of the solder joints with and without the Ni strike layer. The nickel strike on the substrate surface as shown in Figure (4.2.20) has two major roles:

- Create a pristine surface for the substrate.

- Work as a barrier which prevents the diffusion of the base material constituents into the molten solder and consequently in the joint.

As previously discussed, the changes in the soldering temperature will affect the joint thickness. Work done by Manko[8] on the soldering of brass with 60Sn-30Pb solder alloy and in presence of strong flux also indicated that there is an optimum solder joint thickness in which the joint strength is at maximum. This optimum point is reported to be around 0.003 inches (0.076 mm). The results of the electron microscopy and shear testing on the ultrasonically soldered (flux-free) aluminum specimens in this study also showed that the solder joint thickness will change as the soldering temperature changes and the joint thickness influences the joint strength.

Therefore, in ultrasonic soldering of 2024 Alclad and 304 stainless steel, the most important factors affecting bond strength are:

- Tenacity of the oxide layer of the substrate
- Tin-plating of the substrate
- Soldering temperature
- Atmosphere during soldering
- Time of ultrasonic activation while the solder is molten
- Erosion of the substrate

The tenacity of the Cr_2O_3 layer appeared to so great as to completely prevent the wetting of the stainless steel substrate; while the Al_2O_3 layer could be altered by chemical cleaning to permit extensive wetting by the ultrasonic soldering. When both 2024 Alclad and stainless steel substrates were chemically cleaned, the rate of regrowth of the Cr_2O_3 oxide layer was much faster than that for the Al_2O_3 layer. Thus, stainless steel could not be wet by ultrasonic soldering with 70Sn-30Pb regardless of the atmosphere, soldering temperature or time. Only Sn-plating provide a suitable substrate for soldering because all plating procedures effectively remove the oxide layers of the substrate. Even though higher soldering temperatures (up to 300 °C), greater ultrasonic soldering times and the use of argon shielding during soldering all contributed to increased joint strength of chemically cleaned 2024

Alclad, no bonding of the stainless steel substrate was observed. Thus, 2024 Alclad could be readily ultrasonically soldered with or without tin-plating; while the stainless steel substrate could not be soldered unless ultrasonic soldering was preceded by Sn-plating using a Ni strike. The erosion of the substrate by the action of ultrasonic soldering was also possible. The phase diagram for Al-Sn suggests that the maximum possible erosion of aluminum in the solder pool is only about 2% Al and no intermetallic compounds between Al and Sn are possible. In this investigation, 1% erosion of the aluminum substrate in the solder pool was observed only for the chemically cleaned specimen, which ultrasonically soldered at 300 ^{o}C for 12 seconds. When the substrate was Sn-plated, the Ni strike did potentially remain a diffusion barrier to the action of the ultrasonic soldering. There was no dissolution of the aluminum substrate into the molten solder and consequently in the joint.

An ANSYS numerical simulation was employed to investigate the effects of joint strength changing with thickness in relation to the maximum stress concentration along the joint. The maximum shear stresses and von Mises stresses for different joint gaps are simulated in linear elastic and elasto-plastic approaches. The maximum von Mises stress concentrated along the joint (most cases located at two ends) in both elastic and elasto-plastic approaches presented in Figures (5.3.16), (5.3.19), and (5.3.22), under three different constant loads, indicate that there is an optimum joint thickness in which the stress is at minimum. This optimum joint spacing is changing, depending on the applied load and the simulation approach (elastic or elasto-plastic). In fact minimum stress concentration simulated for a particular joint (with an optimum joint gap) in comparison with the others, shows that this joint can endure higher stress to break down. Overall simulation results show that the maximum von Mises stresses simulated in the elasto-plastic approach are in agreement with the experimental results. Because in the von Mises yield criterion, yielding is not dependent on any particular normal stress or shear stress, but it is a function of all three values of principal shearing stress. The advantage of using von

Mises yield criterion is that there is no need to know which are the largest and smallest stresses since the von Mises or equivalent stress is computed in square terms and it is independent of the sign of the individual stresses. At the same time the elasto-plastic approach is quite applicable since the nominal strengths of the base materials used in this study (aluminum alloy and stainless steel) are much higher than the bulk solder alloy.

The experimental results for chemically cleaned aluminum specimens, ultrasonically soldered at different soldering temperatures (between 200 ° to 300 °C) showed that by increasing the soldering temperature, the joint thickness decreases in the range between 0.0002 to 0.002 inches (0.0051 to 0.051mm) and the joint strength increases. The comparison between the experimental results from Manko[8] and the simulation presented in Figure (5.3.27) indicate that there is an optimum joint spacing in which the joint strength is at maximum or the stress concentration at a minimum. At the same time, the results from this study shown in Figure 4.2.17, maintained that an increase in joint spacing decreases the joint strength. This is because, in this study the only factor affecting the joint gap was the temperature. The greater the soldering temperature, the higher is the viscosity of the molten solder and lower the joint gap. Therefore, for the specimens which were ultrasonically soldered without flux at low temperatures, not only the joint gap increased but also the wetting percentage decreased. This is because the wetting percentage is relatively low in flux-free ultrasonic soldering specially at low temperatures. Therefore, the experimental shear results can not be compared to the results from Manko[8] (using strong flux), where 100% wetting achieved.

Conclusions

This study was performed to examine the use of ultrasonic activation for soldering of aluminum and stainless steel without the need of a fluxing agent. Experimental results were also compared with the computer modeling outcomes using ANSYS numerical approach to evaluate strength of the joints with different gap size.

1. Fluxless ultrasonic soldering of aluminum and stainless steel by transmitting the sonic energy through a solid medium is feasible.

2. The highest joint strength is achieved for the chemically cleaned aluminum specimens. It was not the case for the stainless steel specimens.

3. Oxide formation and its growth on the substrate surface or on a tin-plated surface will affect the wetting and the joint strength.

4. Increasing the soldering temperature or time and protecting the surfaces from oxidation improve wetting and the joint strength.

5. By increasing the ultrasonic soldering temperature, the joint thickness decreases.

6. Dissolution of the aluminum substrate into molten solder is mainly caused by the cavitation action and it depends on the soldering temperature, soldering time and the substrate material properties .

7. Simulation results confirm that there is an optimum joint thickness in which the stress concentration is minimized. However the experimental results from this study are not in agreement with the simulation results.

REFERENCES

1. Michael G. Pecht. Soldering Process and Equipment. John Wiley & Sons, 1993 pp. 1,14,15.
2. P.T. Vianco. General Soldering. ASM Handbook. Vol. 6, 1993, pp. 964-972.
3. J.L. Schuster and R.J. Chilko. Ultrasonic Soldering of Aluminum Heat Exchangers. Welding Journal, Vol. 54, No. 10, 1975, pp. 711-717.
4. J.N. Antonevich. Fundamentals of Ultrasonic Soldering. Welding Journal Supplement, Vol. 55, No. 7, 1976, pp. 200s-207s.
5. A. Rabinkin and Howard H. Liebermann. Brazing and Soldering with Rapidly Solidified Alloys. Allied Signal Advanced Materials, Parsippany, New Jersey, pp. 691-697.
6. M.M. Schwartz. Fundamentals of Soldering. ASM Handbook, Vol. 6, 1993, pp. 126-129.
7. S.D. Brandi. S. Liu. J.E. Indacochea. R. Xu. Brazeability and Solderability of Engineering Materials. ASM Handbook, Vol. 6, 1993, pp. 619-623.
8. Howard H. Manko. Solders and Soldering. 3rd Edition, McGraw-Hill, 1992, pp. 1,10,11,373,385.
9. J. Haimovich. Intermetallic Compound Growth in Tin and Tin-Lead Plating Over Nickel and It's Effects on Solderability. Welding Research Supplement, 1989, pp. 102s-104s.
10. H.L. Reynolds. J.W. Morris, Jr. The Role of Cu-Sn Intermetallics in Wettability Degradation. Journal of Electronic Materials, Vol. 24, No. 10, 1995, pp. 1429-1434.
11. D.R. Frear. F.M. Hosking. P.T. Vianco. Mechanical Behavior of Solder Joint Interfacial Intermetallics. Materials Developments in Microelectronic Packaging Conference Proceedings, Montreal, Quebec, Canada, 1991, pp. 229-231.

12. R.J. Fields. S.R. Low III. G.K. Lucey, Jr. Physical and Mechanical Properties of Intermetallic Compounds Commonly Found in Solder Joints. Minerals & Materials Society, 1992, pp. 165-172.

13. W.M. Wolverton. The Mechanisms and Kinetics of Solder Joint Degradation. Brazing & Soldering, No. 13, 1987, pp. 33-38.

14. D.R. Frear. W.B. Jones. K.R. Kinsman. Solder Mechanics. Metals & Materials Society, 1991, pp. 2-6, 30-32.

15. F. Bartels. J.W. Morris, Jr. Intermetallic Phase Formation in Thin Solid-Liquid Diffusion Couples. Journals of Electronics Materials, Vol. 23, No. 8, 1994, pp. 787-790.

16. S.K. Kang. R.S. Rai. S. Purushothman. Interfacial Reactions During Soldering with Lead-Tin Eutectic and Lead-Free, Tin-Rich Solders. Journal of Electronics Materials, Vol. 25, No. 7, 1996, pp. 1113-1120.

17. Wenge Yang. Robert W. Messler, Jr. Microstructure Evolution of Eutectic Sn-Ag Solder Joints. Journal of Electronic Materials, Vol. 23, No. 8, 1994, pp. 765-772.

18. Sun K. Kang. Amitk Sarkhel. Lead-Free Solders for Electronic Packaging. Journal of Electronic Materials, Vol. 23, No. 8, 1994, pp. 701-707.

19. M.K. Hoffmeyer. J.H. Perepezko. Solidification Structure Development and Substrate Interactions in Solder Alloys. The Metal Science of Joining, Edited by M. J. Cieslak. J. H. Perepezko. S. Kang and M. E. Glicksman, Minerals, Metals & Materials Society, 1992, pp. 73-82.

20. F.M. Hosking. D.R. Frear. P.T. Vianco. David M. Keicher. Fluxless Soldering as an Environmentally Compatible Manufacturing Alternative. International Journal of Environmentally Conscious Manufacturing, Vol. 1, No. 1, 1992, pp. 53-64.

21. R. L. Hunicke. Ultrasonic Soldering Pots for Fluxless Production Soldering. Welding Journal, Vol. 55, No. 3, 1976, p. 194.

22. U.S. Patent No. 4763829. Soldering of Electronic Components. W. Sherry, AT&T Bell Laboratories, Aug. 1998.

23. U.S. Patent No. 5762257. Device for Flux-Free Soldering. Garrecht and Ewald, ERSA Lottechnik GMBH, June 1998.

24. R. Kurtz. Ultrasonics Replace Flux. Electronic Production, Vol. 24, No. 7, 1995, pp. 17-21.

25. U.S. Patent No. 288521. Selective Removal of Single Solder Ball From an Array of Solder Balls Using Ultrasonics. International Business Machines Corp., Aug 10, 1994.

26. J.A. Biancini. Chip Mounting Technology. Surface Mount International, Vol. 1, 1993, pp. 17-34.

27. D.W. Chu and D.S. Shen. Maskless Flip Chip Solder Bumping Technique. Proceedings of 43rd Electronic Components and Technology Conference, IEEE, New York, 1993, pp. 610-614.

28. T. Ogashiwa, T. Arikawa. H. Murai. A. Inoue and T. Masumoto. Reflowable Sn-Pb Bump Formation on Al Pad by a Solder Bumping Method. Proceedings of 45th Electronic Components and Technology Conference, IEEE, New York, 1995, pp. 1203-1208.

29. P. Saxty. Ultrasonic Soldering in the Electronics Industry. Metallurgia, Vol. 62, No. 8, 1995, p. 287.

30. F.M. Hosking. Soldering Technologies for Environmentally Conscious Manufacturing. Welding Journal, Vol. 75, No. 2, 1996, p. 106.

31. J.L. Jellison. J. Golden. D.R. Fear. F.M. Hosking. D.M. Keicher and F.G. Yost. Advanced Soldering Processes. The Mechanics of Solder Alloy Wetting and Spreading, Ed: F.G. Yost, F.M. Hosking, and F.M. Frear, Van Nostrand Reinhold, 1993, pp. 227-266.

32. P.T. Vianco. F.M. Hosking and J.A. Rejent. Ultrasonic Soldering for Structural and Electronic Applications. Welding Journal, Vol. 75(11), 1996, pp. 343s-355s.

33. Encyclopedia of Materials Science and Engineering, Volume 6, Pergamon Press, 1986, p. 4489.

34. Soldering Manual. Second Edition. American Welding Society, 1977, pp. 1-3.

35. Michael Santella. Fundamental Metallurgical in Brazing and Soldering. Minerals, Metals & Materials Society, 1992, pp. 61-64.

36. A.W. Adamson. Physical Chemistry of Surfaces. 4th Edition, John Wiley & Sons, 1992, pp. 260-289.

37. Neil Kensington Adam. The Physics and Chemistry of Surfaces. 3rd Edition, Oxford University Press, 1941, pp. 169-178.

38. D.P. Woodruff. The Solid-Liquid Interface. Cambridge University Press, 1973, pp. 1-11.

39. V.K. Semenchenko. Surface Phenomena in Metals and Alloys. Pergamon Press, Ltd., 1962, pp. 37-41.

40. Alvin Hudson. Rex Nelson. University Physics. Harcourt Brace Jovanovich, 1982, pp. 370-372.

41. I.A. Aksay. Carl E. Hoge. and Joseph A. Pask. Wetting Under Chemical Equilibrium and Non-equilibrium Conditions. Journal of Physical Chemistry, Vol. 78, No. 12, 1974, pp. 1178-1183.

42. Rulon E. Johnson, Jr. Conflicts Between Gibbsian Thermodynamics and Recent Treatments of Interfacial Energy in Solid-Liquid-Vapor Systems. Journal of Physical Chemistry, Vol. 63, 1959, pp. 1655-1658.

43. Ralph W. Woodgate. Handbook of Machine Soldering. 3rd Edition, John Wiley & Sons, 1996, pp. 36-38.

44. C.J. Thwaites. Soft-Soldering Handbook. International Tin Research Institute, [1977?], pp. 7-11,20-22,35-41.

45. Brazing Handbook. American Welding Society, 4th Edition, 1991, pp. 43-45.

46. M. McCormack and S. Jin. New, Lead-Free Solders. Journal of Electronic Materials, Vol. 23, No. 7, 1994, pp. 635-640.

47. Chad M. Miller. Iver E. Anderson. and Jack F. Smith. A Viable Tin-Lead Solder Substitute: Sn-Ag-Cu. Journal of Electronic Materials, Vol. 23, No. 7, 1994, pp. 595-601.

48. E.P. Wood and K.L. Nimmo. In Search of New Lead-Free Electronic Solders. Journal of Electronic Materials, Vol. 23, No. 8, 1994, pp. 709-713.

49. I. Artaki and A.M. Jackson. Evaluation of Lead-Free Solder Joints in Electronic Assemblies. Journal of Electronic Materials, Vol. 23, No. 8, 1994, pp. 757-764.

50. M. McCormack. S. Jin and H.S. Chen. New Lead-Free Sn-Zn-In Solder Alloys. Journal of Electronic Materials, Vol. 23, No. 7, 1994, pp. 687-690.

51. S. Jin and M. McCormack. Dispersoid Additions to a Pb-Free Solder for Suppression of Microstructural Coarsening. Journal of Electronic Materials, Vol. 23, No. 8, 1994, pp. 735-739.

52. M. McCormack and S. Jin. Improved Mechanical Properties in New, Pb-Free Solder Alloys. Journal of Electronic Materials, Vol. 23, No. 8, 1994, pp. 715-720.

53. Lenora Quan. Darrel Frear. Dennis Grivas. J.W. Morris, Jr. Tensile Behavior of Pb-Sn Solder / Cu Joints. Journal of Electronic Materials, Vol. 16, No. 3, 1987, pp. 203-208.

54. D.B Martin and W. R. Merwarh. Theory and Applications of Solder Joint Fractography. Proceedings Second Annual Technical Meeting, International Metallography Society, 1969, pp. 211-222.

55. J.M. Parsey, Jr. K. Kyler. W. Cronin. P. Mobley. B.L. Scrivner. S. Valocchi. and L. Sue. Investigation of Sn-Pb-Ag Solder for Die Attach of GAHS Devices. Journal of Electronic Materials, Vol. 25, No. 11, 1996, pp. 1715-1724.

56. Susanne Ohlsson. The Effect of Pre-Tinning on the Strength of a Chip Carrier Solder Joint. Quality and Reliability Engineering International, Vol. 4, 1988, pp. 215-221.

57. D. Tribula. D. Grivas and J.W. Morris, Jr. Stress Relaxation in 60Sn-40Pb Solder Joints. Journal of Electronic Materials, Vol. 17, No. 5, 1988, pp. 387-390.

58. C.A. Mackay. C.J. Thwaites. Some Effects of Solder Joint Geometry on Mechanical Strength. Welding and Metal Fabrication, Vol. 45, No. 1, 1977, pp. 52-56.

59. High-speed Ultrasonic Soldering of Aluminum Air Condition Coils. Industrial Heating, Vol. 46, No. 6, 1979, pp. 42-43, 46.

60. V.P. Panov et. al. Ultrasonic Soldering Heat Exchanging Equipment Made of Aluminum Alloys. Welding Production, (USSR), Vol. 32, No. 2, 1985, pp. 21,22.

61. D. Odlschlagel. H. Abe, K. Yamaji. and Y. Yonezawa. Ultrasonic Soldering Method for Copper-Aluminum Pipe Joints. Welding Journal, Vol. 56, No. 4, 1977, pp. 20-27.

62. M.M. Schwartz. Ultrasonic Soldering. Welding Research Council, Bulletin 244, 1978, pp. 2-5.

63. Alcoa Aims Ultrasonic Soldering Process at Air Condition Biz. Modern Metals, Vol. 28, No. 8, 1972, p. 61.

64. High-speed Ultrasonic Soldering of Aluminum Air Condition Coils. Industrial Heating, Vol. 46, No. 6, 1979, pp. 42,43,46.

65. John Fujii. Hitachi Develops Process for Joining Aluminum, Copper Pipes by Way of Ultrasonic Soldering. American Metal Market, Vol. 86, No. 15, 1978, p. 19.

66. Masaaki Naka. Hiroshi Taniguchi. Ultrasonic Soldering of Aluminum to Copper Using Sn-Pb Solder. Transaction of Japan Welding Research Institute (Published by Welding Research Institue), Vol. 20, No. 2, 1992, pp. 113-118.

67. The Techniques of Ultrasonic Soldering. Sub-Assembly, Components, Fastening. Vol. 10, No. 7, 1992, pp. 37-38.

68. Gary Flood. Ultrasonic Energy Welds Copper to Aluminum. Welding Journal, Vol. 76, No. 1, 1997, pp. 43-45.

69. C.L. Estes. P.W. Turner. Ultrasonic Closure Welding of Small Aluminum Tubes. Welding Research Supplement, Vol. 52, No. 8, 1973, pp. 359s-369s.

70. A.A. Grachev. A.P. Mantulo. Some of the Special Features of Soldering and Ultrasonic Welding Rigid Lead-Outs From the Active Components of Micro-Devices with Pulsed Preheat. Avtomaticheskaia Svarka, No. 8, 1973, pp. 71-73.

71. Mike Judd and Keith Brindley. Soldering in Electronics Assembly, Newnes Publishing, 1992, pp. 15-19.

72. Leo P. Lambert. Soldering for Electronic Assemblies, Marcel Dekker, Inc., 1988, pp. 269-309.

73. C.H. Lee. Y.M. Wong. C. Doherty. K.L. Tai. E. Lane. D.D. Bacon. F. Baiocchi and A. Katz. Study of Ni as a Barrier Metal in AuSn Soldering Application for Laser Chip/Submount Assembly. Journal of Applied Physics, Vol. 72, No. 8, 1992, pp. 3808-3815.

74. M. McCormack. I. Artaki. S. Jin. A.M. Jackson. D.M. Machusak. G.W. Kammlott. and D.W. Finley. Wave Soldering with a Low Melting Point Bi-Sn Alloy: Effects of Soldering Temperatures and Circuit Board Finishes. Journal of Electronic Materials, Vol. 25, No. 7, 1996, pp. 1128-1131.

75. R.L. Williams and A.W. Noblett. Tailored Coefficient of Thermal Expansion Printed Wiring Boards to Improve the Solder Joint Life of Leadless Ceramic Chip Carriers. First International SAMPE Electronics Conference, Santa Clara, California, 1987, pp. 30-32.

76. Don Swanson. Ultrasonic Replaces Flux in Wave Soldering. Electronic Packaging and Production, Vol. 35, No. 4, 1995, p. 26.

77. Michihiko Inaba. Koji Yamakawa and Nobuo Iwase. Solder Bump Formation Using Electroless Plating and Ultrasonic Soldering. IEEE Transactions on Components, Hybrids and Manufacturing Technology, Vol. 13, No. 1, 1989, pp. 119-123.

78. S.J. Horowitz. D.J. Gerry and R.E. Cote. Alloy Element Additions to Gold Thick Film Conductors: Effects on Indium-Lead Soldering and Ultrasonic Aluminum Wire Bonding. Solid State Technology, 1978, pp. 47-54.

79. V.M. Koleshko. V.S. Galkov. Effect of Amplitude of Oscillations on the Quality of the Ultrasonic Soldering of Semiconducting Crystals to Gold-Plated Objects. Avtomaticheskaia Svarka, No. 12, 1969, pp. 24-26.

80. R.B. Cinque. J.W. Morris, Jr. The Effect of Gold-Nickel Metallization Microstructure on Fluxless Soldering. Journal of Electronic Materials, Vol. 23, No. 6, 1994, pp. 533-539.

81. A.J. Sunwoo. J.W. Morris, Jr. G.K. Lucey, Jr. Solderability of Pre-Tinned Cu Sheet. Journal of Electronic Materials, Vol. 21, No. 5, 1992, pp. 549-557.

82. E.I. Stromswold. R.E. Pratt. D. J. Quesnel. Capillary Soldering System for the Material Property Characterization of Solder Joints. Review of Scientific Instrument (USA), Vol. 64, No. 11, 1993, pp. 3314-3320.

83. William J. Boettinger. Carol A. Handwerker. and Leonard C. Smith. On the Wetting of the Intermetallic Cu_6Sn_5 and Cu_3Sn by Pb-Sn Alloys. The Metal Science of Joinig, Edited by M.J. Cieslak. J.H. Perepezko. S. Kang and M.E. Glicksman. Minerals, Metals & Materials Society, 1992, pp. 183-189.

84. Tamar A. Powers. Role of Tin Content in the Wetting of Cu and Au by Tin-Bismuth Solders. Journal of Electronic Materials, Vol. 23, No. 8, 1994, pp. 773-778.

85. T.P. Yin. The Kinetics of Spreading. Journal of Physical Chemistry, Vol. 73, No. 7, 1969, pp. 2413, 2417.

86. M.E. Loomans. S. Vaynman. G. Ghosh and M.E. Fine. Investigation of Multi-Component Lead-Free Solders. Journal of Electronic Materials, Vol. 23, No. 8, 1994, pp. 742-744.

87. R. Strauss. SMT Soldering Handbook, 2nd Edition, Newnes Publishing, 1998, p. 36.

88. I.A. Aksay. C.E. Hoge and J.A. Pask. Wetting Under Chemical Equilibrium and Non-Equilibrium Conditions. Journal of Physical Chemistry, Vol. 78, No. 12 1974, pp. 1178-1183.

89. J.F. Lancaster. Metallurgy of Welding. Allen & Unwin, 1987, pp. 120-122.

90. Gerhard Welsch. Pramond D. Desai. Oxidation and Corrosion of Intermetallic Alloys. Purdue Research Foundation, 1996, pp. 2,3.

91. H. Wiedersich. M. Meshii. Science of Advanced Materials. Conference, Chicago, Illinios, 1988. Source: ASM International, 1990, p. 492.

92. N.S. Stoloff. C.C. Koch. C.T. Liu and O. Izumi. High Temperature Ordered Intermetallic Alloys. Materials Research Society Symposia Proceedings, Vol. 81, 1987, pp. 3-5.

93. C.H. Raeder. L.E. Felton. V.A. Tanzi and D.B. Knorr. The Effect of Aging on Microstructure, Room Temperature Deformation, and Fracture of Sn-Bi/Cu Solder Joints. Journal of Electronic Materials, Vol. 23, No. 7, 1994, pp. 611-617.

94. Darrel Frear. Dennis Grivas. J.W. Morris, Jr. The Effect of Cu_6Sn_5 Whisker Precipitates in Bulk 60Sn-40Pb Solder. Journal of Electronic Materials, Vol. 16, No. 3, 1987, pp. 181-186.

95. Dennis Gravis. Darrel Frear. Lenora Quan and J.W. Morris, Jr. The Formation of Cu_3Sn Intermetallic on the Reaction of Cu with 95Pb-5Sn Solder. Journal of Electronic Materials, Vol. 15, No. 6, 1986, pp. 355-359.

96. M. Schaefer. W. Laub,. J.M. Sabee and R.A. Fournelle. A Numerical Method for Predicting Intermetallic Layer Thickness develop During the formation of Solder joints. Journal of Electronic Materials, Vol. 25, No. 6, 1996, pp. 995-1003.

97. Paul T. Vianco. Paul F. Hlava and Alice C. Kilgo. Intermetallic Compound Layer Formation Between Copper and Hot-Dipped 100In, 50In-50Sn, 100 Sn and 63Sn-37Pb Coatings. Journal of Electronic Materials, Vol. 23, No. 7, 1994, pp. 583-594.

98. P.T. Vianco. K.L. Erickson and P.L. Hopkins. Solid State Intermetallic Compound Growth Between Copper and High Temperature, Tin-Rich Solders. Journal of Electronic Materials, Vol. 23, No. 8, 1994, pp. 721-727.

99. D. Frear. D. Grivas. J.W. Morris, Jr. A Microstructure Study of the Thermal Fatigue Failures of 60Sn-40Pb Solder Joints. Journal of Electronic Materials, Vol. 17, No. 2, 1988, pp. 171-180.

100. J.L. Freer Goldstein and J.W. Morris, Jr. Microstructural Development of Eutectic Bi-Sn and Eutectic In-Sn During High Temperature Deformation. Journal of Electronic Materials, Vol. 23, No. 5, 1994, pp. 477-486.

101. Wenge Yang. Lawrence E. Felton and R.W. Messler, Jr. The Effect of Soldering Process Variables on the Microstructure and Mechanical Properties of Eutectic Sn-Ag/Cu Solder Joints. Journal of Electronic Materials, Vol. 24, No. 10, 1995, pp. 1465-1472.

102. P.L. Hacke. A. F. Sprecher and H. Conrad. Microstructure Coarsening During Thermo-Mechanical Fatigue of Pb-Sn Solder Joints. Journal of Electronic Materials, Vol. 26, No. 7, 1997, pp. 774-782.

103. Y.C. Chan. D.J. Xie. J.K.L. Lai. Characteristics of Porosity in Solder Pastes During Infrared Reflow Soldering, Journal of Materials Science. Vol. 30, 1995, pp. 5543-5550.

104. M.P. Seah and C. Lea, Certainty of Measurement Using an Automated Infrared Laser Inspection Instrument for PCB Solder Joint Integrity, Journal of Physics. Electronics, Scientific Instruments, Vol. 18, 1995, pp. 676-682.

105. D.E. Helling and Boon Wong. Applying a Physics-of-Failure Model to Predicting Surface Mount Solder Joint Reliability. Quality and Reliability Engineering International, Vol. 7, No. 5, 1991, pp. 403-410.

106. Kozo Shimizu. Teru Nakanishi. Kazuaki Karasawa. Solder Joint Reliability of Indium-Alloy Interconnection. Journal of Electronic Materials. Vol. 24, No. 1, 1995, pp. 39-45.

107. Robert Darveaux and K. Linga Murty. Effect of Deformation Behavior on Solder Joint Reliability Prediction. First International Conference on Microstructures and Mechanical Properties of Aging Materials. Minerals, Metals & Materials Society, 1993, pp. 399-408.

108. H.K. Kim. H.K. Liou and K.N. Tu. Three-dimensional Morphology of a Very Rough Interface Formed in the Soldering Reaction Between Eutectic Sn-Pb and Cu. Applied Physics Letters, Vol. 66, No. 18, 1995, pp. 2337-2339.

109. D.R. Liu and Yi-Hsin Pao. Fatigue-Creep Crack Propagation Path in Solder Joints Under Thermal Cycling. Journal of Electronic Materials, Vol. 26, No. 9, 1997, pp. 1058-1064.

110. H. Mavoori. J. Chin. S. Vaynman. B. Moran. L. Keer and M. Fine. Creep, Stress Relaxation, and Plastic Deformation in Sn-Ag and Sn-Zn Eutectic Solders. Journal of Electronic Materials, Vol. 26, No. 7, 1997, pp. 783-790.

111. Harvey D. Solomon. The Creep and Strain Rate Sensitivity of a High Pb Content Solder with Comparisons to 60Sn-40Pb Solder. Journal of Electronic Materials, Vol. 19, No. 9, 1990, pp. 929-936.

112. John. H. Lau. Donald W. Rice. Solder Joint Fatigue in Surface Mount Technology. Solid State Technology, Vol. 28, No. 10, 1985, pp. 91-104.

113. Z. Mei. D. Grivas. M.C. Shine and J.W. Morris, Jr. Superplastic Creep of Eutectic Tin-Lead Solder Joints. Journal of Electronic Materials, Vol. 19, No. 11, 1990, pp. 1273-1280.

114. Giles Humpston and David M. Jacobson. Principles of Soldering and Brazing. ASM International, 1993, pp. 134-137.

115. S.J. Nightingale. Tin Solders: A Modern Study of the Properties of Tin Solders and Solder Joints. Second Edition. Chemical Publishing Co., 1942, pp. 61-71.

116. M. Manoharan. K.S. Siow and M.W. Weiser. On the Shear Strength and Mixed-Mode Fracture Toughness of a Lead-Tin and a Tin-Silver Solder. Materials Research Society Symposium Proceedings, Vol. 515, 1998, pp. 111-116.

117. Amos Gilat and Kavita Krishna. Testing Eutectic Tin-Lead Solder in Pure Shear. Proceedings of the 1993 ASME International Electronics Packaging Conference. Series: EEP, Advances in Electronic Packaging, American Society of Mechanical Engineers, Vol.4-2, 1993, pp. 1017-1018.

118. John W. Winslow. Some Observations of Solder Joint Failure Under Tensile-Compressive Stress. Proceedings of the 1993 ASME International Electronics Packaging Conference. Series: EEP, Advances in Electronic Packaging, American Society of Mechanical Engineers, Vol. 4-2, 1993, pp. 1019-1029.

119. D.B. Barker. Vineet K. Gupta. and Kevin Cluff. Solder Joint Crack Initiation and Crack propagation in a TSOP Using Strain Energy Partitioning. Proceedings of the 1993 ASME International Electronics Packaging Conference. Series: EEP, Advances in Electronic Packaging, American Society of Mechanical Engineers, Vol. 4-2, 1993, pp. 943-949.

120. Pardeep K. Bhatti. Klaus Gschwend. Abel Y. Kwang and Ahmer R. Syed. Computer Simulation of Leaded Surface Mount Devices and Solder Joints in a Thermal Cycling Environment. Proceedings of the 1993 ASME International Electronics Packaging Conference. Series: EEP, Advances in Electronic Packaging, American Society of Mechanical Engineers, Vol. 4-2, 1993, pp. 1047-1053.

121. A. Dasgupta. S. Ling. and S. Verma. A Generalized Stress Analysis Model for Fatigue Prediction of Surface Mount Solder Joint. Proceedings of the 1993 ASME International Electronics Packaging Conference. Series: EEP, Advances in Electronic Packaging, American Society of Mechanical Engineers, Vol. 4-2, 1993, pp. 979-985.

122. T.R. Chandrupatla and A.D. Belegundu. Introduction to Finite Elements in Engineering. Prentice-Hall, 1991, pp. 1-19.

123. William B. Bickford. A First Course in the Finite Element Method. Richard D.Irwin, 1990, pp. 1-20.

124. K. H. Huebner. E.A. Thornton. T. G. Byrom. The Finite Element Method for Engineers. Third Edition. John Wiley & Sons, 1995, pp. 203, 572-575.

125. Donald R. Askeland. The Science and Engineering of Materials. Alternate Edition. PWS Publishers, 1985, pp. 311-313.

126. Kirk-Othmer. Encyclopedia of Chemical Technology. Fourth Edition. John Wiley & Sons, Vol.2, pp. 188-190.

127. Donald D. Wagman. The NBS Tables of Chemical Thermodynamic Properties. Journal of Physical and Chemical Reference Data, Vol. 11, Supplement No. 2, 1982, pp. 2-37, 2-127, 2-197.

128. Denny A. Jones. Principles and Prevention of Corrosion. Second Edition. Prentice-Hall, Inc., 1992, pp. 399-437.

129. N. Cabrera and N.F. Mott. Theory of the Oxidation of Metals. Reports on Progress in Physics, Vol.12, 1948-1949, pp. 163-184.

130. Richard Ghez. On the Mott-Cabrera Oxidation Rate Equation and the Inverse-Logarithmic Law. Journal of Chemical Physics, Vol. 58, No. 5, 1973, pp. 1838-1843

131. Mars G. Fontana. Corrosion Engineering. Third Edition. McGraw-Hill, 1986, pp. 512-517.

132. Francis P. Fehlner. Michael J. Graham. Thin Oxide Film Formation on Metals. Corrosion Mechanisms in Theory and Practice, By P. Marcus. J. Oudar. Marcel Dekker, Inc., 1995, pp. 123-140.

133. W. D. Kingery. H. K. Bowen and D. R. Uhlmann. Introduction to Ceramic. Second Edition. Wiley, New York, 1976, p. 240.

134. F. R. Mollard. M. C. Flemings. Growth of Composites from the Melt – Part I. Transactions of the Metallurgical Society of AIME, Vol. 239, No. 10, 1967, pp. 1526-1533.